JÜLICH
FORSCHUNGSZENTRUM

Peter Grünberg Institute
Bioelectronics

Low-frequency noise and transport characteristics of nanostructures

Viktor Sydoruk

2011

Mitglied der Helmholtz-Gemeinschaft

Low-frequency noise and transport characteristics of nanostructures

Vorgelegt in der Fakultät Physik der Technishe Universität Dortmund zur Erlangung des akademischen Grades eines Doktors der Naturwissenschaften

von

Master of Science

Viktor A. Sydoruk

aus Kovel, Ukraine

Erstgutachter: Prof. Dr.rer.nat Dmitri Yakovlev
Zweitgutachter: Prof. Dr.rer.nat Hans Lüth
Drittgutachter: Dr. habil.rer.nat Svetlana Vitusevich

Table of Content

TABLE OF CONTENT **5**

ACKNOWLEDGMENTS **9**

ZUSAMMENFASSUNG **11**

ABSTRACT **14**

I. INTRODUCTION **17**

1. Nanoscale devices: nanotubes and nanowires 17
   - 1.1. Carbon nanotubes 18
     - *1.1.1. Structure and basic electronic properties of carbon nanotubes 19*
     - *1.1.2. CNT synthesis 26*
     - *1.1.3. Application of CNTs and transport peculiarities 28*
     - *1.1.4. Recently registered noise properties 36*
   - 1.2. Nanowires 40
2. Noise characterization 42
   - 2.1. Noise: mathematical methods and main theorems 42
   - 2.2. Noise components 45
     - *2.2.1. Thermal noise (Johnson-Nyquist noise) 46*
     - *2.2.2. Shot noise 48*
     - *2.2.3. Generation-recombination noise 48*
     - *2.2.4. Burst noise 52*
     - *2.2.5. Flicker noise 53*

II. DEVELOPMENT OF NOISE MEASUREMENT SETUP **59**

III. SYNTHESIS OF CARBON NANOTUBES AND CHARACTERIZATION OF CNT BASED STRUCTURES **65**

1. Synthesis of CNT using CVD method 65
2. Raman spectroscopy 68

IV. TRANSPORT AND NOISE PROPERTIES OF CARBON NANOTUBE BASED DEVICES **71**

1. Single-walled carbon nanotube field-effect transistors (SWCNT-FETs) 71
   - 1.1. Individual carbon nanotube FETs 72
     - *1.1.1. Back gate topography 72*
     - *1.1.2. Top and side gate topography. Comparison of different gate topologies 83*
   - 1.2. Multiple carbon nanotubes FETs 92
   - 1.3. GR-noise components. Comparison of the traps in the structures 99
2. Structures composed of carbon nanotube bundles 101
   - 2.1. Three mechanisms of transport 103
   - 2.2. Noise spectroscopy of different transport regimes 104

V. TRANSPORT AND NOISE PROPERTIES OF NANOWIRES **109**

1. Noise properties of nanowires 109
   - 1.1. Semiconductor AlGaN/GaN nanowires 109

1.2. Metallic nanowires, with constriction tuned by mechanically controlled break junction 120
2. Nanowires noise properties compared with SWCNT based structures 126

VI. SUMMARY AND OUTLOOK 129
1. Summary 129
2. Future work 132

BIBLIOGRAPHY 133

PERSONAL PUBLICATION LIST 141

APPENDIXES 143
1. GetNoiseSpectrum v8 program written using HTBasic 143
2. Getting Flicker & GR v9.1 Optimized program written using Wolfram Mathematica 156
3. Diameters and radial breathing mode (RBM) frequency of typical SWCNTs 168

To my Love
Tetianka

Acknowledgments

First of all, I would like to thank to my supervisor **Dr. Svetlana Vitusevich** for many scientific discussions we had during time of my PhD study and obtaining results of this thesis, for her contribution to my research work at Forschungszentrum Jülich, and for her organizing of the collaborations, which helps me a lot. I am especially grateful to her for providing me with the opportunity to work in her group.

Especially, I would like to thank my first reviewer **Prof. Dr. D. Yakovlev** for his support and fruitful discussions during the analyzing of results and writing this thesis as well as for his contribution and collaboration.

For scientific discussion I would like to express my thanks to **Dr. Mykhailo V. Petrychuk** from National Taras Shevchenko University of Kyiv, Ukraine (who taught me the fundamentals of the noise spectroscopy).

I would like to thank also for scientific discussion to **Prof. B.O. Danylchenko** from the Institute of Physics, NASU, Kyiv, Ukraine.

I highly appreciate help and support of my colleges **Dr. A. Kurakin**, **Dr. S. Danylyuk**, **MSc. S. Pud**, **MSc. J. Li**, **MSc. K. Greben**, **MSc. D. Afanasenkau** and **MSc. V. Belanohava**.

I am grateful **Prof. A. Ural** and **Prof. G. Bosman** (University of Florida, USA); **Dr. K. Goss**, **Dr. C. Meyer**, **Dr. D. Mayer**, **MSc. D. Xiang**, **Prof. Dr. T. Schäpers** and **Dr. H. Hardtdegen** from Forschungszentrum Jülich (Germany) for the pleasant working atmosphere and fruitful collaboration.

I would like to thank my **parents** for help and support, my girlfriend **Tetiana Mychalchuk** for helping and understanding me, and all my friends, especially **Dr. Petro Zoriy** and **Dr. Olga Neucheva** for well-handled time in Jülich.

In particular, I would like to give my most sincere thanks to my second referee **Prof. Dr. H. Lüth** for reviewing my thesis and his support and suggestions during my doctoral study.

Finally, I like to express my thanks to the head of our institute **Prof. Andreas Offenhäusser** and to my former first supervisor **Prof. N. Klein**, who gave me the opportunity to perform my PhD work at the Peter Grünberg Institute, Forschungszentrum Jülich, for their support and concern.

Zusammenfassung

In der vorliegenden Dissertation wurden die Transporteigenschaften von neuartigen auf Kohlenstoffnanoröhren (CNTs) basierenden Strukturen mittels Rauschspektroskopie untersucht. Die genaue Untersuchung von Rauscheigenschaften einzelner einwandiger Kohlenstoff-Nanoröhren-Feldeffekttransistoren (SWCNT-FETs) ermöglichte das Verständnis des Transports im Kanal und die Bestimmung des Rauschens nicht nur der Kohlenstoffnanoröhre, sondern auch in einigen Spannungsbereichen von Schottky-Kontakten. Die Ergebnisse der Untersuchung des Kanalrauschens in Feldeffekttransistoren (FET) zeigten einen von den Fallen beeinflussten Streumechanismus, der bis hinauf zur Raumtemperatur funktionierte. Durch verschiedene Gate-Topographien konnte der Einfluss der Kontaktbereiche auf den Gesamtwiderstand der Struktur verstanden werden. Die Quelle des Rauschens wurde durch die Überlagerung des Rauschens von Schottky-Kontakten mit dem CNT-Kanal ermittelt. Zusätzlich zu den Untersuchungen der Flicker-Rauschkomponenten wurden Rauschkomponenten in Form einer Lorentz-Kurve in einem großen Temperaturbereich untersucht. Solche Untersuchungen ermöglichen eine Charakterisierung der Qualität der Materialien und Bestimmung der Energie, der Position und der Konzentration von Fallen in CNT-FET-Strukturen. Die Aktivierungsenergien der Fallen der Silizium- und Aluminiumoxide wurden bestimmt. Die Eigenschaften der FETs wurden mit Gammastrahlung einer ^{60}Co-Quelle eingestellt. Dafür wurden Strukturen mit einer Dosis von $1x10^6$ rad bestrahlt. So wurde ein verbessertes Transport-und Rauschverhalten erreicht: der Strom des FETs wurde erhöht und das Gesamtrauschen verringert.

CNT-FETs auf Basis von mehreren SWCNTs haben Vorteile gegenüber FETs auf Basis einer Kohlenstoffnanoröhre, wie z. B. ein erhöhtes Signal-Rausch-Verhältnis und einen niedrigen Gesamtwiderstand. Diese Eigenschaften sind die wichtigsten für Sensor-und Hochfrequenzanwendungen. Aus diesem Grund wurden FETs auf der Basis von mehreren parallel ausgerichteten CNTs vor und nach Gamma-Bestrahlung mit Rauschspektroskopie untersucht. Die erhaltenen Ergebnisse zeigen, dass in CNT-FETs mit einer Kanallänge von 10µm der Beitrag der Kontaktbereiche vernachlässigt werden kann. Darüber hinaus liefert die Gamma-Bestrahlung mit einer Dosis von $1x10^6$ rad einen erheblichen Rückgang der parasitären Leitfähigkeit. Vor und nach der Gamma-Bestrahlung mit einer Dosis von $1x10^6$ rad bestimmten Hooge-Parameter liegt über $5x10^{-3}$. Trotz der in der Literatur veröffentlichten relativ hohen Werte des Hooge-Parameter (α_H) zeigen die Ergebnisse dieser Arbeit, dass α_H (im Falle von Rauschen auf Grund der Kanalleitfähigkeit von CNT-FETs) vergleichbare Werte wie bei konventionellen Halbleitern hat.

Die einfachste und kostengünstigste Methode CNT-Bauelemente zu produzieren ist die folgende, bei der ein einaxialer (d.h. in eine Richtung wirkender) Druck auf eine Reihe von Kohlenstoffnanoröhren angewendet wird, wobei dünne Schichten mit CNT-Bündeln entstehen. Ein solches Verfahren ermöglicht die Herstellung von CNT-Strukturen durch die Verarbeitung von dünnen Schichten in Bauelementen mit zwei und drei Kontakten. Dafür wurden Mechanismen der Transportbildung in einwandigen CNT-Bündeln in einem großen Temperaturbereich von 4.2 K bis 300 K untersucht. Die Temperaturabhängigkeit des Widerstandes und der Rauschparameter (logarithmische Steigung der Stromabhängigkeit

der Rauschens sowie des normierten Stromrauschens) wurden verglichen. Bemerkenswerte Veränderungen im Rauschverhalten wurden bei Temperaturen registriert, die typisch für den Übergang von der Hopping-Leitfähigkeit zur Luttingerflüssigkeit und diffusen Leitfähigkeit sind. Im ersten Übergangsbereich, ändert sich die Steigung des normierten Rauschens in Abhängikeit vom Strom deutlich als Funktion der Temperatur. In der Region der diffusen Leitfähigkeit ergab sich eine stärkere Variation des normierten Rauschpegels. Diese Veränderungen der Rauscheigenschaften sind von den Veränderungen der Transporteigenschaften von SWCNT-Bündels abhängig, was eine angemessene Erklärung für das Mechanismus der Leitfähigkeit in diesem System ist.

Der Transport in CNT-Bauelementen ist quasi 1D. Dashalb sind die Transporteigenschaften und Rauschen in Nanoröhren mit denen in einigen anderen Bauelementen, z. B. mit den Bauelementen auf der Basis von Nanodrähten aus AlGaN/GaN-Heterostrukturen, vergleichbar. Durch piezoelektrische Effekte und spontane Polarisation an der Heterostruktur-Grenzfläche bildet sich ein zweidimensionales Elektronengas (2DEG) mit hoher Elektronenbeweglichkeit. Das Energieband-Diagramm der Heterostruktur wurde berechnet. Nanodrähte mit unterschiedlicher Dicke wurden untersucht. Die ermittelte Abhängigkeit des Stroms von der Breite zeigt, dass eine Verarmungsschicht von 200 nm Dicke vorliegt, was die Ursache für die verminderte effektive Breite des Drahtes im Vergleich mit Verarbeiteten ist. In dieser Arbeit wurden Elektronenaustauschprozesse zwischen den tiefen Energiefallen und dem Kanal nach dem Anlegen einer Hochspannung und unter UV-Strahlung untersucht. Die Bestimmung der Temperaturverhalten der Generations-Rekombinations-Rauschkomponenten ermöglichte die Ermittlung der Aktivierungsenergien der Störstellen. Die Ergebnisse der Rauschuntersuchungen zeigen, dass die Probe mit 360 nm Breite den niedrigsten Rauschpegel hat. Das kann man durch den Einschluss des 2D-Elektronengases durch die Verarmungsschicht erklären. Die Verarmungsschicht beschränkt die Leitfähigkeit des dünnen Kanals, was zu einer erhöhten Elektronenbeweglichkeit führt. Der Hooge-Parameter war $\alpha_H \simeq 10^{-4}$, was viel niedriger als der Wert für herkömmliche Halbleiter ist.

Zusätzlich zu Halbleiterstrukturen wurden auch Eigenschaften von metallischen Drähten untersucht. Golddrähte wurden mit einem Durchmesser bis zu einem Atom angefertigt. Bei noch kleinen Durchmesser kam es zum Bruch. Nach dem Bruch wurden Nanospalt-Strukturen mit und ohne Molekül untersucht. So konnten wichtige spezifische Rauschquellen in Nanostrukturen verstanden werden. Eine dieser Rauschquellen ist die Bewegung eines Goldatoms auf der Oberfläche, was zum Flickerrauschen führen kann, hervorgerufen durch Modulation des Tunnelstroms. Nach einer genauen Literaturrecherche wird hier nun von einem neuen Verhalten der Flickerrauschkomponente berichtet. Das wichtigste Charakteristikum des Rauschens ist ein zusätzlicher Lorentz-förmiger Rauschanteil, der zu sehen ist, wenn ein einzelnes Molekül die Nanoelektroden überbrückt. In der untersuchten Gruppe von Molekülproben wurden charakteristische Zeitkonstanten bei einem kleinen Strom bestimmt. Es wurde festgestellt, dass die Zeitkonstante für kleine Ströme linear vom Strom abhängig ist. Die aufgezeichneten Lorentzförmigen Rauschanteile für einzelne Molekülbrücken sind als

Manifestation einer dynamischen Rekonfiguration der molekularen Kopplung der Metallelektroden während des Stromflusses zu interpretieren. Die Rekonfigurationsänderungen treten auf, wenn kein vollständiger Bruch des Moleküls stattfindet und in der Nähe der Konfigurationszustände mit sehr ähnlichen elektrischen Eigenschaften. Die zweite Rauschquelle wurde durch die Rekonfiguration der Bindungen bei Anregung des Systems durch Lorentzförmige Rauschspektren offenbart. Diese Lorentzspektren waren Folge der Veränderungsprozesse zwischen zwei Zuständen: Anregung und Relaxation. Das Rauschverhalten wurde im Rahmen eines phänomenologischen Modells beschrieben. Die Ergebnisse sollten in Hinblick auf die Entwicklung von Biosensoren und Basiskomponenten der molekularen Elektronik betrachtet werden.

Abstract

In this thesis, a study of transport properties of novel structures based on carbon nanotubes (CNTs) using noise spectroscopy is presented. The precise study of the noise characteristics of the individual single-walled CNT-field-effect transistors (SWCNT-FETs) allows to understand the transport in the channel and to recognize noise coming not only from the CNT, but also in some voltage range from the Schottky barriers in the contact regions. The results of the study of channel noise of the FETs showed a trap-assisted scattering mechanism observed up to room temperature. Different gate topographies allow to understand the influence of the contact regions on the total resistance of the structure. The origin of noise was explained by a combination of noise of the Schottky barriers and noise of the CNT channel. In addition to the flicker noise, the Lorentzian-shape noise components were analyzed in a wide temperature range. The analysis enables us to characterize the quality of the materials and find the energy, position and concentration of traps in the CNT-FET structures. The activation energies of traps associated with SiO_2 and Al_2O_3 oxides were obtained. The gamma radiation treatment was used to tune the characteristics of the FETs. The devices were irradiated by a ^{60}Co source with a dose of $1x10^6$ rad. Improved transport and noise characteristics were obtained, namely an increased current of the FETs and a decrease of total noise.

The CNT-FETs based on multiple SWCNT have advantages in comparison to those fabricated based on individual CNTs, such as an increased signal-to-noise ratio and lower device resistance. These characteristics are the most important ones for sensors and high-frequency applications. Therefore, the FETs based on multiple parallel-aligned CNTs were also studied before and after gamma radiation treatment using noise spectroscopy. The obtained results demonstrate that in long channel CNT-FETs with a length of 10μm the contribution of contact regions can be neglected. Moreover, radiation treatment with a dose of $1x10^6$ rad allows a considerable decrease of the parasitic conductivity. The Hooge parameter (α_H) obtained before and after gamma radiation treatment with a dose of $1x10^6$ rad is found to be about $5x10^{-3}$. In spite of relatively high values of the Hooge parameters published in literature, our results show that α_H has comparable values with conventional semiconductors (in the case of noise related with channel conductivity of CNT-FETs).

The easiest and most cost-effective method of producing the CNT devices is based on fabrication of structure by applying uniaxial pressure to a number of carbon nanotubes to produce the thin films containing the CNT bundles. Such a method allows obtaining CNT structures by processing the thin films in devices with two and three contacts. Therefore, we studied the mechanisms of transport formation in single-wall carbon nanotube bundles over a wide temperature range from 4.2 K to 300 K. The temperature dependence of the resistance and the noise parameters (the logarithmic slope of the current dependence of noise as well as the normalized current noise) were compared. Remarkable changes in noise characteristics were registered at temperatures typical for the transition from the hopping conductivity to the Luttinger liquid conductivity and the transition from the Luttinger liquid conductivity to the diffusion conductivity. In the first transition region, the slope of the normalized noise level of the current changes significantly as a function of temperature. In the region of the diffusion conductivity, a stronger variation of the

normalized noise level was revealed. These changes in noise properties were correlated with changes in the transport characteristics of SWCNT bundles that allowed us to adequately explain the mechanisms of conductivity in the system.

Transport in carbon nanotube devices is quasi 1D, therefore to compare the transport properties and noise in nanotubes with those in other devices, we performed an investigation of nanowires based on AlGaN/GaN heterostructures. Such a structure contains a 2-dimensional electron gas (2DEG) with high electron mobility at the heterostructure interface due to piezoelectrical and spontaneous polarization effects. The energy band diagram of the heterostructure was calculated. Nanowires with different widths were studied. The measured current dependence on width showed a depletion layer of 200 nm which is the reason of the decreased effective width of the wire in comparison with processed one. Using ultraviolet and high-voltage treatments, we studied electrons exchange processes between the deep energy traps and the channel. The temperature behavior of the generation-recombination noise components allows to find the traps with different activation energies. The noise investigation showed that the sample with 360 nm width has the lowest noise level. This fact can be explained by the confinement of a 2D electron gas due to conductivity being restricted to a thin channel by a depletion layer resulting in an increased electron mobility. The Hooge constant was found to be $\alpha_H \simeq 10^{-4}$, which is lower than the value for conventional semiconductors.

In addition to the semiconductor structures, the properties of metallic wires were studied. Using the break junction technique we fabricated gold wires with diameter tuned down to one gold atom. Further tuning led to the break of the wires which gave us an oppotrunity to investigate the nanogap structure with and without a molecule. This allowed us to understand the important specific sources of noise in nanostructures. One of them is migration of the gold atoms, which can lead to flicker noise fluctuations, caused by modulation of the tunneling current. In this case, a novel behavior of flicker noise component was revealed and compared with the one reported previously in literature. The most striking feature of noise is an additional Lorentzian-shaped noise component clearly revealed in the case in which a single molecule bridged the nanoelectrodes. In the examined set of molecule containing samples a well-defined time constant at a certain small current was extracted. It was found that the time constant has a linear dependence as a function of current in the small current regime. The recorded Lorentzian-shaped noise component of a single bridging molecule is interpreted as a manifestation of a dynamic reconfiguration of molecular coupling to the metal electrodes during current flow. The reconfiguration changes occur without complete bond breaking and involve near-configuration states with very similar electric properties. The second one of the noise sources revealed is the reconfiguration of the bonds at excitation of the system by current, which lead to Lorentzian-shaped noise spectra as a result of the change processes between two states: excited and relaxed. The noise behavior was explained in frame of a phenomenological model. The results should be taken into account for the development of devices such as biosensors and base components of molecular electronics.

I. INTRODUCTION

The introduction of this work consists of two important topics with several expanded subtopics inside. The first one is “Nanoscale devices: nanotubes and nanowires”. Here, the basic properties of nanotubes and nanowires are discussed. Because the main subject of this work is the carbon-based materials, especially carbon nanotubes (CNTs), the synthesis of CNTs is discussed, and properties of the field-effect transistors (FETs) fabricated on the basis of the materials are compared. In our sudies we focus on the transport and noise properties of the carbon nanotubes. This area attracs the attention of the scientific communities worldwide in terms of different applications of the CNTs.

The second topic is “Noise characterization”, which represents one of the most powerful method for characterization different materials and devices. The understanding of the noise nature has a long history, starting from the first observation and continue with developing of quantum theory of flicker noise. The mathematical and physical aspects of the noise will be described at the first place. The current flux inside the carbon nanotubes leads to charge carriers trapping, scattering, etc. which in terms influence the noise level in the channel.The contribution of each process will be discussed in detail.

1. Nanoscale devices: nanotubes and nanowires

During the past decades the attention of the scientists was focused on finding the new materials as well as reducing the size to the nanometer scale. Decreasing the size usually leads to power saving, low production cost, and increasing the autonomous running time, those are very important important for implants and mobile phones. The discovery of new materials can solve a lot of existing problems leading to increasing the sensitivity of bio-sensors, revealing new effects for high-speed information processing and novel information technologies.

Nowadays, the processors inside the computers have almost reached the limit in their speed and transistors density. They still followed the Moore’s law[1]: the number of transistors that can be processed on an integrated circuit doubles approximately every two years. This tendency has been observed for more than half a century and is expected to last

until 2015 or 2020. After Moore's article, several researches also noted that transistors would eventually reach the limits of miniaturization at atomic level. This year Intel Corp. has announced chips based on the 32-nm technological process (Sandy Bridge). Next year 22-nm technological process (Ivy Bridge) is expected, and reducing the size to 10nm "Skymont" in 2018[2].

The miniaturization process demands new materials which can replace the existing well-known Si based devices. Numerous materials with advanced properties have been proposed, namely: carbon nanobutes, GaN, etc. However, these materials still cannot replace the Si technology due to the higher cost and lack of studies. One of these materials is carbon nanotubes (CNTs), transport properties and technical implementation of which are still under discussion.

1.1. Carbon nanotubes

Carbon nanotubes (CNTs) are composite materials from carbon atoms in the tube form. CNTs are members of the fullerene structural family, which also includes the spherical buckyballs, and the ends of a nanotube may be capped with a hemisphere of the buckyball structure[3]. By characterizing in term of dimensions, CNT is 1D structure, whereas the fullerene is 0D. Other carbon family materials are graphene and graphite that have 2D and 3D dimensions, respectively. CNTs have cylindrical shape with length-to-diameter ratio from 1 to 132,000,000[4]; with the usual diameter in the range of 1nm they can reach the length up to 10 centimeters or even more. This is one of the reasons determining why CNTs are very important material.

The first who discovered carbon nanotubes were L.V. Radushkevich and V.M. Lukyanovich. In 1952 they published clear images of 50 nanometer diameter tubes made from carbons in the Soviet Journal of Physical Chemistry.[5] But this discovery was unnoticed, as it was published in Russian language and Western scientists had limited access to Soviet press during the Cold War. The authors didn't continue the investigation of the discovered CNTs. Therefore, almost 40 years past till the next group of scientists brought this topic for their research. The invention of the TEM opened a new possibility for the CNTs investigations since the reserchers can have the "eyes" to see them.[6]

The world-wide interest to the CNTs is closely related to the fullerene investigations. The first became possible after creating the technology of obtaining fullerenes and producing them in macroscopic quantities. This method of production is based on thermal sputtering of graphite in electric arc with graphite electrodes in helium atmosphere[7]. In 1991, S. Iijima and co-workers beside conventional fullerenes (C_{60}, C_{70}) were able to produce the first extencive nanotubes with the multiwall shape.[6] Two years later, two research groups (Iijama and D. Bethune) independently showed carbon nanotubes in single-walled form. The tubes have unusual properties that is valuable for many fields of material science and technology, such as nanotechnology, electronics, optics, mechanics, etc. Because of their extraordinary thermal conductivity, mechanical and electrical

properties, CNTs may find applications as additives to various structural materials or even replace them.

It should be noted that the possibility of existence of fullerene "tubules" was theoretically predicted by J.W. Mintmire et al.[8] Authors calculated the electronic properties and predict the existence of metallic conductivity and zero band-gap. Unfortunately, the article was rejected initially but later was published after the experimental results proofed the existance of the CNTs.[6]

1.1.1. Structure and basic electronic properties of carbon nanotubes

As it was emphasized above, carbon nanotubes have extremely long length comparing to diameter. What makes these tubes so stable? It is their strength with which carbon atoms are bonded to each other. In the nanotubes, the atoms arrange themselves in hexagonal rings like honeycombs and the chemical bonds are established entirely by sp^2-hybridized bonds. These bonds are stronger than sp^3- hybridization bonds which are common for the alkanes giving the nanotubes their unique mechanical properties.

Carbon nanotubes can be divided into two categories: single-walled carbon nanotubes (SWCNTs) and multi-walled carbon nanotubes (MWCNTs). MWCNTs consist of a few to a few tens of concentric cylinders placed around a common central hole with the interlayer spacing close to that of graphite (0.34nm). Their inner diameter varies from 0.4nm to a few nm and their outer diameter ranges typically from 2nm up to 20-30nm depending on the number of layers.[9] The conductivity of MWCNTs is metallic.

Single-walled carbon nanotubes can be presented as a part from an infinite graphene sheet and rolled up forming a tube, see Figure I.1(a). Therefore, the tubes are usually labeled in terms of the graphene lattice vectors shown on Figure I.1(b). The unit cell is spanned by the two vectors $\boldsymbol{a_1}$ and $\boldsymbol{a_2}$ and contains two carbon atoms. In carbon nanotubes, a graphene lattice vector $\boldsymbol{C_h} = n\boldsymbol{a_1}+m\boldsymbol{a_2}$ becomes the circumference of the tube. It is usually denoted by the pair of integers (n, m) (called the chiral vector), which uniquely define a particular tube. The achiral cases, $(n, 0)$ zigzag, and (n, n) are indicated with dashed lines. The translation vector $\boldsymbol{T}$ is defined to be along the tube axis and orthogonal to $\boldsymbol{C_h}$ and its magnitude represents the length of the unit cell of an (n, m) tube. The rolled up area swept out by $\boldsymbol{T}$ and $\boldsymbol{C_h}$ corresponds to the repeat unit of an (n, m) tube and determines the size of its unit cell, which can vary greatly among the tubes. For example, the (10,10) tube contains only 40 atoms in the unit cell as the very near (10,9) tube with 1084 atoms in the unit cell.[10]

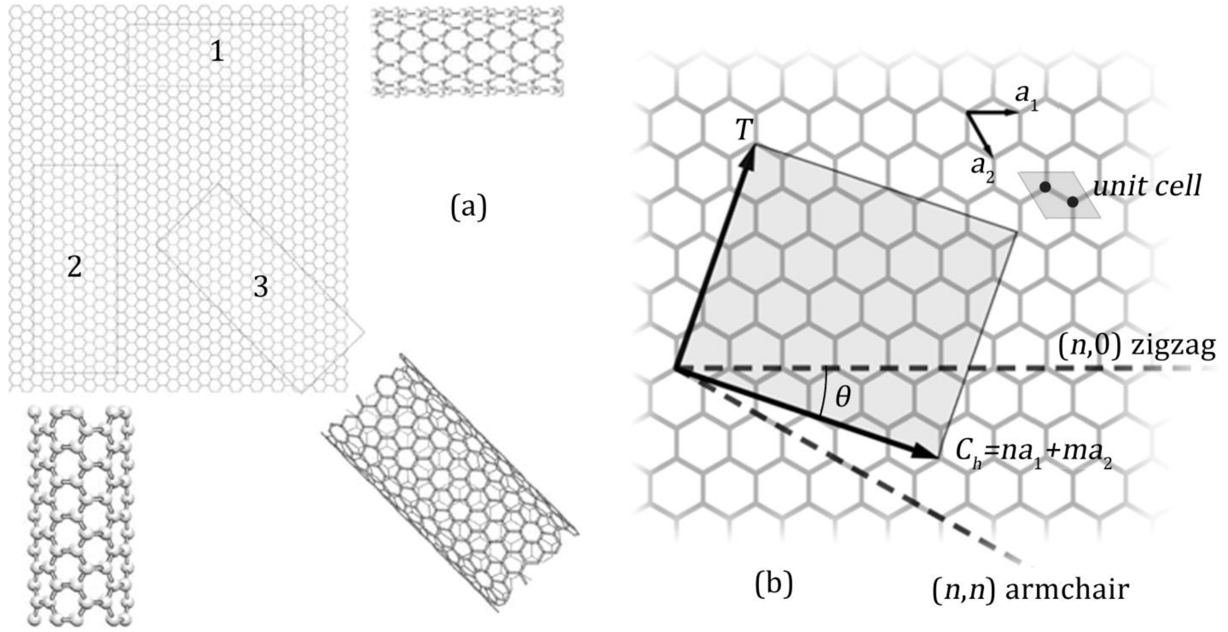

Figure I.1.[3] (a) Different parts of graphene sheet that form zigzag (1), armchair (2) and general chiral (3) tubes. (b) Graphene honeycomb lattice with the lattice vectors $\boldsymbol{a_1}$ and $\boldsymbol{a_2}$. The chiral vector $\boldsymbol{C_h}=\boldsymbol{na_1}+\boldsymbol{ma_2}$ describes how to "roll up" the graphene sheet to make the nanotube. $\boldsymbol{T}$ denotes the tube axis.

The geometry of the graphene lattice and the chiral vector of the nanotube determine its structural parameters such as diameter, unit cell, and the number of carbon atoms in the unit cell. The diameter of the tube is given by the length of the chiral vector:

$$d = \frac{|\boldsymbol{C_h}|}{\pi} = \frac{\sqrt{3}a_0}{\pi}\sqrt{n^2 + nm + m^2}, \tag{I.1}$$

where a_0=0.142 nm is the C-C bond length in the graphite plane and $|\boldsymbol{a_1}| = |\boldsymbol{a_1}| = \sqrt{3}a_0$. On the other hand, the chiral angle, θ, is related with chiral numbers (n, m) of the SWCNT by following equation:

$$\cos\theta = \frac{\boldsymbol{a_1} \cdot \boldsymbol{C_h}}{|\boldsymbol{a_1}||\boldsymbol{C_h}|} = \frac{n + m/2}{\sqrt{n^2 + nm + m^2}}, \tag{I.2}$$

θ is limited to the angles range of $0° \leq \theta \leq 30°$ due to the geometrical symmetry of the hexagon network. For zigzag nanotubes θ = 0° and for the armchair configuration θ = 30°.

Talking about the size we would like to know where is the limit and how small the nanotube's diameter can be. Theoretical calculations predict that the smallest diameter for a stable SWCNT is around 0.4nm with chiral index (3,3), (5,0), or (4,2). The discovery of the CNTs with diameter of ~0.4nm was done by L. Qin et al.[11] using high-resolution transmission electron microscopy (HRTEM). In 2008, Guan et al. used the SWCNT with the diameter of 1.0-1.2 nm to grow the nanotube of a smaller size inside.[12] As a result ~0.4 nm nanotubes were made with the chiral indexes of (3,3), (4,3), or (5,1). They grew the CNTs inside SWCNTs with the diameter of 1.0-1.2nm. The values of chiral indexes were checked experimentally by the HRTEM and found in a good agreement with the predicted ones.

As it was mentioned above, the smallest graphene lattice vector $\boldsymbol{T}$, which is perpendicular to $\boldsymbol{C_h}$ defines the translational period T along the tube axis. In general, the translational period T is determined by the chiral numbers (n, m) by

$$\boldsymbol{T} = -\frac{2m+n}{N\mathcal{R}}\boldsymbol{a_1} + \frac{2n+m}{N\mathcal{R}}\boldsymbol{a_2}, \tag{I.3}$$

and

$$T = |\boldsymbol{T}| = \frac{3a_0\sqrt{n^2+nm+m^2}}{N\mathcal{R}}, \tag{I.4}$$

where N is the greatest common divisor of (n, m), $\mathcal{R} = 3$ if $(n-m)/3N$ is integer and $\mathcal{R} = 1$ otherwise. It should be noted that in Figure I.1(b) translation vector $\boldsymbol{T}$ is shown in opposite direction. Thus, the nanotube unit cell is formed by a cylindrical surface with height T and diameter d. The height T varies strongly with the chirality of the tube; chiral tubes often have very long unit cells as shown in Figure I.2.

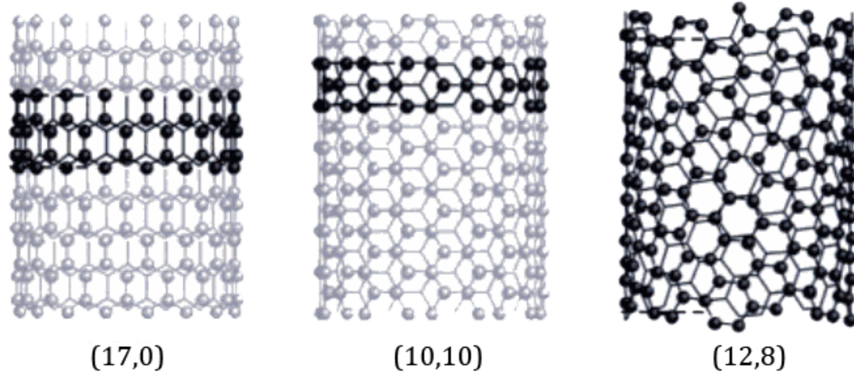

Figure I.2.[10] Structure of the (17,0), the (10,0) and the (12,8) tube. The unit cells of the tubes are highlighted.

To calculate the number of carbon atoms in the unit cell one has to use the

$$N_C = \frac{2S_t}{S_g} = \frac{4(n^2+nm+m^2)}{N\mathcal{R}}, \tag{I.5}$$

where $S_t = T \cdot C_h$ is cylinder surface area and $S_g = \frac{3\sqrt{3}}{2}a_0^2$ is hexagonal graphene unit cell area. For armchair (n, n) and zigzag $(n, 0)$ tubes the number of carbon atoms is $4n$ in the unit cell.

To understand the basic conductance properties of SWCNTs we should consider the tubes in k-reciprocal space. In the z-direction of the CNT (along the tube) the reciprocal lattice vector $\boldsymbol{k_z}$ corresponds to the translational period $\boldsymbol{T}$ as follows

$$\boldsymbol{k_z} = \frac{2\pi}{\boldsymbol{T}}. \tag{I.6}$$

As CNT consider to be infinitely long the wave vector $\boldsymbol{k_z}$ is continuous. The first Brillouin zone is the interval $(-\pi/T, \pi/T]$ in z-direction. Along the circumference $\boldsymbol{C_h}$ of the tube, any wave vector $\boldsymbol{k_p}$ is quantized according to the boundary condition

$$m\lambda = |\boldsymbol{C_h}| = \pi d, \tag{I.7}$$

and

$$k_{p,m} = \frac{2\pi}{\lambda} = \frac{2}{d}i, \tag{I.8}$$

where i is the integer number taking the values $-q/2+1,\ldots,0,1,\ldots,q/2$ ($q=N_C/2$ is the number of hexagons in carbon nanotubes unit cell). A wave with wave vector $k_{p,m}=2i/d$ has $2i$ nodes around the circumference. The minimum wavelength can be calculated from the number of atoms N_C in the unit cell. At least 4 atoms are necessary for defining a wavelength, i.e. $|i| \leq q/2 = N_C/4$. Thus, the first Brillouin zone consists of q lines parallel to the z-axis separated by $k_{p,m}=2/d$.

The quantized wave vector $\boldsymbol{k_p}$ and the reciprocal lattice vector $\boldsymbol{k_z}$ can be found from the conditions:

$$\begin{array}{ll} \boldsymbol{k_p} \cdot \boldsymbol{C_h} = 2\pi & \boldsymbol{k_p} \cdot \boldsymbol{T} = 0 \\ \boldsymbol{k_z} \cdot \boldsymbol{C_h} = 0 & \boldsymbol{k_z} \cdot \boldsymbol{T} = 2\pi' \end{array} \tag{I.9}$$

as following

$$\boldsymbol{k_p} = \frac{2n+m}{qN\mathcal{R}}\boldsymbol{k_1} + \frac{2m+n}{qN\mathcal{R}}\boldsymbol{k_2}, \tag{I.10}$$

$$\boldsymbol{k_z} = -\frac{m}{q}\boldsymbol{k_1} + \frac{n}{q}\boldsymbol{k_2}, \tag{I.11}$$

where $\boldsymbol{k_1}$ and $\boldsymbol{k_2}$ are the reciprocal lattice vectors. In Cartesian coordinates $\boldsymbol{k_1} = (0,1)4\pi/3a_0$ and $\boldsymbol{k_2} = (0.5\sqrt{3},-0.5)4\pi/3a_0$.

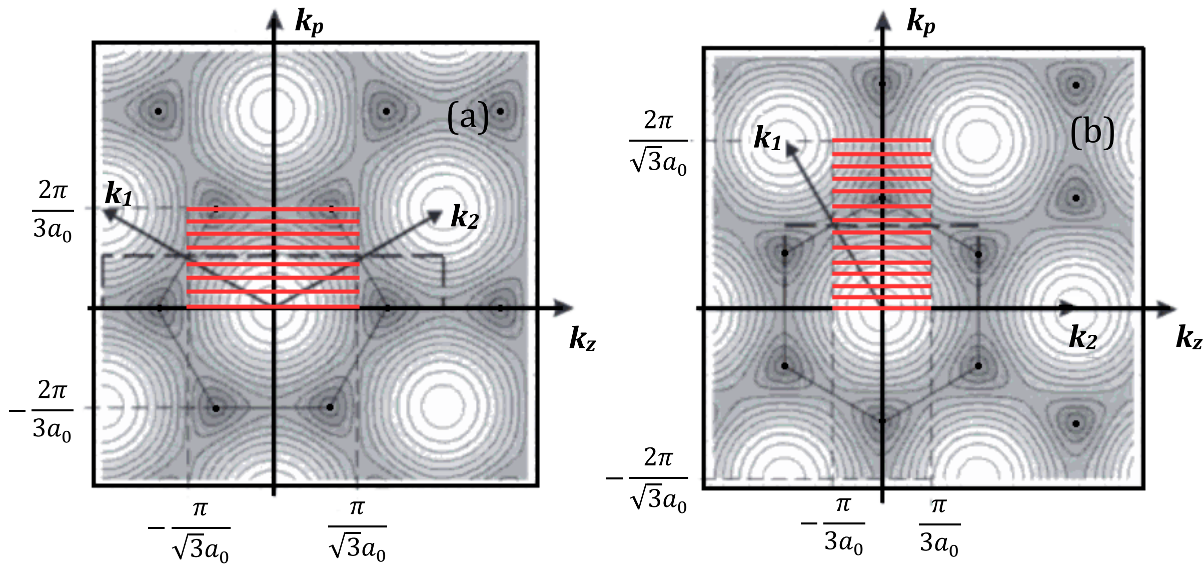

Figure I.3.[10] Brillouin zones of a (7.7) armchair (a) and a (13,0) zigzag tube (b) (thick lines). The background is a contour plot of the electronic band structure of graphene (white indicates the maximum energy). The Brillouin zone consists of $2N$ (14 and 26, respectively) lines parallel to $\boldsymbol{k_z}$ (red lines), where $\boldsymbol{k_z}$ is the reciprocal lattice vector along the tube axis. Each line is indexed by $m \in [-N, N]$, where m = 0 corresponds to the line through the graphene Γ point (k = 0).

The Brillouin zones of a (7,7) armchair (a) and a (13,0) zigzag tube (b) are shown in Figure I.3. With increasing diameter of the CNTs the number of lines increases while the distance between them reduces.

To the first approximation, the properties of SWCNTs are related to those of graphene by taking the lines that correspond to the nanotube Brillouin zone, according to Eqs. (I.10) and (I.11). For example, the electronic band structure of a particular nanotube can be found by cutting the two-dimensional band structure of graphene into q lines of length $2\pi/T$ and distance $2/d$ parallel to the direction of the tube axis. This approach is called *zone folding* and is commonly used in nanotube research.

Carbon nanotubes have two types of bonds. The σ-bonds form the hexagonal network along the cylinder wall. The π-bonds point perpendicular to the nanotubes' surface. They are responsible for the weak van-der-Waals interactions between different tubes and for the sensitivity of the CNTs as sensors. It was expected that in-plane σ-bonds are the most important for the electronic properties of CNTs. However, they are too far from the Fermi level leading to the weak contribution to the electronic properties. In contrast, the bonding and antibonding π-bands are close to the Fermi level. This defines properties of one third of carbon nanotubes as metallic or quasi-metallic.

It was shown above that the allowed wave vectors around the nanotube circumference are quantized, i.e. they take only discrete values. However, along the nanotube axis the wave vectors are continuous. The electronic states along the k_z-direction are Bloch functions as in the case of the tree-dimensional crystals. By plotting the allowed wave vectors of a nanotube onto the Brillouin zone of graphene we will find a series of parallel lines. The length, the number, and the orientation of these lines depend on the chiral indices (n, m) of the tube. The property of SWCNTs to be either metallic or semiconducting is explained by the Fermi surface of graphene. If the graphene K point is among the allowed states of a carbon nanotube then it is metallic. Otherwise the nanotube is semiconducting with a moderate band gap. The K point of graphene is at $(\boldsymbol{k_1} - \boldsymbol{k_2})/3$. Since $\boldsymbol{k}\cdot\boldsymbol{C_h} = 2\pi i$, where i is an integer, then nanotube is a metal if

$$\boldsymbol{k}\cdot\boldsymbol{C_h} = 2\pi i = \frac{1}{3}(\boldsymbol{k_1} - \boldsymbol{k_2})(n\boldsymbol{a_1} + m\boldsymbol{a_2}) = \frac{2\pi}{3}(n-m), \qquad \text{(I.12)}$$

or

$$3i = n - m. \qquad \text{(I.13)}$$

This famous result was firstly presented by N. Hamada et al.[13] and R. Saito et al.[14]

With the concept of zone folding and the graphene tight-binding dispersion it is possible to calculate the full band structure of carbon nanotubes. The example of such calculation done by S. Reich et al.[15] for (10,10) armchair and for (19,0) zigzag nanotubes is shown in the Figure I.4.

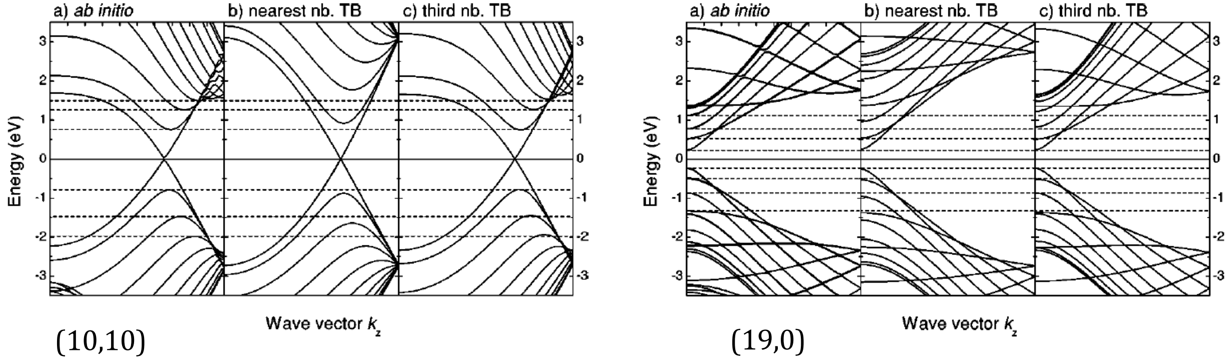

Figure I.4.[15] Band structure of a (10,10) armchair and a (19,0) zigzag nanotubes. (a) *Ab initio* calculation. (b) Nearest-neighbor tight-binding calculation with an interaction parameter γ_0 = -2.7eV. (c) Third-nearest-neighbor tight-binding calculation with parameters obtained from a fit to the optical energy range. The dashed lines denote *ab initio* calculated energies of the singularities in the density of states.

The one-dimensional energy band of SWCNT can be calculated using the expression for tight-binding π-band structure of two-dimensional graphite sheet:

$$E_{2D} = \pm\gamma_0 \left(1 + 4\cos\left(\frac{\sqrt{3}k_x a_0}{2}\right)\cos\left(\frac{k_y}{2}\right) + 4\cos^2\left(\frac{k_y}{2}\right)\right)^{\frac{1}{2}}, \qquad (I.14)$$

and applying a periodic boundary condition for any chiral vectors.[16] Here, γ_0 is the overlap integral and a_0 is a lattice constant. Gap energies for all CNTs with the chiral indexes larger than (5,5) are plotted in Figure I.5. These calculations were performed to investigate the optical absorption properties. The main gap energies, which will define the transport through SWCNTs, are the 1st set of band gaps with zero energy for metallic and with the lowest energies for semiconductor nanotubes. Probably, in addition to optical, noise characterization can reveal other band gaps with energies higher than 1eV.

The calculation of the first energy band-gap for semiconducting nanotubes gave[17–19]

$$E_g = \frac{2\gamma_0 a_0}{d}, \qquad (I.15)$$

where d is the diameter of nanotubes, γ_0 is the overlap integral taken as 2.5eV[17], 2.45eV[18] or 2.7eV[19].

It should be noted that CNTs has so called Curvature Effects[10]. The zone folding concept considered the electronic properties of SWCNTs that was based on the confinement of the carriers in small stripes of graphene. However, the nanotubes are not just stripes of graphene, but small cylinders, where the carbon atoms are placed onto a curved wall. Therefore, we should expect a change in the electronic properties by the curvature of the wall. The first change will be due to the in the carbon-carbon distance. The second is due to change the angles of the hexagon of rolled up graphene sheet. When in graphene the π-orbitals cannot mix with the σ states because they are perpendicular to each other, on the curved wall of CNTs they mix and form σ–π hybrids that are partly of sp^2 and partly of sp^3 character. Mainly due this fact, the smallest nanotubes have not so high hardness as larger diameter ones.[12]

Because of curvature effects, the electronic band structure of SWCNTs changes. The quasi-metallic nanotubes which have zero band gaps can obtain secondary gaps with energy:[20]

$$E_{sec.gap} = \frac{3\gamma_0 a_0^2}{d^2}\cos 3\theta, \tag{I.16}$$

where γ_0 is the overlap integral, a_0 is the distance between carbon atoms, d is the diameter of the nanotube and θ is the chiral angle. This magnitude is of the order 10meV and too small for an experimental verification, but the quasi-metallic character of many nanotubes was observed in transport measurements. Therefore we have to expect the effect of the gaps in noise characterization.

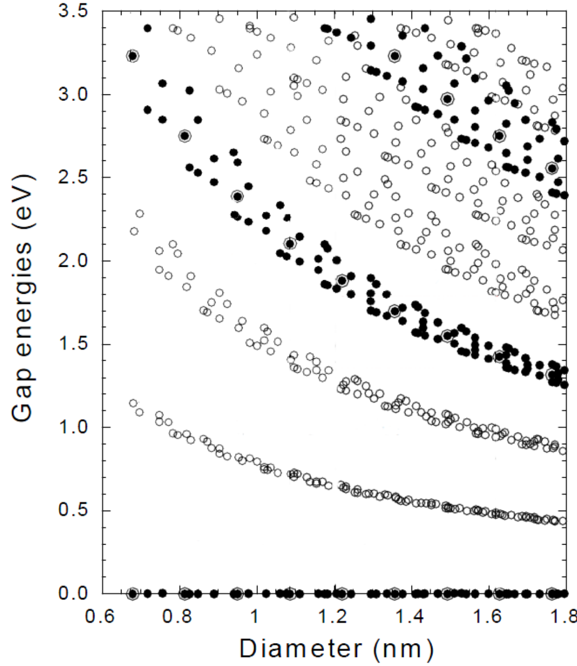

Figure I.5.[16] Calculated gap energies between mirror-image spikes in density of states for γ_0 = 2.75eV. Solid circles indicate the metallic SWNTs and open circles the semiconducting ones. Double circles indicate the armchair-type SWCNTs. Gap energies for all the chiral indexes with larger diameter than (5,5) are plotted as a function of diameter.

The enhanced σ–π hybridization effects which lead to changing the electronic band structure of SWCNTs occur also because of radial deformations perpendicular to the tube axis. The calculations showed that the deformation open the gap in metallic armchair tubes and change or even close the gap in semiconducting nanotubes.[21] Such deformation can occur in the place where the nanotube bends to the electrode contacts and this may lead to the formation of a quantum dot or multiple quantum dots. The article[22] shows the estimation as 7.4N/m the force per unit length that must be applied to a (10,0) nanotube (for example, by a STM or an AFM tip) in order to produce the semiconductor to metal transition. An uniaxial stress of a few kbar can even collapse the tubes followed by reversible restoring the prime geomentry.[23] The electronic response from nanotube collapse reveals two sharply contrasting behaviors. Some tubes (n,n) and (3n,0) have an extreme sensitivity to transverse pressure which arises from the delicate nature of the degenerate low-energy electronic states and the softness of nanotubes under transverse deformations. Other tubes exhibit a surprising insensitivity to collapse. Beside the radial the same effect can be caused by elongation deformation. The results of semiconductor-metal and metal-semiconductor transitions in (8,0) and (9,0) carbon nanotubes are described by Y. Ren et al.[24] The direct experimental observation of the semiconductor-metal transition in SWCNTs induced by compression was demonstrated using the tip of an atomic force microscope[25].

1.1.2. CNT synthesis

For commercial production of the devices based on CNTs is very important to find a way for mass production of SWCNTs and to control the length, diameter, high purity, and chirality of them. However, it is still under development.

Carbon nanotubes can be grown under considerably different conditions. The first macroscopic quantity production of carbon nanotubes was made in 1992 by two researchers at NEC's Fundamental Research Laboratory[26]. They used ***Arc-discharge method*** which was successful for synthesis of gram quantities of nanotubes. During the evaporation and deposition of carbon species through the medium of arc-discharge plasma, nanotubes are formed inside rod-shaped deposits with growth rate of approximately 1μm/min on the cathode surface[27]. The optimal experimental conditions for the growth of MWCNTs were found to be approximately 20V on the electrodes, a current density of 150A/cm^2, a helium gas pressure of 500Torr in the chamber, and a constant interelectrode separation of about 1mm. Both electrodes have to be effectively water cooled and in general the anode has to be smaller than the cathode. The temperature in the interelectrode region has to be about 3500°C.

SWCNTs were firstly produced by the arc discharge method through the usage of the catalyst particles along with the evaporated carbon. A hole is drilled in the center of the anode and filled in with mixtures of metal catalysts and graphite powder in proportion 1-10: 99-90 by weight. Several catalysts have been used but the best results were obtained for Ni, Co and bimetallic systems such as Ni-Y, Co-Ni, Co-Pt. The obtained mixture contains large amounts of SWCNTs bundles (10-100 SWCNTs) deposited along with amorphous carbon and nanoparticles of the catalyst atoms. The use of a Ni-Y catalyst (4 to 1 ratio) in the arc-discharge method allowed to produce a large quantity provided big amount of SWCNTs, more than 75%[28]. Semi-continuous procedure of SWCNTs synthesis by a hydrogen arc-discharge with a mixture of 2.6% Ni, 0.7% Fe, 0.7% Co and 0.75% FeS yielded more than 1.0g of nanotubes per hour.

Another efficient way of producing single-walled nanotubes has also been demonstrated by using a ***laser evaporation (laser ablation)*** technique.[29,30] Direct laser vaporization of transition metal-graphite composite electrodes that were placed in helium or argon atmosphere and in an oven heated to about 1200°C (or even without a furnace by using a continuous-wave 250W CO_2 laser operation at 10.6μm wave length[31]) has yielded SWCNTs with improved concentration (>80%). The amount of carbon deposited as soot is also minimized by the use of two successive laser pulses: the first to ablate the carbon-metal mixture and the second to break up the larger ablated particles and feed them into the growing nanotubes structures. In laser ablation and arc discharge, the yield of SWCNTs was high when NiCo catalyst was used and other catalysts followed in the order NiCo > Ni ~ NiFe >> Co ~ Fe > Pd ~ Pt[32]. The poor catalytic ability of Pd and Pt as graphitization catalyst caused their low catalytic activity in SWCNT formation. NiCo, Ni and NiFe had high efficiencies as graphitization catalysts, low solubility in carbon and stable crystal phase and orientation on graphite. The use of a mixture of Ni and Y (4-6:1) is leading to the production a large amount of SWCNTs by arc discharge[32].

The other method of production of SWCNTs and MWCNTs is catalytic ***chemical vapor deposition (CVD)***. The catalytic vapor phase deposition of carbon was first reported in 1959 and only in 1993 carbon nanotubes were formed by this process[33]. By varying the size of the active particles on the surface of the catalyst the nanotube diameter can be tailored. This method is a widely used as a very efficient method which can be easily scaled down. The nanotubes can be grown from various catalyst-impregnated substrates in the temperature range 500-1200°C. To initiate the growth of nanotubes, two gases are bled into the reactor: a process gas (such as ammonia, nitrogen or hydrogen) and a carbon-containing gas (such as acetylene, ethylene, ethanol or methane). Nanotubes can be also grown at the sites of the metal catalyst; the carbon-containing gas is broken apart at the surface of the catalyst particle, and the carbon is transported to the edges of the particle, where it forms the nanotubes. This mechanism is still being studied. The catalyst particles can stay at the tips of the growing nanotube during the growth process, or remain at the nanotube base, depending on the adhesion between the catalyst particle and the substrate[3].

The resulting deposits may contain a huge amount of single or multi-walled CNTs with diameters in the 1.5-20 nm range. They are usually arranged in bundles smaller than 100 nm in diameter that may be up to tens of mm in length. The total number of SWCNTs in such a 40 nm bundle is estimated to be 600 or more.

The direct synthesis of long strands of ordered SWCNTs by an optimized CVD technique with a floating catalyst method in a vertical furnace[34,35], where n-hexane solution with a given composition of ferrocene (0.018g/ml) and thiophene (sulfur additive 0.4% weight) was introduced into reactor at a rate of 0.5ml/min after heating the reactor to the pyrolysis temperature (1150°C), with hydrogen as the carrier gas flowing at a rate of 250ml/min. SWCNTs yield achieves 0.5g/hour during this continuous procedure. The formation of very long (up to 20 cm) SWCNT strands is the unique characteristic of this vertical floating process.

The deposition of carbon under extreme conditions (that is, using rapid heating and cooling cycles) can generate structures with very unusual morphologies.

The addition of CVD method is ***Super-growth CVD (water-assisted chemical vapor deposition)*** process. It was developed by K. Hata et al.[36] In this process, the activity and lifetime of the catalyst are enhanced by addition of water into the CVD reactor. High density millimeter-tall nanotube "forests", aligned normal to the substrate, were produced. The synthesis efficiency is about 100 times higher than for the laser ablation method. The time required to make SWNT forests of the height of 2.5 mm by this method was 10 minutes.

Usually to obtain pure CNTs after all processes described above the additional process of purification is needed. All purification procedures follow certain essential steps; preliminary filtration of large graphite particles, dissolution to remove fullerenes (in organic solvents) and catalyst particles (in concentrated acids), and microfiltration and chromatography to either size separate MWCNT and nanoparticles or SWCNT and the amorphous carbon clusters.

1.1.3. Application of CNTs and transport peculiarities

There are a lot of promising applications for CNTs in different fields of life: in medicine, in electromagnetic field, chemical, mechanical, in electrical circuits etc[3].

One of the features of CNTs is their strength and flexibility. Probably in future it will have an important role in nanotechnology engineering. The highest tensile strength of an individual multi-walled carbon nanotube has been tested to be 63 GPa. It is interesting to note that carbon nanotubes were found in Damascus steel from the 17th century, possibly helping to account for the legendary strength of the swords made of it. Because of the CNTs' superior mechanical properties, they were proposed as threads for clothes and combat jackets (stab-proof and bulletproof clothing), as wires for space elevators, as synthetic muscles, for bridges and flywheels etc. It was already shown that single and multi-walled nanotubes can produce materials with toughness unmatched in the man-made and natural worlds.

Almost all CNTs are perfect conductors. The fabricated wire from them can have conductivity exceeding copper and aluminum. In theory, metallic nanotubes can carry an electric current density of 4×10^{9}A/cm^{2}, which is more than 1,000 times greater than those of metals such as copper, where for copper interconnects current densities are limited by electromigration. A paper battery where nanotubes act as electrodes can be comparable to a conventional battery and as a supercapacitor quick burst of high energy. The application as solar cells was developed at the New Jersey Institute of Technology using a carbon nanotube complex, formed by a mixture of carbon nanotubes and carbon buckyballs (known as fullerenes) to form snake-like structures. Buckyballs trap electrons, although they can't make electrons flow. The usage of addition of sunlight to excite the polymers, and the buckyballs will grab the electrons. Nanotubes, behaving like copper wires, will then be able to make the electrons or current flow.

In the Kanzius cancer therapy, single-walled carbon nanotubes are inserted around cancerous cells, and then excited with radio waves, which causes them to heat up and kill the surrounding cells. Another medical application was shown that carbon nanotubes and their polymer nanocomposites are suitable scaffold materials for bone cell proliferation and bone formation. Ultra-short SWNTs (US-tubes) have been used as nanoscaled capsules for delivering Magnetic Resonance Imaging (MRI) contrast agents in vivo.

Carbon nanotubes have been implemented in nanoelectromechanical systems, including mechanical memory elements and nanoscale electric motors.

Because of having big surface to volume ratio, CNTs are perfect material for sensors. In 2005, a hydrogen sensor that integrated carbon nanotubes on a silicon platform was placed on the market.

Nanotube films are promised for use in displays for computers, cell phones, PDAs, and ATMs. Transparent, electrically conductive films of carbon nanotubes are developed to replace indium tin oxide (ITO). CNTs films are substantially more mechanically robust than ITO films, making them ideal for high-reliability touchscreens and flexible displays. Printable water-based inks of carbon nanotubes are desired to enable the production of these films to replace ITO.

A nanoradio, a radio receiver consisting of a single nanotube, was demonstrated in 2007. In 2008 it was shown that a sheet of nanotubes can operate as a loudspeaker if an alternating current is applied. The sound is not produced through vibration but thermoacoustically. In 2008 the novel design for nanomotors was theoretically predicted using double-walled CNT formed from an achiral outer tube encompassing a chiral inner tube.

The main goal of this PhD work is investigation of transport and noise properties of CNTs for biosensor applications. Devices based on carbon nanotubes offer several advantages for the detection of biological species.[37] The first is that nanotubes form the conducting channel in a transistor, the most essential part of the architecture. The second advantage is following: nanotubes are typically located on the surface of the supporting substrate and therefore they are in direct contact with the environment. For conventional CMOS-fabricated transistors, the conducting channel is buried in the material in which the depletion layer is formed. And the third advantage, probably the main, is that total current flows at the surface of the tubes.

For the sensor applications, two different device architectures of FETs have been developed and explored by various groups working in this area. In one device architecture, a single nanotube connects the source and the drain. However, there are a lot of variations in parameters of devices fabricated. One of them reflects the geometry-dependent variation in the electronic characteristics of individual nanotubes, the other – the interface between the nanotube and the metallic contacts, which may vary from device to device. The alternative device architecture is following: the devices contain a set of random array or parallel oriented CNTs. In this case current flows along several conducting channels that determine the overall device resistance and the device operation depends upon the density of nanotubes. Usually, devices of such architecture differ in parameters with based on single CNT devices. Therefore, the important advantages are reproducibility and manufacturability.

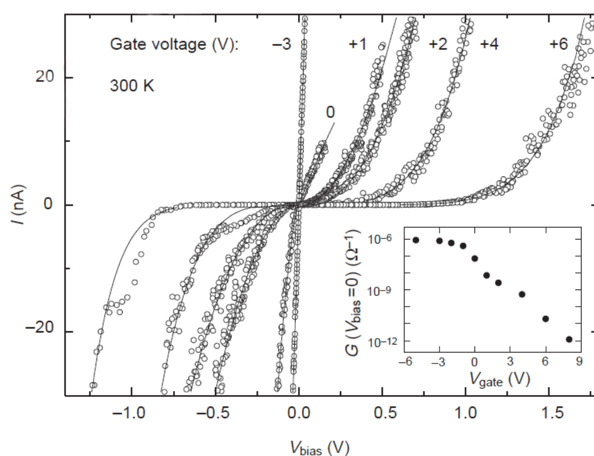

Figure I.6.[38] Two probe I-V_{bias} curves measured for various values of the gate voltage (V_{gate}). Data were taken at room temperature and in vacuum (~10^{-4} mbar). Inset, conductance at $V_{bias} = 0$ as a function of V_{gate}. The conductance through this single molecular switch can be varied over at least six orders of magnitude and saturates at $10^{-6}\Omega^{-1}$.

The first ***field-effect transistor (CNTFET)*** with CNT as conductive channels was demonstrated in 1998 by S.J. Tans et al.[38] The devices consist of individual CNTs and three contacted Pt electrodes to them. The nanotubes were produced by laser-vaporization of carbon with an admixture of Ni/Co and deposited on Si substrate, covered with a 300nm layer of thermally grown SiO_2. The back side of substrate was used as a back-gate. The length between contacts was 100nm. The obtained current-voltage characteristics for various gate voltages are shown in Figure I.6. The strong suppression of the current at low bias voltage was obtained at positive V_{gate}, what means the *p*-

type behavior of carbon nanotube. The conductance through CNT can be varied over at least six orders of magnitude. The fact places the CNTFETs on the same level of the importance as Si based FETs technology.

After this establishment the scientists try to find the best configurations of CNTFETs for several important fields of applications. The solution includes: variation of contact metallization, utilization of different number of nanotubes and various insulators between the CNTs and gate electrode, different topographies of gate electrodes.

To select a proper element for the contacts metallization we have to know the electrochemical affinity of CNTs (it will be comparable with the CNTs' work function). The influence of work functions, electron affinities and ionization potentials for (5,5) and (7,0) finite size carbon nanotubes have been studied using ab initio calculations in the work of F. Buonocore et al.[39] The (5,5) nanotube and the (7,0) nanotube are a zero band gap metals for which the authors have obtained the work function of 4.37eV and 4.82eV, respectively. Moreover, the comparison with the many experimental data available was acceptable. Transmission electron microscopy (TEM) measurements on multiwall nanotubes give 4.6-4.8eV, photoelectron emission gives 4.95eV and 5.05eV for multi- and single wall, thermionic emission for multi-wall gives 4.54-4.64eV, ultraviolet photoemission spectroscopy (UPS) measurements on single wall gives 4.8eV. The authors also showed that the work function has a weaker dependence on the nanotube length with an overall variation of about 0.4-0.5eV. Therefore, we can conclude that the work function (and therefore the electrochemical affinity) of SWCNTs lies in the range of 4.4-5.0eV.

The work functions for several appropriate metals are listed in Table I.1. Because of difference in electrochemical potentials of CNTs and work functions of the metals it is possible to build different configurations of the contacts, such as Ohmic, Schottky barrier contacts for electrons and for holes. The first Ohmic contact p-type CNTFETs were fabricated by depositing Pd pads onto CNTs and annealing in Ar while near-Ohmic Al contacts were obtained for n-type FETs[40]. The doping level of CNTs is of an importance here. For example, to fabricate the Ohmic contacts to n-doped CNTs lower than 4.4eV of contacted metals' work function has to be used, and p-doped – higher than 5eV. The last is clearly shown in the work of Z. Chen et al.[41], where the role of metal–nanotube contacts on the performance of CNTFETs was established using Al, Ti and Pd.

Table I.1. Electron work functions of transition metals. The data are taken from http://wikipedia.org. Green color shows element that ought to create the Ohmic contacts to CNTs. Orange and Blue color metals should to create Schottky barriers for holes and for electrons, respectively. It should be noted that work function can change for crystalline elements based upon the orientation.

El.	eV	El.	eV	El.	eV	El.	eV	El.	eV
Ag	**4.52-4.74**	Al	4.06-4.26	Au	5.1-5.47	Bi	4.34	Cd	4.08
Co	5	**Cr**	**4.5**	**Cu**	**4.53-5.10**	**Fe**	**4.67-4.81**	**Ga**	**4.32**
Hg	**4.475**	In	4.09	Ir	**5.00**-5.67	Mg	3.66	Mn	4.1
Mo	**4.36-4.95**	Nb	3.95-**4.87**	Ni	5.04-5.35	Os	5.93	Pb	4.25
Pd	5.22-5.6	Pt	5.12-5.93	**Re**	**4.72**	**Rh**	**4.98**	**Ru**	**4.71**
Sc	3.5	**Sn**	**4.42**	**Ta**	**4.00-4.80**	Ti	4.33	Tl	~3.84
V	4.3	**W**	**4.32-5.22**	Y	3.1	Zn	3.63-**4.9**	Zr	4.05

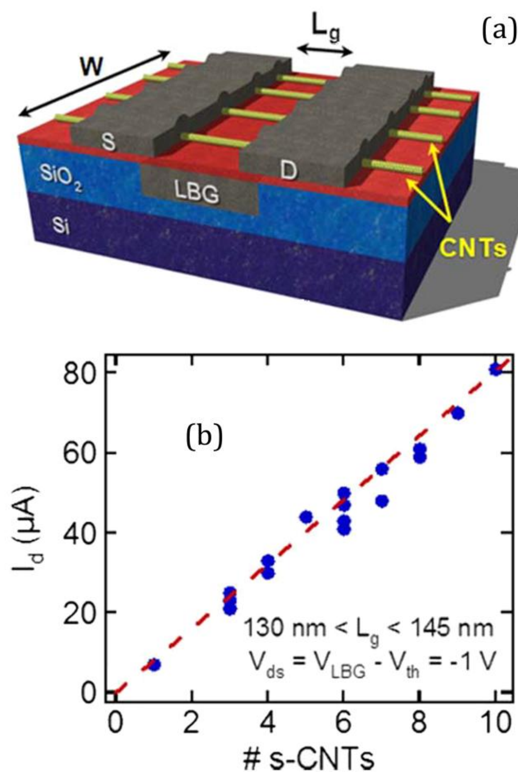

Figure I.7.[43] (a) Schematic of the device structure. (b) ON-current versus number of s-CNTs from a set of LBG-CNTFETs at the same overdrive. Note the clear linear scaling of the current with the number of CNTs.

The next configuration which can be varied is gate topography (or geometry) of FETs. There are 6 main types of them: back-gate (BG), local-bottom-gate (LBG), top-gate (TG), gate-all-around gate (GAA), side-gate (SG) and liquid-gate (LG) topographies. The **back-gate topography** is the easiest one in processing. Usually, scientists grow nanotubes on the Si\SiO$_2$ substrates with gate dielectrics of thickness about ~100 nm or more. In this case substrate can be used as a gate. As a result, high gate voltages are required to switch the devices on. In addition, using of the substrate as a gate contact allows all devices turning on simultaneously. The first investigation of FETs based on CNTs was done by using this topography, as it was shown above[38].

A **local-bottom-gate (LBG) configuration** (Figure I.7(a)) is improved BG topography was introduced for CNTFETs in the work of A. Bachtold et al.[42] The demonstration of logic circuits with FETs based on single CNT was done using small gate voltages. Later, using LBG geometry A.D. Franklin et al.[43] demonstrated one of the best performances of CNTFETs to date: with current density >40μA/μm (no metallic nanotubes), inverse threshold slope of 70mV/decade, and ON/OFF-current ratio >10^5 on highly aligned nanotubes (4 SWCNTs/μm). The authors showed that ON-current is scaled linearly with the number of nanotube channels (see Figure I.7(b)).

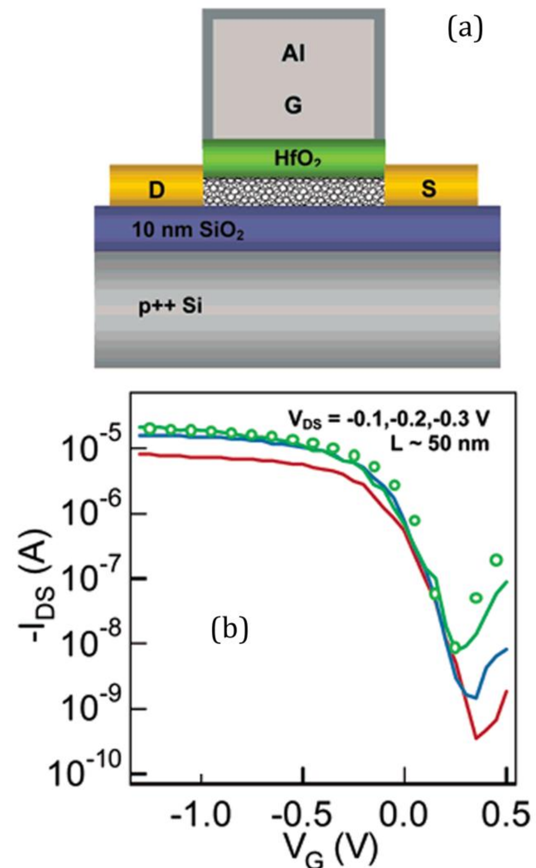

Figure I.8.[46] (a) Side-view schematic of a device. SWCNTs were grown by CVD on Si(p^{2+})/SiO$_2$ substrates. (b) Current vs top-gate voltage for a device with L~50nm and d~1.7nm SWCNT at different biases, V_{DS}. Symbols correspond to V_{DS}=0.3V.

With LBG geometry a CNTFET with diameter of the nanotube ~1.2nm exhibited ~18μA at L_g~38nm and equivalent oxide thickness of ~2nm[44]. Processing of the device with 200 such s-CNT channels per micrometer would provide ~4mA/μm. The last is well beyond the projected Si-based technology.

The fabrication of CNTFETs in a conventional metal-oxide-semiconductor FET (MOSFET) structure, with gate electrodes above the conduction channel – **top-gate TG topography** – was demonstrated as most technologically relevant CNT transistors (see the work of S.J. Wind et al.[45]). The authors showed both the usually observed *p*-type and uncommon *n*-type behaviors of CNTFETs. The *n*-type devices were obtained by annealing of the samples at 425°C in N_2 and depositing of gate oxide film to protect the CNTs from further effects of ambient gases. A top-gated CNTFETs are promising devices in electronics because of their great performance, such as ~20μA of ON-current at L_g~50nm with equivalent oxide thickness of ~2nm[46] (Figure I.8) and because of small capacitance which is crucial at high-speed operation. However, TG topography is not proper for bio-sensing applications.

Gate-all-around (GAA) CNTFETs, also known as wrap-around gate CNTFETs were developed by Zh. Chen et al.[47] The FETs consisted of functionalized nanotubes wrapped by an Al_2O_3 dielectric and tungsten nitride (WN) gate metal (Figure I.9). GAA is a further improvement upon the TG device geometry. In this device the entire circumference of the nanotube is gated. This should ideally improve the electrical performance of the CNTFET, reducing leakage current and improving the device ON/OFF ratio.

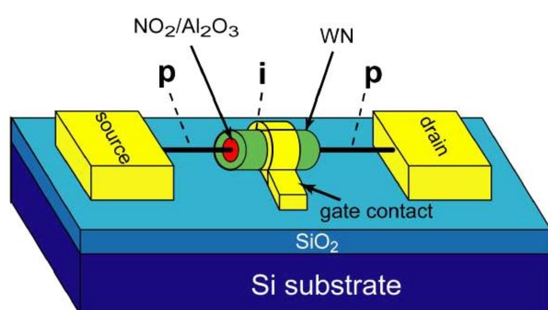

Figure I.9.[47] Schematic of a GAA-CNTFET. A MOSFET like p(n)/i/p(n) structure is realized by gating only the middle segment of the CNT with an all-around WN metal gate and Al_2O_3 dielectric.

The wrap around process is described in the work of D.B. Farmer and R.G. Gordon[48]. They showed that exposure to NO_2 and $Al_2(CH_3)_6$ vapor leads to fictionalization of the surfaces of CNTs with self-limited monolayer. The functionalized CNT surfaces are susceptible to atomic layer deposition (ALD), which allows to create coaxial nanotube structures with precisely controlled diameters. To process the GAA-CNTFETs the Al_2O_3 film of 7nm around the tube was deposited by ALD. These wrapped nanotubes are then placed on an insulating substrate, where the wrappings were partially etched off, exposing the ends of the nanotube. The source, drain, gate contacts and the metallic outer gate wrapping were then deposited.

One of the ways to design biosensors is **side-gate (SG) topography** of FETs. Usually SG is deposited with contacts to nanotubes using e-beam lithography on the distances of tens-hundreds nanometers from CNTs. However, interesting technique of processing SG are shown by L.A.W. Robinson et al.[49] They have fabricated self-aligned, side-gated suspended MWCNTs, with nanotube-to-gate spacing of less than 10 nm by using the nanotube as a mask shielding the substrate (Figure I.10).

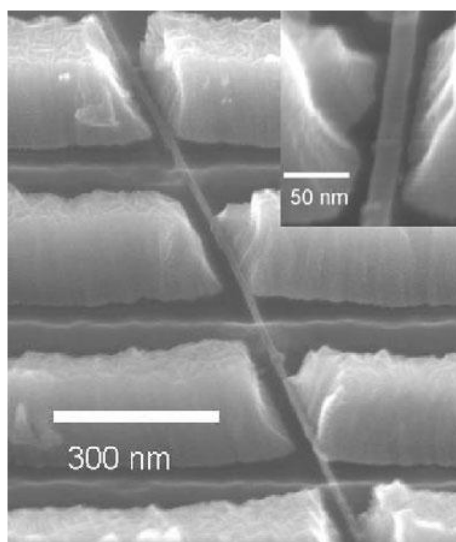

Figure I.10.[49] Chrome was the most successful metal for the fabrication of self-aligned side gates. The nanotube is running from top left to bottom right.

Liquid-gate (LG) topography is usually using for investigating different solutions. This scheme works when the molecules that should be detected are dissolved in conductive physiological buffer (Figure I.11). In this case several precautions should be taken into account[37]. At large gate voltages electrochemical reactions may occur, which can be controlled by monitoring the current between gate and channel. All electrodes, including source and drain, have to be isolated to avoid undesirable reactions. Using this topography and monitoring the current in the DC regime, for example, the attachment of charged proteins to the device the protein detector sensor can be demonstrated.

The gate electrode of FETs based on semiconductor CNTs allows their operation in different regimes, which can be important for bio-sensing and for investigating transport and noise properties of CNTs. The sensitivity of sensors is different in hole- (or electron-) accumulation and depletion regimes. The main difference is in the signal to noise ratio. To obtain the best sensor both of these parameters should be optimized. One of the goals of this work is the investigation of the CNTs noise properties, which can be used for optimization of the second parameter.

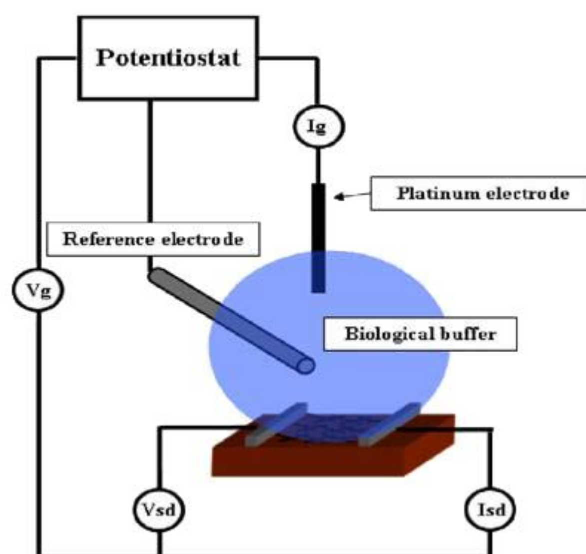

Figure I.11.[37] Device arrangement for LG. The gating is accomplished by immersing a Pt electrode in the conducting liquid that surrounds the network and the source and drain.

Carbon nanotubes, especially SWCNTs, are size comparable with many biomolecules (such as DNA). The unique electrical properties and their sensitivity due to increased surface-to-volume ratio have made CNTs ideal candidate for chemical and biological sensors.[50] The current that flows in CNTFETs is extremely sensitive to the substance adsorption or conductivity changes related to these events. Based on this approaches a wide variety of devices have been explored. The main principles of devices include: the detection of proteins, antibody-antigen interactions, glucose, DNA and DNA hybridization, and single nucleotide polymorphism.

The first biosensor based on an individual SWCNT was demonstrated by K. Besteman et al. in 2003.[51] The author showed that glucose oxidase (GOx) coated semiconducting SWCNTs act as sensitive pH sensors. Moreover, changes of conductance of the GOx-coated

CNTs upon increasing of glucose indicated that an enzyme-activity sensor can be realized at the single molecule level of an individual SWCNT.

Later, numerous sensors were presented based on CNTFETs. Highly sensitive single CNTFETs have been shown which can detect protein adsorptions and specific protein-protein interactions at 1pM concentrations[52], what is in 10^4 lower than previous published results[53]. The authors proposed that the relatively high sensitivity can be reached by the increased Schottky contact area which accommodates relatively more numbers of proteins even at very low concentration. By using shadow mask it was possible to allow the penetration of metal underneath the mask efficiently, forming a thin and wide Schottky contact area on SWCNT channels. The conductance of devices changes due to the instant modulation of the work function of metal contacts by increased number of absorbed proteins.

For highly selective biosensing usually it is necessary to use specific targeting agents, such as antibodies[52–54] (Figure I.12), synthetic oligonucleotides (aptamers)[55] etc. The FETs based on aptamer-modified CNTs were used for the detection of immunoglobulin E (IgE)[55]. The sharp decrease in the source-drain current was observed in the presence of the targeted IgE, and the current change increased with the IgE concentration. The detection limit was demonstrated to be about 250pM.

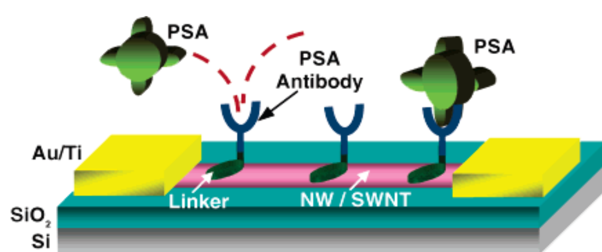

Figure I.12.[54] Schematic diagram of the nanosensor. Anti-prostate-specific antigen (PSA) monoclonal antibodies are anchored to the CNT surface and function as specific recognition groups for PSA binding.

Scientists form Osaka University (Japan)[56] have fabricated *n*-type CNTFET biosensors and using LG topography (keeping zero back-gate voltage) showed the successful detection of negatively charged proteins (bovine serum albumin) without any modification process.

A. Star et al.[57] showed the possibility of DNA immobilization and hybridization detection by using FETs based on CNT networks. It was found that the network can be selectively functionalized with DNA oligonucleotides and retain hybridization specificity. Thus, the FETs with immobilized synthetic oligonucleotides have been demonstrated to selectively recognize target DNA sequences with single-nucleotide polymorphism. The limit of detection was 14 pM at a signal-to-noise ratio of 2. Later E. Gui et al.[58] employed the same FET configuration in the fabrication of a device with two different metal contacts (Au and Cr) for electrical detection of DNA hybridization.

Another sensor application was proposed by J.R. Siqueira, Jr. et al.[59] They proposed to use layer-by-layer (LbL) technique to obtain two types of sensors incorporating CNTs (Figure I.13): an amperometric sensor to detect dopamine, and a capacitive sensor to detect pH changes and penicillin G. The sensitivity was 106mV/(mM*L) and 54.5mV/pH, respectively. And detection limit for the first sensor $1.0x10^{-4}$ M/L, which is sufficiently low for a possible use in commercial application.

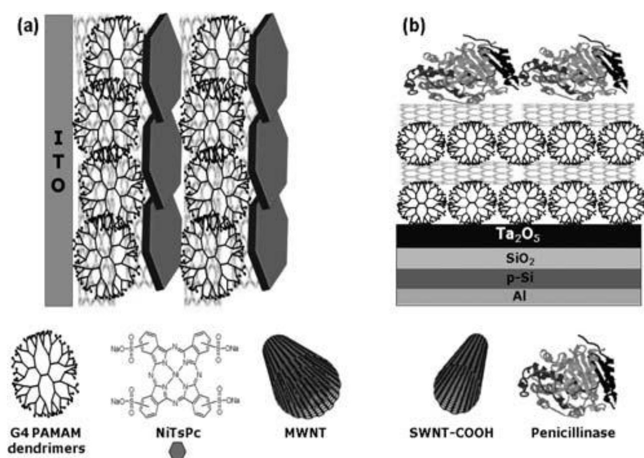

Figure I.13.[59] Idealized schemes of the modified electrodes containing PAMAM-NT/NiTsPc LbL film (a), capacitive EIS sensor containing PAMAM/SWCNT LbL film with the immobilized enzyme penicillinase (b).

J.C. Claussen at al.[60] employed networks of SWCNTs decorated with Au-coated Pd (Au/Pd) nanocubes as electrochemical biosensors that exhibited excellent sensitivity (2.6mA*mM^{-1}*cm^{-2}) and a low estimated detection limit (2.3nM) at a signal-to-noise ratio of 3 in the amperometric sensing of hydrogen peroxide. To demonstrate an important medical application, the Au/Pb nanocubes were selectively immobilized with glucose oxidase (GOx) via thiol linking for amperometric glucose detection. As a result, authors exhibited glucose detection limit of 1.3μM and linear range spanning from 10μM to 50mM.

The DNA sensors was reported by X. Dong et al.[61] They demonstrated a dramatic sensitivity enhancement in electrical detection of DNA hybridization using SWCNT-FETs via introducing reporter DNA-Au nanoparticle (AuNP) conjugates in the hybridization step (Figure I.14). The change in drain current allows to reliably determining the DNA concentration down to ~100fM.

Figure I.14.[61] Schematic illustration of DNA detection enhancement by reporter DNA-AuNP conjugates.

By modification of glassy carbon rotating disk electrode with catalase and MWCNTs it is possible to realize the amperometric detection of nitrite, iodate and periodate.[62] Under optimized condition of the amperometry method the concentration range, detection limit and sensitivity were determined to be from 1μM to 6mM, 0.15μM and 55.6nA/μM for periodate, from 1μM to 5mM, 0.2μM and 44.4nA/μM for iodate and from 5μM to 10mM, 1.35μM and 7nA/μM for nitrite, respectively. The authors also presented fast response within 5s time scale.

The controlling of nanotube density in CNT network is important for the performance of the CNT-based sensors.[63] It was shown that devices fabricated on the basis of low density CNTs allow a detection limit of 1pM in an electrolyte buffer. Results of further investigation demonstrated that the enhanced sensitivity arises from the semiconductor-like behavior of the CNT network at low density. The developed biosensors with optimized nanotube density were used as a quick diagnostic tool for such diseases as severe acute respiratory syndrome (SARS).

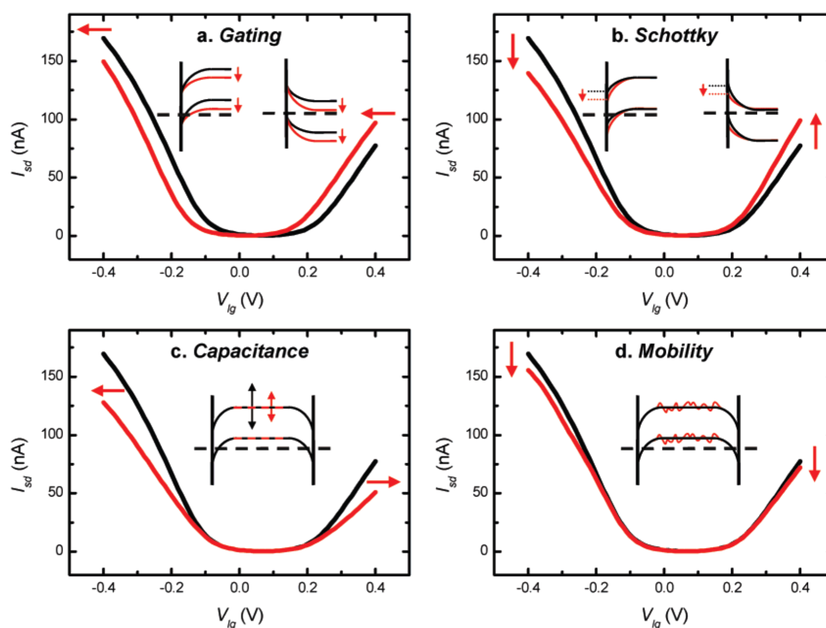

Figure I.15.[64] Calculated I-V_{LG} curves before (black) and after (red) protein adsorption for four different sensing mechanisms. The bias voltage is 10mV.

Nevertheless, the sensing mechanism of CNT based sensors is not fully understood and possibly includes charge transfer from adsorbed species, modifications of contact work function, substrate interactions, and carrier scattering by adsorbed species. The possible detection mechanisms were discussed by I. Heller et al.[64] and D. Kauffman et al.[65] Figure I.15 illustrates the characteristic qualitative effect of protein adsorption on I-V_{LG} curve for different previously mentioned sensing mechanisms (the curves were calculated using the model described in the Supporting Information of the work of I. Heller et al.). Figure I.15(a) shows the change in the current dependence on liquid gate voltage, I-V_{LG}, in the case of electrostatic gating by adsorbed charged species that induce a screening charge in the SWCNTs. The Schottky barrier mechanisms are demonstrated in Figure I.15(b) where adsorbed biomolecules at the metal contact modulate the local work function and thus the band alignment. Figure I.15(c) shows the effect of a reduced gate efficiency, which may occur when the gate capacitance is reduced due to low permittivity, ε, of adsorbed biomolecules relative to the electrolyte. Finally, Figure I.15(d) illustrates the effect of reduced carrier mobility, suppressing the conductance in both p- and n-branches.

1.1.4. Recently registered noise properties

CNTs are interesting materials for studying noise because of several reasons. Usually, the nanotubes exhibit $1/f$-noise in a wide frequency range, which gives an opportunity to understand phenomenon of $1/f$-noise in 1D conductors and semiconductors (more detail information about $1/f$-noise components see chapter 2.2.5). The SWCNTs also have all their atoms on the surface which can result in increased noise than their 2D and 3D dimensional counterparts have. The current in nanotubes also has a one dimensional behavior, therefore any contaminant or adsorbent that interacts with an atom on the tube can

interrupt the flow of current. In contrast, removing of a single atom in 3D systems will have a negligible effect on the conductivity of the device.[66]

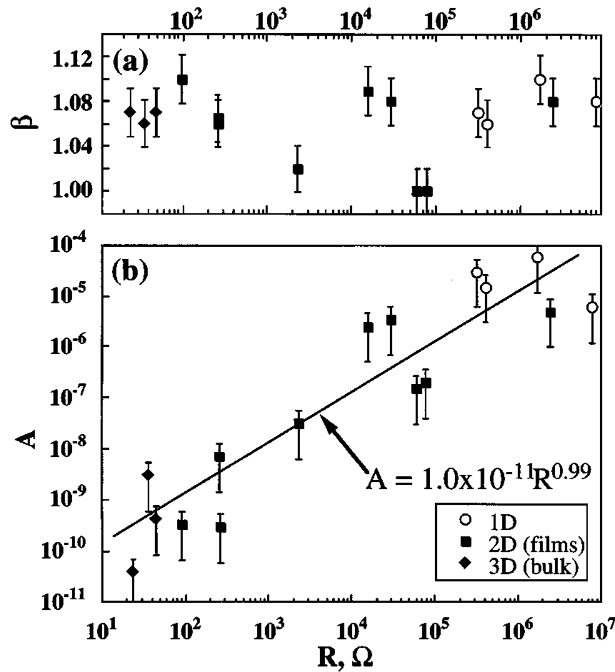

Figure I.16.[67] Excess noise parameters for a wide range of nanotube-based conductors, as a function of sample resistance. The excess noise of each sample has the functional form $S_V = AV^2/f^\beta$. (a) Variation of β for the sample set. (b) Variation of A for the sample set.

The first results on CNTs $1/f$-noise study were reported by P.G. Collins et all.[67] Three important systems were measured: individual isolated SWCNTs (1D), thin films of interconnected nanotubes (2D), and bulk nanotube mats (3D), consisted of no less than 10^6 SWCNTs. The anomalously large bias-dependent $1/f$ noise was registered. The noise magnitude greatly exceeds noise level commonly observed in metal films, carbon resistors, or even carbon fibers with comparable values of resistances. A single empirical expression describing the noise for all measured nanotube samples, allow suggesting a common noise-generating mechanism, which is proportional only to the number of nanotubes in the conductor. A least-squares power law fitting suggested a direct proportionality between noise amplitude A and sample resistance R (see Figure I.16). In the paper an estimation of Hooge's constant (see chapter 2.2.5, Eq.(I.82)), α_H, was done taking the number of carriers as the number of atoms. The obtained value α_H=0.2 was in 100 times higher as value experimentally obtained by Hooge for semiconductors.[68] One of the reasons for such a large value of Hooge's constant was suggested that the calculation of the number of carriers being equal to the number of atoms is not appropriate.

M. Ishigami et al.[69] showed that Hooge's empirical rule adequately describes the low-frequency noise in CNTFETs with α_H=(9.3±0.4)x10^{-3}. The amplitude of $1/f$-noise was found to be inversely proportional to $|V_G-V_{th}|$ indicating mobility fluctuations. It was concluded that the noise is a property of the CNT and not the electronic contacts, because its amplitude was also inversely proportional to the device length. Furthermore, the authors have shown that surface adsorbents due to air exposure do not increase the magnitude of the $1/f$-noise, contrary to expectations. Later this group demonstrated the temperature measurement of Hooge's constant and propose some physisorbed species (e.g. H_2O and CO_2) that can be responsible for the room temperature noise of individual SWCNT.[70] The proving of Hooge's relation also was done by Yu-M. Lin et al.[71] It was shown here that the Hooge's constant in nanotubes is comparable to most bulk materials and the noise amplitude (A) can be quite significant because of the small number of carriers.

The contacts to CNTs can play crucial role as it was shown in the work of K. Kim et al.[72], where low-frequency noise of individual MWCNTs was investigated with Ti/Au, Cr/Au, Pt/Au, and Pd/Au electrodes. The noise was clearly observed and has $1/f$-shape with amplitude that strongly depended on the different metals (Figure I.17). Pd and Pt contacted devices showed much smaller noise level than Ti and Cr contacted devices. The improved electrical contacts using Pd or Pt metals demonstrated a quasi-ballistic transport with an increased exponent $S_I \sim R^{4.8}$, similar to 2D metallic films or graphene. In the case of Cr or Ti electrodes the noise was almost linear as a function of the nanotubes resistance. It was suggested that this may be a reason of the influence of the contacts.

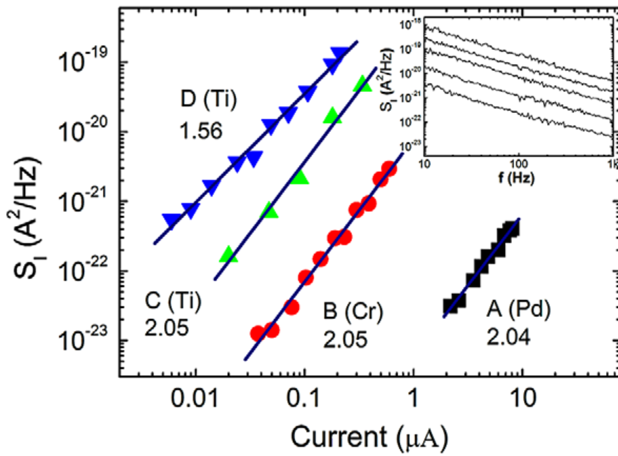

Figure I.17.[72] Current noise power spectra as a function of current at the 20 Hz. The exponent for the nonlinear I–V sample was smaller than the expected number of 2. The inset is the noise power spectrum of a single MWNT depending on the current level, I = 15, 40, 140, 400, and 600 nA from the bottom to the top at room temperature.

By investigating the temperature dependence of resistivity of CNT films two mechanisms of current formation was demonstrated by A. Behnam et al.[73] One of the mechanisms is three-dimensional Mott variable-range hopping at low temperatures. In this case the localization effects result in an insulating behavior in CNT films. And at higher temperatures, fluctuation-induced tunneling mechanism was registered. In the temperature regime, the authors analyzed the temperature dependence of the noise amplitude and extracted the density of fluctuators that are responsible for the $1/f$-noise as a function of their energy using method demonstrated in the work of D. Tobias et al.[70]

E.S. Snow et al.[74] demonstrated that to predict the noise in SWCNT network following an empirical formula can be used:

$$S_V = 9 \times 10^{-11} \frac{R}{L^{1.3}} \frac{V^2}{f}, \qquad \text{(I.17)}$$

where R is the device resistance, L is the spacing between the contacts, V is the voltage applied to the device, and f is the frequency. The applicability of the equation was proved by studies of the networks that range in size from 10 to 10^8 μm^2 in the resistance range from 10^4 to 10^7 Ω. It was shown that it can be a useful tool for assessing the noise characteristics of SWCNT devices.

The charge trapping in the gate oxide of CNTFETs can cause the shift of the threshold voltage and increased low-frequency noise. The calculation of this effect, using the nonequilibrium Greens function method in a tight-binding approximation, was performed by N.-P. Wang et al.[75] The authors found that a single charge can shift and even rescale the entire transfer characteristic of the device. Such changes may lead to giant amplitudes of "random telegraph signal" (RTS) noise (more detail information about RTS-noise

components see chapter 2.2.4) in agreement with recent experiments.[76] It was suggested that thinner gate oxides and high-k dielectrics may allow greatly reduce these effects.

There are few methods to reduce the noise of CNT based devices. One of them was proposed and demonstrated by J. Appenzeller et al.[77] A substantial reduction of the $1/f$-noise was reported in various ballistic carbon nanotube devices for a tube transistor with multiple CNTs in parallel. By contacting semiconducting tubes with different metal electrodes it was established that a small ratio of the noise amplitude A and the sample resistance R cannot be indication of a suitable metal/tube combination for logic applications.

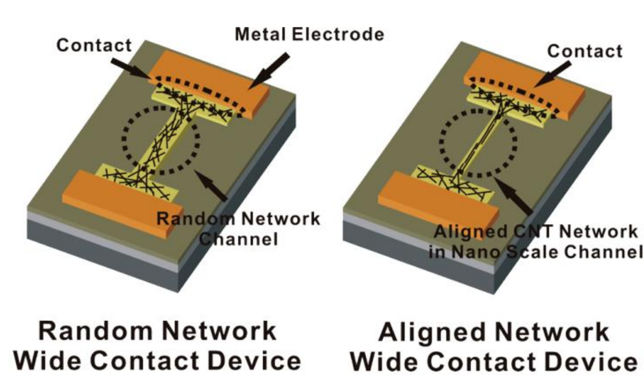

Figure I.18.[78] Schematic diagram depicting the structure of wide CNT/electrode contact device.

H. Lee et al.[78] proposed a wide contact strategy for fabrication low-noise nanochannel devices based on aligned and randomly oriented CNT networks (Figure I.18). The authors demonstrated a dumbbell-shaped CNT network channel composed of a narrow long channel region and wide CNT/electrode contacts. The reducing of noise coming from CNT/electrode contact region was observed. Interestingly, that the analysis revealed different behavior of the noise amplitude in aligned and randomly oriented CNT networks.

1.2. Nanowires

A nanowire is a physical structure, the diameter of which is a value of the order of nanometers. Moreover, nanowires with cross-section dimension compareable with the de Broglie wave of charge carrier in the material showed the quantum mechanical effects and therefore the term "quantum wires" can be used. There are many different types of nanowires, including metallic (such as Ni, Pt, Au, etc.), semiconducting (such as Si, InP, GaN, etc.), and insulating (such as SiO_2, TiO_2, etc.).[79]

In the near future, the nanowires could be used to link tiny components in extremely small circuits. Using nanotechnology, such components could be fabricated from chemical compounds. The basic physical properties of different type of nanowires are shown in Table I.2. There are many advantages of them for different field of applications. The metallic/semiconductor nanowires together with break junctions can be easily externally connected (see Table I.2). The carbon nanotubes have extremely high flexibility, which allows producing of the long and very thin wires with unique properties. Together with carbon nanotubes the quantum wires have perfect electrical characteristics with extremely high mobilities measured in thousands of $cm^2/V*s$.

Table I.2. Comparison of basic physical properties of different type of nanowires.

	Metallic,.. nanowire	Break Junction	Carbon nanotube	Molecular wire	Quantum wire
Composition	Cu, Ag, Au, Si…	Cu, Ag, Au…	C	C, N, H, S	GaAs/AlGaAs, GaN/AlGaN
Geometry	Cylindrical, polygonal	n.a.	Tubular	Fixed by Q.M.	Planar (2D)
Width	Atomic - …	Atomic	0.4-20 nm	< 1nm	10’s nms
Length	Atomic - …	1-1000nm	Up to more than 1m	Few nanometers	2-1000μm
External Connections	Easy	Easy	Problematic	Challenging	Straightforward
Fabrication	Synthesis, Contact mechanics, …	Contact Mechanics	CVD, Carbon Arc	Test Tube	High Resolution Lithography
Conduction Mechanism	Quasi-ballistic, ballistic, ?	Quasi-ballistic, Quantum	Quasi-ballistic	Tunneling, Quantum, ?	Ballistic

The electronic properties of nanowires strongly depend on the diameter. With decreasing of the diameter the electronic density of states (D.O.S.) contains the specific energies, called van Hove singularities, where D.O.S. becomes very large (Figure I.19). In

such cases, nanowires behavior can be similar to the case of molecules and atoms and very different from the case of crystalline solids or even two-dimensional system.[80]

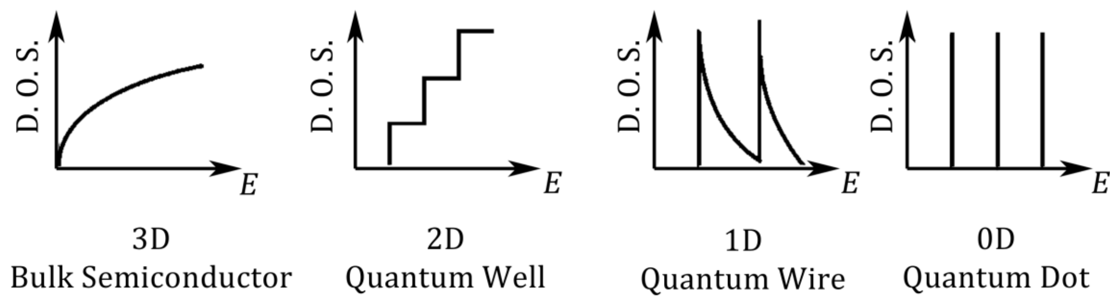

Figure I.19.[80] Electronic density of states for bulk 3D crystalline semiconductor, 2D quantum well, 1D nanowire or nanotube and 0D quantum dot.

Therefore, at small diameters the specific behavior of electronic density of states may result in extraordinary optical and electrical effects that can be used in practice. For example, when the length of nanowires is lower than the electron free path length the current has ballistic character. In this work we analyzed transport of the carbon nanotubes including ballistic as well as quasi-ballistic (when the length of them are in the order of magnitude with the mean free path length) resimes.

2. Noise characterization

In electronics, *noise* is random fluctuations of the electrical signal in electronic devices. Noise can be a result of bad contacts or other parasitic effects. In these cases it can be easily removed. The most interesting noise is the noise inherented to the system itself and usually it is increased when size of the devices decreases. Therefore, one of the main techniques in physics for characterizing of any material, especially at nanoscale, is noise characterization. It allows getting information about nonuniformity, defects and traps in materials, about life cycles of the devices etc.

The first theoretical consideration of electrical noise, or fluctuations, was done by W. Schottky[81] in 1918. He described the possibility of recognition of a measurable disturbance in amplifiers created by the heat motion of electricity under certain conditions. Later, J.B. Johnson[82] and H. Nyquist[83] independently, but almost simultaneously proved and demonstrated such possibility experimentally.

2.1. Noise: mathematical methods and main theorems

Usually noise can be registered as fluctuations of voltage or current on the terminal of each device[84]. These fluctuations are time depended function whose instantaneous values are variable in time scale. Therefore, it is necessary to use statistical methods to describe noise in a proper way. Usually, a huge number of measurements and/or long time observations are needed to understand the noise phenomena.

The fluctuation of voltage or current can be explained by consideration of time depended unit charge inside the material. Such behavior can be inconspicuous on the background of real signal and creates only extremely small deviations from the operating point. In this case, we can apply the theory of small signals to the noise fluctuations. For stable operations devices at certain conditions noise is statistically stationary, i.e. the device properties don't depend on time of measurements. These features simplify the analysis and understanding of the noise.

The mathematical analysis of noise deals with probabilistic characteristic in time and frequency domains. Therefore, the main statistical characteristics used for description of noise processes are mean value, autocorrelation function and spectrum density.

Mean value. Statistical properties of the fluctuation process are features that appear during long time or relatively large number of measurements. Consequently, this process can be mathematically investigated using imaginary ensemble of similar processes describing by the functions of time: $x^{(1)}(t)$, $x^{(2)}(t)$, ... , $x^{(N)}(t)$. There are two different methods of averaging that can be applied to this functional ensemble – the time and ensemble averaging.

Time averaging of the i-term of ensemble is

$$< x^{(i)}(t) >= \lim_{T\to\infty} \frac{1}{T} \int_0^T x^{(i)}(t)dt, \tag{I.18}$$

where T is duration of observation interval.

Ensemble averaging is an average value taken at any time t_1:

$$\overline{x(t_1)} \equiv \mathrm{E}\big[x^{(i)}(t_1)\big] = \lim_{N\to\infty}\frac{1}{N}\sum_{i=1}^{N}x^{(i)}(t_1) = \int_{-\infty}^{\infty}x_1p_1(x_1,t_1)dx_1, \quad (I.19)$$

where E is the mathematical expectation; N is number of functions in ensemble; x_1 is the short cut of $x(t_1)$; $p_1(x_1, t1)$ is the function of density of the joint probability. For stationary processes the ensemble averaging doesn't depend on time constant t_1, but for nonstationary – this is not the case.

Autocorrelation function. This function allows to define an extent of correlation time or so called "memory" of the process. It defines as

$$\varphi_n^{(i)}(\tau) \equiv < x^{(i)}(t)x^{(i)}(t+\tau) > = \lim_{T\to\infty}\frac{1}{T}\int_0^T x^{(i)}(t)x^{(i)}(t+\tau)dt. \quad (I.20)$$

It should be noted that autocorrelation function is also a function of time delay τ and it is the mean square value of the process at τ=0.

Power spectral density. The power of noise process is convenient to consider in terms of Parseval's theorem which shows correlation of a function of time with its Fourier transform:

$$\int_{-\infty}^{\infty}[x(t)]^2dt = \frac{1}{2\pi}\int_{-\infty}^{\infty}|X(j\omega)|^2d\omega. \quad (I.21)$$

Each part of the Eq. (I.21) is equal to total energy in $x(t)$. The value $|X(j\omega)|^2$ can be interpreted as an energy density of the process (in energy unit divided by hertz). To obtain the mean power of the noise process we should divide the full energy by time during which this energy was released:

$$\lim_{T\to\infty}\frac{1}{T}\int_{-\infty}^{\infty}[x(t)]^2dt = \lim_{T\to\infty}\frac{1}{2\pi}\int_0^{\infty}\frac{2|X(j\omega)|^2}{T}d\omega. \quad (I.22)$$

We are dealing with function $x(t)$ that are a part of an ensemble therefore, after using the ensemble averaging the sings "lim" and integral can be swapped. Then, the power spectral density determines as

$$\overline{S_x(\omega)} = \lim_{T\to\infty}2\frac{\overline{|X(j\omega)|^2}}{T}. \quad (I.23)$$

The power spectral density of a stationary process unambiguously associated with the autocorrelation function of this process:

$$\overline{\varphi_x(\tau)} = \lim_{T\to\infty}\frac{1}{T}\int_{-\infty}^{\infty}\overline{x(t+\tau)x(t)}dt = \lim_{T\to\infty}\frac{1}{2\pi}\int_0^{\infty}\frac{2|X(j\omega)|^2}{T}\cos\omega\tau\, d\omega. \quad (I.24)$$

Using the Eq. (I.23) we can obtain

$$\overline{\varphi_x(\tau)} = \frac{1}{2\pi}\int_0^\infty \overline{S_x(\omega)}\cos\omega\tau\, d\omega, \tag{I.25}$$

and inversely

$$\overline{S_x(\omega)} = 4\int_0^\infty \overline{\varphi_x(\tau)}\cos\omega\tau\, d\tau, \tag{I.26}$$

The Eq. (I.25) and (I.26) form the theorem of ***Wiener-Khintchine***.[85,86]

The Wiener-Khintchine's theorem is an important instrument for analysis. For example, let's consider a relaxation process. It describes by exponentially decreasing autocorrelation function

$$\overline{\varphi_x(\tau)} = \overline{\varphi_x(0)}e^{-\frac{|\tau|}{\tau_1}}, \tag{I.27}$$

where $\overline{\varphi_x(0)}$ is the dispersion of the process, and τ_1 is the decay constant. Using Eq. (I.26) we can obtain power spectral density as

$$\overline{S_x(\omega)} = 4\overline{\varphi_x(0)}\frac{\tau_1}{1+\omega^2\tau_1^2}. \tag{I.28}$$

Almost all noise processes are relaxation type processes, except the $1/f$-noise. Its spectral density depends on frequency as $|f|^{-\alpha}$, where α is the value between 0.8 and 1.2.

Carson's theorem. Let us consider the form of noise signal described by function $x(t)$ that consists of random pulse train with form $f(t)$, moreover $f(t) = 0$ when $t < 0$:

$$x(t) = \sum_k a_k f(t - t_k), \tag{I.29}$$

where a_k is the amplitude of the k-pulse, t_k is the moment of time when the k-pulse starts. The distribution of t_k obeys the Poisson's law. The power spectral density of this noise signal can be written as

$$\overline{S_x(\omega)} = 2\nu\overline{a^2}|F(j\omega)|^2, \tag{I.30}$$

here ω is the angular frequency, $F(j\omega)$ is the Fourier transform of $f(t)$, ν is the mean frequency of event and $\overline{a^2}$ is the mean square of the amplitude of the pulse.

Campbell's theorem. If in the signal (I.29) all events are independent, then the values t_k are distributed by the Poisson distribution with the probability density function equal to 1/T, where T is time of observation. The ensemble averaging is given by

$$\overline{x(t)} = \upsilon\bar{a}\int_{-\infty}^{\infty} f(t)dt, \tag{I.31}$$

where $\upsilon = \lim_{T\to\infty}(k/\mathrm{T})$ is the mean number of events and $\bar{a}$ is the mean value of the amplitude a_k. The Eq. (I.31) is called Campbell's theorem.

2.2. Noise components

There are several important noise components. At the same time, noise has a lot of spectral shapes due to their dependence on different parameters of circuit and experimental conditions. To obtain the same spectra of noise as, for example, obtained yesterday it is necessary to keep all conditions precisely as they were that day. Usually the measurements of noise are very sensitive to external environment. Therefore, measured spectra contain components of noise which are noise pickups. These components completely depend on the cables that are used in the experiments, on the place where the device under test is placed and on the design of the measurement setup. Usually, noise pickups appear in the measured noise power spectral density as sharp spikes. In Figure I.20 it is shown that measured spectrum differs from theoretically calculated measured thermal noise of 1.3kΩ resistance. The difference is represented by sharp spikes up to 5 orders of magnitude higher than the minimum value. Almost all of them appear from power supply (50Hz and its harmonics). We are using batteries to apply voltage to the sample but all devices used to amplify and record noise are connected to the network power that has AC signal with the frequency equal to 50Hz. The higher frequency noise pickups, such as 20kHz and its harmonics, probably come from the devices, for example, switch-mode power supply of the laptop computer (18-50kHz) that is used to save and analyze measured noises.

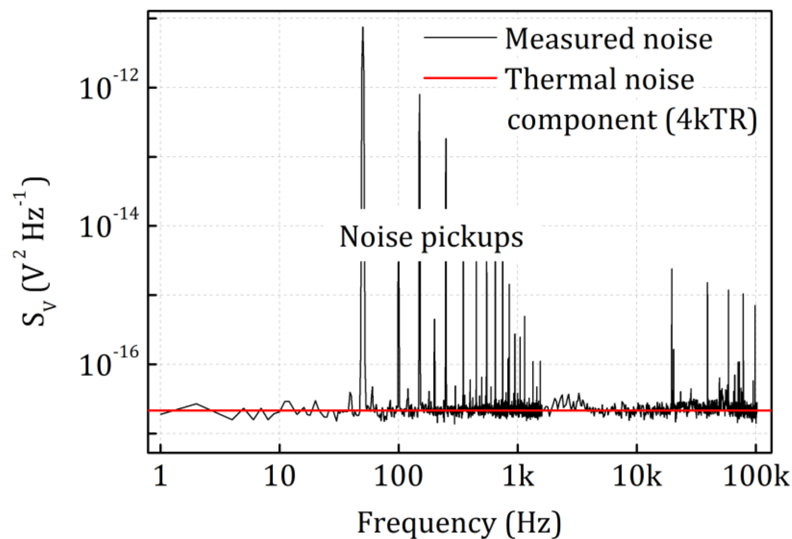

Figure I.20. Measured voltage noise power spectral density dependence on frequency (black curve) and theoretically calculated thermal noise (red line) of 1.3kΩ resistance at room temperature.

Usually, sample under test is placed in well shielded and grounded box to completely separate it from the “external world”. However, to measure noise properties we use preamplifier connected to the sample. There are several requirements to choose the proper preamplifier such as low intrinsic noise, low noise power source, linearity etc. Therefore, the second component that should be carefully optimized is the intrinsic noise of the amplifier system. It is important to make this component as small as possible, because

every time it is added to the noise of the sample. More detailed information about the design of the amplifier used in our measurement system is described in the Chapter II.

After noise optimization of the measurement setup, the following noise components can be separately studied: thermal, shot, generation-recombination (GR), burst and flicker noise components.

2.2.1. Thermal noise (Johnson-Nyquist noise)

Thermal noise is one of the main noise components. Every system under investigation can be characterized by certain resistance being at thermal equilibrium with its environment. Depending on the type of the circuit (shot or open) thermal fluctuations appear on the terminals as current or voltage fluctuations, respectively. At the first time, this noise was registered by J.B. Johnson[82] and H. Nyquist[83] after W. Schottky's theoretical prediction[81]. Therefore, the thermal noise is often called the Johnson-Nyquist noise. Johnson, in his work, described the obtained results of these statistical fluctuations of electric charge in a conductor measured using a vacuum tube amplifier and a thermocouple. Using thermal noise data, he obtained the value of Boltzmann's constant that was close to it'd accepted value.

The electrons/holes inside the semiconductors have thermal energy and travel in the material in a random way dissipating energy and absorbing energy of atoms of the crystal. These movements cause the thermal noise. Such fluctuations can be considered as independent and random events that have initial and relaxation stages. The initial stage, when an electron/hole moves between two collisions, is a stage of inducing of charge disbalance inside of the material. The next stage – so called relaxation stage – is charge redistribution one to restore the equilibrium.

Statistical characteristics of Johnson-Nyquist noise can be obtained from the model of resistance with cross section A and length L. Because of events described above, electrical pulses will appear on the terminals of this resistance. The initial stage of these events can be visualized as instantaneous appearance of two charged planes with density of charge $\pm q/A$ at the distance of the electron free path l_f. By assuming that the terminals of the resistance are open, in the relaxation stage of the event, the charge should decrease because of the reverse flow between the planes.

The equivalent circuit of such event has the resistance, R_f, and the capacitance, C_f, parallel connected to the current generator, $q\delta(t)$, that represent the initial stage. Additionally, the bulk resistance, $R \equiv R_f L/l_f$, is connected between this circuit and one of the terminals. In this situation, the motion equation has following form:

$$C\frac{dv_n(t)}{dt} = -\frac{v_n(t)}{R} + q\delta(t), \tag{I.32}$$

where $C = C_f l_f/L$, $v_n(t)$ is pulse of voltage on the terminals of the resistance[87]. The Fourier transform of the both sides of the Eq. (I.32) gives the transform of $v_n(t)$:

$$V_n(j\omega) = \frac{ql_f(R/L)}{1 + j\omega\tau_1}, \tag{I.33}$$

Here $\tau_1 = RC = \rho\varepsilon$ is dielectric relaxation time; ρ is resistivity and ε is relative permeability of the material. Usually τ_1 has a value of picoseconds.

Using Carson's theorem (I.30) and Eq. (I.33) the power spectral density can be obtained in the following way

$$\overline{S_{v_n}(\omega)} = \frac{2\upsilon q^2 \overline{l_f}^2 (R/L)^2}{1+\omega^2 {\tau_1}^2}, \tag{I.34}$$

where υ is the average number of events which appear during one second in the volume of the resistor. If n is electron density in the material, $\overline{\tau_f}$ is mean free time between collisions and μ is mobility, than

$$\nu = \frac{nAL}{\overline{\tau_f}}, \tag{I.35}$$

$$R = \frac{L}{nq\mu A}, \tag{I.36}$$

$$\mu = \frac{q\overline{l_f^2}}{2\overline{\tau_f}kT}, \tag{I.37}$$

where k is Boltzmann constant and T is the absolute temperature. By combining the Eq. (I.34)-(I.37) we can obtain the power spectrum density of the voltage and current fluctuations in the following form

$$\overline{S_{v_n}(\omega)} = \frac{4kTR}{1+\omega^2 {\tau_1}^2}, \tag{I.38}$$

$$\overline{S_{\iota_n}(\omega)} = \frac{4kT/R}{1+\omega^2 {\tau_1}^2} \tag{I.39}$$

for the open and short circuits, respectively. For all frequency ranges the term $\omega^2 {\tau_1}^2$ has negligibly small value and therefore the thermal noise usually can be described in the form:

$$\overline{S_{v_n}(\omega)} = 4kTR, \tag{I.40}$$

$$\overline{S_{\iota_n}(\omega)} = \frac{4kT}{R}, \tag{I.41}$$

for the open and short circuit, respectively.

The autocorrelation function for the case of thermal voltage fluctuations is exponentially decreasing function, like it should be for relaxation process (Eq. (I.27))

$$\overline{\varphi_{v_n}(\tau)} = \frac{2kTR}{\pi}\int_0^\infty \frac{\cos\omega\tau}{1+\omega^2\tau_1^2}\,d\omega = \left(\frac{kTR}{\tau_1}\right)e^{-\frac{|\tau|}{\tau_1}}. \tag{I.42}$$

The thermal noise can be described as a random pulsed process. It can be found in every resistive material and usually it determines the lowest limit down to what the whole noise can be decreased. For example, for sensor applications it is important to know the lowest level of signal that can be detected. Ideally, any sensor allows to detect the smallest signal, but because of noise small signals can not be detected. If the sensor resistance is R and its working frequency range is Δf, the root mean square (RMS) value of voltage that will be generated on the terminals of the resistor due to the thermal noise is

$$v_n = \sqrt{4k_B TR\Delta f}. \qquad (I.43)$$

This is one of the levels that have to be overcome to register the signal. For R=5kΩ, T=300K and Δf=100kHz the RMS value of voltage v_n=2.9μV.

2.2.2. Shot noise

Shot noise is the results of discreteness or particle properties of charge carriers. It appears when the system has potential barriers, for example *p-n* junctions, as a result of random overcoming of the barrier by charge carriers independently to each other. Assuming that time of transition of the charge carrier is small the current in the circuit is represented as a pulse-like process. The area under each of these pulses is equal to electron charge. Therefore, the current can be written as

$$i(t) = -q\sum_{k=1}^{K}\delta(t - t_k), \qquad (I.44)$$

where q is the electron charge, t_k is the moment of time, when k-electron starts to flow through the barrier, and K is the whole number of pulses.

According to Campbell's theorem the mean value of the direct current of shot noise can be represented by following relation:

$$-I \equiv \overline{\imath(t)} = -qv, \qquad (I.45)$$

here v is the mean emission speed of the electrons. The autocorrelation function of this process is:

$$\overline{\varphi_\imath(\tau)} = qI\delta(\tau) + I^2, \qquad (I.46)$$

and the current power spectral density is:

$$\overline{S_\imath(\omega)} = 2qI + 4\pi I^2\delta(\omega). \qquad (I.47)$$

The term $2qI$ is the current power spectral density of the shot noise component.

It should be noted, that if the pulses have a correlation in a pulse train, then the deviation from the usual shot noise behavior is observed. It could happen, for example, when the interaction between electrons plays an important role. In this situation the decreasing of noise can be registered.

2.2.3. Generation-recombination noise

The generation-recombination noise (GR-noise) is named due to generation-recombination processes taking place in the system. It appears as a result of random character of generation and recombination. The characteristics of this noise contain the information about life time of free charge carriers and about the energy levels between which the generation and recombination occur[88] (concentration of the centers, capture cross-section, energy level depth). Therefore the investigation of GR-noise is of fundamental importance. These measurements allow to reveal defects and impurity

structure in semiconductors, i.e. to implement the noise spectroscopy to study the energy levels.

GR-noise can be a result of different processes in the system:

- band-to-band generation-recombination;
- exchange of charge carriers between shallow states in the forbidden zone (capture levels) and one of the allowed bands;
- generation-recombination via deep levels (so called recombination centers).

Let's consider the noise spectroscopy of the impurity states in a semiconductor sample in more details. The GR-noise (Lorentzian shape noise) power spectral density of the equilibrium conductivity of the semiconductor can be represented by a superposition of several terms in the form $A/(1+\omega^2\tau^2)$, determined by different types of energy centers. Because of different dependences of A and τ on temperature and the parameters of the centers, the number of GR-components of the spectrum usually is not higher than three in the measured spectrum. By changing the temperature, it is possible to observe GR-noise components from different energy states, and therefore to obtain the basic characteristics of them.

Let us consider that the resistor is the n-type semiconductor (with 1cm^3 in sizes) which has the fluctuations of conductivity caused by generation-recombination process of electrons with energy state E_t under conduction band (c-band). Let concentration of the centers to be N_t, and the trapping coefficient of electrons to the centers to be C_t. Also, we will consider the deeper and shallower centers with the concentration N_a and N_d, respectively. Because the first type of centers is fully filled up and the second ones are almost empty they give negligibly small GR-noise.

The power spectrum density of a number of free electrons for such semiconductor resistor can be described as:[89–91]

$$S_n(\omega) = \frac{4\overline{\Delta n^2}\tau}{1+\omega^2\tau^2}, \tag{I.48}$$

$$\overline{\Delta n^2} = (n^{-1} + n_t^{-1} + p_t^{-1})^{-1}, \tag{I.49}$$

$$\tau = [C_t(n + n_1 + p_t)]^{-1}, \tag{I.50}$$

where n is the mean concentration of free electrons:

$$n = N_c e^{-E_F/kT}, \tag{I.51}$$

n_t and p_t are the mean concentrations of electrons and holes on t-centers, respectively:

$$n_t = N_t\left(1 + ge^{-\frac{E_t - E_F}{kT}}\right)^{-1} = \frac{nN_t}{n + n_1}, \tag{I.52}$$

$$p_t = N_t - n_t, \tag{I.53}$$

n_1 is the statistical factor c-band relatively to t-level depth:

$$n_1 = gN_c e^{-E_t/kT}, \tag{I.54}$$

N_c is the density of states in the c-band, E_F is the Fermi level depth relatively to the c-band, and g is the degeneration factor of the t-level.

The neutrality equation can be written as:

$$n + n_t = C = \begin{cases} N_t - N_a \\ N_t + N_d \end{cases}. \qquad (I.55)$$

In practice, the voltage or current power spectral density, $S_v(\omega)$ or $S_i(\omega)$, are measured instead of $S_n(\omega)$. But these three quantities have the following relation:

$$\frac{S_N(\omega)}{N^2} = \frac{S_v(\omega)}{v^2} = \frac{S_i(\omega)}{i^2}. \qquad (I.56)$$

Therefore

$$S_v(\omega) = \frac{v^2}{N^2} S_N(\omega) = \frac{v^2}{N^2} \frac{4\overline{\Delta N^2}\tau}{1+\omega^2\tau^2} = \frac{v^2}{n^2 V^2} \frac{4\overline{\Delta n^2}V\tau}{1+\omega^2\tau^2} = \frac{v^2}{n^2 V} S_n(\omega), \qquad (I.57)$$

where N is the number of free electrons inside the sample, V is its volume.

It is convenient to use such a ratio for the analysis:

$$\gamma(\omega) = \frac{S_v(\omega)V}{v^2} = 4\frac{\overline{\Delta n^2}}{n^2}\frac{\tau}{1+\omega^2\tau^2} = \frac{A}{1+\omega^2\tau^2}, \text{where} \qquad (I.58)$$

$$A = 4\frac{\overline{\Delta n^2}\tau}{n^2}. \qquad (I.59)$$

The temperature dependences of A and τ are described in Table I.3.

Table I.3. Characteristics of GR-noise of impurity conduction at low (T_L) and high (T_H) temperatures[90]

	$N_t \gg N_a > N_d$	$N_t \geq N_a > N_d$	$N_t < N_d$; $N_a < N_d$
$\tau(T_L)$	$\left(2C_t\sqrt{gN_cN_t}e^{-\frac{E_t}{2kT}}\right)^{-1}$	$\frac{1}{C_tN_a}$	$\frac{1}{C_tN_d}$
$\tau(T_H)$	$\left(C_tgN_ce^{-\frac{E_t}{kT}}\right)^{-1}$	$\left(C_tgN_ce^{-\frac{E_t}{kT}}\right)^{-1}$	$\left(C_tgN_ce^{-\frac{E_t}{kT}}\right)^{-1}$
$A(T_L)$	$\left(C_tgN_cN_te^{-\frac{E_t}{kT}}\right)^{-1}$	$\left(C_t\frac{N_t-N_a}{4}gN_ce^{-\frac{E_t}{kT}}\right)^{-1}$	$\frac{4N_t}{C_t}\frac{gN_c}{N_d^4}e^{-\frac{E_t}{kT}}$
$A(T_H)$	$\left(\frac{C_t}{4}g^2N_c^2e^{-\frac{2E_t}{kT}}\right)^{-1}$	$\left(C_t\frac{N_t-N_a}{4N_t}g^2N_c^2e^{-\frac{2E_t}{kT}}\right)^{-1}$	$\left(C_t\frac{N_d+N_t}{4N_t}g^2N_c^2e^{-\frac{2E_t}{kT}}\right)^{-1}$

Therefore, by investigating the temperature dependences of A and τ we can obtain the parameters of the t-level (N_t, E_t, and C_t) and determine the existence of additional impurities. After that, we can calculate the temperature dependence of the free charge concentration $n(T)$ using the Eq. (I.52), (I.54), and (I.55), and then measure the semiconductor conductance $\sigma(T) = en(T)\mu_n(T)$ to determine the temperature dependence of electron mobility $\mu_n(T)$.

All calculations described above are applicable also for p-type semiconductors.

The main device structures investigated in this work are field-effect transistors based on different materials. Several GR-noise components have been registered in the structures. Different positions of the centers that produce GR-noise fluctuations have been considered in FETs.

GR-noise of depletion region of the channel-gate interface. One of the positions of the centers that produce GR-noise fluctuations is the depletion region of the channel-gate interface. This GR-noise appears because of electrons/holes emitted from the centers near the interface modulate locally the width of depletion region and therefore the width of the channel. Their behavior can be considered like voltage generator on the input of FET. The equivalent noise resistance of such generator is

$$R_n = \frac{F(V_G, V_D)\tau_t}{1+\omega^2\tau_t^2}, \tag{I.60}$$

where $F(V_G, V_D)$ is the function that depends on the bias drain and gate voltages,

$$\tau_t = (c_p p_1 + c_n n_1)^{-1} \tag{I.61}$$

is the time constant of the centers, c_p and c_n are the captures probability of holes and electrons;

$$p_1 = n_i e^{(E_F - E_t)/kT}, \tag{I.62}$$

$$n_1 = n_i e^{(E_t - E_F)/kT}, \tag{I.63}$$

n_i is the intrinsic-carrier concentration.

If the energy level of impurity coincides with Fermi level then the temperature dependence of τ_t can be described as:

$$\tau_t \sim n_i^{-1} \sim T^{-3/2} e^{E_{G0}/2kT}, \tag{I.64}$$

E_{G0} is the band-gap of the semiconductor at T=0K.

GR-noise of the channel of FET. The next part of the FET device that can be responsible for GR-fluctuations is the channel of FET. This noise was described by A. Van der Ziel[92], and later by K.M. Van Vliet and C.F. Hiatt[93]. The power noise spectrum here can be represented by the noise resistance R_n in the form:

$$R_n \sim \frac{\tau}{1+\omega^2\tau^2}, \tag{I.65}$$

where τ is the fluctuation time constant.

GR-noise of leakage current. Another source in FET devices where GR-noise can appear is leakage current between the source of FET and the gate, I_g. The power spectral density of this noise can be described:

$$\overline{S_{\iota_g}(\omega)} = 2qI_g, \tag{I.66}$$

i.e. it behaves like shot noise, but it has the cutoff frequency that can be calculated as:

$$f_c = f_T \left(\frac{2qI_g}{kTg_{msat}}\right)^{\frac{1}{2}}, \tag{I.67}$$

where $f_T = g_m/2\pi C$ is the cutoff frequency of FET, g_{msat} is the transconductance at the saturation regime.

GR-noise of the contact areas. The next part of the device with the possibility of generation of GR-noise is the source and the drain contact areas. The channel of FET can have the impurities with deep energy states that are far from the Fermi level and at the normal conditions they are completely full. Usually they don't play any role in transport characteristics of the channel. But, they can become closer to the Fermi level nearly the contact region where the Schottky contacts can appear due to differences in the work functions. The trapping/detrapping processes to/from these centers can modulate the spatial charge region of the contacts and therefore GR-noise can appear. This region of FET becomes more important with decreasing of device's dimension down to nanometer sizes.

2.2.4. Burst noise

This noise component is a special case of GR-noise when the number of GR-centers decreases down to only one center. It is also called popcorn noise, impulse noise, bi-stable noise, or random telegraph signal (RTS) noise. Burst noise was originally observed in the waveform of germanium point contact diodes[94]. It consists of two- or multi-level impulses. The two-level burst noise is shown in Figure I.21. Usually at nanoscale sized, RTS noise dominates over all other noise components, such as thermal, shot, flicker and GR- noises and becomes a major component in low frequency noise.

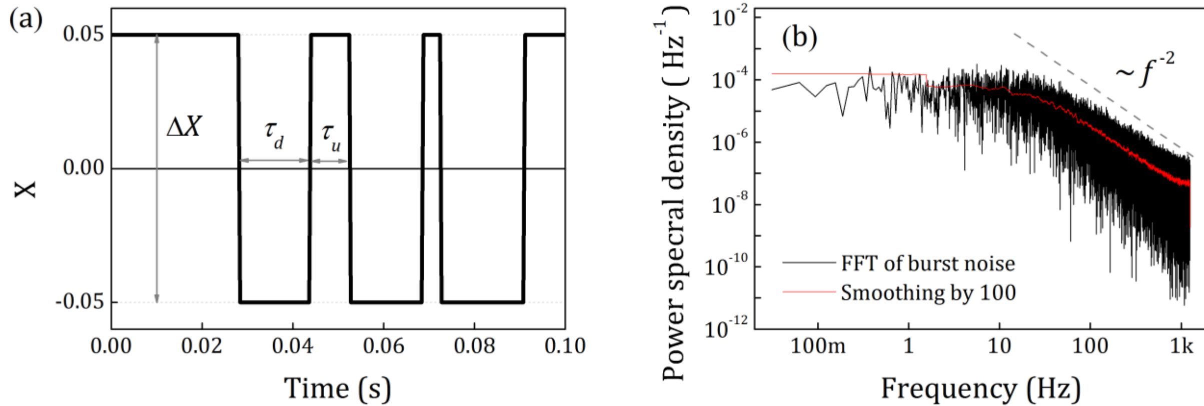

Figure I.21. (a) Typical two-level burst noise, where τ_d is the time corresponded to the down-state, τ_u is the time of finding system in up-state, and ΔX is the amplitude of burst noise. (b) Power spectrum density dependence on frequency of the typical burst noise.

The analysis of RTS noise is typically performed in both time and frequency domains. The power spectral density of burst noise has the same dependence on frequency as GR-noise. Therefore the time dependence is necessary to distinguish it. From the analysis of time domain two mean times, τ_d and τ_u, can be obtained. Usually there are time intervals exist when the system stays in various metastable states, such as capture and emission of an electron to the GR-center, or reconfiguration of bands, etc. The probability of a transition from upper-state to lower-state is given by $1/\overline{\tau_u}$, and by $1/\overline{\tau_d}$ as the corresponding probability of transition from down to up. These transitions take place instantaneous and the times in up- and down-states are exponentially distributed, i.e. the switching is a Poisson process.

The power spectral density of the burst noise can be evaluated using the Wiener-Khintchine theorem:

$$S_X(f) = \frac{4(\Delta X)^2}{(\overline{\tau_u} + \overline{\tau_d})\left[\left(\frac{1}{\overline{\tau_u}} + \frac{1}{\overline{\tau_d}}\right)^2 + (2\pi f)^2\right]}, \tag{I.68}$$

For the case shown in Figure I.21(a), when $\overline{\tau_u} = 0.01$, $\overline{\tau_d} = 0.02$ and $\Delta X = 0.1$, this equation can be represented as:

$$S_X(f) = \frac{4(0.1)^2}{(0.01 + 0.02)\left[\left(\frac{1}{0.01} + \frac{1}{0.02}\right)^2 + (2\pi f)^2\right]} = \frac{5.9 \times 10^{-5}}{1 + \left(\frac{f}{23.9}\right)^2}. \tag{I.69}$$

The power spectral density of typical burst noise is shown in Figure I.21(a) and a theoretically calculated curve (Eq. (I.69)) are demonstrated in Figure I.21(b).

RTS noise can be very useful for performance characterization in very small electronic devices, where the alternate capture and emission of carriers at an individual defect site generates these discrete switching in the device resistance. The bias-voltage dependence of the capture and emission times allows to determine the location of the defects in respect to the channel of conduction[95]. It is found that in MOSFETs the traps reside in the oxide up to a few nanometers from the interface and hence within tunneling distance of the inversion layer. For the metal-insulator-metal (MIM) tunnel junctions, the traps are also located in the insulator. Through the study of the temperature and bias-voltage dependence of these capture and emission times for a single defect, one can extract parameters such as the capture cross-section, activation energy for capture and emission, and the temperature dependence of the trap energy level.

2.2.5. Flicker noise

By applying some small voltage to any device additionally to thermal noise another kind of fluctuations can be observed. The power spectrum density of these fluctuations is inversely proportional to frequency, so this type of noise is called $1/f$- or flicker noise. Initially it was called as current noise, excess noise, flicker-noise (here scientists usually define the fluctuations of electron emission of thermionic cathode), then semiconductor noise (before it was found in different metals and liquid electrolytes) and contact noise. Later this kind of fluctuations was found in the earth's rate of rotation, in undersea currents, in the hourglass flow of sand fluctuations etc. Even the best music has $1/f$ spectrum[96]. It should be noted that all of these processes don't have the same reason for flicker noise.

For the first time, flicker noise was observed in probability fluctuations of electron emission from filaments when effect of the absence of space charge was much larger in the lower frequency range than the theory predicts by R.G.Ray[97]. After that, a lot of scientists started to investigate on $1/f$-noise. They produce several theories that proper describe it, but the main physical process and the reason of $1/f$-noise is still under debates.

It should be noted, that flicker noise was found even in biologic system. Normal heartbeat of every human and the waves of the brain. Particularly α-waves have this type of fluctuations. Two of these facts are shown by T. Musha[98]. With his group, he did also an observation of flicker noise of neurons[99] and later he proposed three possible generation mechanisms of $1/f$-like rhythm fluctuations in biological systems[100], such as $1/f$ ionic conductance fluctuations of the cellular membrane, a Hopfield-type of artificial neural network consisting of neurons and the clustering Poisson process in which sequences of randomly occurring point events (clusters) overlap each other.

The form of signal $x(t)$ of $1/f$-noise characterizes by spectral power density

$$\overline{S_x(\omega)} = c/|\omega|^{\alpha}. \tag{I.70}$$

Usually α=1 and c doesn't depend on frequency. This form is very interesting because it has no limit at zero frequency. Scientists tried to find the lowest frequency where flicker noise transforms to another law, but their attempts were unsuccessful. The measurements of MOSFETs were performed down to 5x10^{-5} Hz, later the semiconductor materials where investigated down to 5x10^{-7} Hz (during ~23 days), but deviation from the $1/f$ behavior was not observed. The low frequency limit of flicker noise of each device can be explained for example by life time of this device or even by the age of the Universe (13.7 billion years what corresponds to a frequency equal to 2x10^{-18} Hz). The high-frequency limit depends on the characteristics of mechanism which determine the noise. After this frequency flicker noise should decrease by the $1/f^2$-law.

There are two mathematical representations of the flicker noise. The first one is a random pulse train with special type of the impulse. It was invented by H. Schönfeld[101] and later it was supplemented by A. Van der Ziel[102] who used such impulse. The second one is the superposition of numerous relaxation processes with wide variation of characteristic time constant[103]. This model is based on surface mechanisms of flicker noise and it has been widely recognized.

Let's consider both of these representations:

Model of 1/f-noise based on random pulse train. To obtain the $1/f$-like spectral dependence, we should consider random pulse train with such type of impulse:

$$f(t) = u(t)t^{-(1-\frac{\alpha}{2})}e^{-\omega_x t}, \tag{I.71}$$

where $u(t)$ – unit step function, α and ω_x are independent on time and have positive value. By integrating this function and substituting in Carson's theorem (Eq. (I.30)) the power spectral density of the impulse can be described as

$$\overline{S_x(\omega)} = \frac{2\upsilon\overline{a^2}\Gamma^2(\frac{\alpha}{2})}{|\omega_x^2 + \omega^2|^{\alpha/2}}, \tag{I.72}$$

Here Γ( ) is the gamma-function. ω_x is the low frequency limit after which spectrum becomes independent on frequency. At frequency range $\omega \gg \omega_x$ the usual form of flicker noise can be obtained in the form:

$$\overline{S_x(\omega)} = \frac{c}{|\omega|^{\alpha}}, \tag{I.73}$$

where $\alpha = 1, c = 2\upsilon\overline{a^2}\Gamma^2(\alpha/2)$. The function (I.71) is similar to the law of evanescent wave and could be explained by transmitting energy obtained by scattering of the electron from one atom to another. In the middle of 1970th the mechanism that can have such random pulse train was described using effect of the thermal diffusion. It was not completely refused but deviate shortly from the expectations.

Model of superposition of numerous relaxation processes. The spectral density of relaxation process $z(t)$ can be written as:

$$\overline{S_z(\omega)} = \frac{g(\tau_z)}{(1+\omega^2\tau_z^2)}, \tag{I.74}$$

where τ_z is the relaxation time, $g(\tau_z)$ is a function that is defined by the physical mechanism that determines the noise.

By composing the linear superposition $x(t)$ of relaxation processes with the time constants that are distributed between τ_1 and τ_2, the total power spectral density can be obtained as:

$$\overline{S_x(\omega)} = \int_{\tau_1}^{\tau_2} \overline{S_z(\omega)} p(\tau_z) d\,\tau_z = \int_{\tau_1}^{\tau_2} \frac{p(\tau_z)g(\tau_z)}{(1+\omega^2\tau_z^2)} d\tau_z, \tag{I.75}$$

$p(\tau_z)$ is the probability density. When $p(\tau_z)g(\tau_z)$ is equal to P which doesn't depend on τ_z:

$$\overline{S_x(\omega)} = \frac{P\big(\mathrm{arctg}(\omega\tau_2) - \mathrm{arctg}(\omega\tau_1)\big)}{\omega}, \tag{I.76}$$

and at $\omega\tau_2 \gg 1$ and $0 \le \omega\tau_1 \le 1$ it simplifies to:

$$\overline{S_x(\omega)} = \frac{\pi P}{2|\omega|}. \tag{I.77}$$

Therefore the superposition of relaxation processes can describe the $1/f$-like dependence of power spectral density.

There are few ***physical mechanisms*** responsible for appearance of $1/f$-noise. Historically the first was ***McWorter's model of 1/f-noise of number of charge carriers.*** The model suggested the flicker noise coming from GR-processes on the surface of semiconductor or on its interfaces with other materials. The McWorter's model allows to prove the Equations (I.74)-(I.77). The time constant for traps situated at a depth of ω from a surface is equal to:

$$\tau_z = \tau_0 e^{\gamma\omega}, \tag{I.78}$$

where τ_0 and $\gamma \sim 10^8$ cm^{-1} are constants. For the uniform trap distribution in interval of depth from ω_1 to ω_2, for the time constants τ_1 and τ_2, we can write:

$$p(\tau_z)d\tau_z = \begin{cases} \dfrac{d\tau_z}{\tau_z \ln\left(\dfrac{\tau_2}{\tau_1}\right)} & when\ \tau_1 \le \tau_z \le \tau_2 \\ 0 & in\ other\ cases \end{cases}, \tag{I.79}$$

By substituting of Eq. (I.79) to the formula of power spectral density of the total number of fluctuations $n(t)$ we can obtain:

$$\overline{S_n(\omega)} = 4\overline{\varphi_n(0)} \int_0^\infty \frac{\tau_z p(\tau_z)}{(1+\omega^2\tau_z^2)} d\tau_z, \tag{I.80}$$

where $\overline{\varphi_n(0)}$ is the value of mean square of $n(t)$, and then:

$$\overline{S_x(\omega)} = \frac{4\overline{\varphi_n(0)}}{\ln\left(\frac{\tau_2}{\tau_1}\right)} \frac{\left(\text{arctg}(\omega\tau_2) - \text{arctg}(\omega\tau_1)\right)}{\omega} \tag{I.81}$$

which is a good approximation of $1/|f|$ law at $\omega\tau_2 \gg 1$ and $0 \leq \omega\tau_1 \leq 1$.

Hooge's law. Many years scientists supposed that flicker noise can be found only in nonmetallic materials. But F.N. Hooge and A.M.H. Hoppenbrouwers showed that $1/f$ behavior can be found in thin gold films. F.N. Hooge[68] suggested an empirical formula for $1/f$ fluctuations:

$$\frac{\overline{S_r(\omega)}}{R_0^2} = \frac{\alpha_H}{N_{tot}|f|}, \tag{I.82}$$

where N_{tot} is the total number of charge carriers, R_0 is the mean value of sample resistance, and $\alpha_H \approx 2 \times 10^{-3}$ is universal constant, which has weak dependence on temperature. Later this law was changed for the case of large scattering on impurities. It was shown that Hooge's constant can have different values. However, even today the Hooge's law and the Hooge's constant are used to compare the noise level in various materials.

1/f-noise due to fluctuations of charge carriers' mobility. There are a lot of experiments demonstrating that the $1/f$-noise of homogeneous conductors can be expressed by the Hooge's law. Investigation of noise in the open circuit thermo electromotive force of both intrinsic germanium and extrinsic germanium and silicon[104] and in the voltage of thermo cells and concentration cells[105] proved that the fluctuations in the conductivity are due to fluctuations in mobility and not in the number of the charge carriers. This means that all scattering mechanisms resulting in change of the mobility have to show $1/f$-noise behavior.

The Hooge's constant has been obtained for samples with dominant lattice scattering mechanism. Therefore, in the most cases the expression holds following:

$$\alpha_H \sim (\mu/\mu_i)^2, \tag{I.83}$$

where μ is measured mobility and μ_i is mobility caused by scattering on the lattice.[106]

The idea of mobility fluctuations was strongly criticized because it is not possible to find a physical mechanism of scattering noise, which would give $1/f$ spectrum in wide frequency range.

Self-organized criticality(SOC)-model of 1/f-noise. The self-organized criticality concept was introduced as one of the causes of $1/f$-noise. According to this concept a huge dynamic system consisting of a large number of interacting elements in the process of evolution tend to the critical self-supported state. As a structure it represents a set of metastable states which pass into each other with "avalanches" that occur after a small external action applied to the system.

One of the first researches who proposed such a model were Bak, Tang, and Wiesenfeld (BTW-model). They used a table on which they poured sand and watched what happened. After some time, avalanches were observed. The system became stable when the sand started to pour out the table. It was noticed that the larger avalanche the less it appears. The same property has $1/f$-noise.

Taking the BTW-model as background, P. De Los Rios and Yi-Ch. Zhang[107] performed a mathematical description. They showed that such system can give $1/f$-noise regardless of the dimension. By introducing dissipation, they observed changes in the spectrum of this noise.

Slightly different model, which also based on the concept of BTM, described in Ref.[108]. It also gives flicker noise, exponent of which doesn't depend on the system dimension.

But it is very hard to apply the SOC-model to really existing systems.

Quantum 1/f-noise. For the first time the concept of quantum $1/f$-noise was introduced by P.H. Handel in 1975 as the effect caused by infrared radiative correction when carriers interact with quantum electromagnetic field[109,110].

This model is very controversial and led to debates and a great criticism. Nevertheless, K.M. Van Vliet continued to develop the theory, which was based on quantum electrodynamics. She came to the conclusions that quantum $1/f$-noise of electromagnetic nature is inevitable (like Jonson-Nyquist noise and GR-noise). This noise is the noise of mobility fluctuations, and the result can be applied to all quasi-electrical processes such as electron scattering on impurities and electron-phonon scattering. However, there is no infrared radiative correction.

The disadvantage of this model is that it assumes the value of the $\alpha_H \sim 10^{-8}$ for normal dispersion, and it is a very small value compared to the experimental values obtained in homogeneous, almost perfect semiconductor devices.

At the same time, K.M. Van Vliet made the conclusion that, contrary to common opinion, $1/f$-noise is not a variation of the technological effect. This idea could revolutionary change the understanding of the noise physics in general.

II. DEVELOPMENT OF NOISE MEASUREMENT SETUP

During fulfillment of this PhD work the noise measurement setup was modified to reduce the intrinsic noise level, and it was fully automated. We also decreased also the noise pickups and developed several additional programs to analyze the obtained data. The big work was done in the development of algorithms to clean the obtained noise spectra and to make them smoother. This allows precise fitting of the noises by set of the existing noise components. Additionally, it makes it possible to distinguish up to four (five under special conditions) generation-recombination components and to obtain their parameters with an error not exceeding 10%. The common fitting of noise spectra by set of the uncorrelated components allows more accurate reception of the components amplitudes.

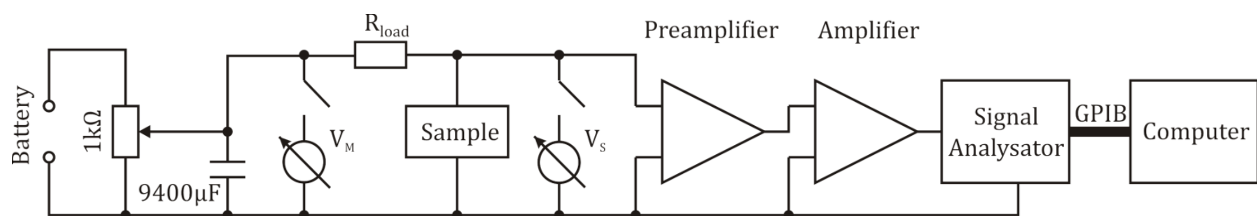

Figure II.1. The schematic diagram of noise measurement setup.

Schematically, the measurement setup is shown in Figure II.1. A lead-acid battery is used to apply voltage to the sample, which can be controlled by using a variable resistor of 1kΩ. Such a power supply system allows us to reduce noise pickups during the measurements. A capacitance of 9400μF which is in parallel to the variable resistor, decreases the value of the resistor to <16.7Ω at 1Hz. This in turn reduces the thermal noise. The sample is connected to the power source in series with the load resistance, R_{load}. The load resistance is a high-precision, low-inductance resistance box, produced by IET Labs Inc. (formerly manufactured by GenRad). The resistance can be changed in the range from 1Ω to 1MΩ.

Such a circuit allows us to control the bias voltage from zero to voltage (related to the number of ~6.3V connected in series liquid-acid accumulators) and specifying the regime

of measurements. Short circuit and open circuit regimes can be used by changing the load resistance. Because of the total capacitance (~350pF) of the cables connected to the sample, at large values of R_{load}, the measured spectra can have a roll-off in the high-frequency range. For example, at R_{load} =5kΩ the cut-off frequency $f_{cut\text{-}off} \approx$ 91kHz, which should be controlled and taken into account.

The multimeters V_S and V_M allow to measure voltages, V_S and V_M, on the sample and on the whole circuit, respectively. After that, the DC current can be calculated as $I_S=(V_M-V_S)/R_{load}$. Applying the DC voltage to the sample is necessary for specifying the working point of the measured device and for measurements of fluctuations, such as shot, GR, RTS, and flicker noise components. The multimeters are connected to the measurement setup before and after noise measurements to get the current and voltage applied to the sample, and to check the stability of the system during the noise measurements. In between the multimeters are disconnected to avoid the influence of their intrinsic noise to the whole spectra. It was specially proved that connecting the V_M multimeter during the measurements of noise doesn't influence the noise spectrum. Therefore later, the scheme was optimized using one multimeter for measurements of V_S and V_M voltages by switching it on V_S using a relay, and leaving this multimeter at the V_M position during the noise measurements.

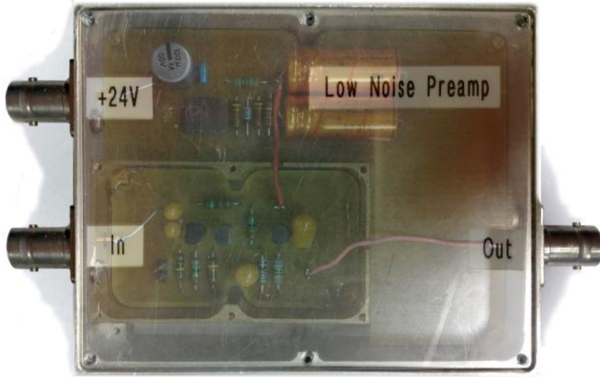

Figure II.2. Homemade low noise preamplifier consisting of 2-stage amplifier and biased using the low noise power source.

The noise signal was preamplified by a homemade preamplifier (see Figure II.2) with gain ~173 and amplified using a commercial amplifier ITHACO 1201 with a variable gain (from 1 to 10^5). The preamplifier was designed on the basis of a 2-stage amplifier biased with a low noise power source. The first amplification stage is very important in a noise measurement setup. Its intrinsic noise should be as low as possible. Therefore, to build it, tens of FETs were checked and the one with the lowest noise was selected.

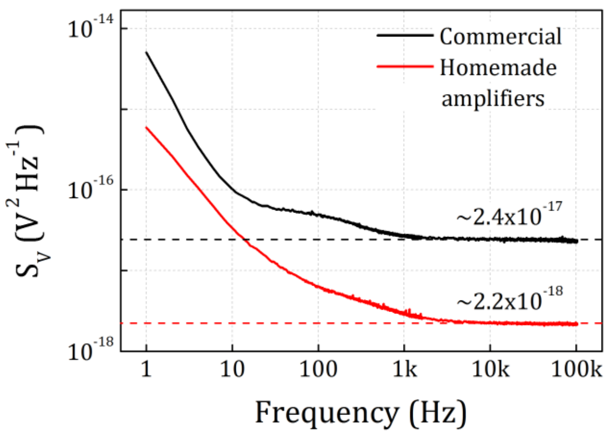

Figure II.3. Calibration curves for commercial and homemade amplifiers. The values of intrinsic noise levels are shown in the right-down part of the plot.

While the homemade amplifier had its own intrinsic thermal noise $S_V^{preampl} = 2.2 \times 10^{-18}\mathrm{V^2Hz^{-1}}$ the factory amplifier had – $S_V^{ampl} = 2.4 \times 10^{-17}\mathrm{V^2Hz^{-1}}$ at 10kHz (see Figure II.3). These correspond to the thermal noises of ~130Ω and ~1.4kΩ resistances respectively at a temperature of T=300K.

This means that using our noise measurement setup it is possible to measure the thermal noises of the resistances down to 10 times lower than 130Ω. It should be noted, that increased values of low frequency noise, below (1kHz) can affect the measurement of flicker and low frequency GR noises.

The amplified signal goes to a dynamic signal analyzer HP35670A which is used for obtaining spectra of noises and to transfer them through a GPIB interface to the computer for further analysis. The measured levels of intrinsic noise of the amplifiers are shown in Figure II.3. They were used in the analysis of the obtained spectra. The real voltage noise power spectral density, $S_V^{(real)}$, of the sample under test can be calculated using the measured power spectral density, $S_V^{(meas)}$, by following relation:

$$S_V^{(real)} = \frac{\frac{S_V^{(meas)}}{k_{ampl}^2} - S_V^{(ampl)}}{k_{preampl}^2} - S_V^{(preampl)}, \tag{II.1}$$

where $S_V^{(ampl)}$ and $S_V^{(preampl)}$ are the calibration curves for the manufactured amplifier and for the homemade preamplifier, respectively; k_{ampl} and $k_{preampl}$ are the gains of the amplifier and preamplifier, respectively.

The gains of amplifiers have certain frequency dependences too; therefore, all quantities in equation (II.1) are functions of frequency. Additionally, in the case of large resistance of the sample, because of the RC-circuit, on the input of the preamplifier the decay of measured noise spectrum should be taken into account at high-frequency range. The characteristic time of the RC-circuit will be a product of the equivalent resistance of the circuit and the total capacitance of the cables, conductors to the sample and the input of the preamplifier. The estimated total capacitance was found to be equal to 350pF. For the open circuit measurement or for the measurement of the sample with high equivalent resistance (>5kΩ) the characteristic time constant should be calculated and the data should be correctly used.

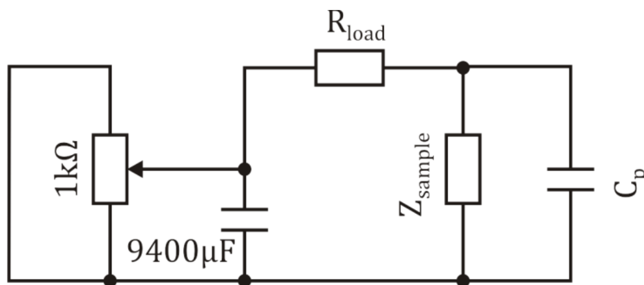

Figure II.4. Equivalent AC scheme of the connected to the preamplifier part of the measurement setup. C_p is the total parasitic capacitance of the cables, connectors etc. Z_{sample} is the differential resistance of the sample.

The equivalent AC scheme of measured part of the noise measurement setup is shown in Figure II.4. Here, the variable resistance of 1kΩ and capacitance of 9400μF give in sum a negligible influence to the total impedance of the scheme (<4.2Ω at frequencies >1Hz for AC measurements). The parasitic capacitance, C_p, as it was discussed before, can lead to decay of the measured noise spectra at high-frequency depending on the selected load resistance and differential resistance of the sample, Z_{sample}. Therefore, the equivalent resistance of the measured scheme can be calculated as:

$$R_{eq} = \frac{R_{load} Z_{sample}}{R_{load} + Z_{sample}} = \frac{R_{load} \left(\frac{\partial I}{\partial V}_{V=V_S} \right)^{-1}}{R_{load} + \left(\frac{\partial I}{\partial V}_{V=V_S} \right)^{-1}}, \tag{II.2}$$

where $\frac{\partial I}{\partial V}_{V=V_S}$ is the differential of the current voltage characteristic of the sample at the point of voltage equal to V_S. In the open circuit regime of measurement of noise, when $R_{load} \gg Z_{sample}$, R_{eq} is equal to Z_{sample} and in the short circuit regime, when $R_{load} \ll Z_{sample}$, R_{eq} is equal to R_{load}. The choice of the proper noise measurements regime has to be done to simplify the late analysis of the obtained data.

Our setup allows us to measure the voltage noise power spectral density, S_V. For the analysis of noise it is suitable to use the current noise power spectral density, S_I, and the normalized current noise power spectral density multiplied by frequency, fS_I/I^2. The S_I has the following relation with S_V:

$$S_I = \frac{S_V}{R_{eq}^2}, \tag{II.3}$$

where R_{eq} is the equivalent resistance of the measured scheme calculated using the Eq. (II.2).

As it was mentioned before, the amplified AC signal from the sample goes to the input of the dynamic signal analyzer HP35670A, which measures voltage fluctuations and using fast Fourier transform calculates the noise spectrum of them. In one channel regime the analyzer allows us to obtain 1600 points of a spectrum at the frequency range from zero up to 102.4kHz with various spans up to 64Hz. To obtain a noise spectrum which is clearly visible and applicable for further analysis, it is necessary to use at least two spans of analyzer. Usually we measure noise spectra in two ranges: firstly at lower (up to 1600Hz) and then at higher (up to 102.4kHz) frequency ranges using 1Hz and 64Hz steps, respectively. Then we combine the spectra. Therefore, the obtained noise power spectrum usually consists of 3175 points (1600 from 1Hz to 1600Hz and 1575 from 1600Hz to 102.4kHz) at the frequency range of 1Hz to 102.4kHz.

The error in each point of the measured spectra can be estimated as inversely proportional to the root of the average number that was used during the measurements of noise. The average number should be at least 100 to obtain suitable for analysis noise curve and at least 1000 for calibration curves.

The developed homemade noise measurement setup is shown in Figure II.5. The samples under test have to be placed as in the steel box (1) or in the vacuum chamber (2). The turbomolecular pump together with forepump (3) allows to obtain the level of vacuum down to 10^{-5}mBar in the chamber. The measurements of noise spectra at different temperatures were performed using a Stirling cooler (4), which allows to decrease the temperature down to 60K at the cooper finger inside the vacuum chamber. The sample under test is connected through dampened vibration cooper sheets to the finger. The temperature on the sample is controlled by a temperature monitor (6). All circuits with batteries are placed inside of the steel box to avoid additional noise pickups. The temperature monitor, temperature controller, multimeter (7) and spectrum analyzer (8)

are connected to a computer through GPIB and COM interfaces to measure the noise spectra in fully automated regime.

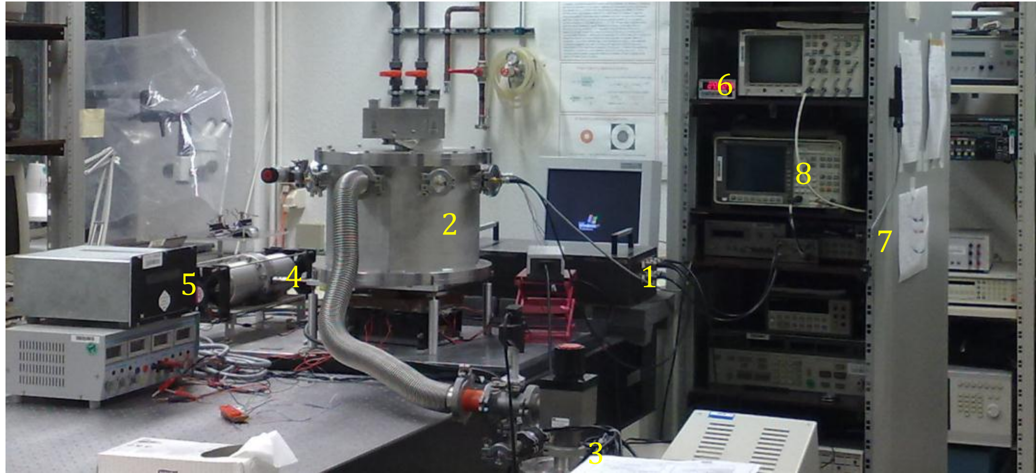

Figure II.5. Noise measurement setup: steel box with preamplifier circuit (1), vacuum chamber (2), turbomolecular pump under vacuum forepump (3), Stirling cooler (4) and temperature controller (5), temperature monitor (6), multimeter (7) and spectrum analyzer (8).

To automate the setup, the program code GetNoiseSpectrum v8 was developed using HTBasic. The text of the program can be found in the Appendix 1. The program allows to measure both noise spectrum and time dependence of voltage fluctuations on the sample.

The measured noise spectra usually contain thermal, flicker, and GR noise components. In the case of uncorrelated or weakly correlated fluctuators, these components can be separated in the whole range of the measured noise spectrum. The example of such a separation is demonstrated in Figure II.6. To distinguish noise components it is convenient to multiply the density (Figure II.6(b)) on frequency as it is shown in Figure II.6(b). Here, the bumps denote the GR noise components, while the flicker noise component will be almost horizontal.

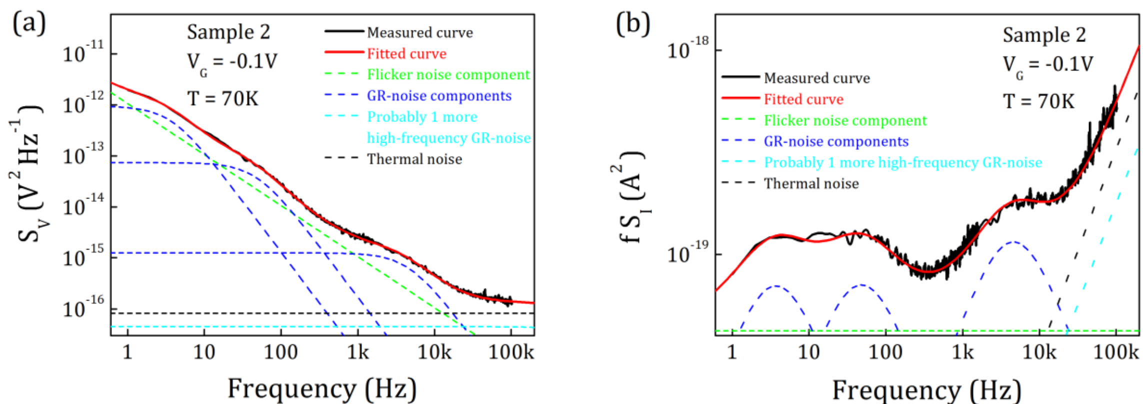

Figure II.6. Typical measured noise spectra of one of the individual SWCNT-FETs represented as voltage noise power spectral density (a) and current noise power spectral density (b) as a function of frequency. The measurement was done at T=70K and at biases V_{DS} and V_G equal to 30mV and -0.1V, respectively.

The additional program was developed for analysis of each component of the measured spectrum. The program description can be found in the Appendix 2 (Getting Flicker & GR v9.1 Optimized program written using Wolfram Mathematica).

III. SYNTHESIS OF CARBON NANOTUBES AND CHARACTERIZATION OF CNT BASED STRUCTURES

Several methods of carbon nanotube growing were shortly described in chapter I.1.1.2. During this work, the CVC method was precisely studied and applied to produce part of samples. This method allows to obtain single-walled carbon nanotube with diameters not exceeding 2nm. By controlling the catalyst density and growth time it was possible to obtain just one nanotube per tens of micrometers with lengths more than five micrometers. This density of nanotubes allows to process FETs based on individual CNTs using e-beam lithography.

1. Synthesis of CNT using CVD method

Nowadays, the CVD method is widely used by many scientist groups to obtain high quality single walled CNTs of semiconducting type of conductivity. It has a lot of advantages, such as allowing to control the diameter of nanotubes in a small range, obtaining very pure CNTs, controlling the density of tubes, growing single-walled CNTs etc. By using sapphire substrate it allows to obtain a quite well-aligned network of nanotubes.

The schematic diagram of the CVD experimental setup is shown in Figure III.1. A homemade system consists of the quartz tube, which is placed in furnace and contacted to the gas flow system. The rate and composition of the gas mixture is determined by gas flow controllers that are connected to a PC. The available gases include methane, hydrogen and argon.

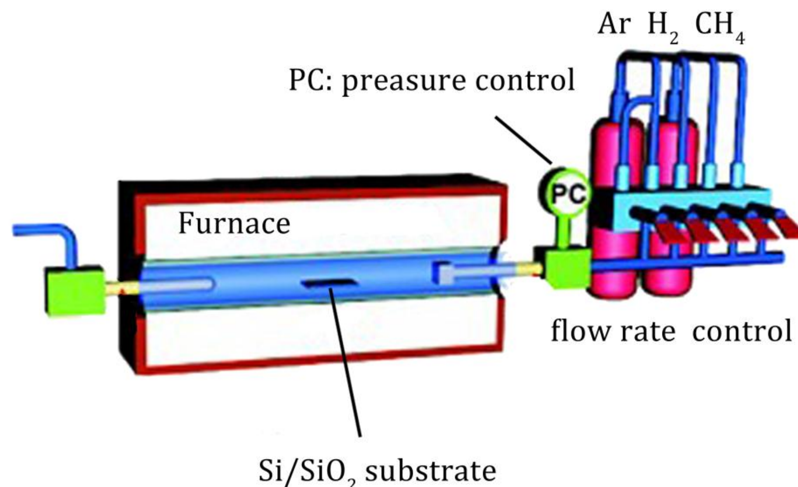

Figure III.1. Schematic diagram of CVD setup.

The process starts with the preparation of the substrate and catalyst. The proposed method for the ***cleaning of the substrate*** is given below:

- At first, the substrate is placed in HNO_3 acid and sonicated for at least 1 minute.
- Then the substrate is cleaned in distilled water with sonication too.
- After that – 1 minute in acetone with sonication to dissolve the organic substances.
- And as finally, the substrate is sonicated in propanol during 1 minute.

To obtain the SWCNTs mixture on the substrate the special catalyst should be prepared. One of the suitable ***mixtures of the catalyst*** has following compounds:

53.6mg – $Fe(NO_3)_3$,
10.8mg – $MoO_2(C_5H_5O_2)_2$,
39.5mg – Al_2O_3,
40.0ml – *Methanol*.

The mixture has to be sonicated for 2 hours and setting down for 2-3 hours, to obtain the smallest particles on the top. Once prepared, the mixture can be used many times for the growth of carbon nanotubes. But it should be noted that before using the mixture, every time, it is necessary to sonicate the mixture for 15 min and to wait for 15 min for the large-size particles to sink. Then put a droplet of the catalyst on the substrate and bake it at 150°C for 10 minutes.

During the CVD growth the substrate is placed in the quartz tube, through which several gases flow. And the tube is placed in furnace under high temperature. The CVD process consists of the following steps:

1. All gasses are turned on for 2 min with the follow flow rates: 1.52 L/min, 0.52 L/min and 0.7 L/min for Ar, CH_4 and H_2, respectively. This step can be called "blow-through", when all unnecessary gases are blowing out.

2. The next step is switching off CH_4 and H_2, but leaving Ar switched on with the mentioned flow rate for 2 min. The quartz tube is filled by inert gas, prepared for the heating by the furnace.
3. Turning on the furnace (controller temperature 925°C equivalent to 1000°C in the furnace). The flow rate of Ar is kept the same. The stable temperature will be controlled by a temperature monitoring system.
4. When the desirable regime of the setup is reached, the growth process starts by switching on H_2 (0.7 L/min) and CH_4 (0.52 L/min) and switching off Ar. Leaving the setup for at least 10 minutes in this stage will give a low density CNT network on the substrate. The time of the growth process is related to with the density of nanoparticles on the substrate and therefore directly connected to the density of the obtained CNT network.
5. The last stage is turning off the furnace and switching off the flows of H_2 and CH_4. It is better to switch on Ar (1.52 L/min) during the cooling down process, but it is no necessity.

The samples grown by such CVD method with low density networks of CNTs are shown in Figure III.2. The large-size catalyst particles on the substrate can be removed by etching in solution. The further deposition of the contacts allows to produce the CNTs devices with low density of the tubes. By decreasing the density of catalyst particles the FETs based on individual SWCNT can be fabricated. In this case, the personal mask for electron beam lithography should be designed for each device to process the contacts to the tube. In this work, the FETs based on individual CNT with different gate topographies were fabricated in collaboration with K. Goss from the group of Dr. C. Meyer and analyzed using our noise measurement technique (see chapter IV.1.1.2). The conductivity of the obtained CNTs can be studied by analysis of Raman spectra.

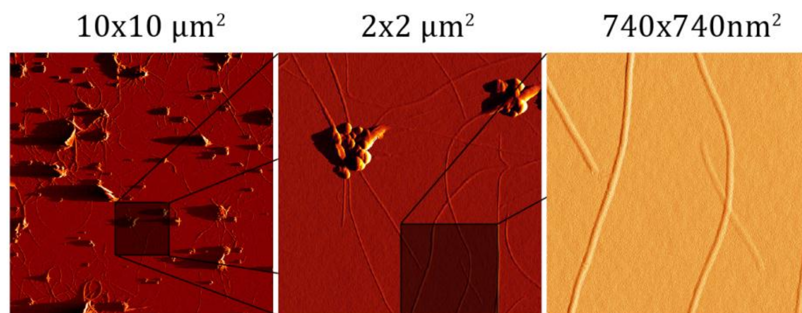

Figure III.2. AFM images of grown CNT network using CVD technique obtained at different scales.

2. Raman spectroscopy

Raman spectroscopy, named after C.V. Raman, is a spectroscopic technique used to study vibrational, rotational, and other low-frequency modes in a system.[111] It relies on inelastic scattering, or Raman scattering, of monochromatic light, usually from a laser in the visible, near infrared, or near ultraviolet range. The laser light interacts with molecular vibrations, phonons or other excitations in the system, resulting in the energy shift up or down. The shift in energy gives information about the vibrational modes in the system.

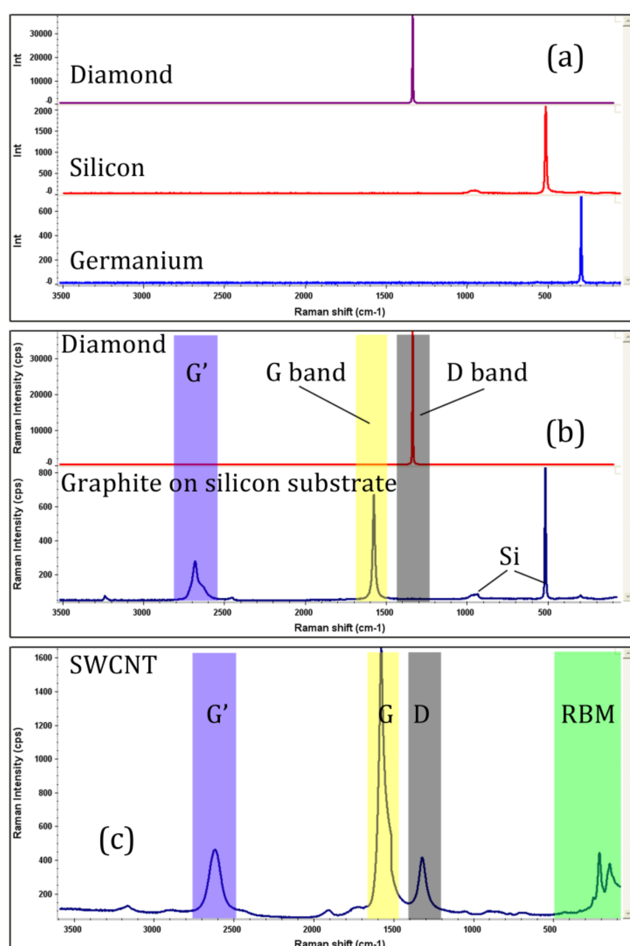

Figure III.3. (a) Raman spectra of diamond, silicon and germanium. (b) Raman spectra of diamond and graphite on silicon substrate. (c) Raman spectrum of SWCNT. The new RBM band is introduced.

Concerning the carbon atom, Raman spectroscopy can identify it and distinguish it from other materials (Figure III.3(a)).[112] The diamond spectrum is very similar to that of crystalline silicon and germanium except that the lighter weight carbon bonds vibrate at higher frequency. Raman can easily differentiate different allotropes (Figure III.3(b)), such as sp^3-bonds (tetrahedral configurations and sp^2-bonds (planar configurations) which are represented by the D band and G band, respectively. The G' band is related to the graphene layer. The examination of it reveals that graphene has one primary mode as multilayer graphite exhibits multiple modes. The D, G and G' bands form the core of the Raman carbon spectrum.

SWCNT introduce a new mode – Radial Breathing Modes (RBM) (Figure III.3(c)). The RBM frequency correlates to the tube diameter and can be described theoretically as follow:

$$d_{SWCNT} = \frac{248}{\text{RBM frequency in cm}^{-1}}, \qquad \text{(III.1)}$$

where d_{SWCNT} is the diameter of SWCNT in nm. In practice, the exact RBM frequency can be influenced and shifted by other factors, therefore better use the frequencies as a rough estimate.

The other forms of CNTs, MWCNTs, do not exhibit RBM modes and typically have a higher ratio between D and G bands than SWCNTs.

As it was mentioned above, the smallest CNT that can be obtained is the (5,0) zigzag tube with the diameter of ~0.4nm (see chapter I.1.1.1). Therefore, the highest estimated RBM frequency is about 620cm^{-1}. The typical diameters and corresponding RBM frequencies of SWCNTs are shown in the Appendix 3 on the page 168.

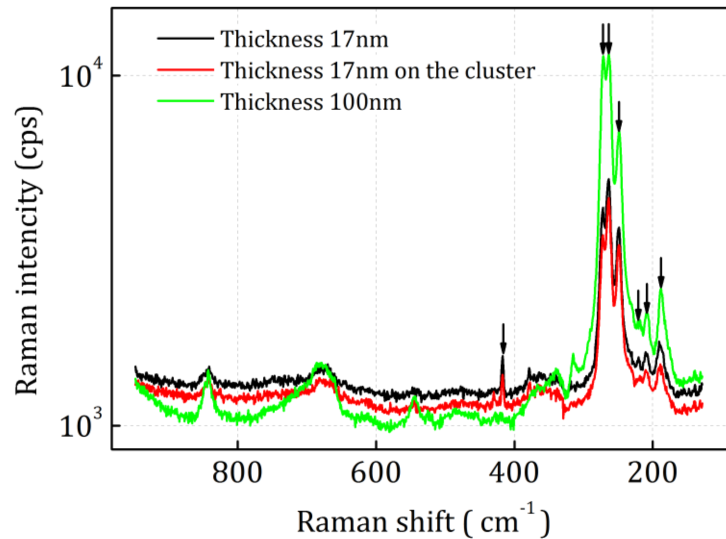

Figure III.4. RBM part of the Raman spectra obtained for SWCNT layers with thicknesses of 17 nm and 100 nm. The picks corresponding to different diameters of the tubes are shown by arrows.

We measured Raman spectra of the few SWCNTs layers (see Figure III.4), which were produced with the same technique as some of the FETs based on individual CNTs, of which the transport and noise properties were studied in this work. Several clearly visible picks were observed on the spectra: 416 cm^{-1}, 272 cm^{-1}, 263 cm^{-1}, 249 cm^{-1}, 221 cm^{-1}, 209 cm^{-1} and 188 cm^{-1}, corresponding to 0.59 nm, 0.90 nm, 0.94 nm, 1.00 nm, 1.12 nm, 1.18 nm and 1.32 nm diameters of SWCNTs, respectively. The first pick is not observed in the thick SWCNT layer. Therefore, it can be related to the alumina substrate, which the layers were placed on. Analyzing the Raman measurements we can conclude that the diameter of the nanotubes (on which the fabricated FETs were based), which were used to process some of the FETs analyzed below, varies from 0.90 nm to 1.32 nm. Moreover, the Raman intensity is directly related to the number of nanotubes in the layers, which leads to the most probable diameters being in the range of 0.90 nm to 1.00 nm.

IV. TRANSPORT AND NOISE PROPERTIES OF CARBON NANOTUBE BASED DEVICES

This chapter contains the results obtained researching CNTs based devices. It is divided into two parts.

The first part is focused on the investigation of transport and noise properties of the single-walled carbon nanotube field-effect transistors (SWCNT-FETs). High sensitivity, low power consumption, fast reaction times make SWCNT-FETs very promising for a variety of applications.[113] Different technology techniques and active treatments can be used for FETs performance optimization.[26–36] The influence of gate topology and/or Ohmic contacts on noise characteristics of the devices is analyzed. It is known from previous studies that gamma-ray irradiation of conventional FETs and HEMTs devices can cause the rearrangements of defect structure and to some extent the improvement of device performance. [114–116] The results of gamma-ray treatment of SWCNT-FETs are presented.

In the second part recently obtained results on bundles carbon nanotube structures are discussed. Three mechanisms of transport were revealed analyzed using noise spectroscopy.

1. Single-walled carbon nanotube field-effect transistors (SWCNT-FETs)

The first investigation of SWCNT-FETs was done by S.J. Tans in 1998.[38] The transistors consisted of an individual CNT connected by Pt electrodes, Si/SiO_2 substrate was used as a back gate. The strong modulation of channel current (up to six orders of magnitude) with gate voltage was shown for *p*-type channel SWCNT-FETs, which gave an opportunity to rival Si based FETs.

1.1. Individual carbon nanotube FETs

The individual carbon nanotube FET can be fabricated by several methods. The first is to process the network of contacts on the substrate and then spin-coat CNTs, which are dissolved in solution. The method demands the precise choose of the concentration of the CNTs in the solution and the regime of spin-coating. The second method is the following. The nanotubes are grown by catalytic CVD, and individual CNTs are located by AFM. Then, the electrodes are deposited using e-beam lithography. It takes a long time to fabricate the FETs by this technique, but it allows to process FETs with different gate topography, and that is an advantage in the investigation of FETs with different geometry.

1.1.1. Back gate topography

The devices in this study were fabricated on the basis of individual SWCNTs spin-coated on a Si/SiO_2 substrate. The Radial Breathing Modes (RBM) of Raman spectra measured for carbon nanotubes layers with different thicknesses are demonstrated in Figure III.4. Analyzing the Raman measurements we can conclude that the diameter of the nanotubes varies from 0.90 nm to 1.32 nm. Moreover, the Raman intensity of the RBM peaks directly reflects the most probable nanotube diameters, being in the range from 0.90 nm to 1.00 nm. Before the deposition of CNTs, the network of paired contacts (with various distances between them) was processed. Working devices were searched by measurements of current-voltage characteristics for each of paired electrodes of the network as a function of back gate voltage. Only those samples, which demonstrated excellent controllability by gate voltage, were used for further investigations. Thus, the FET devices under study are as follows. The channel consists of the individual nanotubes contacted by two molybdenum electrodes which operate as source and drain contacts (Figure IV.1). The width of the electrodes is ~100μm and the distance between them ~6μm. Typical CNTFET structures are shown in Figure IV.1 with total length of the CNT channel as (6±1) μm. The heavily doped Si substrate was used as the back gate of the FETs.

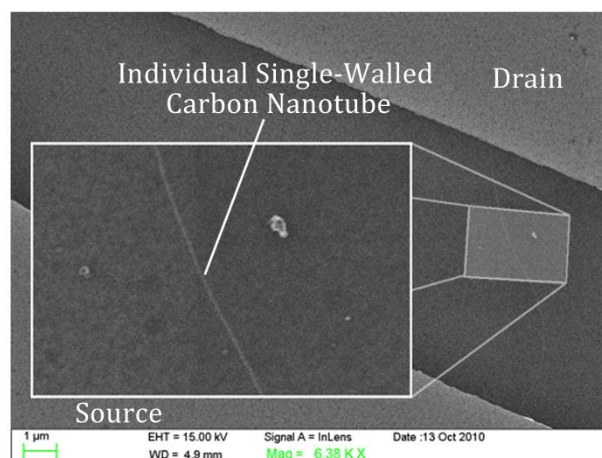

Figure IV.1. SEM image of a typical SWCNT-FET under study.

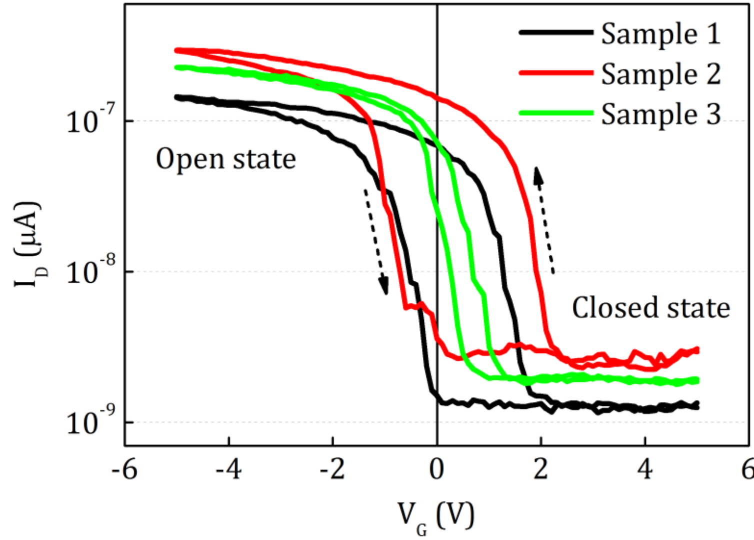

Figure IV.2. Typical transfer characteristics of different samples under investigation. Different values of hysteresis are observed for different samples.

In order to study the transport mechanisms in the FETs, current voltage and noise characteristics of CNT-FET samples were measured at different temperatures and applied gate voltages. I-V curves measured for 3 samples at room temperature and at a drain-source bias of 30mV are shown in Figure IV.2. The characteristics studied in a wide gate voltage range from -5V to +5V and back demonstrate hysteresis effects. This behavior is explained by charging of the deep traps at the interfaces between the CNT and the back gate. The maximum transconductance, g_m, is found to be as high as 0.1µS, which is typical taking into account the thick dielectric layer between the gate and the CNT channel. The effective mobility, μ, of the CNT can be estimated using the following equation[117] for long-channel FETs at low drain-source voltage:

$$\mu = \frac{L_{DS}^2 g_m}{C_G V_{DS}}, \tag{IV.1}$$

where $C_G = 2\pi L_{DS}\varepsilon_r\varepsilon_0/\ln(2t/r)$ is the gate capacitance, L_{DS} is the transistor channel length, V_{DS} is the drain-source voltage, ε_r is the dielectric constant of SiO_2, t is the thickness of the SiO_2 layer, and r is the radius of the SWCNT. Using $\varepsilon_r = 3.9$, $t = 500$nm, $V_{DS} = 30$mV, $L_{DS} = 6$µm, and $r = 0.5$nm (details for radius determination of the CNTs see chapter III.2 page 68), we obtain $\mu \approx 7000$ cm^2 V^{-1} s^{-1}. Then the total number of carriers, N, in the bias point with maximum transconductance can be calculated from:

$$\boldsymbol{j} = en\mu\boldsymbol{E} \Rightarrow \frac{I}{S} = e\frac{N}{L_{DS}S}\mu\frac{V_{DS}}{L_{DS}}, \tag{IV.2}$$

$$N = \frac{L_{DS}^2}{R_N e\mu} \approx 320, \tag{IV.3}$$

where $\boldsymbol{j}$ is the current density, n is the concentration of carriers in the SWCNT, $\boldsymbol{E}$ is the electric field, I is the current, S is the radial section area of the SWCNT, and $R_N = 1$MΩ is the resistance of the SWCNT-FET.

To investigate the noise properties of the samples we used quasi-equilibrium conditions by applying small biases to the nanotubes, $V_{DS} \leq 50$mV. Additionally, we used small gate voltages. In this case the hysteresis was not observed, and therefore, the influence of charging effects in the dielectric layer of the structure can be neglected in the analysis of traps in our structures. Noise spectra have been measured for each point of the current-voltage characteristics shown in Figure IV.3, at different gate voltages and temperatures. The data demonstrate weak temperature dependence of the transconductances. Such a behavior is characteristic of tunnel transport in the structure.

The threshold voltage, V_{th}, has a linear dependence in a wide temperature range (Figure IV.3 inset). Like in traditional metal-oxide-semiconductor FETs (MOSFETs), the temperature dependence of the surface inversion potential induces changes in the threshold voltage over temperature. This dependence can be expressed as:

$$V_{th}(T) = V_{th}(T_0) - \alpha_{V_{th}}(T - T_0), \tag{IV.4}$$

where $\alpha_{V_{th}}$ is the threshold voltage temperature coefficient. From a linear fitt of the dependence presented in the inset of Figure IV.3 we obtain $\alpha_{V_{th}} = -1.6\text{mV/K}$. It should be noted that such value is typical for FET devices. For complementary metal oxide semiconductor (CMOS) devices the coefficient typically ranges from -1mV/K to -4mV/K. It is calculated that this value for Macronix Nonvolatile Memory Solutions (MXIC) 0.5µm technology is about -1.22mV/K and -1.783mV/K for *n*-channel and *p*-channel MOSFETs, respectively.[118]

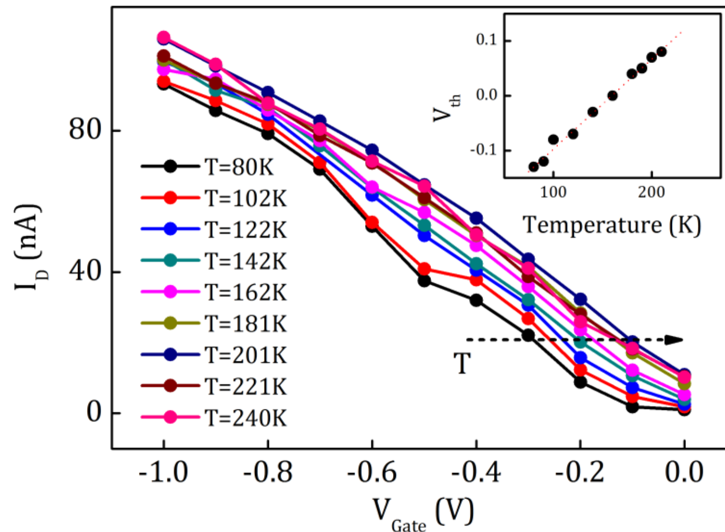

Figure IV.3. Typical transconductance characteristics of FET based on SWCNT measured at different temperatures near the bias point with maximum transconductance. Inset: threshold voltage dependence on temperature. V_{DS}=30mV.

Typical noise characteristics measured at different gate biases and at T=80K are shown in Figure IV.4. Noise spectra demonstrate thermal, flicker and GR noise components. The lowest horizontal value in Figure IV.4(a) corresponds to the thermal noise component,

which is calculated from Eq. (I.40). It should be noted that at high gate voltages the normalized noise spectra have almost the same noise level (Figure IV.4(b)).

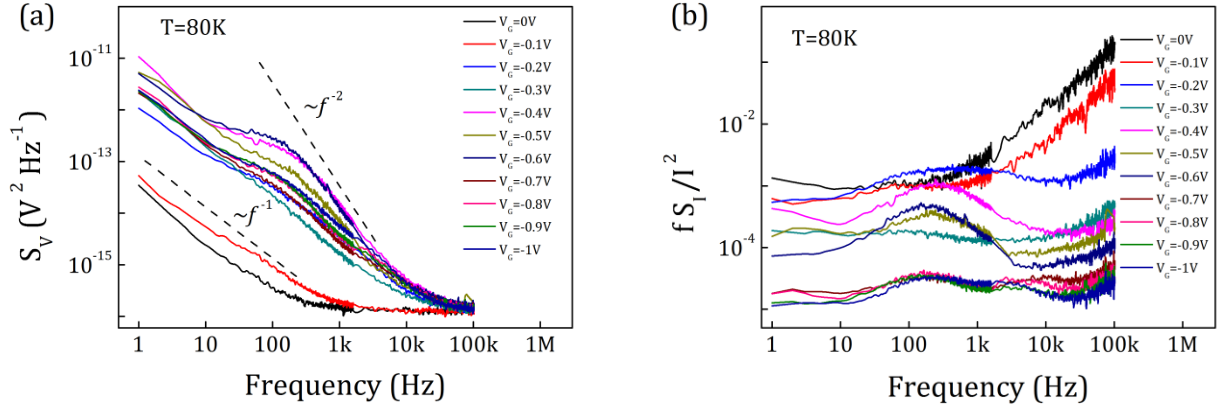

Figure IV.4. (a) Typical noise spectra measured at different gate biases, T=80K, V_{DS}=30mV. The normalized current noise power spectra (b) shows the same noise level at gate voltages higher than -0.7V. The characteristic frequency of GR-noise is almost independent on gate bias.

The noise spectra dependence on temperature is shown in Figure IV.5. Samples demonstrate GR noise components in wide temperature and gate ranges. The decrease of the characteristic frequency occurs with cooling down because of increases in the time constants of GR processes inside the FET channel. Therefore, by using the proposed model of GR-noise (see chapter I.2.2.3) the traps energy and density can be estimated, which will be shown later. The analysis of GR noise components reveals few traps with different activation energies.

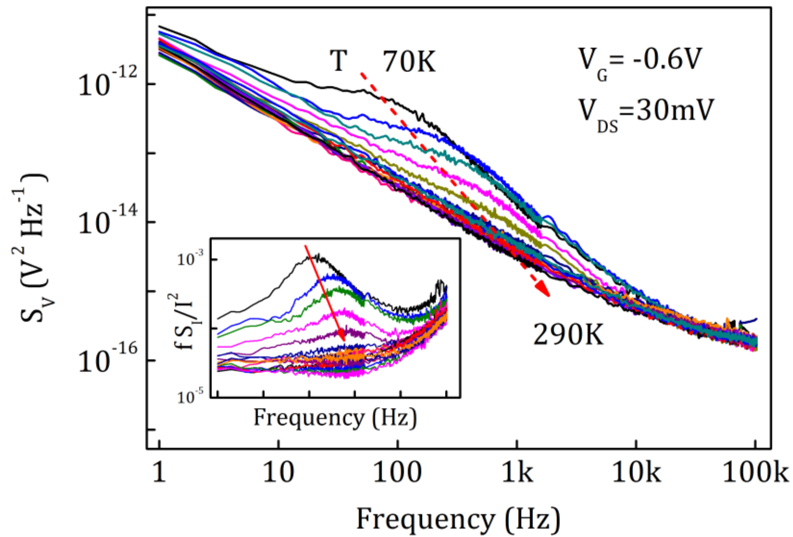

Figure IV.5. Typical noise characteristics measured at V_G=-0.6V and at different temperatures. Inset: normalized current noise power spectrum density as a function of frequency demonstrating the temperature behavior of a GR noise component.

The normalized current noise spectral density of the flicker noise component as a function of current and temperature is shown in Figure IV.6. The noise level doesn't

depend on the drain-source bias in sub-threshold and above threshold regimes at different temperatures (Figure IV.6(a)). It should be noted that in the sub-threshold regime the noise is higher compared to the channel regime (above threshold). The observed behavior is typical for field-effect transistors in the linear regime. Additionally the noise spectral density is almost independent on temperature at fixed drain current or resistance of the SWCNT-FET (Figure IV.6(b)). This demonstrates that the number of carriers is independent on temperature. Since the plots were built at fixed resistances the mobility is almost independent on temperature in several working points of the devices. Such a behavior is usually a characteristic of tunneling transport observed at gate voltages from -1V to 0V.

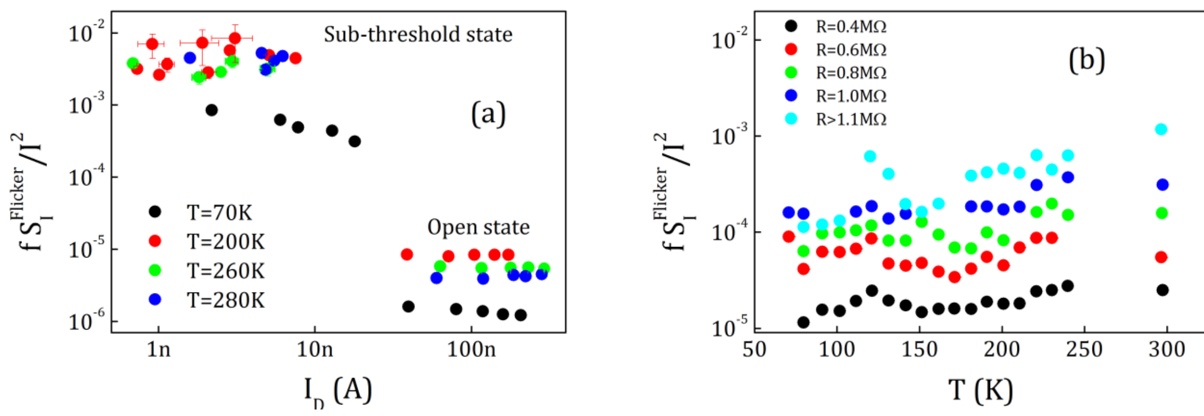

Figure IV.6. (a) Normalized current noise power spectral density of the flicker noise component dependence on drain current measured at different temperatures in channel (open) and sub-threshold states of the SWCNT-FET. Drain-source bias was varied from 10mV to 50mV. (b) Typical flicker noise component dependence on temperature at f=1Hz for different resistances of the SWCNT-channel of the FET controlled by the gate voltage V_G. V_{DS}=30mV.

The equivalent input gate voltage spectral density, $S_U = S_I / g_m^2$, (where g_m is the transconductance of the FET, S_I is the current noise spectral density), dependence on excess gate voltage is shown at different temperatures in Figure IV.7(a). The data demonstrate that the major source of flicker noise is located near an interface between the carbon nanotube and Si/SiO_2 substrate.

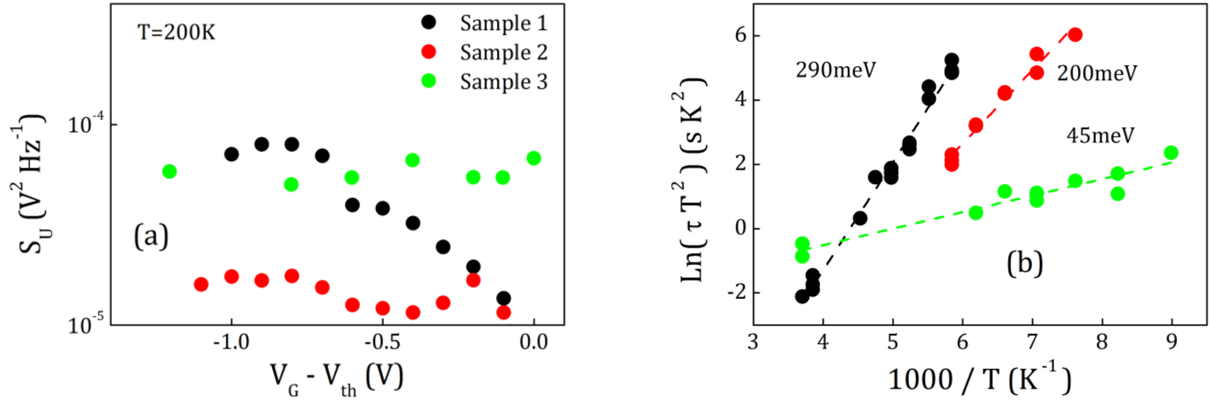

Figure IV.7. (a) Typical equivalent input gate voltage spectral density dependence on excess gate voltage measured for three SWCNT-FETs at V_{DS} = 30mV and T = 200K. (b) Arrhenius plot shown for sample 1. Dashed lines correspond to linear fitting, which allows us to calculate the energy levels of the traps.

It is known that the relative noise level of different kinds of materials can be estimated according to the Hooge relation (see chapter I.2.2.5). The substitution of the total number of carriers that can be found from $N = L_{DS}^2/e\mu R_N$ into Eq. (I.82) and using the value of effective mobility for the carriers calculated above allows us to estimate Hooge parameter as $\alpha_H = 3.8\times10^{-2}$.

Table IV.1. Activation energies obtained in different bias points of a SWCNT-FET. *the activation energy was difficult to estimate due to the overlapping GR noise components.

R (MΩ)	GR_1 (meV)	GR_2 (meV)	GR_3 (meV)
0.6 ± 0.1	280 ± 10	--	--
0.8 ± 0.1	290 ± 9	200 ± 10	45±5
1.0 ± 0.1	154 ± 6	184 ± 5	160 ± 9
1.2 ± 0.1	170 ± 30	94 ± 5	75 ± 4
> 1.3	?*	?*	66 ± 4

In addition to the flicker noise, GR or Lorentzian-shaped (LS) noise components were clearly registered for all samples in the investigated temperature range. Using an Arrhenius plot (Figure IV.7(b)) we estimated the energy level of the traps, E_t (also see chapter I.2.2.3). The energies are found to be 290±10 meV, 200±10 meV and 45±5 meV for the case of the bias point corresponding to the sample resistance of about 0.8 MOhm at a certain gate voltage. The activation energies obtained at different bias points (different gate voltages) of the SWCNT-FET are shown in the Table IV.1 for one of the samples. The trap energies for other samples are almost the same. These traps are located near the interface between the CNT and the SiO_2.

One of the samples has a relatively large GR noise component that behaves in an unusual way also in the Arrhenius plot; therefore it was impossible to calculate the activation energy of the trap (Figure IV.8). As it was shown above this sample has minimum current in open state. Additionally it will be shown below that the gate voltage influence on Schottky barriers in this sample was more effective.

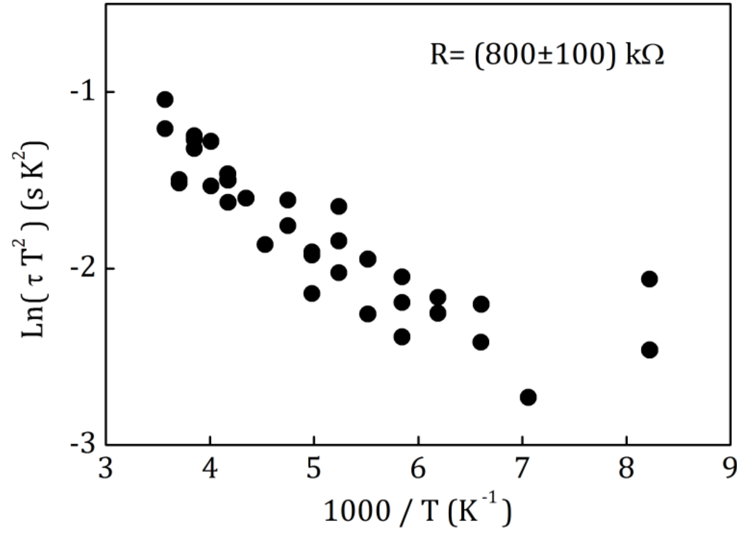

Figure IV.8. Arrhenius plot for the case of the GR noise component with unusual behavior.

Additional information about trap density can be obtained from the plateau of the Lorentzian-shaped noise.[88] This component of the noise spectrum is described by Eqs. (I.56)-(I.57):

$$\frac{f_0 S_I^{LS}}{I^2} = \frac{1}{\pi \cdot N} \frac{\overline{\Delta n^2}}{n} \frac{2}{1 + (f/f_0)^2}, \tag{IV.5}$$

where N, n are the total number and the concentration of carriers, f_0 and S_I^{LS} are the characteristic frequency and the current noise spectral density of the Lorentzian-shaped process, respectively. Here

$$\overline{\Delta n^2} = (n^{-1} + n_t^{-1} + p_t^{-1})^{-1}, \tag{IV.6}$$

n_t and p_t are the concentrations of the electrons and holes on the trap-levels, respectively. The temperature dependence of the normalized current noise power spectral density is shown in Figure IV.9, where $f_0 S_{I0}^{LS}/I^2$ corresponds to $f_0 S_I^{LS}/I^2$ at zero frequency. Estimating the number of carriers from the formula $N = L_{DS}^2/e\mu R_N$ (at R_N = 1.0×10^6 Ω, μ = 7000cm^2 V^{-1} s^{-1}), and using the maximum of $f_0 S_{I0}^{LS}/I^2$, we can calculate that $\overline{\Delta n^2}/n \sim 1$. This fact demonstrates that n is smaller than n_t and p_t taking into account equation (IV.6). Therefore the concentration of the traps is much higher than the concentration of free carriers. On the other hand, if the relation $\overline{\Delta n^2}/n \sim 1$ holds, the concentration of the carriers can be determined using equation (IV.5). The latter allows us to find unambiguously the value of carrier mobility in the channel.

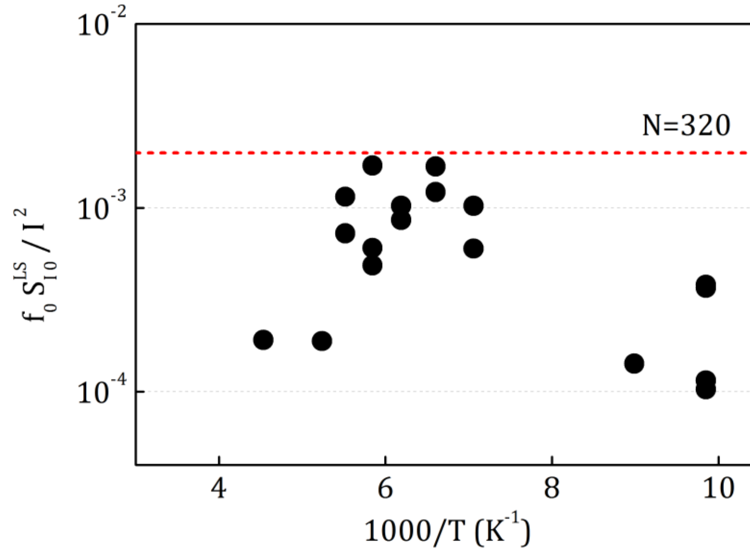

Figure IV.9. Normalized noise power spectral density of the plateau of a Lorentzian-shape noise component (measured in the bias point with maximum transconductance at V_{DS} = 30mV) as a function of reverse inverse temperature. The dashed line shows the value corresponding to N = 320 calculated for $\overline{\Delta n^2}/n = 1$ using Eq. (IV.5).

Analysis of influence of the Schottky contacts. A more precise analysis of the flicker noise component of the SWCNT-FETs in larger gate voltages allowed us to recognize two different regions (Figure IV.10(a)) separated by a resistance change of approximately $R\sim 600\text{k}\Omega$ (V_G-$V_{th}\sim$ -0.6V). The first region is the nonlinear region of the transfer characteristic whereas the second region shows the saturation regime (Figure IV.10(b)). Decreasing of the current noise power spectral density with decreasing of the channel conductivity corresponds to a reduction of the current fluctuations. However because of a stronger suppression of the channel current the "noisiness" of the sample is still increasing (Figure IV.6(b) and Figure IV.10(c)). Let us consider the reason for this increase more precisely below.

The work function of the Pd (used as contacts to SWCNT) has value that lies in the range of 5.22-5.6eV (see Table I.1) while the electrochemical affinity of the CNT is in the range of 4.4-5.0eV. Therefore, it is expected that Pd metallization results in Ohmic contacts to the nanotube. We observed a decrease of the current with an increase of the gate voltage of the FETs that normally corresponds to the p-type behavior of the channel. The diameter of the nanotubes in the FET devices has the value ~1nm corresponding to an energy band-gap in the range of 0.70-0.77eV (Eq. (I.15)). At small values of the applied drain-source voltage Schottky barriers at the interface between CNT and metallization can determine the peculiarities of transport and fluctuations in the system as it is shown in Figure IV.10(d).

By applying positive gate voltage the width of the Schottky barriers changes resulting in controlling of the hole current in the structure. The current through Schotky-barriers has an exponential behaviour as a function of applied voltage:

$$I_b \sim T^2 \exp\left(-\frac{eV_b}{kT}\right), \tag{IV.7}$$

where T is the temperature, e is the electron charge, k is Boltzmann constant, and V_b is the voltage applied to the barrier. In the case of a SWCNT-FET, V_b depends on the applied drain-source voltage, V_{DS}, and gate voltage, V_G. At the constant value of V_{DS} Eq. (IV.7) can be written as:

$$I_D \sim T^2 \exp\left(-\frac{erV_G}{kT}\right), \tag{IV.8}$$

where r is a coefficient that shows how gate voltages influence the barriers. Using the Hooge relation (I.82) and assuming that the Hooge parameter, α_H, doesn't depend on gate bias, the following relation can be obtained:

$$\frac{fS_I T^2}{I^2} \sim \exp\left(\frac{erV_G}{kT}\right). \tag{IV.9}$$

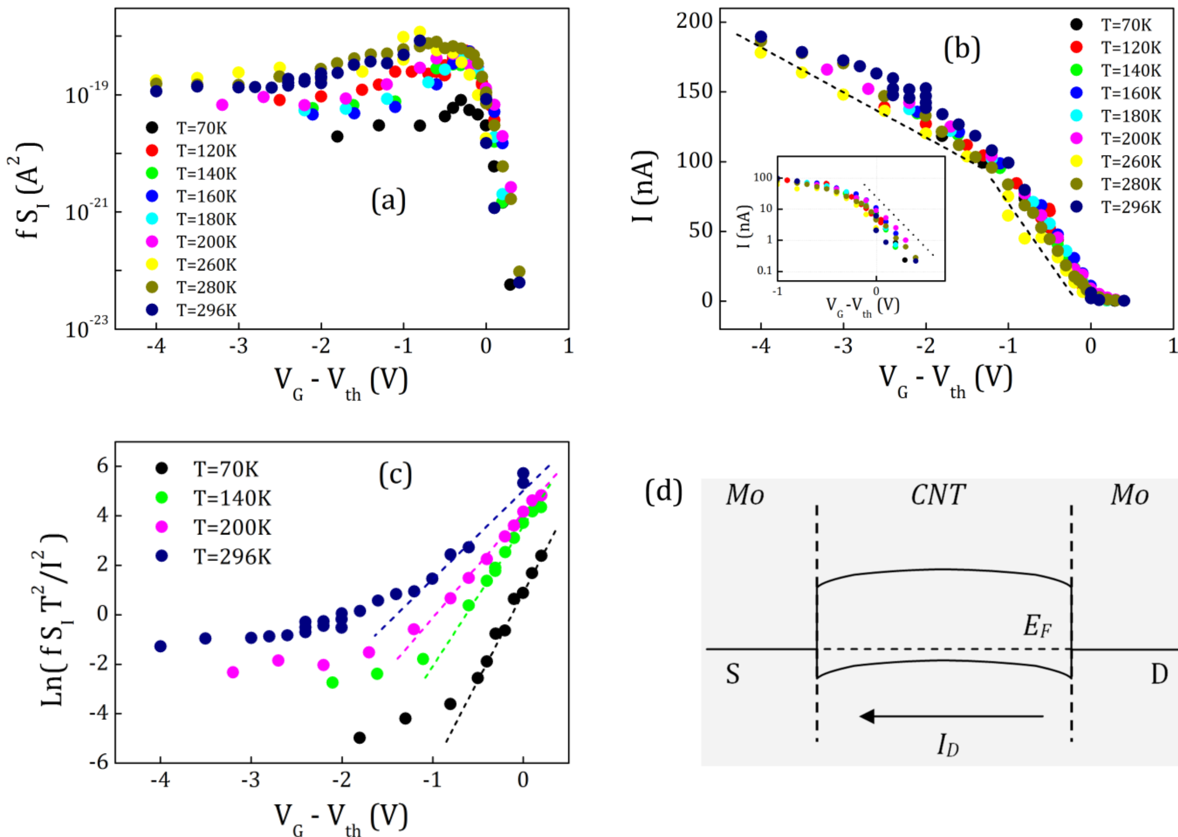

Figure IV.10. (a) Current noise power spectral density of the flicker noise component as a function of excess gate voltage measured at V_{DS} = 30mV, f = 1Hz measured at different temperatures, T(K): 70, 120, 140, 160, 180, 200, 260, 280, and 296. (b) Drain current dependence on excess gate voltage measured at different temperature. Inset represents the exponential behavior near zero excess gate voltage. (c) Logarithm of normalized current noise power spectral density multiplied by squared temperature as a function of excess gate voltage. (d) Schematic band diagram of the SWCNT-FET at zero gate and drain voltages.

We observed two different regions in the flicker noise dependences on gate voltage at different temperatures (Figure IV.10(a)). The first region, at large negative gate voltages, is

almost independent of (V_G-V_{th}). Here the CNT-FET is in open state, therefore a relatively large hole current through the channel and very thin tunable Schottky contacts can be expected. The second region has an exponential dependence on gate voltage. The exponential behavior is also observed in the transfer characteristic as a function of temperature (Figure IV.10(b) inset). Here, the hole current decreases with increasing gate voltage. Because of the exponential behavior of the flicker noise component, we can suggest that the main noise source is due to the Schottky barriers in this range of gate voltages. Using Eq. (IV.9) we can calculate the coefficient r. Figure IV.11 shows a linear dependences of the slope er/kT as a function of inverse temperature for two measured samples. We obtained r values equal to (0.22±0.02), (0.02±0.01) and (0.050±0.007) for samples 1, 2 and 3, respectively. Values of these coefficients reflect how strong the influence of the back gate voltage on the barriers is.

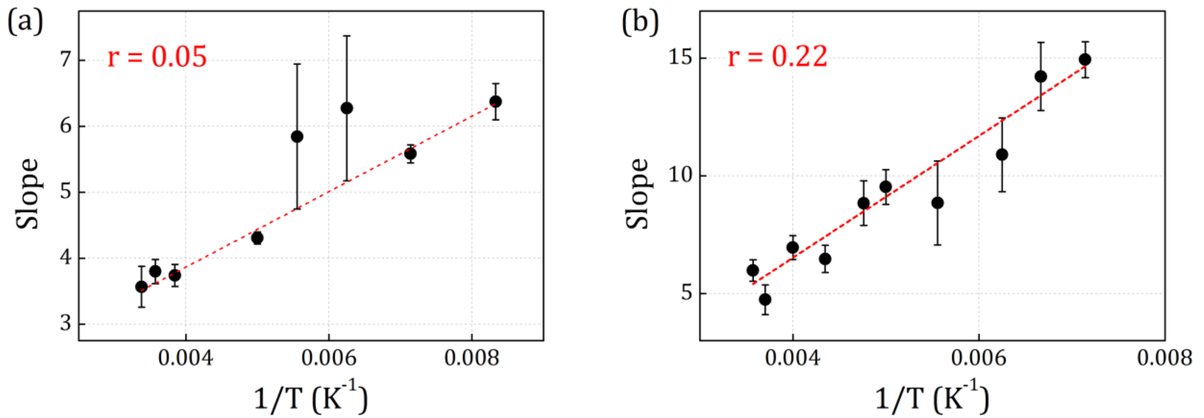

Figure IV.11. The dependences of the slope of the flicker noise component (dashed lines in Figure IV.10(c)) on inverse temperature obtained for sample 3 (a) with low and sample 1 (b) with a strong influence of the gate voltage on contact areas. V_{DS} = 30mV.

The small values of coefficient r obtained for some of the samples can be explained by the decreased influence of the contact area on the transport properties of the SWCNT-FETs. This is confirmed also by increased current in the transfer characteristics of the samples in open state at high gate voltages (Figure IV.2). It should be noted that the sample with a stronger influence of the gate voltage on the contact regions has a GR noise component with unusual behavior in terms of the Arrhenius plot (Figure IV.8). It is found that this unusual behavior and strong influence of the gate voltage on the contacts correlate. The characteristic time of the "unusual" GR-noise is independent on temperature (Figure IV.12) in different bias points of the CNT-FET. Therefore, instead of the usual trapping/detrapping process it can be explained by additional traps-aided GR-processes, either deep or shallow impurities (see Table I.3). The fact that the gate voltage results in changes of the Schottky barriers makes that the spatial charge regions are strongly affected by the gate voltage. This can lead to concentration changes of the impurity that takes place in trapping/detrapping processes. Such an effect is observed, i.e. an increase of the characteristic time with an increase of the channel resistance when decreasing the gate voltage magnitude (Figure IV.12). The data allow to conclude that in this regime the gate

voltage more effectively influences the contact region, attracts charge carriers of the CNT into contact regions, and thus changes their effective concentration.

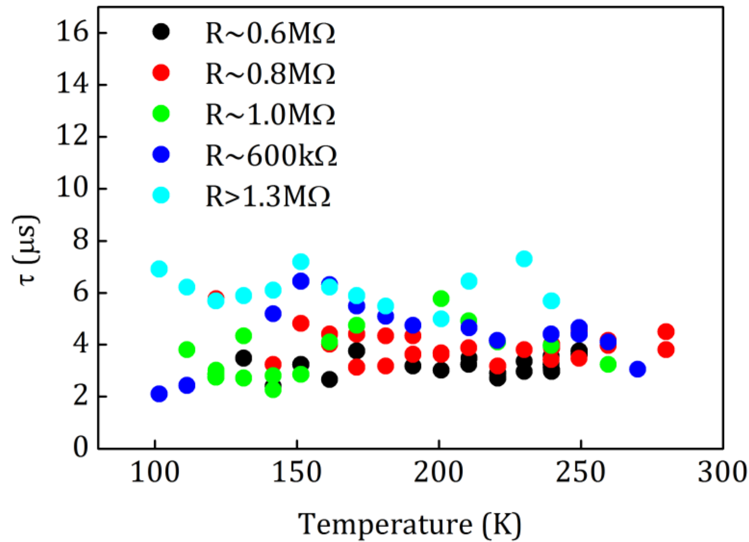

Figure IV.12. Characteristic time of the "unusual" GR-noise component observed on sample 1 plotted as a function of temperature measured at different gate voltages.

In conclusion, we analyzed transport and noise properties of FETs based on individual semiconductor CNTs. It was demonstrated that the main source of flicker noise at small gate voltages is related with fluctuations of the Schottky barriers in the contact region of the carbon nanotube. The FETs demonstrate stable properties at various temperatures, which is promising for biosensors applications. The analysis of Lorentzian-shaped noise components allows us to find the energy of traps near the interface between CNT and SiO_2. The obtained data are listed in Table IV.1. Trap concentrations were found to be higher than the concentration of carriers in the CNT channel. The number of carriers in the bias point of FETs with maximum transconductance was found to be no more than 320. The detailed analysis of the flicker noise component gives information about the influence of the gate voltage not only on the channel region, but also on the contacts. This finding allows us to explain the unusual behavior of one of the GR-noise components.

The high values of the obtained mobility are characteristic of high-speed transport in the channel of the CNT-FETs, and demonstrate good promise for high-speed sensors applications.

1.1.2. Top and side gate topography. Comparison of different gate topologies

We designed and investigated FETs fabricated on the basis of individual carbon nanotubes with top and side gate topographies. The approach is briefly described above in the introduction to the chapter 1.1. At first a set of markers were deposited on the Si/SiO_2 substrate for later positioning of individual nanotubes. After that the catalyst was spin-coated to obtain the lowest density of the catalytic particles on the top of the substrate. The CNTs were grown using CVD method described in section III.1. Thus, the substrates with low density of CNTs and with markers were obtained. The next step was obtaining an exact location of the nanotubes. This was performed using atomic force microscope (AFM) that also allows simultaneously obtaining the diameter of the investigated tubes. The precise position of the CNTs was used for following e-beam mask producing. For each of the found CNTs the source, drain contacts, top and side gates were processed. Before the fabrication of the electrodes 25nm Al_2O_3 was deposited on the top of the CNTs. This material was used as a dielectric layer for the top as well as side gates. The last step was deposition of the contacts using Pd, which has relatively large electron work function in the range of 5.22-5.6eV (see Table I.1 on page 30). Such metallization allows to produce the Ohmic contacts to the *p*-type CNTs.

AFM image of one of the produced devices is shown in Figure IV.13. The schematic diagram of the contacts is shown in inset to the figure. The Al_2O_3 dielectric layer is a square region under gate electrodes. The five gates: two side and three top, were used to investigate the properties of SWCNT-FETs.

We investigated the transport and noise characteristics of the FETs before and after their treatment using γ-radiation. Gamma irradiation is widely used for modifying of various characteristics of different materials. One of the examples is the improvement of DC and RF electrical performances of GaAs-based FETs, which was observed by Y. Guhel et al.[114], when the devices were irradiated with a gamma dose of 4.28×10^4 rad. Both the drain-source saturation current and the maximum transconductance were shown to be increased from 124 up to 136mA and from 415 up to 438mS/mm, respectively. The performances of the devices remained stable up to a radiation dose of 8.5×10^5 rad, demonstrating the high radiation hardness. The GaAs-based FETs were proved to be working up to 1×10^8 rad.[115,116]

It is important to note that gamma radiation treatments allow to obtain the broadened interfaces, to decrease of the structural defects and their spread, to make the materials more homogeneous.

Concerning CNTs, the study of the effect of small radiation doses on parameters of FETs and their radiation hardness has not yet been reported. Up to nowaday, only high radiation doses were used to tune the characteristics of CNT-based devices for special applications. For example, the work of V. Skákalová et al.[119] proposed to use a dose of 1.7×10^7 rad of gamma irradiation for increasing the Young modulus and electrical conductivity of SWCNT paper in air. Surprisingly, under vacuum there was only a small effect of irradiation registered. The Raman studies of the irradiated samples showed the

formation of defects in CNTs. The results were explained on the basis of radiation induced cross-links between nanotubes.

S.P. Jovanović et al. investigated the effects of γ–irradiation on the efficiency of functionalization of SWCNTs by single stranded deoxyribonucleic acid (ssDNA) wrapping.[120] SWCNTs were irradiated with dose of $5x10^6$ rad in three media: water, ammonia and air. The irradiation in ammonia was the most efficient. Based on obtained results the authors suggested that γ-irradiation can significantly improve the functionalization of SWCNTs for test of DNA.

In this work we studied the influence of γ-irradiation treatment on the transport and noise properties of SWCNT-based devices. We investigated FETs with two gates, side gate (SG1) and top gate (TG1), topographies (Figure IV.13). The transconductance characteristic of the FET showed the improved controlling and the increasing of the current in open state of the transistor after the radiation treatment (Figure IV.14) by a dose of $1x10^6$ rad. The maximum of transconductance before irradiation was measured to be $7.3x10^{-8}$ S and $1.8x10^{-7}$ S and after the irradiation the transconductance became about $1.5x10^{-7}$ S and $2.1x10^{-7}$ S for top and side gates, respectively. Such an improving of the FET characteristics can be explained by interface process between the drain and source electrodes and the tube because of rearrangement of Pd atoms on the top of the CNTs and radiation stimulated diffusion.[121] It should be noted that the controlling of the FET was improved using side-gate compared to top gate. Such behavior is explained by increased area of controlling of the nanotube in the case of side gate.

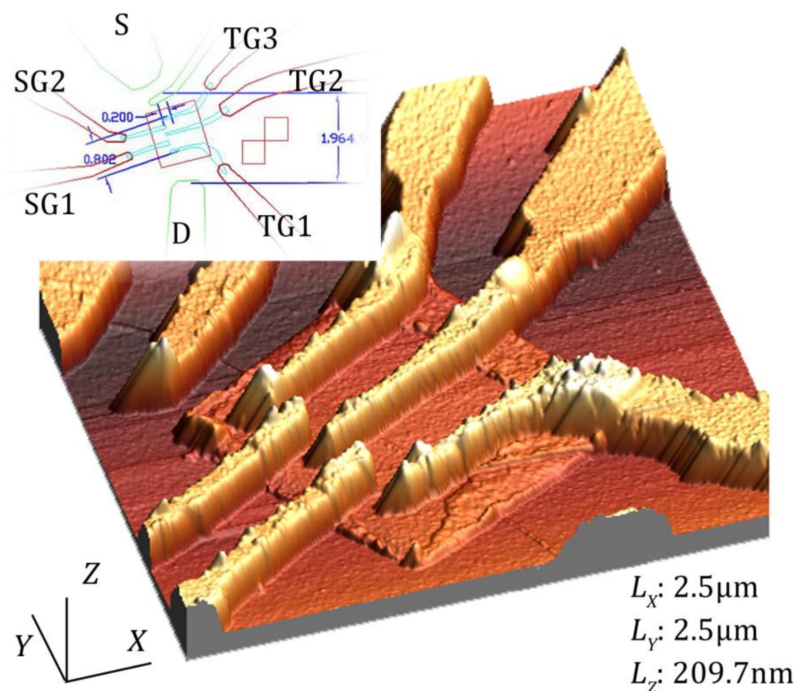

Figure IV.13. AFM image of the SWCNT-FET with two side (SG1, SG2) and three top (TG1, TG2, TG3) gates. Inset: schematic of the electrodes. S is the source and D is the drain electrodes.

Noise spectra were measured in different points of the transconductance curves before and after irradiation. Such investigations allow to analyze the influence of contacts

on the conductivity in the system. In spite of Pd, which was used as a metallization of the contacts, is the metal with large electron working function, we revealed the influence of the Schottky barriers appeared in the CNTs/Pd and Pd/CNT regions. The diameter of the CNT was estimated by AFM to be in the range of 1.7-2nm. The nanotube with such a diameter has small “first” energy gap equal to 0.35-0.45eV. Therefore, the band-to-band transition can be found in the noise measured spectra as will be shown below. These transitions have low probability but because of a low value of the charge carriers it can be found in the temperature range close to the room temperature.

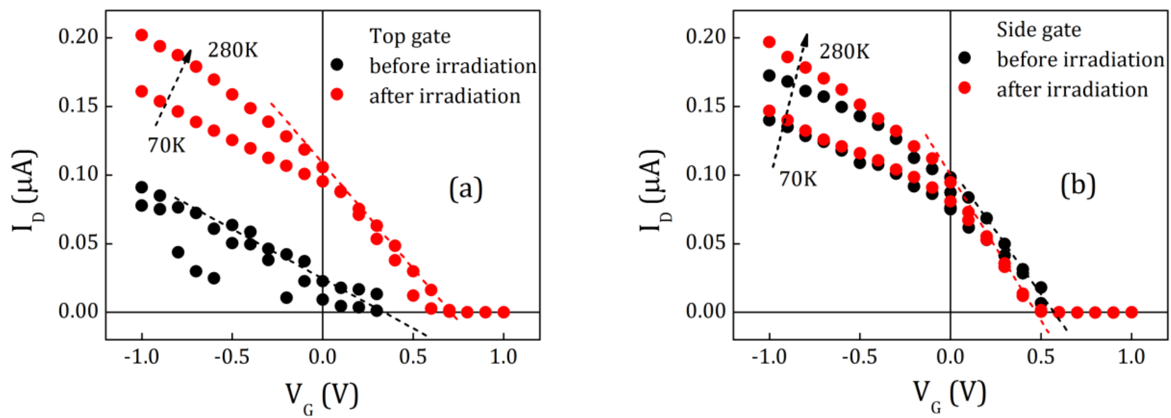

Figure IV.14. Transconductance characteristics of SWCNT-FET before and after $1x10^6$ rad dose of gamma rays measured at different temperatures measured at different (a) top gate voltages and (b) side gate voltages. The irradiation treatment results in improving the current in open state and maximum of transconductance of the transistor. V_{DS}=30mV.

Typical noise spectra measured at different temperatures for top gate topography are shown in Figure IV.15. The measurements were performed after finding the point of maximum transconductance, which lies between -0.5V and 0V gate voltages. The noise curves revealed GR-noise components in addition to flicker noise. It should be noted that similar type of noise spectra were observed and discussed in section 1.1.1 for the back gate topography FETs. The characteristic frequencies of GR-noises had clearly visible dependences on temperature (dashed lines in Figure IV.15). This fact allows to find the activation energies of traps resulting in appearance of GR noise components.

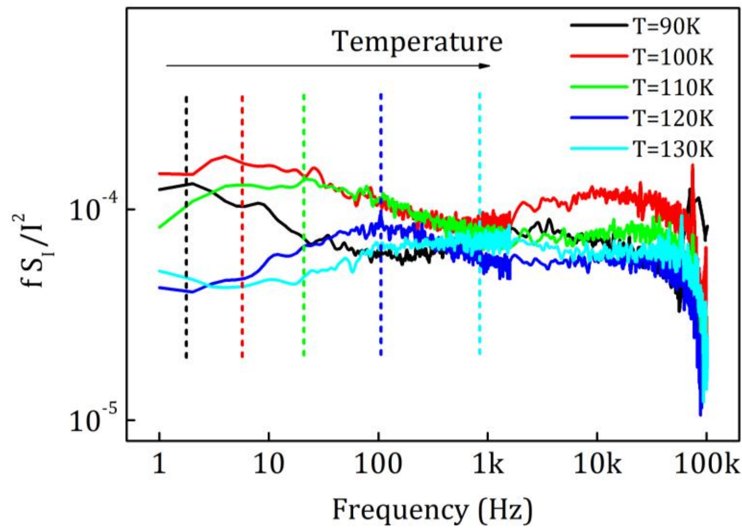

Figure IV.15. Normalized current noise power spectral density measured at different temperatures for top gate topography before irradiation in the points of maximum transconductance. Dashed lines show the position of the characteristic frequencies of GR-noise components at different temperatures. V_{DS}=30mV.

GR noise components were clearly registered before irradiation, as it is shown in Figure IV.15. after irradiation they became hardly recognizable from the total noise spectra even at low number of carriers (near the closed state of the transistor), where the GR processes was observed clearly before the radiation. Normalized current noise spectral densities measured at temperature of 120K and at different gate voltages are shown in Figure IV.16. It is clear that almost all noise spectra can be described by only flicker noise component. For example, the blue curve in the plot. It was measured at the same conditions as the blue-colored curve in Figure IV.15 (at temperature equal to 120K and at 0.4V of gate bias). The main difference between them is the bump that was registered before the irradiation in the blue-colored curve. It corresponds to GR-noise component.

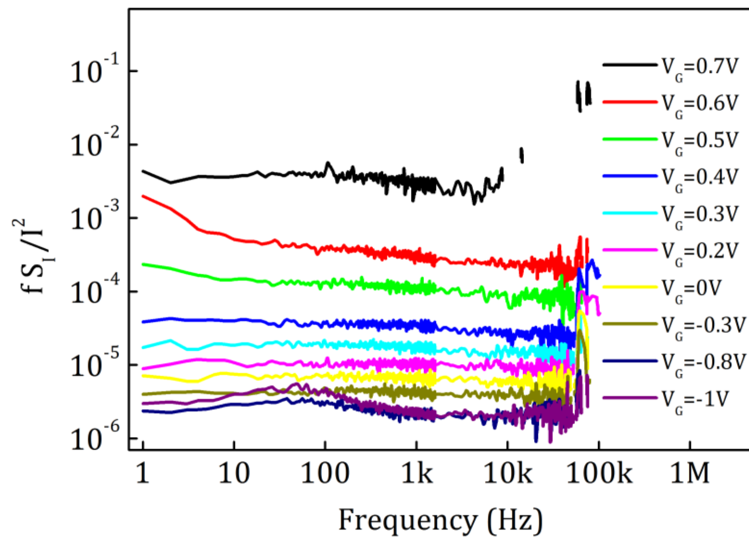

Figure IV.16. Normalized current noise power spectral density of the FET measured at different gate biases and at T=120K after gamma irradiation using top gate.

Using the automated noise measurements at working point of maximum transconductance with small temperature step in 2K and program described in Appendix 2 for extracting the noise components we obtained dependences τT^2 vs 1000/T (Arrhenius plot) for GR noise components. Here τ is the characteristic time of the GR-process, T is the temperature. The Arrhenius plots built for side and top gate before irradiation are shown in Figure IV.17.

The activation energies of traps were obtained to be around 25meV, 130meV, 240meV and 370meV. Because of small band gap of the CNT the energy of 370meV can be interpreted as a valence band-to-conductance band transition. The other values as will be shown below are related to the traps near the interface of the CNT with dialectric layer. It should be noted that the nanotube is sandwitched by Al_2O_3 from the top and SiO_2 layer from the bottom. Therefore, the obtained energies can be associated with both of the oxides.

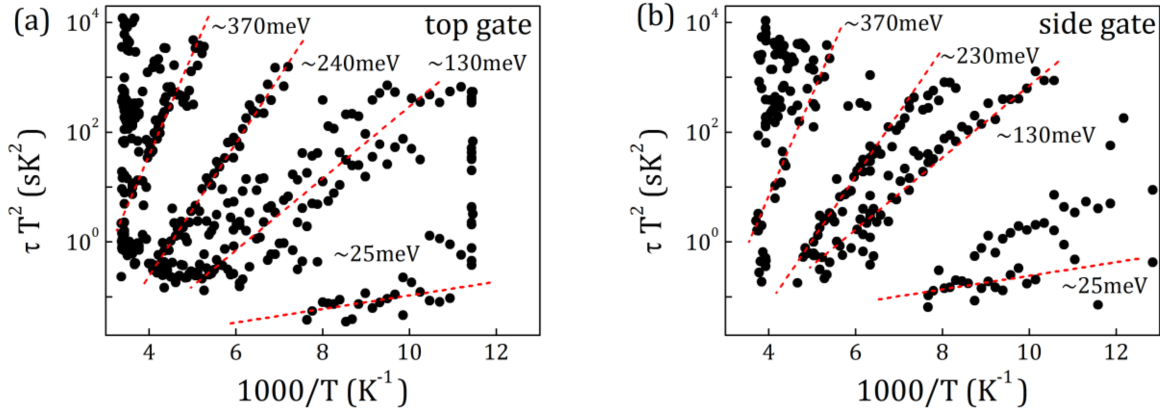

Figure IV.17. Arrhenius plots of GR-noise components obtained at different temperatures by measuring CNT-FET device at working point with maximum transconductance using (a) top and (b) side gates before irradiation. V_{DS}=30mV.

The results described above showed the energy traps for charge carriers near the interfaces of the CNT with dielectric layers. The trapping/detrapping processes were generating the GR-noise components. At the same time the main source of the noise fluctuations resulted in flicker noise component on the spectra.

Analysis of Schottky barriers influence on transport and noise properties. As it was mentioned before Pd metallization was used to form the Ohmic contact with the CNT. However, the applied gate biases can change energy diagram resulting in increasing or decreasing Schottky barriers for charge carriers flowing through the contacts regions, as it was previously shown for back gate topography (chapter 1.1.1 Figure IV.10(d)). In the case of Mo metallization Schottky contacts are already formed at zero gate voltage and the existence of them was observed down to -1V in the case of back gate geometry. Concerning Pd metallization, the larger in comparison to Mo metallization work function and small band gap of the CNT allow to create Ohmic contacts at V_G=0V. However, starting from ~0.2V of side gate bias the influence of the Schottky barriers were revealed as it is shown

in Figure IV.18 for the side gate. Here, the exponential behavior of flicker noise as a function of gate voltage was registered, and such a behavior is temperature dependent.

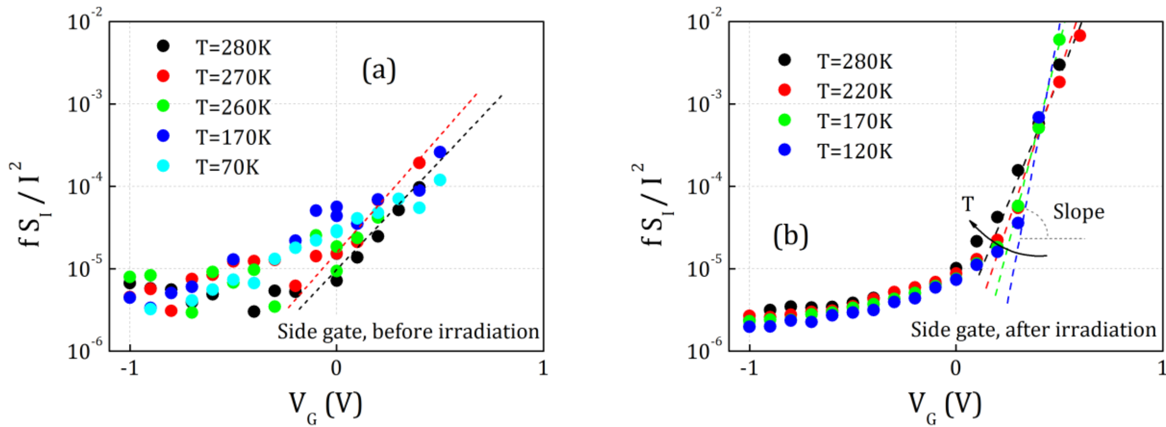

Figure IV.18. Normalized current noise spectral density of flicker noise component measured for side gate geometry (a) before and (b) after irradiation at different temperatures. The slope of the fitted dashed lines was found changes as a function of temperature.

The temperature dependence of the slope, as it was mentioned in chapter 1.1.1, allows to calculate the influence coefficient, r, of the gates to Schottky barriers (see (IV.9)). It can be made by extraction of the slope from the dependence of Ln(fS_I/I^2) on V_G and plotting it versus inversed temperature. In Figure IV.19 we demonstrate such an approach. Using linear fitting of the points, the coefficient r was calculated. Its values were found to be 0.07 and 0.27 for top and side gates, respectively.

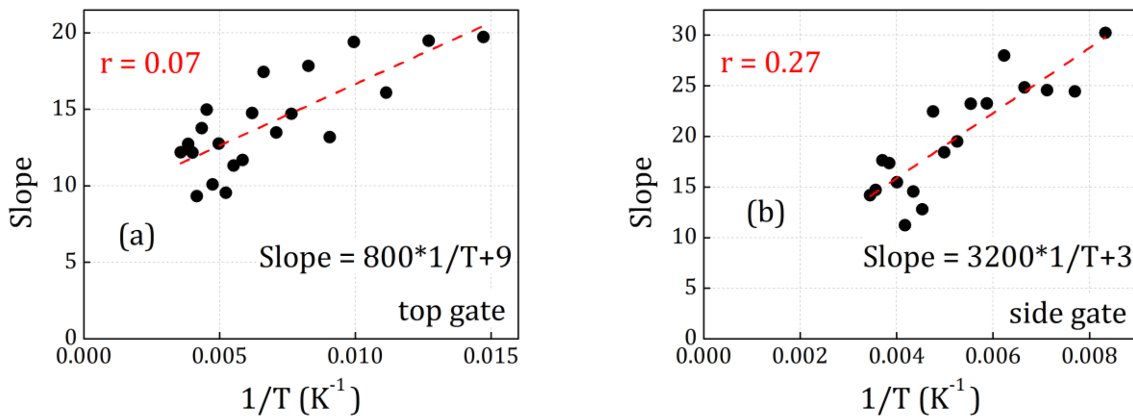

Figure IV.19. Slope of the flicker noise component dependences on inversed temperature for top (TG) and side (SG) gates after irradiation. The coefficient r that shows the influence of gates to Schottky barriers was found to be higher for SG than for TG topographies.

The obtained values for the coefficient show that influence of the gate bias onto Schottky contacts regions in side gate topography is higher than in the case of top gate one. The fact can be explained by difference in distances of the gates to the CNT. Top gate is approximately in ten times closer in our topography to the channel and therefore it controls small region under the gate of the tube compared to the case of side gate. It should be noted that these calculatione were done for the measurement after gamma radiation

treatment. Before the irradiation, the noise spectra of CNTs demonstrated a large number of GR components that reflects increased trapping/detrapping processes with participation a large number of traps. The carriers hoping conductivity through the traps can modulate the current in different regions of the tube and can influence the contact regions too. Therefore, the coefficient *r* was not possible to obtain before irradiation, only the existence of exponential behavior of the dependences was proved (Figure IV.18(a)).

Additionally to exponential region on the plots (Figure IV.18) we obtained almost independent normalized current noise power spectral density as a function of gate biases at high negative gate voltages, when the FET is in open state. In this region the Schottky barriers became thinner and the main source of flicker noise came from the tube itself. Here, we registered temperature dependences of the drain current (Figure IV.14) and normalized spectral density (Figure IV.18). The current in CNTFET has quasi-ballistic character[122], therefore we can use only drift component of the current to describe the transport in the channel. Using the Eq. (IV.2), we can obtain the number of carriers in the CNT:

$$N = \frac{I_D L_{DS}^2}{V_{DS} e \mu}, \qquad \text{(IV.10)}$$

where I_D is the drain current, L_{DS} is the length of the CNT, V_{DS} is the voltage applied between drain and source, e is the electron charge and μ is the carriers' mobility. By substitution of the number of carriers from Eq. (IV.10) in Hooge's relation (I.82) we can obtain the following:

$$f \frac{S_I}{I_D^2} = \frac{\alpha_H V_{DS} e \mu}{I_D L_{DS}^2}, \qquad \text{(IV.11)}$$

where α_H is the Hooge constant. Supposing that $\alpha_H = 2\text{x}10^{-3}$ and using the temperature dependences of current and flicker noise power spectral density measured at high negative gate voltages we can obtain the carriers mobility in the CNT channel of the FET. The estimatimated mobility values at 200K were found to be 4100cm^{2}V^{-1}s^{-1} and 1700cm^{2}V^{-1}s^{-1} before and after irradiation, respectively. The temperature dependences of the mobility before and after irradiation are shown in Figure IV.20.

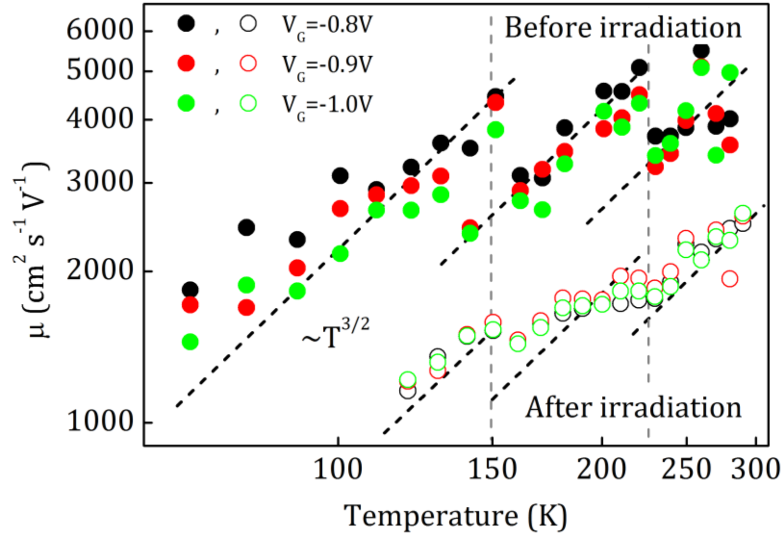

Figure IV.20. Temperature dependences of calculated mobility before and after irradiation at different side gate voltages.

The measurements of noise and current were performed at different gate biases and at V_{DS} = 30mV. It is shown that temperature dependence of mobility has the same behavior as the traps-assisted mobility. Usually, the last is related to the number of carriers, N, to the concentration of impurities, N_I, and to the temperature, T, in such a form[123]:

$$\mu_{imp} \sim \frac{T^{3/2}}{N^2 N_I}. \tag{IV.12}$$

The temperature dependences of mobility also show two drops at 150K and 215K. This behavior can be related with charged impurity or transition of the charge carriers to other valley. In addition, the mobility decreases after the irradiation. This behavior can be explained by increased number of free carriers in the channel. The same tendency was revealed in behavior of flicker noise. The possible source of the carriers may be π-bonds of the CNT that were linked to the absorbed molecules before irradiation. They became free after the gamma radiation treatment. This results in increasing current and decreasing the flicker noise component. Our estimations of numbers of free carriers at temperature 200K gave values of carriers equal to ~300 and ~760 before and after irradiation, when changing in mobility was from 4100cm^{2}V^{-1}s^{-1} down to 1700cm^{2}V^{-1}s^{-1}, respectively. Using the Eq. (IV.12) by comparison of the mobility before and after treatment, we can obtain

$$\frac{\mu_{imp}^{(bi)}}{\mu_{imp}^{(ai)}} = \frac{N_{ai}^2 N_I^{(ai)}}{N_{bi}^2 N_I^{(bi)}}, \tag{IV.13}$$

where $\mu_{imp}^{(bi)}$, $\mu_{imp}^{(ai)}$ is the cariers mobilities; N_{bi}, N_{ai} is the numbers of carriers; $N_I^{(bi)}$, $N_I^{(ai)}$ is the numbers of impurities before and after irradiation, respectively. By substitution values obtained above we can obtain the reducing of the impurity number after the treatment:

$$\frac{N_I^{(ai)}}{N_I^{(bi)}} = \frac{300^2 \times 4100}{760^2 \times 1700} \sim 0.4. \tag{IV.14}$$

The increase of carriers' number related with decreasing of the impurity number can lead to decreasing of GR-noise components. This behavior was registered experimentally as described above.

To conclude, the individual carbon nanotube FETs with top and side gate topographies are investigated before and after gamma radiation treatment. It is demonstrated that the transport characteristics are improved after gamma-irradiation treatment with small dose of 1×10^6 rad. The analysis of flicker noise component allows to reveal the noise related with the channel and the Schottky barrier regions, respectively. The decreasing of the channel noise was registered after the gamma treatment. This fact was explained by increasing the number of carriers and decreasing the number of impurities. The analysis of the GR-noise components before gamma-irradiation allows to calculate the activation energies of the traps to be around 25meV, 130meV, 240meV and 370meV. The analysis of flicker noise related with fluctuations in Schottky barrier regions showed stronger influence of side gate in comparison to top gate. Such a behaviour can be explained by almost ten times greater distance between the side gate and the nanotube, which lead to increased influence of potential field on the contact regions. The flicker noise related with channel shows temperature dependended characteristic for the traps-assisted scattering mechanism in whole measured temperature range. The estimatimated mobility values at 200K were found to be $4100 cm^2V^{-1}s^{-1}$ and $1700 cm^2V^{-1}s^{-1}$ before and after irradiation, respectively. At the same time the number of carriers in the channel increased resulting in increasing of the total current.

1.2. Multiple carbon nanotubes FETs

Multiple carbon nanotubes FETs with backside gate configuration were investigated. Such a configuration allows us to use a simple and convenient method of studying transport phenomena in an ensemble of CNTs. Structures under study consist of two Mo contacts deposited at a distance of 10μm on SiO_2 on the top of heavily doped Si substrate, where the Si substrate is used as a back gate. The catalyst regions were processed as 5μm×2mm strips. Nanotubes were grown using an alumina supported Fe/Mo catalyst placed on the contacts. The catalyst strips were positioned 5μm away from the edges of the Mo electrodes. The structure under study is shown schematically in the inset to Figure IV.21. CNTs were grown at 900°C for 2min under 720ml/min of methane, 500ml/min of hydrogen, and 12ml/min of ethylene flow. Electric fields of the order of 1V/μm were used to control the orientation of the growth.[124] In the structures under test typically 500–600 nanotubes were found to be connected in parallel between the contacts using scanning electron microscope. Using parallel aligned CNTs it is possible to remove crossover among CNTs and considerably reduce noise level by removing the noise generated by tube-tube junctions.[125] As it will be shown below that such a structural design with a sufficiently large length between the contacts allows effective current control through the CNTs of FET structures rather than the contact resistance.

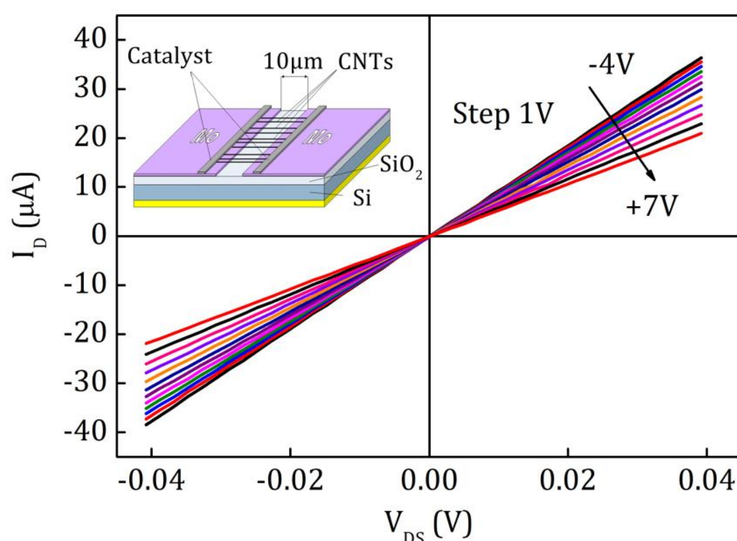

Figure IV.21. I-V characteristics of the investigated CNTFETs measured at different gate voltages with 1V step. Inset: schematic of the investigated CNT-FETs.

The diameters of the nanotubes were measured using an atomic force microscope and found to be about 1.3nm. The scanning electron beam microscope images were obtained demonstrating clear alignment in the direction of the electric field, perpendicular to the edges of the Mo electrodes. A standard isotope ^{60}Co source was used to emit characteristic gamma rays with a flux of 10^2 rad/s and energy of 1.2MeV. We measured the I-V characteristics of the FETs and the low-frequency noise spectra in the frequency range from 1 Hz to 100 kHz before and after gamma radiation treatment.

Figure IV.21 shows the output characteristics of the FET measured at different gate biases. The device displays symmetric behavior for positive and negative drain voltages. As can be seen from the figure, pinch-off is not reached in the device. This is related to the conductivity through the metallic CNTs and the conductance which cannot be controlled by the gate voltage.

Typical transfer characteristics obtained before irradiation are shown in Figure IV.22. The semiconducting CNTs at fixed drain-source voltage, V_{DS}, display characteristic *p*-type behavior by decreasing current with increasing (from the negative to positive) gate voltage applied to the substrate. The maximum transconductance, g_m, measured at a drain-source bias of 50mV and gate-source bias of 9V is found to be as high as 2.7μS. The relatively low ratio of the current in off and on states is due to one third of metallic CNTs being arranged in parallel to two thirds semiconducting CNTs in the channel. Such switching behaviour with applied gate voltage is widely adopted in analogue RF systems where some voltage region is used around a fixed working point.

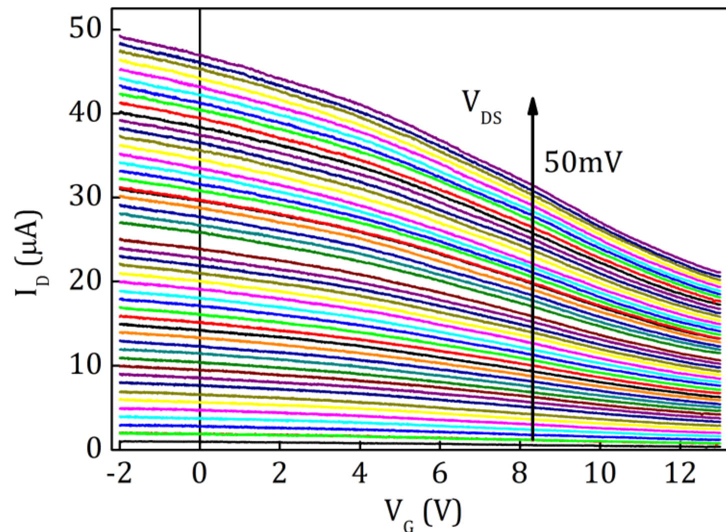

Figure IV.22. Transfer characteristics measured at different drain-source voltages in the range from 0 V to 50 mV.

The effective mobility, μ, of the CNT can be estimated using the following equation for long-channel FET at low drain-source voltage, as it was described above (see Eq. (IV.1)). Using ε_r = 3.9, t = 500nm, V_{DS} = 50mV, L_{DS} = 10μm, and $d = 2r$ = 1.3nm, we obtain μ = 1.5x10^{5}cm^2/Vs. Such a mobility value is characteristic of good quality CNTs. This estimation is based on results obtained for large area FETs. The Eq. (IV.1) has in denominator the capacitance, C_G, which can be calculated from the relation $C_G = 2\pi L_{DS}\varepsilon_r\varepsilon_0/\ln(2t/r)$. This relation is deduced using the method of electrical images for an infinite wire under metallic surface. The investigated structures have 500-600 CNTs, i.e. 1 tube per 4μm, which is only in 4 times higher than the doubled thickness (for method of electrical images) of SiO_2. In such distances the capacitance obtained above should be corrected (in the case of multiplying it on the number of semiconducting CNTs, it should be

taken into account that the tubes interact with each other. Therefore, to estimate the real effective mobility let's multiply the capacitance, C_G, obtained above on the two thirds of whole number of CNTs in the channel. By doing this we will obtain $\mu \sim$ 540cm²/Vs.

A small dose of gamma radiation treatment results in positive changes in I-V characteristics of the FET. The increase of the current ratio in off and on states and shift of the threshold voltage in direction to zero voltage are registered. In addition, the influence of parasitic conduction channels on DC characteristics of the device decreases, as this will be shown below. The transfer characteristics of the FET measured after irradiation with a dose of 1x10⁶ rad are shown by dotted lines in Figure IV.23(a). The current through the structure can be effectively controlled by the gate with the same amplitude of modulation recorded before radiation treatment. The transconductance of the FETs practically did not change (Figure IV.23(a)), but the level of the current decreases. This difference in current measured before, I_{D0}, and after irradiation, I_{DR}, is a linear function on drain voltage (Figure IV.23(b,c)), which indicates that either some linear resistance was added in series to the nanotubes or a parallel resistance was removed by irradiation. The dotted line is a linear fit of difference in drain current on V_{DS}:

$$\Delta I_D = -1.85 \times 10^4 V_{DS} - 8.48 \times 10^{-8} \approx -\frac{V_{DS}}{5400}. \quad \text{(IV.15)}$$

If we assume that a serial resistance, R_{add}, was added to the total resistance, R_T, by irradiation, then the current difference should be a function of gate voltage, V_G:

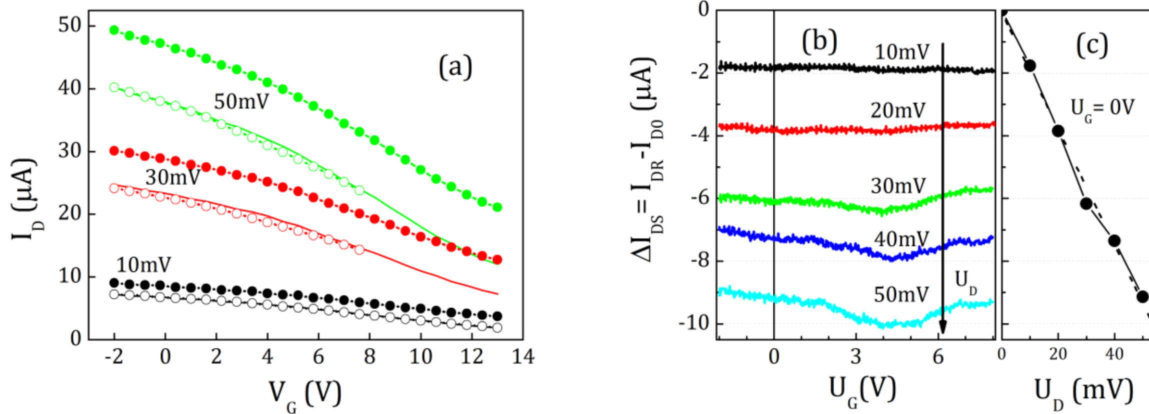

Figure IV.23. Comparison of transfer characteristics of CNT-FETs measured before and after gamma radiation treatment with a dose of 1x10⁶ rad measured at different drain-source voltages: (a) solid lines with filled circles – before irradiation, dotted lines with open circles – after irradiation; (b) dependences of the difference between currents after and before irradiation on gate voltage, V_G, at different drain-source voltages; (c) difference between currents after and before irradiation as a function of drain-source voltage measured at V_G = 0V, dotted curves show calculated dependences.

$$\Delta I_D = \frac{V_{DS}}{R_T(V_G) + R_{add}} - \frac{V_{DS}}{R_T(V_G)} = -\frac{V_{DS} \cdot R_{add}}{(R_T(V_G) + R_{add}) \cdot R_T(V_G)} = f(V_G). \quad \text{(IV.16)}$$

Indeed I-V characteristics measured after 1x10⁶ rad dose demonstrate about the same effective control of the drain current at different gates, which indicates that the resistance of the contact regions are about the same after 1x10⁶ rad dose of gamma rays.

If we assume that radiation removed a resistance parallel to the nanotubes, then the current difference should be independent of V_G:

$$\Delta I_D = \frac{V_{DS}}{R_T(V_G)} - \left(\frac{V_{DS}}{R_T(V_G)} + \frac{V_{DS}}{R_{add}}\right) = -\frac{V_{DS}}{R_{add}} \neq f(V_G). \tag{IV.17}$$

From experimental data (Figure IV.23(b, c)) it is found that the decreasing of current is independent of gate voltage. Therefore, the difference between the drain currents before and after radiation treatment (which can be accounted for by the contribution of a parallel resistance of 5.4kΩ) is due to changes of the structure in the channel region but not due to changes in contact resistance.

Let us consider the ionization processes under the influence of gamma radiation with a small dose in our CNT-FET structure. It has been previously established that the main changes in the layered structure occurred in more resistive regions as result of changes introduced by the Compton effect. Therefore, we will consider gamma radiation processes starting from dielectric SiO_2 layer grown on the top of the heavily doped Si substrate.

The effect of irradiation on metal-oxide-silicon field effect transistors has been widely studied.[126] The energy of ionization on silicon oxide has been estimated to be roughly 18 eV. The electrons generated by radiation have mobility of the order of 20 cm^2/V*s at room temperature. The mobility of the holes is in the range of 10^{-4} cm^2/Vs. Although without an applied electric field the generated electron/hole pairs have a higher probability of recombining, the fraction of non-recombined charge might nevertheless be up to 30 % in the case of cobalt irradiation**.** In addition, the electric field applied between the source and drain sweeps the electrons out from the oxide rapidly in comparison with holes.

Gamma irradiation results in the trapping of holes in the SiO_2 near the Si/SiO_2 interface and the creation of interface states at the Si/SiO_2 boundrary[127]. The density of radiation-induced states of the first type of center is roughly equal to the density of radiation-induced interface states. The density of a radiation-induced second type of center was found to be of the same order of magnitude as that of holes trapped in the oxide and situated very near the Si/SiO_2 interface, all within about 10 nm. A third type of centers is the nonbridging oxygen center. The radiation-induced positive charge (mainly holes) is transferred to the Si/SiO_2 interface by positive bias applied to the oxide layer with respect to substrate and is found to interact with precursors of the interface traps.

Therefore, the insulating oxide layer is the part of our device most sensitive to such ionization due to its high resistance so that conductivity is strongly sensitive to defects introduced by gamma radiation. The interface between the amorphous oxide and the crystalline silicon is generally deficient in oxygen, giving rise to dangling silicon bonds. These dangling bonds act as interface traps with energy levels within one or two atomic bond distances (0.5 nm) from the silicon lattice. High-quality Si/SiO_2 structures have pre-irradiation interface traps densities in the range of 10^9-10^{10} traps/cm^2. In the bulk of the oxide film, the silicon ionization and the interstitial oxygen donor centers are shown to be responsible for the radiation-generated positive space charge build-up (oxide charge) in thermally grown silicon oxide**.**[128] Usually non-recombined holes remain initially close to

their points of creation and cause a negative shift of the flat band voltage and the threshold voltage.[129] Holes created by gamma irradiation result in decreasing summary resistance.

In the investigated CNT-FET structures, we did not observed any shift in threshold voltage or decrease of the summary resistance after a small dose of gamma radiation of 1x10^6 rad. Moreover, increasing summary resistance was registered. This fact demonstrates that the main changes in transport properties after gamma radiation treatment are related to channel conductivity determined by CNTs. The origin of this modification can be explained by a slight modification of surface atom ordering in CNT due to the introduction of vacancies and interstitial point defects. The results of noise spectroscopy give additional important information about the processes and mechanisms of transport formation in the structure. An analysis of the current noise power spectra allows us to confirm that the main noise source is caused by transport phenomena in carbon nanotubes as will be shown below.

As in the case of output characteristics, the resistance of CNTs increases by about 25% after 1x10^6 rad irradiation in comparison with the resistance before gamma treatment. The results of noise measurements are shown in Figure IV.24 and they correlate with transport results. The level of normalized current noise power spectra was found to be independent of drain and gate voltages (Figure IV.24(a)). This fact confirms that the main source of noise in the structure is related to the transport phenomena in the region between the contacts of the structure and that contact noise contribution can be neglected. At the same time, after normalization to frequency, f, small changes of the noise level in the high-frequency region of the spectra can be found (Figure IV.24(b, c)). After gamma irradiation this flicker noise component shifts to the lower frequency range and demonstrates decreased changes with V_G.

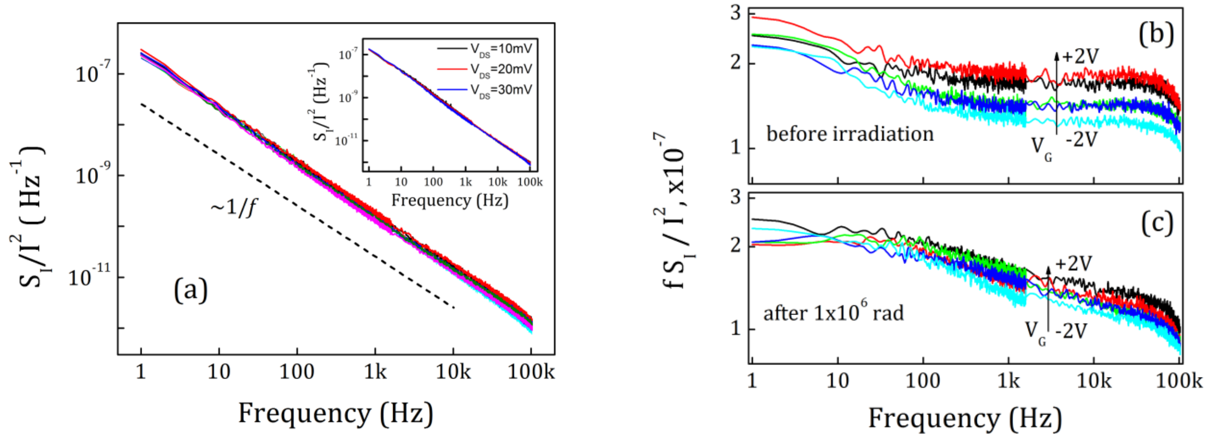

Figure IV.24. Normalized current noise power spectra of CNT-FETs (a) measured before and after irradiation at different V_G in the range from -2V to 2V with step 1V and V_{DS} =30 mV (inset: the noise spectra density measured at different V_{DS} and V_G = 0V before irradiation); (b) measured at V_{DS} =30 mV and different V_G before gamma radiation treatment; (c) measured at V_{DS} =30 mV and different V_G after gamma radiation treatment with a dose of 1x10^6 rad.

It is known that the relative noise level in different kinds of materials can be estimated according to the Hooge relation (see Eq. (I.82)). The substitution of the total number of carriers that can be found as $N = L_{DS}^2/e\mu R_N$ into Eq. (I.82) yields

$$\alpha_H = \frac{f S_I L_{DS}^2}{I^2 e \mu R_N}, \tag{IV.18}$$

where α_H is the Hooge parameter, N is the total number of carriers in the system, f is the frequency, S_I is the current noise power spectral density, I is the current, e is the electron charge, and R_N is the resistance of CNTs.

If the current, I, drops due to the mobility, μ, decreasing then value of $f S_I / I^2$ increases 1.3 times and this result in the increase of α_H. In the spectra of the low-frequency range, the noise level at f = 1Hz also increases by about 1.3 times. This fact confirms the suggestion that the noise in CNT is caused by defects introduced by gamma radiation. Taking into account the measured value of mobility 1.5x10^5 cm^2/Vs and Eq. (IV.18) one can obtain the Hooge parameter as $\alpha_H = 3.8 \times 10^{-3}$ before gamma irradiation and 5.3x 10^{-3} after irradiation. This low value of the parameter is even better than the values obtained previously for carbon nanotube samples with a long length of the tube without gamma irradiation treatment and is comparable with those of conventional semiconductors such as GaAs, GaN, and Si, which indicates the low noise level of the carbon nanotubes themselves.

We found for the $1/f$ noise component (in pure form resolved at 19 kHz) from $f S_I / I^2$ that the dependence on gate voltage at increasing V_G from -2V to +2V noise level increases 1.25 times and the current decreases 1.11 times. Such noise behaviour is approximately the same before and after gamma irradiation. According to Eq. (IV.18), the value $f S_I / I^2$ increased with decreasing current as $1/I$ in 1.11 times. The remaining 1.13 times can be explained by decreasing in $\sqrt{1.13} = 1.06$ times the active part of the length of the channel. The latter is usually observed in FETs and confirms that the origin of $1/f$ noise is not due to the contact noise.

In addition to the flicker noise component, the GR noise component can be resolved in the low frequency range of the spectra. From this part of noise spectra, the numerator increases twofold after gamma irradiation with respect to noise level before irradiation, at the same time the denominator change is caused by decreasing time constant, τ, as a result of the influence of radiation. It should be noted that the GR component has weak dependence on gate voltage, but the dependence is nonmonotonous in both cases before as well as after gamma irradiation. The noise spectra after subtracting the $1/f$ noise component are shown in Figure IV.25(a) (before gamma irradiation) and Figure IV.25(a) (after irradiation). The main difference between the spectra is the shift of regions with $1/f^2$ dependence to the higher frequency range. The result indicates that traps with different energy levels were activated as a device was exposed to small doses of gamma radiation. At the same time, the noise level has approximately the same value for both cases and the concentration of the traps does not change very much at this low exposure dose.

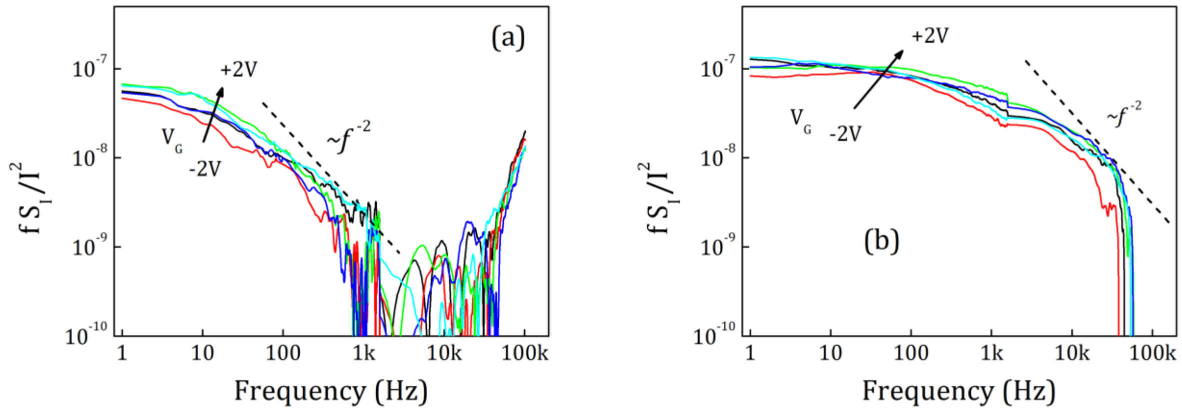

Figure IV.25. Normalized current noise power spectra of CNT-FETs: (a) measured at different V_G before gamma radiation treatment, plotted after subtraction of the $1/f$ noise component; (b) measured at different V_G after gamma radiation treatment with a dose of 1x10^6 rad, plotted after subtraction of the $1/f$ noise component.

In addition, the results of transport and noise measurements obtained after gamma radiation treatment with a dose of 2x10^6 rad confirm such behaviour. Figure IV.26(a) shows the transfer characteristics of the CNT-FET measured after such a dose of gamma irradiation. The I-V characteristics demonstrate an additional decrease of the total resistance which is even stronger than in the case of 1x10^6 rad gamma radiation dose. With an increase of the radiation dose to 2x10^6 rad the threshold voltage is reduced with improved on/off current ratio. The value of the maximum transconductance is found to be 1.7μS and only decreases slightly in comparison to g_m before gamma radiation treatment. The transfer characteristics of CNT-FETs demonstrate that the current through the structure can be effectively controlled in the region to nearly V_G = 0 by the gate voltage, also after gamma radiation treatment. The region around zero gate voltage with only plus and minus 1V voltage applied to the gate is ideal for different kinds of applications.

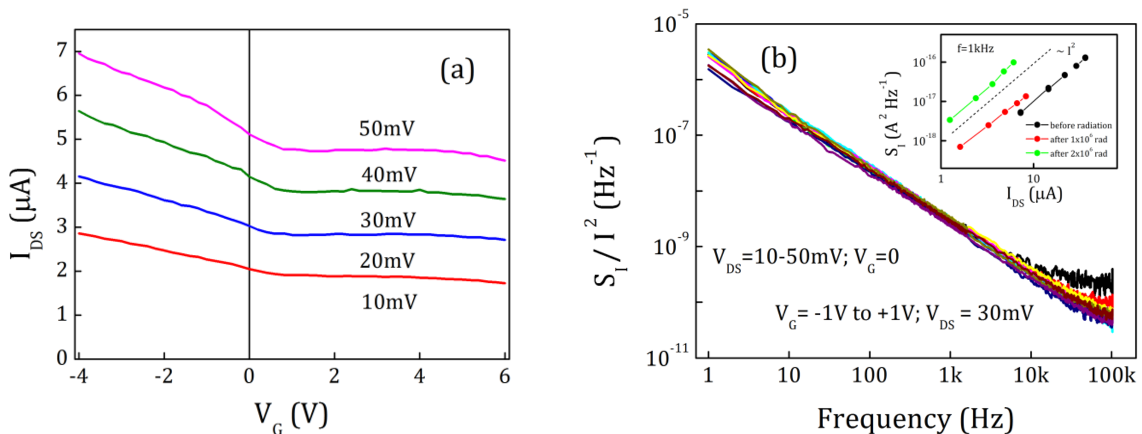

Figure IV.26. (a) Transfer characteristics of CNT-FETs measured at different V_{DS} after gamma radiation treatment with a dose of 2x10^6 rad; (b) Normalized current noise power spectra of CNT-FETs measured at different V_G and constant V_{DS} and vice versa before and after gamma radiation treatment with a dose of 1x10^6 rad and 2x10^6 rad; (inset) current noise power spectral density at 1kHz of CNT-FETs plotted as a function of I_{DS}.

The radiation also does not have any significant influence on the noise properties (Figure IV.26(b)), which proves the radiation hardness of the nanotubes. The noise behaviour follows the flicker ($\sim 1/f^{\alpha}$) noise with slope α equal to 1 (Figure IV.26(b)). The Hooge parameter obtained after radiation dose of $2\mathrm{x}10^{6}$ rad was found to be $\alpha_H = 2.4 \times 10^{-2}$. The magnitude of the $1/f$ noise increased as $I_{DS}{}^{2}$ with drain-source current up to 50μA, as shown in inset to Figure IV.26(b).

The level of normalized current noise power spectra was also found to be independent on drain and gate voltages. These experiments rule out any predominant contribution from the contacts and confirm that the main source of noise in the structure is related to the transport phenomena in CNTs.

In summary, our analysis shows that the difference in output characteristics of the FETs before and after small doses of gamma radiation treatment is due to a reduced contribution of parasitic channel to the total current parallel to the nanotube resistance. The transconductance of the CNT-FETs and level of noise did not change strongly after γ-irradiation at doses of 1×10^{6} and 2×10^{6} rad. The results show that active γ-radiation treatment can improve the transport and noise properties of CNT-FETs at some small optimal dose. The radiation treatment was found to decrease the influence of parasitic conduction channels on dc characteristics of the device. The Hooge parameters obtained are comparable with typical values reported for conventional semiconductors. The obtained results should be taken into account for the development of future chemical and biological sensors.

1.3. GR-noise components. Comparison of the traps in the structures

Measurements of the individual carbon nanotube FETs revealed clearly visible GR-noise components, which have usual temperature dependences for trapping/detrapping process. We suppose that the traps are situated in the interface of the CNTs with the oxides that were used between the nanotube and gate electrodes. In the part 1.1.1 of this section SWCNT-FETs with SiO_2 as a dielectric layer were investigated. The obtained activation energy of the traps has the value listed in Table IV.1. The FETs were fabricated using spin-coating method of the solved CNTs. Such method could give the addition impurities on the surface of nanotube. The lithography processed samples were shown in the part 1.1.2. Here, additionally to the silicon dioxide, Al_2O_3 was deposited on the top of the CNT. The CVD method that was used to grow nanotubes is promising to give the clear surface of the tubes. But lithography process could add some traps to the CNTs.

To compare different dielectrics we measured additionally the FET fabricated with only SiO_2 dielectric layer by using the method described in the part 1.1.2 of this section. Unfortunately, the FET demonstrated very bad controlling on gate voltage. The channel consisted of three wrapped CNTs, one or two of them had metallic properties. The current-voltage characteristic showed linear dependence at measured voltage and temperature ranges (Figure IV.27(a)). The noise spectra consisted of flicker and GR noise components. The metallic CNT should not give any GR noises therefore, this existed component belong

to semiconducting CNT. The amplitude of flicker noise dependence on current at various temperatures is shown in Figure IV.27(b). Such behavior, together with current-voltage characteristic, shows that the number of carriers and mobility almost independent on temperature and applied voltage, V_{DS}.

The analysis of the GR-noise components revealed several types of traps with different activation energies (Figure IV.27(c)). They were clearly observed to be 400meV, 310meV and 140meV. The values between 150meV and 300meV were hard to obtain.

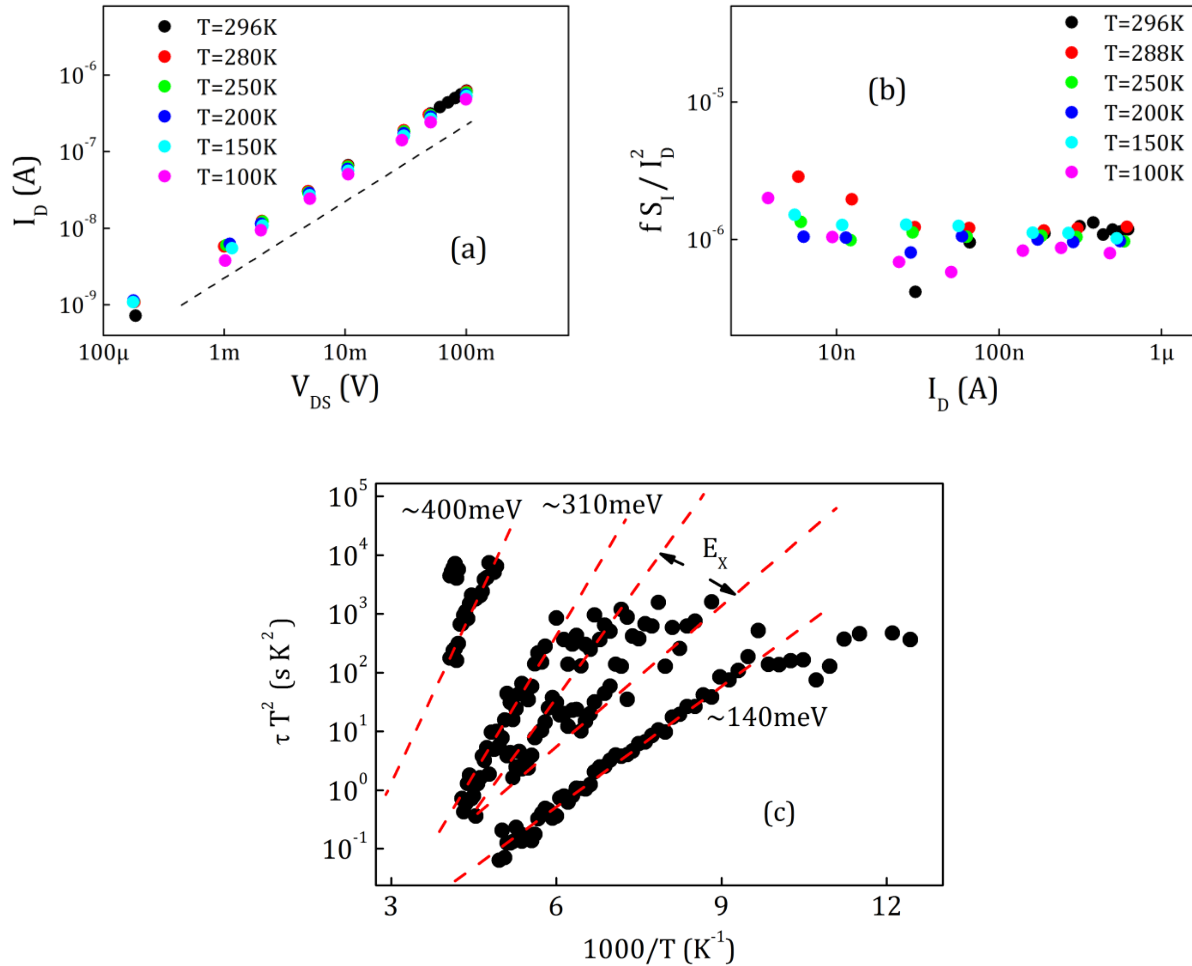

Figure IV.27. (a) Current-voltage characteristic of FET based on three wrapped CNTs measured at different temperature. (b) Normalized current noise power spectral density of the flicker noise amplitude dependence on current measured at different temperature. (c) Arrhenius plot built on the measurements at V_{DS} = 30mV. E_X is in the interval between 150meV and 300meV.

The comparison of the all activation energies of traps obtained during this work for individual SWCNT-FETs are shown in Table IV.2. It should be noted that the traps with activation energies equal to 230-240meV are respond to Al_2O_3 as 130-170meV – SiO_2.

Table IV.2. The activation energy calculated using Arrhenius plot for different individual SWCNT-FETs.

SiO_2, spin-coated CNT, chapter 1.1.1 (meV)	SiO_2+Al_2O_3, lithography, chapter 1.1.2 (meV)	SiO_2, lithography, chapter 1.3 (meV)
-	370	400
280-290	-	310
-	230-240	-
185-200	-	150-300
150-170	130	140
90	-	-
45-75	25	-

2. Structures composed of carbon nanotube bundles

The phenomena of charge transport were studied in structures consisting of bundles of carbon nanotubes prepared by applying uniaxial pressure. The source powder was compressed at room temperature and a pressure of 1 GPa. The initial powder contained 90% single-walled carbon nanotubes. According to the previously obtained results[130], the structures formed at a pressure represented by bundles, mainly oriented in the plane perpendicular to the axis of the applied pressure. Nanotubes bind together by weak van der Waals forces. The lengths of the bundles of nanotubes were in the range of 5-30 μm. After pressing the powder, the structure of the sample represents a system of multiple twisted bundles, which form a set of overlapping contacts, as can be seen from a fragment of the structure shown in Figure IV.28. Images were obtained using high-resolution electron microscopy. The material structure of the sample displays the twisted and overlapped strands of carbon nanotubes. Nanotubes in the individual bundle are parallel to each other.

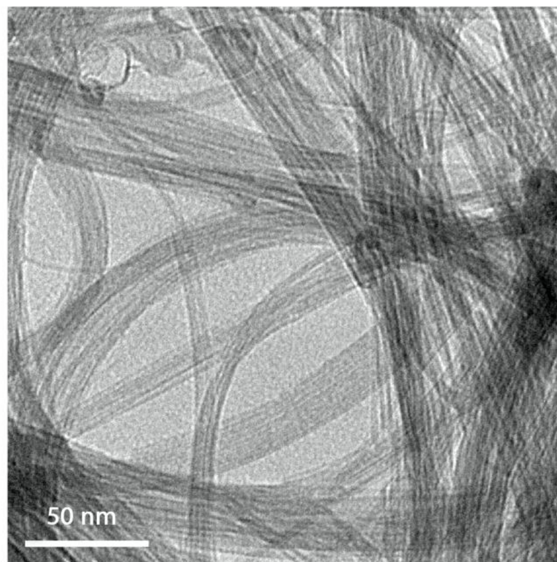

Figure IV.28. TEM micrograph of carbon nanotubes.

A Raman spectrum shows the main peak at 1602cm^{-1} due to the covalent bonds between carbon atoms, and two peaks at 137cm^{-1} and 235cm^{-1}, which correspond to the breathing modes of single nanotubes with a diameter of (1.02–1.05)nm and (1.68–1.73)nm, respectively. The data demonstrate that the bundles mainly consist of single-walled nanotubes of two diameters. As will be shown below, the conductivity of the structures has a metallic character with characteristic features of a one-dimensional metal system.

Low-frequency noise and transport properties of the structures were studied for samples in the two-terminal configuration. Samples were prepared in the form of dumbbells, containing a constriction with a characteristic size of 100×100 μm^2 in a cross-sectional area and a length of about 200 μm.

The configuration of the sample is similar to the described in Ref.[131]. Electrical contacts were prepared using a conductive paste of silver powder. Such contacts were Ohmic over the entire temperature range of 4.2–300K and remained stable during repeated processes of cooling and heating of the samples under study.

In a wide temperature range, the conductivity of the structures was investigated by applying a constant voltage. The resistance of the samples changes over the whole temperature range from 7Ω to 100Ω. These resistance values allow us to measure the current-voltage and noise characteristics with high accuracy. Electrical measurements were performed at voltages not exceeding 100mV at a power dissipation of less than 3x10^{-5} W over the entire temperature range. This allowed us to avoid the influence of self-heating effects on the results obtained. In the voltage range investigated, the deviation of current-voltage characteristics from linear behavior was negligibly small.

2.1. Three mechanisms of transport

The temperature dependence of the sample resistance is shown in Figure IV.29. The data demonstrate three regions with different temperature behavior. Above $T \approx 20$K, the power low dependence of the resistance is measured to be: $R \sim T^{-\alpha}$ (Figure IV.29(a)) with a characteristic Luttinger liquid exponent of $\alpha = 0.4$. Such characteristic for Luttinger liquid behavior was previously also reported for bulk-contacted CNTs. At lower temperatures, $T \approx (4.2 - 20)$K, the resistance follows an exponential function $R = \exp(T_0/T)^{0.25}$ (Figure IV.29(b)). Exponential dependence of the resistance versus the sample temperature with an exponent of 0.25 indicates the hopping mechanism of conductivity with variable hopping length.

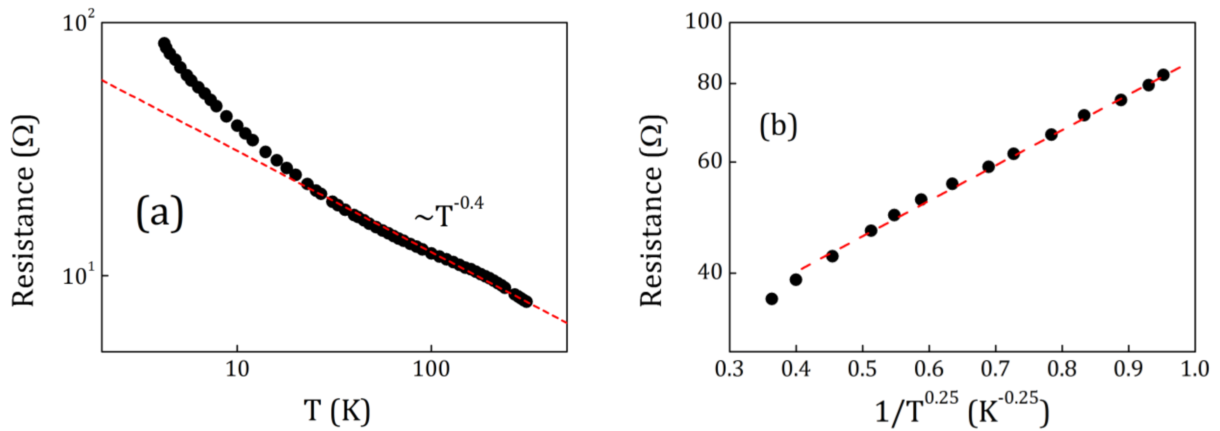

Figure IV.29. The resistance of SWCNT bundles as a function of temperature: (a) plotted in the double logarithmic scale, symbols are experimental data, solid line is fitting of the data with power low function $R \propto T^{-\alpha}$ with $\alpha = 0.4$; (b) plotted on a semi-logarithmic scale with dependence of $1/T^{0.25}$ in the temperature interval 5-25K. The solid line is an exponential function $R \propto \exp(T_0/T)^{0.25}$ with $T_0 = 800$K.

The measurement results presented here allow us to analyze the mechanisms of conductivity in the carbon nanotube bundles and their correlation with the noise characteristics. Three different mechanisms of conductivity are considered depending on temperature. Experimental temperature dependence of the resistance (Figure IV.29) shows a transition from hopping conductivity to Luttinger liquid conductivity at temperatures of about 20K. In the dependence of the noise characteristic parameter on temperature (showed below in Figure IV.32), there is also a transition from the value equal to 1 to a value equal to 2 of the logarithmic slope in current noise dependence on current. A transition region is recorded in the temperature range $T = (8 - 25)$K, which includes the transition temperature from hopping conductivity to Luttinger liquid conductivity.

At higher temperatures, the logarithmic slope reaches a value of about 1.9, while above T = 200 K the slope is equal to 2. In the temperature dependence of the resistance (Figure IV.29), this transition is very weakly resolved. At the same time, more pronounced changes in the behavior of the noise at $T > 200$K are visible in the temperature dependence of the normalized current noise (showed below in Figure IV.33). In this dependence, a slow increase in the level of noise as a function of temperature is registered in the temperature range from $T = 20$K to $T = 215$K. At higher temperatures, the noise increases sharply, in the

range from T = 215K to 300K, the noise level increases to a value about 3 times higher than in the previous case. Based on the results of Ref.[131], the following conclusion can be drawn. The temperature of the sharp bend in the temperature dependence of the noise corresponds to the transition temperature from Luttinger liquid conductivity to diffusion conductivity.

2.2. Noise spectroscopy of different transport regimes

The noise spectra of the sample have $1/f^{\gamma}$ dependence with $\gamma \approx 1$ (Figure IV.30), which is a characteristic function of flicker noise. Such kind of noise is typical for the case of conductivity in disordered structures. Pressed nanotubes constituting the sample studied are just one example of such a structure. Moreover, the deviations from the $1/f$ spectrum in disordered structures have to be regarded as an anomaly and are characterized from the point of view of the sample-specific features in conductivity under certain measurement conditions.

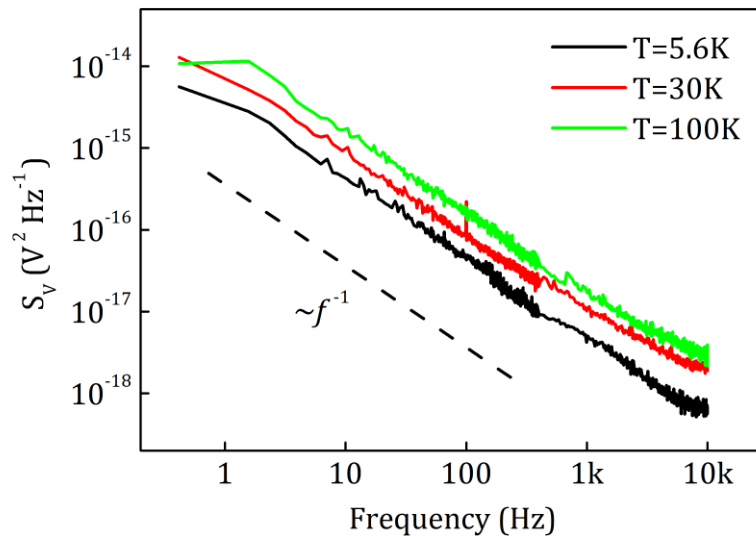

Figure IV.30. Typical voltage noise spectral density of metallic carbon nanotubes bundles, measured at applied voltage V = 50mV and different ambient temperatures T.

The shape of the noise spectra shown in Figure IV.30 does not change with variation of temperature over a wide range (4.2K - 300K). Therefore, the noise analysis can be further performed at a certain fixed frequency. The most convenient value of this frequency, for technical reasons, is the frequency value of f = 10Hz. Below, we analyze how this noise varies with temperature and applied voltage or current. Figure IV.31 shows the spectral density of current noise as a function of the current flowing through the sample, $S_I \propto I^{\beta}$, at different temperatures.

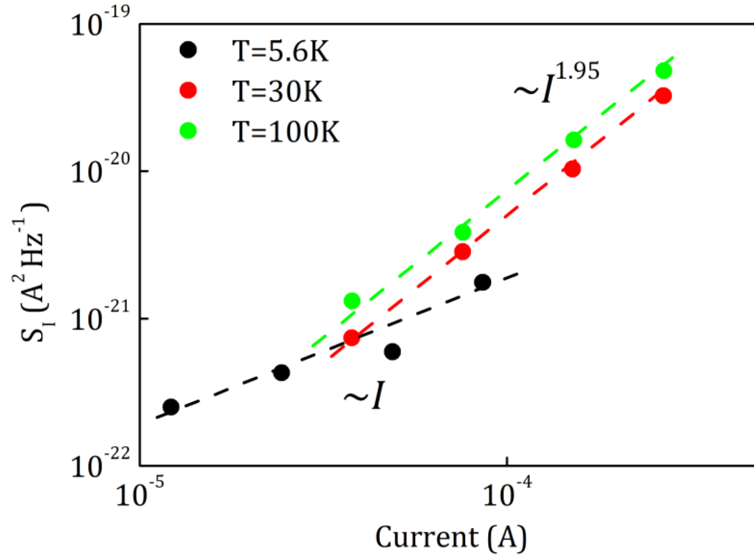

Figure IV.31. Current noise power spectral density as a function of current, measured at frequency f = 10Hz and different temperatures.

At temperatures of 30K and 100K, the dependencies have a nearly quadratic function. Usually, this behavior corresponds to the bulk noise in the conducting structures with a diffusion conductivity, which can be described by the formula (I.82):

$$\frac{\overline{S_r(\omega)}}{R_0^2} = \frac{\overline{S_I(\omega)}}{I^2} = \frac{\alpha_H}{N_{tot}|f|}, \tag{IV.19}$$

where α_H is the dimensionless parameter Hooge, N_{tot} is the total number of carries, I is the current, f is the frequency.

At the same time, the current dependence of noise at a temperature of 5.6K is nearly linear. Such a dependence is registered in the temperature range corresponding to hopping conductivity (T = 4.2K–20K, Figure IV.29(b)) in the current range of $I \approx 10^{-5}$–10^{-4} A. Noise models of hopping conductivity in the semiconductors predict a quadratic dependence of the noise as a function of the current through the sample (β = 2). The experimental results confirm these findings.[73,132–134] Since our results contradict these data, we consider the origin of such a disagreement in more detail based on the analysis of experimentally obtained results.

Conductivity of the sample is determined primarily by metal nanotubes. At the same time, up to now the noise models of hopping conductivity have been developed for the case of semiconductor materials. It is logical to assume that the mechanism of hopping conductivity in metallic carbon nanotubes may differ from well-known mechanisms in semiconductors. For example, it is known that in high-temperature superconductors in the region of hopping conductivity values of β = 1–2 are recorded.[135] The authors relate the hopping conductivity in these materials to the hopping of carriers between the weakly localized states. In our case, the analog of these states can be a grid of bundles of carbon nanotubes (Figure IV.28). In this system, the mechanism of charge transfer at low temperatures is assumed as a hopping conductivity.[131,135,136] The dependence (IV.19)

describes the current fluctuations that occur due to changes of the linear resistance. In the case of $\beta < 2$ the situation is different because of two reasons. Firstly, such relations are observed in nonlinear systems. For example, the shot noise inherent in the current passing through a potential barrier (non-linear system) has the relation (I.47):

$$S_I = 2eI, \qquad \text{(IV.20)}$$

where e is the electron charge. Of course, the shape of the noise spectrum for the investigated nanotubes is far from the noise spectrum of shot noise, since the latter does not depend on frequency in a wide range of frequencies ("white" noise). However, linear noise dependence on current, as well as the assumption of hopping conductivity generating current, allows us to suggest that the noise at low temperatures can be considered as quasi-shot noise.

Secondly, in the case of $\beta < 2$ the voltage applied to the sample affects the development of fluctuations. It reduces or increases the potential barrier height of a *p-n* junction or a Schottky junction and reduces the potential barrier height for isolated charges (Poole-Frenkel effect). These, in fact, lead to nonlinear current-voltage characteristics of such objects. Flicker noise in these systems for $\beta = 1$ is described by the model of Hooge-Kleinpenning for current flowing through the p-n junction:

$$S_I = \frac{\alpha_H eI}{\tau f} M, \qquad \text{(IV.21)}$$

where τ is the minority carrier lifetime, M is the dimensionless coefficient, which has a value in the range from 0.25 to 2.5. This expression is obtained using Eq. (IV.20) for the shot noise.[137–139] To test the applicability of this model of flicker noise to the particular situation it is usually necessary to calculate the value of α_H and compare it with the most commonly obtained value of 2×10^{-3}.

In the paper Ref.[140], a new approach is proposed for estimating the value of flicker noise using the coefficient α_H/τ, which has a narrow range of value dispersion of $(10^2 - 5 \times 10^3)$ s^{-1} .This range has much smaller range of dispersion in comparison with $\alpha_H = 10^{-2} - 10^{-9}$. Based on the data shown in Figure IV.31, the estimated value of $\alpha_H/\tau = f S_I / e I M$ obtained using Eq. (IV.21) is found to be equal to $\alpha_H/\tau = 1250/M$ s^{-1}. This estimated value falls within the above-mentioned range for α_H/τ.

This estimation allows us to suggest that the mechanism of current flow through carbon nanotubes in the regime of hopping conductivity is similar to the mechanism of current flow in the system with potential barriers. The linear dependence of current noise on the current of CNT bundles in a temperature range with characteristic hopping conductivity can be described by the model of Hooge-Kleinpenning.[137–139]

To analyze the nature of the noise current in the nanotube bundles, we measured the spectral density of current noise, S_I, as a function of the current at different temperatures in the range from 4.2K to 300K. Typical dependencies are shown in Figure IV.31. Based on these results, we found the dependence of the coefficient β on the temperature (Figure IV.32). Up to the temperature of $T = 8$K the parameter is constant: $\beta = 1$. Above this temperature a transition region was registered, where the parameter increases up to a

value of 1.9 ($S_I \sim I^{1.9}$). In the high temperature range at $T > 200$K, the parameter value is equal to 2.

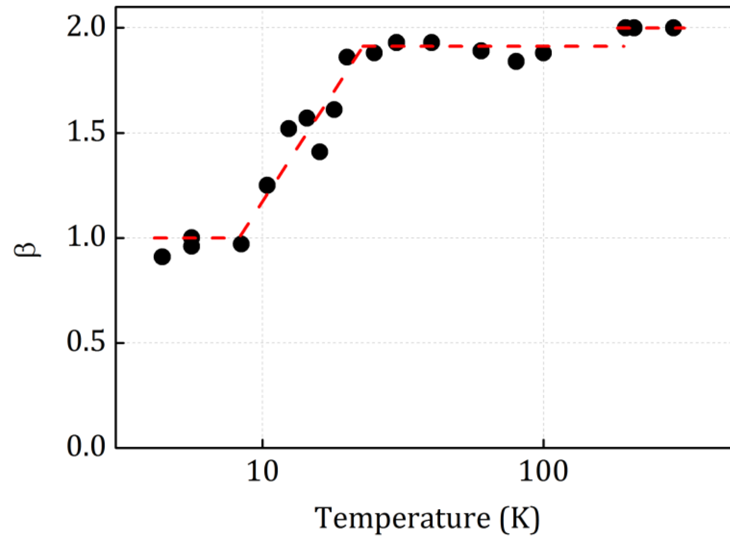

Figure IV.32. The current noise exponent, β, of power function $S_I \propto I^{\beta}$ determined from measured noise spectra as a function of temperature. The lines are guides for the eye.

In the temperature range relevant to $\beta \cong 2$, we determined the dependence of the normalized level of current noise on the temperature (Figure IV.33). A characteristic feature of the dependence is a weak increase in noise ($S_I/I^2{\sim}T^{0.16}$) in the temperature range 20K–215K with a further transition to a stronger dependence ($S_I/I^2{\sim}T^{3.28}$) at temperature higher than 215K. As can be found from the data (Figure IV.33), the ratio of noise levels at 300K and 100K is about 3. It is important that in the temperature range corresponding to the conductivity of Luttinger liquid the temperature dependence of the noise is weak. Above the temperatures corresponding to Luttinger liquid conductivity, a sharp increase in the normalized current noise is registered.

Our experimental results show that the conductivity of Luttinger liquid is a less "noisy" process than diffusion conductivity. A sharp increase of the noise in the case of diffusion conductivity can be explained by increased scattering processes of the carriers by phonons. At the same time, the conductivity of Luttinger liquid combines the conductivities determined by the quantum of resistances, which by their definition do not depend on temperature.

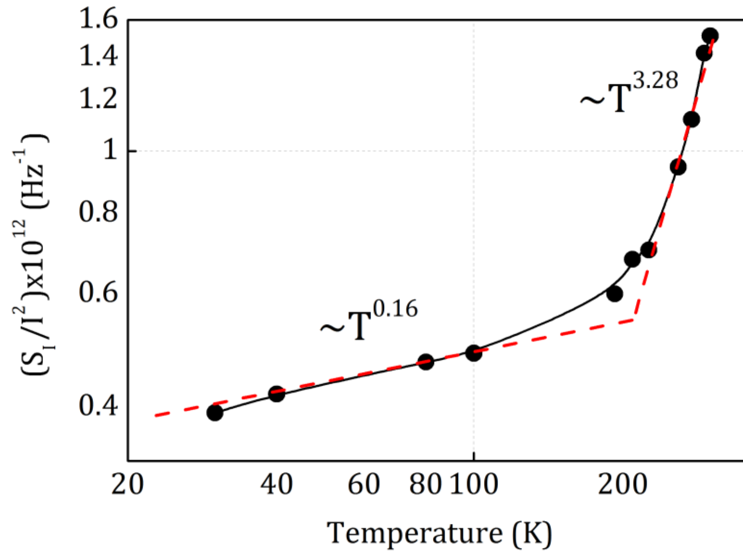

Figure IV.33. Temperature dependence of the normalized current noise on the temperature at *f* = 10Hz. Straight lines correspond to the slope of 0.16 and 3.28.

In conclusion, the results obtained allow us to analyze the mechanisms of conductivity in the system with carbon nanotube bundles and find their correlation with noise characteristics. Three different mechanisms of conductivity are considered depending on temperature. Experimental data show that the transition temperature from hopping conductivity to Luttinger liquid conductivity is about 20K. It should be emphasized that also in this case the noise characteristics display a transition from the value of the logarithmic slope of the current dependence of noise equal to 1 to a value equal to 1.95. The transition region corresponds to the range of temperatures T = (8 - 25) K, which includes the transition temperature from hopping conductivity to Luttinger liquid conductivity.

At higher temperatures, the logarithmic slope increases to a value of about 1.95, while above T = 200 K, the slope is equal to 2. In contrast to relatively weak resistance dependence on temperature, more pronounced changes in the behavior of the transport at T> 200K are registered in the temperature dependence of the normalized current noise. The latter demonstrates a slow increase in the noise level as the temperature increases from T = 20K to T = 215K. At higher temperatures, the noise increases sharply. There is a roughly threefold increase in the range T = 215K to 300K. The temperature of the sharp bend in the temperature dependence of the noise corresponds to the upper temperature of the existence of Luttinger liquid in bundles of carbon nanotubes.

V. TRANSPORT AND NOISE PROPERTIES OF NANOWIRES

1. Noise properties of nanowires

Additionally to the CNTs based devices, we investigated nanowires (NW) based on AlGaN/GaN junction with two dimensional electron gases (2DEG) and based on Au with possibility to decrease the thickness of the wire down to single gold atom by mechanically controlled break junction (MCBJ) technique. The latter allows to produce nanoelectrodes for contacting to a single molecule and to establish some general properties, such as resistance, level and type of noise.

Comparing to CNTs, nanowires as the other materials for producing different type of devices have some advantages and disadvantages. Usually, NWs are processed using optical and e-beam lithographies, therefore they can be placed in precisely controlled directions and positions, which still cannot be done for CNTs. By decreasing the surface-to-volume ratio NWs can rival with the nanotubes but the last are still the first. Using AlGaN/GaN junction it is possible to obtain 2DEG channel or even 1DEG, the mobility of which will be comparable with that one of CNTs.

1.1. Semiconductor AlGaN/GaN nanowires

III-nitride materials are particularly promising for high-sensitivity label-free biosensensor applications[141], chemical and gas detectors[142] due to their unique properties such as low density of the surface states, high drift velocity, high-speed response, and availability of high density two dimensional gas even under undoped conditions that avoid the doping related noise fluctuations in nanodevices. One-dimensional (1D) semiconductor nanowires offer interesting properties different from those of the bulks[143] and additional advantages, since they have an improved surface-to-volume ratio, a predicted enhanced mobility due to the 1D confinement effect, and the possibility of room temperature operation based on quantum effects. Authors of Ref.[144] show that nanowires can be used

for future label-free biosensor development. At the same time the increase in average relative nanowire stability with increasing diameters of the nanowire has been found[145]. As dimensions are scaled down the material properties and underlying physics have to be explored systematically and precisely to utilize the full potential of the unique properties for nano-applications. Noise spectroscopy allows not only to determine information on the signal-to-noise ratio, but also to extract important data concerning the materials properties and monitor dynamical processes with time scale resolution.[88,146] Recently it was showed that the properties of AlGaN/GaN heterostructures with sufficiently large width of the channel of 100μm can be successfully monitored by noise spectra studies.[147]

The high electron mobility transistor structures used in this study were grown on *c*-plane Al_2O_3 substrates by metal organic chemical vapour deposition (MOCVD). The layer structure includes an initial 3μm-thick undoped GaN buffer followed by a 40nm thick unintentionally doped $Al_{0.1}Ga_{0.9}N$ layer. The investigated nanowires were processed from AlGaN/GaN structures using electron beam lithography. Figure V.1 shows a schematic cross section of a set of parallel wires demonstrating the relevant design dimensions. The quantum wire structures were prepared by first defining of Ti etching mask using electron beam lithography and lift-off process. Subsequently, the AlGaN/GaN wires were formed by Ar+ ion beam etching.[148] The scanning electron beam microscopy confirms that 160 identical wires with widths W in the range from 1109 down to 185nm were achieved reproducibly.

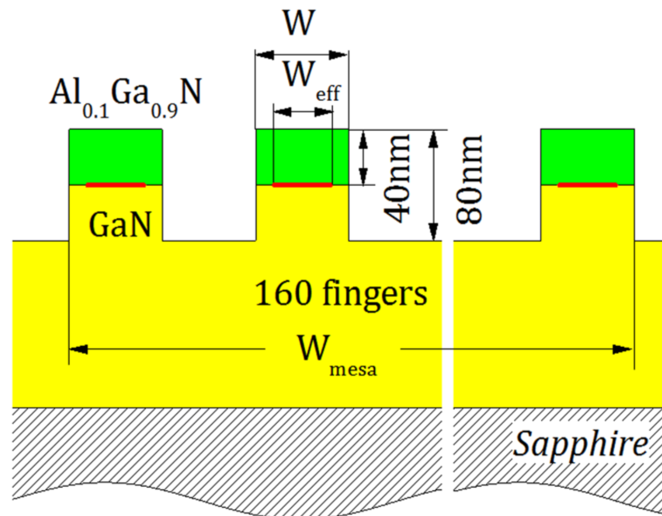

Figure V.1. Schematic cross section of the set of parallel wires demonstrating the relevant design dimensions.

It is known that the fabrication of Ohmic contact to nanowires is more difficult than to large area materials.[142] Therefore to prevent the contribution of the contact resistance in the total resistance of the devices we processed the structure with the long channel length of 620μm. The Ohmic contacts were produced by standard Ti/Al/Ni/Au metallization followed by annealing at 900°C for 30s. I-V characteristics and low-frequency noise spectra were measured in a wide temperature range by cooling down from T=300K to temperatures below liquid-nitrogen temperature. Additionally, ultraviolet excitation was

used to restore trap states after treatment of the structures at a high applied voltage of 20V.

Before the investigation of the NWs, we measured temperature dependences of mobility and carriers concentration of Hall bar structure, produced from the same substrate as the NWs. The result is demonstrated in Figure V.2. The sheet carrier concentration was determined to be 2.2×10^{12} cm^{-2} with a mobility of 1200cm^2/V*s at room temperature. It is important to note that the 2DEG was obtained as a result of the unique polarization induced interface charge in AlGaN/GaN heterostructures without using any doping. Therefore, the lattice scattering as a main mechanism was observed after temperature 100K by analysing the mobility dependence (the phonon energy was found to be ~90meV, which is typical for GaN structures).

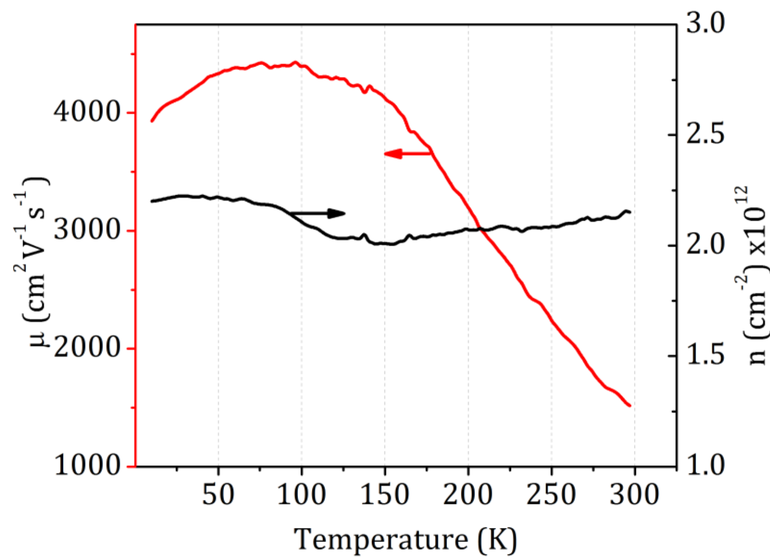

Figure V.2. Mobility (red) and carriers concentration (black) dependences on temperature of Hall bar AlGaN/GaN structure.

The effective conducting width W_{eff} of the wires is expected to be smaller than W due to the large surface potential of GaN and the formation of surface carrier depletion regions at the mesa edges. In order to get information on the W_{eff} of the wires we plotted their conductance extracted from the measured I-V characteristics as a function of different wire widths (Figure V.3). The conductance of single wires was determined by dividing the total conductance by the number of wires connected in parallel.

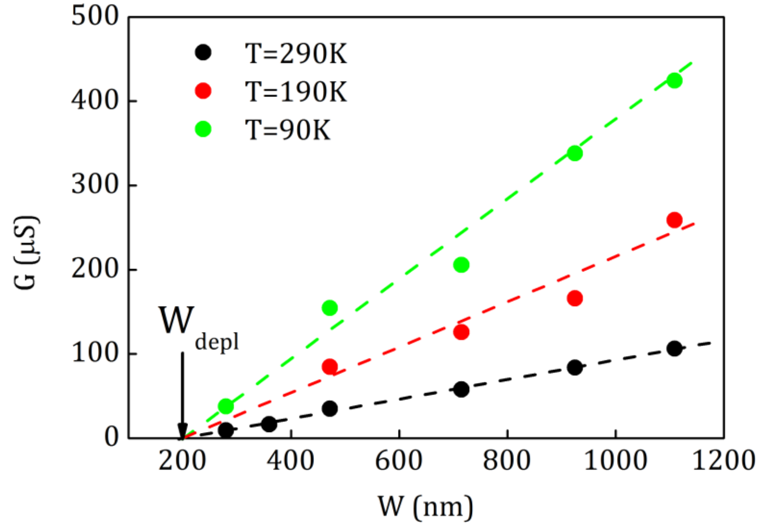

Figure V.3. The conductance of the samples as a function of the geometrical width, *W*, of the wires.

The measured width, *W*, determined using the electron microscope and the effective 2DEG width, W_{eff}, are listed in Table IV.1 for wire samples.

Table V.1. Characteristic widths of AlGaN/GaN structures.

W (nm)	185	280	360	470	715	925	1110
W_{eff} (nm)	-	80	160	270	515	725	910

The calculated potential profile and charge distribution in quantum well are shown in Figure V.4(a) (black and blue line, respectively). As it can be seen, the height of conducting channel of the nanowires is roughly equal to 10nm (the thickness of the blue lined distribution). The concentration of 2DEG is obtained to be n_{2DEG}~3x10^{12} cm^{-2} as the square under blue line. This result is in a good agreement with measured value, which is equal to 2.2x10^{12} cm^{-2} (see above). The charge occupation of the quantum well appeared on the interface is shown in Figure V.4(b).

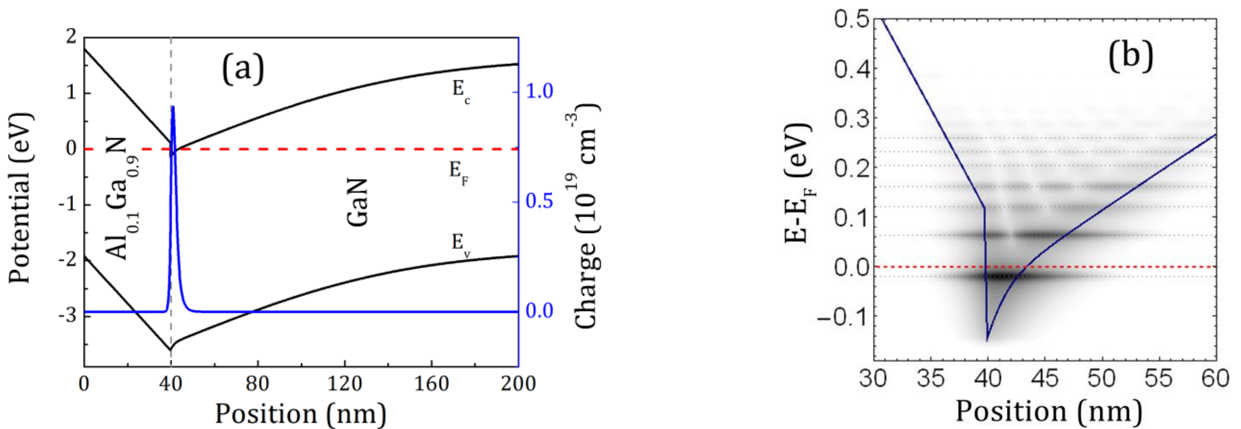

Figure V.4. (a) Energy diagram calculated for AlGaN/GaN heterojunction. Blue line represents the charge distribution of electrons depending on distance from the surface. Red dashed line is the Fermi level. (b) Electron occupation in quantum well on the energy levels (calculated from E_F): -0.02eV, 0.064eV, 0.12eV, 0.162eV, 0.204eV, 0.232eV, 0.26eV, etc.

Current-voltage characteristics of the NWs have linear behaviour in a wide voltage range (Figure V.5). This linear region can be fitted by following equation:

$$I = 160 W_{eff} en\mu V/L, \tag{V.1}$$

where W_{eff} is the effective width of 2DEG; e is the electron charge; n is the concentration and μ is the mobility of electrons (taken from the hall-measurements); V is the applied bias; and L is the length of the wires.

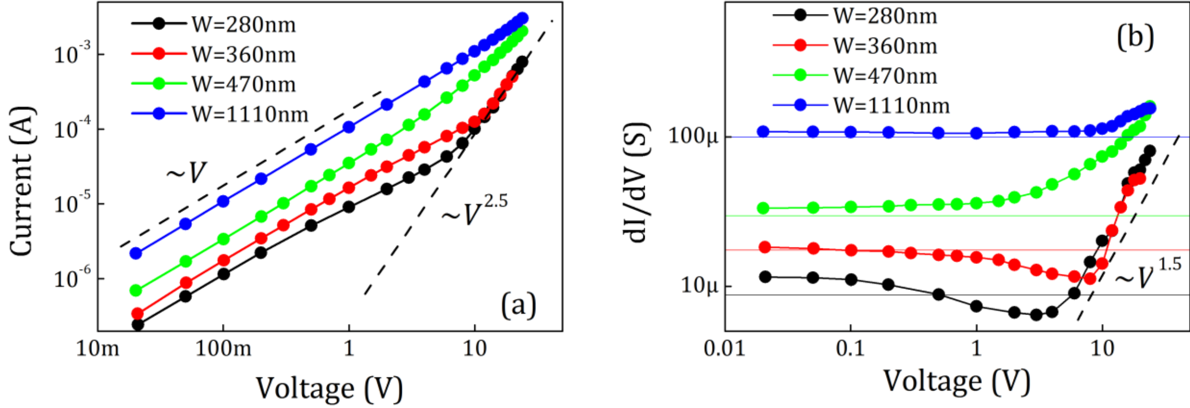

Figure V.5. Current-voltage characteristics (a) and their differentials (b) of the AlGaN/GaN nanowires with different width of the channel measured at room temperature. Thin lines show calculated value using Eq.(V.1).

For the small width samples we also observed a saturation regime of the current starting at bias of approximately 1V, and following by power law current dependence at high voltages. We suppose that the last is caused by leakage current since it was observed even at 185nm-width nanowires, where the 2DEG doesn't appear because of side relaxation effects.

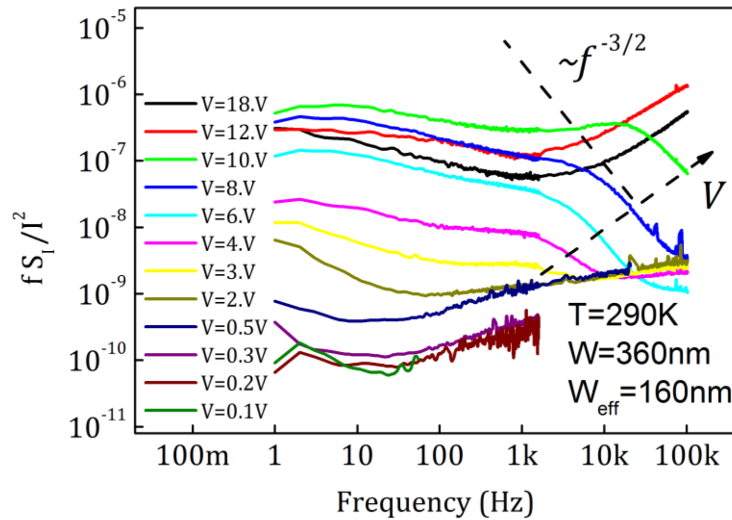

Figure V.6. Normalized noise power spectral density multiplied by frequency, measured for the 360nm sample at T=290K. The unusual GR-noise component was found at high-frequencies. The arrow indicates GR-component increasing with applied voltage.

On the other hand, the measured noise spectra showed that the GR-noise component has power spectrum density dependence on frequency with value of the slope higher than 2. Figure V.6 demonstrates the normalized noise power spectral density measured at different voltages. The total noise was found to be increased with the applied voltages and starting from 3V the unusual GR-like noise component was observed. The characteristic frequency together with its amplitude were shifting with increasing of the voltage. In the coordinates of Figure V.6 the slope is equal to -3/2, which means that the unusual component is relaxation process that has quasi Lorentzian-shaped spectrum (Eq.(I.28)) with the power of 5/2 instead of 2 in the dominator (see Chapter I.2.1). The autocorrelation function of such relaxation process shows the smaller value of correlation between the nearby points in time domain in comparison with autocorrelation function written by Eq.(I.27). This shows that the near-simultaneously occurring events are more independent than in the usual relaxation process. In addition, the autocorrelation function of this process is large than that shown by Eq.(I.27) at times higher than its characteristic time. This shows that any events will influence more on the next events in comparison with processes, which caused the usually observed GR-noise.

We suggest that unusual behaviour of current and noise at high voltages can be related with transport phenomena with participating of several energy levels in the quantum well. The high voltage can transfer the electrons from the lowest to higher states, which will lead to the appearing of a vacancy. This vacancy will be almost immediately filled by the injected electron. Such process can result in the nonstandard GR-noise behaviour and the increasing of the current.

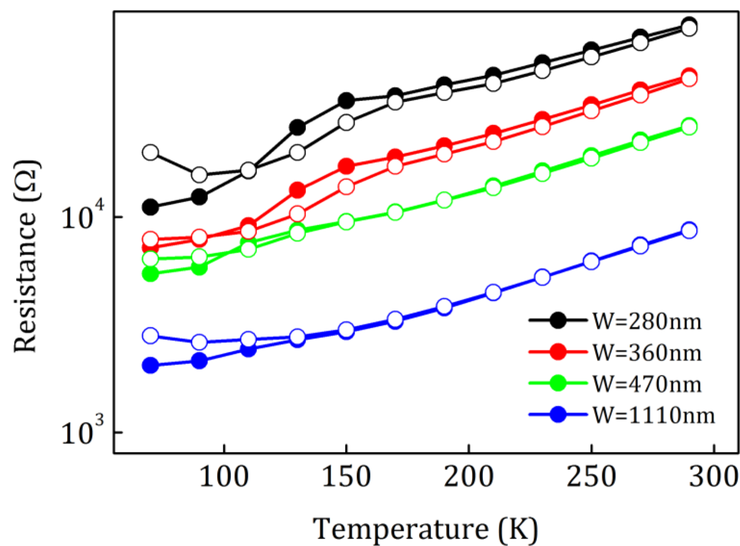

Figure V.7. The resistance of wires in linear region of I-V characteristics dependence on temperature measured after ultraviolet treatment (solid circles) and after treatment of the structures by a high applied voltage of 20V (open circles).

The current-voltage characteristics of the wires with small widths demonstrate nonmonotonic temperature dependence reflecting the charge carrier redistribution in nanoscaled samples. The resistances of the wires with different width measured at linear region of the I-V characteristics dependences on temperature are shown in Figure V.7. The

measurements were performed after the ultraviolet treatment at room temperature and after the applying high voltage of 20V at temperature 70K. The increasing of the resistance was observed after the high-voltage treatment at low temperatures for all samples. This effect is related with the trapping of electrons to metastable states. The states can be made free after the ultraviolet treatment. This can lead to increasing of the scattering processes caused by charged impurities. As can be seen in Figure V.7 , this effect plays a role in small width samples. Because of width comparable or even smaller than the depletion layer the edge effects here can play the crucial role.

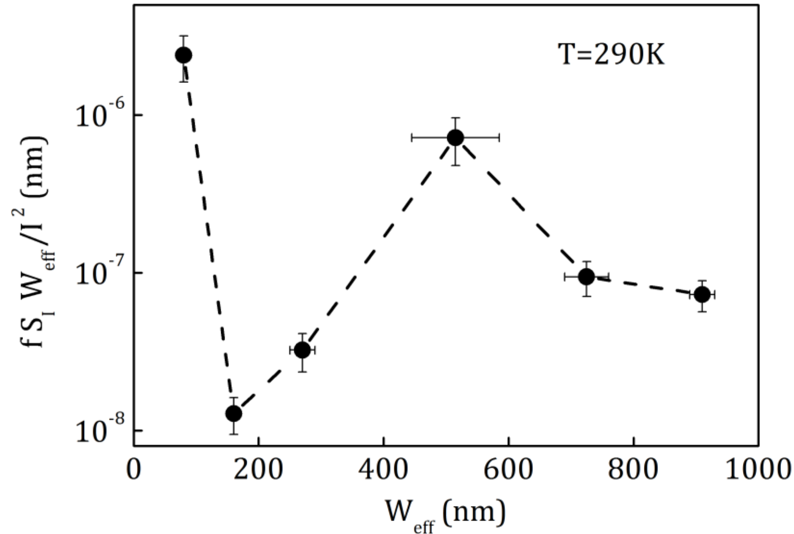

Figure V.8. Normalized current noise power spectral density of the flicker noise component multiplied by effective width of the NW dependence on the effective width.

The measured noise spectra consist of a $1/f^{\alpha}$ noise with $\alpha \sim 1$ and several GR-noise components for structures with several widths scaling down to nanoscale. By comparing the noise spectra density it was found a sample with a specific width which shows the lowest noise level. The sample with 360 nm widths shows lower noise level in comparison with samples with other widths (Figure V.8). Such an effect can be explained by confinement of 2D electron gas due to depletion layers and restricted conductivity to thin channel resulting in increased electron mobility. The Hooge constant for the sample was found to be $\alpha_H \simeq 10^{-4}$ at the linear region of current-voltage characteristic.

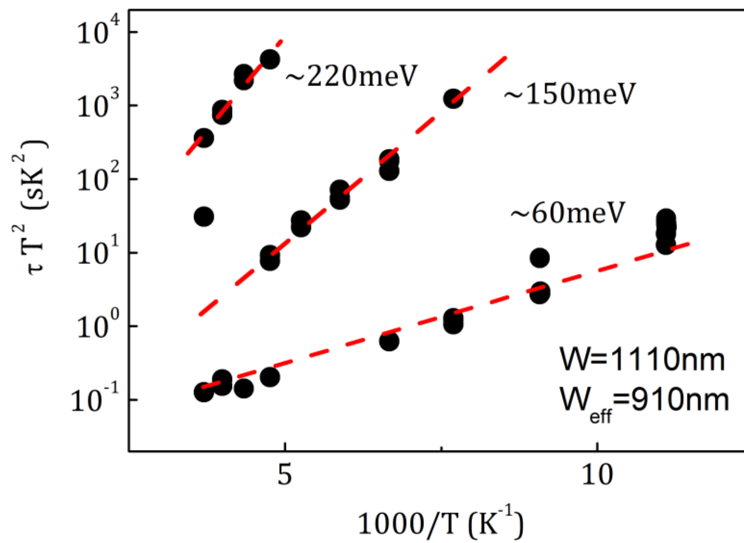

Figure V.9. Typical Arrhenius plots measured for the sample with 910nm effective width in the linear region of the current-voltage characteristic.

Generation-recombination components of the noise were registered in a wide temperature range. The temperature dependence of the spectra allows to use Arrhenius plot to obtain the activation energies of the traps (Figure V.9). The energies were found to be correlated with the band structure of the quantum well. For samples with different width of the NWs we found following energies of the traps (in meV, with error ~15%): 25, 60, 120, 150, 195, 220, 250, 290, and 360. The experimentally obtained values are in good agreement with energy levels in quantum well (Figure V.4(b)). The direct transitions between levels cannot show low-frequency GR-noises, because of the smaller in orders of magnitude the characteristic times of it. The correlation fact can be explained by existing of impurity levels in GaN, which crosses the Fermi level at any temperature. In Figure V.10 we showed the impurity levels, E_{t1} and E_{t2}, which can take a part in generation (red arrows) and recombination (black arrows) processes caused the GR-noise components. Unfortunately, the position of the traps cannot be easy calculated.

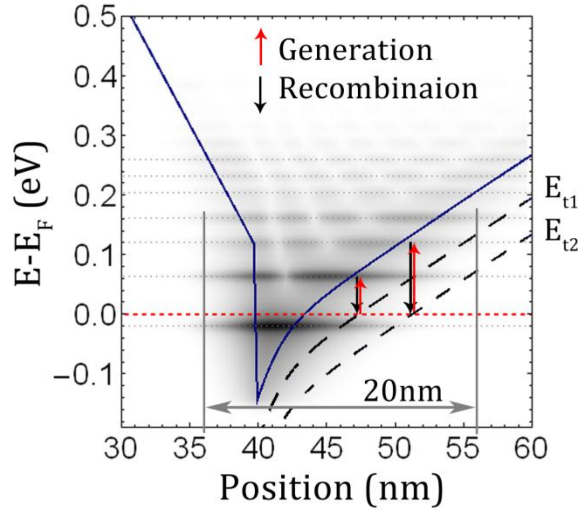

Figure V.10. Electron occupation in quantum well on the energy levels. E_{t1} and E_{t2} are the impurity energy levels. Red arrows show generation and black arrows show recombination of the electrons from and to traps level, respectively.

The same effect we could observe with deep impurities in AlGaN, or with the traps situated on the interface AlGaN/GaN.

To change the characteristics of the nanowires we treat the samples using the gamma-irradiation with dose of 1x10^6 rad, as it was done to the CNT-FETs (shown above). The noise measurements were performed before and after irradiation. Flicker noise component was increased slightly at low temperature range after the treatment. At the same time changes in the GR noise components are stronger.

Figure V.11 shows the influence of the gamma treatment on the one of the GR-noise component with activation energy $E_t = 200$meV for NWs with 725nm effective width. Dashed lines reflect different behaviour on the temperature. Such a behaviour is typical for the bulk material with the GR-centres E_t. This situation is described in Section I.2.2.3 and the obtained dependences on temperature are shown in Table I.3. By fitting the low and high temperature ranges of the amplitude and characteristic times of the GR-noise, following characteristics can be obtained: trapping coefficient of electrons, C_t, concentration of the GR-centres, N_t, and the concentration of shallow centres, N_d. Unfortunately, the exact values was not possible to obtain, because of the worse possibility to fit the normalized noise amplitude at low temperatures (see Figure V.11(b)). We estimate C_t is above 8x10^{-14} cm^{-3}s^{-1} and 6.2x10^{-14} cm^{-3}s^{-1}; N_d lower than 3.6x10^{15} cm^{-3} and 5.3x10^{14} cm^{-3} before and after irradiation, respectively. It should be noted that $N_d > N_t$. We can conclude that either the electrons trapping coefficient of the GR-centres or the number of shallow traps, or both were decreased after the irradiation. Because of small changes of the C_t, most likely, that some shallow states disappeared after the treatment. It can be explained by relaxation processes on the interface AlGaN/GaN.

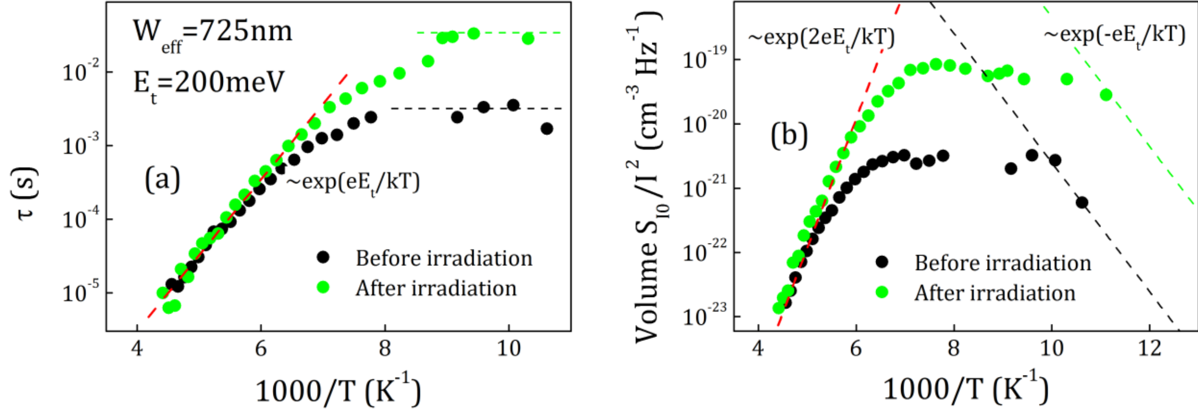

Figure V.11. Results of measurements of 725nm nanowires before and after irradiation. (a) Characteristic time dependence on inversed temperature. The red dashed lines reflect the exponent behavior, from which we can obtain the activation energy, E_t = 200meV, of traps. The green and black dashed lines correspond to independent on temperature range of characteristic times. (b) Temperature dependence of the normalized amplitude of the GR-noise components of the traps multiplied on the effective volume related with the quantum well region. Dashed lines show different exponential dependences on temperature.

In conclusion, we investigated the nanowires based on AlGaN/GaN heterostructure with 10% of Al. Different widths of the nanowires were studied, starting from 1110nm with 2D electron gas down to 185nm with possibility of 1D conductivity. The measured current dependence on width showed the depletion layer of 200nm that is the reason of the decreased effective length of the 2DEG in comparison with processed width. The energy diagram and charge distribution were calculated. The quantum well at the interface of AlGaN/GaN heterostructure contained several energy levels. The lowest of them was almost completely filled by electrons at room temperature. Current-voltage characteristics of the samples showed three regions: linear, saturation and power dependence. The existing of the third region in the I-V characteristic was discussed taking into an account of its correlation with measured noise spectra. Using Hall bar structure we measured the concentration of the electrons in the 2DEG and their mobility (1200cm^{2}s^{-1} at room temperature). The concentrations are in agreement with calculated values. Using the ultraviolet and high-voltage treatments we observed the effect of electrons trapping to deep energy levels. The noise investigations showed that the sample with 360nm width has the lowest noise, which can be explained by the formation of the low noise 1D-conductivite channel, when the depletion layers have no strong influence to the noise properties. The Hooge constant was found to be $\alpha_H \simeq 10^{-4}$. The temperature investigation of the GR-noise components allows to reveal the traps with different activation energies. These energies were correlated with levels in quantum well. The proposed mechanism of the GR-processes considered an existence of the traps states at the interface AlGaN/GaN heterostructure. The analysis of the GR-noise component with 200meV energy for W_{eff} =725nm nanowires revealed in addition to GR-centers the shallow impurities with increased concentration. This concentration was found to be decreased after gamma-irradiation treatment with dose of 1x10^6 rad, which can be explained by the relaxation processes at the interface AlGaN/GaN heterostructure after the treatment.

The obtained results should be taken into account for implementing of the devices based on the AlGaN/GaN heterostructures. To decrease the flicker noise component in these structures the optimized widths have to be used. This allows reducing the scattering effects and increase the mobility of the channel.

1.2. Metallic nanowires, with constriction tuned by mechanically controlled break junction

One of the structures that we have studied is Au based nanowires. Unfortunately, the nanowires were produced by chemical method and therefore we observed only contact noises. The investigation of the channels was impossible. The other technique which allows to produce the nanometers in diameter nanowires but with small lengths is mechanically controlled break junction (MCBJ). Additionally to the investigation of the wires down to one atom chains it allows to study transport properties of the individual molecules by using the metal as a contacts to them.

Theoretical and experimental investigations of charge transport through organic molecules attract increasing attention driven by the interest in fundamental aspects of charge transfer mechanisms and the vision of future applications in molecular electronics. During the past decade, experimental and theoretical advances have yielded significant insights into electron transport in metal-molecule-metal junctions.[149–153] In particular, charge transfer investigations have become feasible for individual molecules by realizing different nanoelectrode configurations where the electrodes are separated by a gap of molecular dimensions.[154–159]

Break junction setups with tunable distance between the nanocontacts, such as scanning tunneling microscopy, atomic force microscopy, or mechanically controllable break junctions (MCBJs), make it possible to control the number of molecules electrically connected in the junction.[159–161] Particularly MCBJs make use of an attenuation factor to control the electrode distance with unique accuracy which allows to investigate noise properties of nanocontacts in different regimes from fully connected to tunneling. The noise characteristics of bare metal break junctions were previously studied in different transport regimes up to break of the MCBJ.[162] It was shown that measured $1/f$ noise had two different power dependences on resistance of junctions corresponding to the transition from diffusive to ballistic transport. Additionally to the $1/f$ noise the random telegraph noise was observed in alkyl-based metal/molecule/metal junctions at high bias voltages and was explained as trapping-detrapping process via localized energy states.[163,164] In the present work, a high-stability break junction device was employed to investigate current behavior and noise characteristics of metal/single-molecule/metal (MSM) junctions at room temperature and low bias voltages. It should be noted that noise spectroscopy allows us to study special features of nanojunction transport which are not accessible by standard current-voltage measurements.[162,165–170] In addition, noise intensity strongly influences the performance and the reliability of molecular electronic devices. The results obtained in this paper demonstrate unusual noise behavior when a single molecule bridges two gold nanoelectrodes.

MCBJ chips under study were fabricated on the basis of spring steel substrates with a length of 44 mm, a width of 12 mm and a thickness of 0.1mm. The typical view and fabrication process are shown in Figure V.12. Five important steps were done to produce a very stable junction (Figure V.12(b)). The first is to deposit an insulating layer. A polyimide (HD-4100, HD Microsystem) about 3 μm thick was spin coated on the substrate. After

baking it at 200°C for 20 minutes, the substrate was annealed for one hour at 300 °C at a pressure of 10^{-3} mbar to improve the stability and structure of the layer. After that, the e-beam lithography process was done. It consists of three separate steps. First, 200 nm of the positive tone resist (PMMA, Polymethylmetacylate 649.04 from ALLRESIST) is spin coated onto the substrate and baked at 180°C for 2 minutes. Second, the electrode pattern is written by means of a Leica Vistec EBPG-5000 plus lithography System. Finally, a standard development procedure is applied by inserting the substrate into development solution (ALLESIST AR 600-55) for about 50 seconds, then the substrate was transferred into 2-propanol to stop the development. After the development, the resist layer serves as a mask for the metal deposition. At this step, 2 nm Ti and 40 nm Au are deposited on the substrate surface in a vacuum chamber by e-beam evaporation. Then, the sample is immersed in acetone for lift off. And in the final step, the polyimide is isotropically dry etched to obtain a suspended metal bridge. This is done by reactive ion etching (RIE) at the following conditions: 32 sccm of oxygen and 8 sccm of CHF_3 and a power of 100 W.

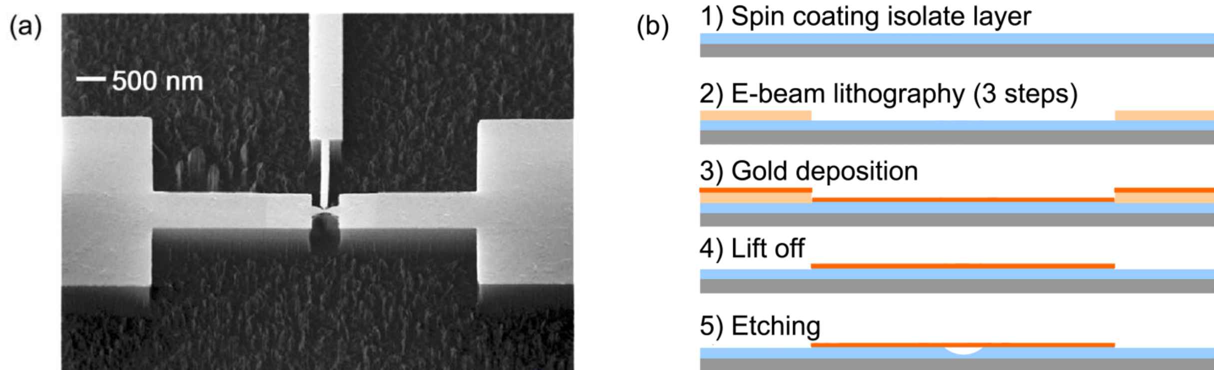

Figure V.12. (a) Scanning electron microscopy (SEM) image of a micro-fabricated MCBJ chip consisting of a freestanding metal bridge, with a central constriction, on top of an insulating spring steel substrate. A nano-gap appeared after the central constriction broke as the push rod applied a force to bend the substrate. (b) Chip fabrication process, which consist of five steps: spin coating isolate layer, e-beam lithography, gold deposition, lift off, etching.

The MCBJ chips were mounted into a home-made three-point bending apparatus. The basic principle of it is next: the two outer posts of the three-point bending apparatus are fixed while the third one functions as a push rod in the Z direction. When the push rod exerts a bending force on the substrate, the movement in the Z direction causes an elongation of the constriction until the bridge breaks resulting in the formation of two separate nanoelectrodes which can be used to contact molecules.

Immediately before the break, the two electrodes are bridged by a few gold atoms. This stage demonstrates a typical discreteness in the junction conductance[155,157,160,171], $G = n\,G_0$, where $G_0 = 2e^2/h$ and n is an integer. It is important that each quantized value of G can be maintained for longer than two minutes in our setup. The latter demonstrates that we have achieved very high mechanical stability.

After breaking the bridge, electron transport occurs due to tunneling processes. The distance between the electrodes (the gap) for both opening and closing operation modes was tuned by bending or relaxing the substrate, respectively. Precision of the gap control is determined by the attenuation factor, r. The attenuation factor is defined by the geometrical

configuration of the system $r = \Delta x / \Delta z = 6ut/L^2$, where Δx is the gap change, Δz is the push rod displacement, u is the length of the suspend bridge, t is the thickness of the steel substrate and L is the length between the two outer posts.[157] For the setup used, an attenuation factor of $r \approx 6\times10^{-6}$ was achieved. This implies that the gap between the electrodes can be controlled, in principle, with sub-angstrom accuracy. A similar value for the attenuation factor was determined from the change of tunneling current as a function of the displacement of the push rod.

The noise characteristics of bare metal break junctions were previously investigated in detail from the diffusive to the ballistic transport regime.[162] We measured MCBJ with molecule as well as without it. Later, the molecule-free nanogap is used as a reference system for molecule-containing junctions. The voltage power noise spectral density measured over a bandwidth from 1Hz to 100kHz at different gap dimensions is shown in Figure V.13. The spectra follow exclusively $1/f^{\alpha}$-noise behavior ($0.9 < \alpha < 1.2$). For relaxed MCBJ and for large gaps, the thermal noise of the nanojunctions dominates the $1/f$-noise.

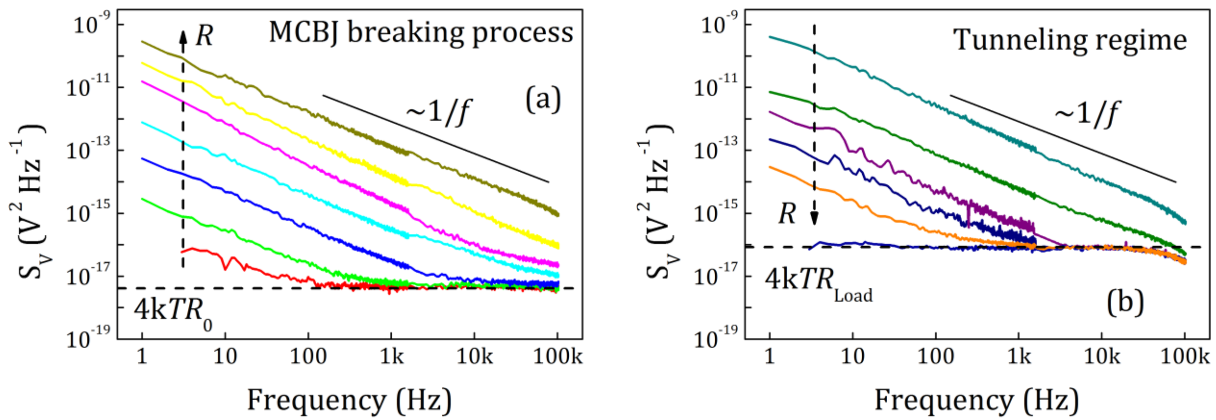

Figure V.13. The voltage noise power spectral density of the junctions (a) in the breaking process and (b) in the tunneling regime. The fixed bias voltage applied to the junction is V_B = 20 mV. The horizontal black line represents the theoretically calculated thermal noise ($4kTR$) for R equal to equivalent resistance of the relaxed MCBJ, R_0~250Ω, (a) and completely open MCBJ (b), when thermal noise is equal to it for load resistance. The spectra show exclusively $1/f^{\alpha}$ ($0.9 \leq \alpha \leq 1.2$) noise behavior.

The normalized current noise power spectral density measured at 1Hz revealed two dependences: the power dependence on resistance during the breaking process and the independence on the resistance in tunneling regime (Figure V.14).

After investigation of noise characteristics of the molecule-free-gap junction, 1,4-Benzenediamine (BDA), a molecule which contains two amine termini as binding groups, was integrated between the nanoelectrodes by a self-assembly process to generate a metal/single-molecule/metal junction. Therefore, a 1 mM ethanolic solution of 1,4-Benzenediamine was prepared in a protective atmosphere where the oxygen level was less than 1 ppm. A 10 μL droplet of this solution was placed on the junction area under nitrogen atmosphere.

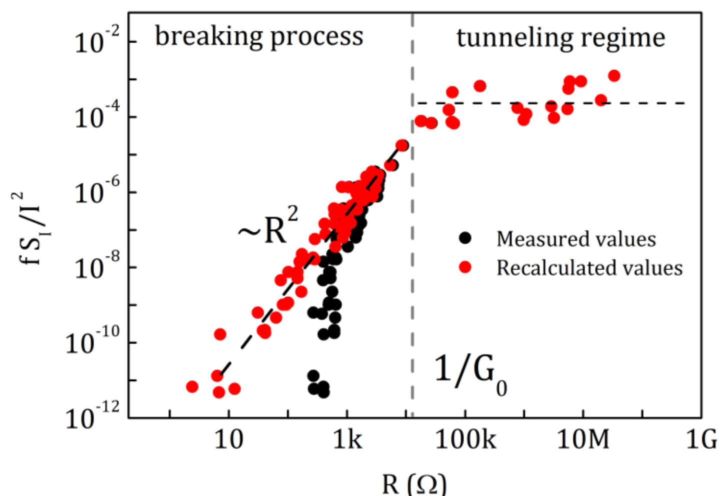

Figure V.14. Normalized current noise power spectral density measured at 1Hz during the breaking process and in the tunneling regime. Recalculation was done by the total resistance minus contact resistance. $G_0 = 2e^2/h$.

The breaking process of the molecule modified nanowire was again followed by monitoring the conductance of the heterojunction. Figure V.15 one can observe the whole breaking process of the metal wire resulting in a sharp drop of the conductance after breaking the metal wire into two separated parts with terminal nanoelectrodes. Due to the two amine groups of BDA, the molecule is able to bind to both nanoelectrodes and a metal-molecules-metal junction is formed. The molecular junction finally transforms into lock-in state which can be assigned to a configuration where the electrode gap is bridged by a single molecule. The conductance of the junction in this device configuration is found to be equal $(6 \pm 1)\times10^{-3}$ G_0. This value corresponds to the conductance of individual BDA molecules bridging the nanogap by establishing bonds to both electrodes.[171,172]

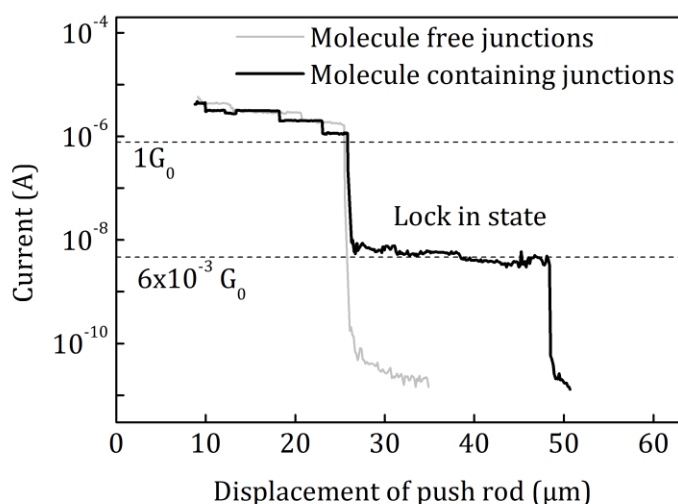

Figure V.15. Representative tunnelling current responses of mechanically controlled break junctions as a function of push rod displacement in the gap opening period with an applied bias of 10mV. In the case of the molecule-containing junction (thick black curve), the current jumps to a lock-in state during the opening period. In the lock-in state, the current is almost independent of the gap size. In

contrast, the lock-in state is absent in the molecule-free junction (thin grey curve). $G_0 = 2e^2/h$. The value $G = 6\times10^{-3}\ G_0$ is a typical conductance for bridged 1,4-Benzenediamine molecule.

Similar lock-in configurations can be obtained when the molecules were applied to the junction in opening operation mode, however with lower yield. In the opening operation mode the gap between the electrodes exceeds the size of the molecule. Under this condition, $1/f$ and thermal noise components were observed, similar to the case of molecule-free junctions. When the gap between the two separated electrodes became equal to the length of the molecule, the tunneling current suddenly jumped to the stable lock-in state, where the current became almost independent of the gap size. The typical plateaus at values below $1G_0$ are absent for molecule free junctions, Figure V.15.

In this lock-in state, with a fixed gap, the noise characteristics were studied at the linear region of current-voltage characteristic with a bias of $V < 0.1$V (see Figure V.16(a)). It should be emphasized that in addition to the $1/f$-noise characteristic for the molecule-free junction, Lorentzian-shaped noise components were revealed for the BDA molecule-bridged nanogap, as shown in Figure V.16(b).

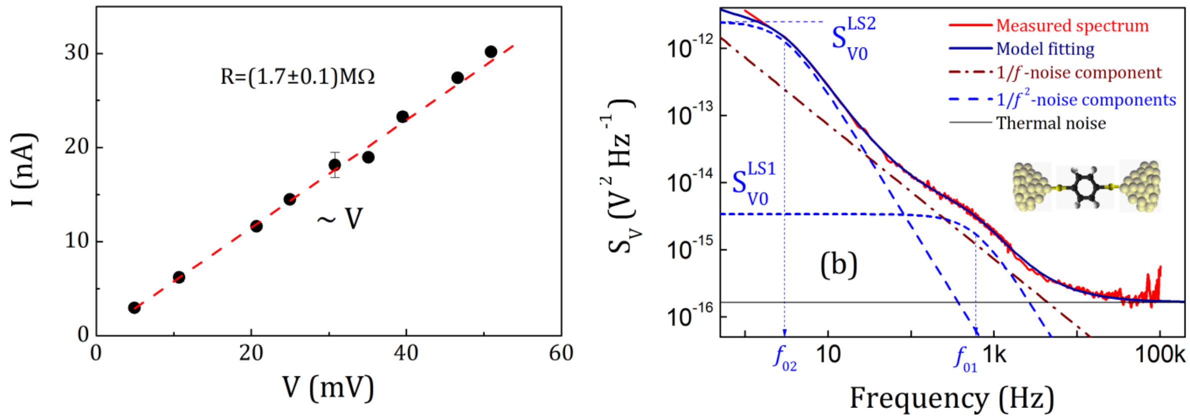

Figure V.16. (a) I-V characteristics of MSM junction recorded in the lock in state at low bias voltages $V < 0.1$ V; (b) The voltage noise power spectral density of the molecule-containing junction in the lock-in state, corresponding to a single BDA molecule bridging two electrodes measured at $V = 45$mV. The solid red curve is the measured noise density and the solid blue curve presents the model fitting. The fitting curve is the superposition of $1/f$, $1/f^2$ and thermal noise components shown by a brown dash-dotted line, blue dashed curves, and thin gray line, respectively.

We measured noise characteristics attributed to charge transfer via individual molecule for stable lock-in state of the current over time. Separating the $1/f$-noise of the gold electrodes and the thermal noise from the whole noise spectrum, we found $1/f^2$ noise components that are specifically inherent in a single bridging molecule.

For the flicker noise component, we found that the noise spectral density scales quadratically with the current in both molecule-free and molecule-containing junctions. For the Lorentzian-shaped noise component, linear dependence of the noise spectral density and the characteristic frequency on current were observed. The results are shown in Figure V.17.

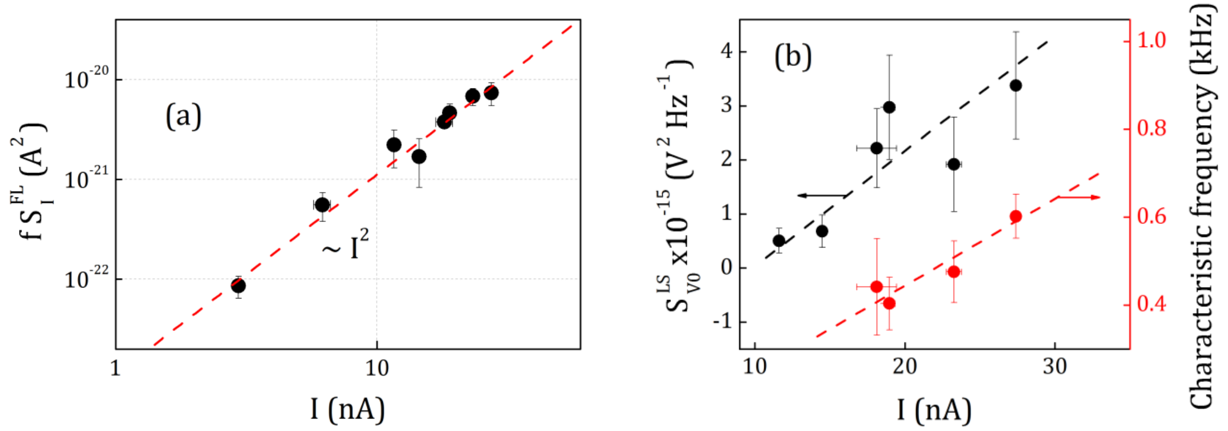

Figure V.17. (a) The measured at f = 1Hz normalized power noise spectral density of the flicker noise component, fS_I^{FL}, has a quadratic dependence on current in molecule-containing as well as in molecule-free junctions; (b) Both the plateaus of Lorentzian-shape noise component, S_{V0}^{LS}, and the characteristic frequencies, f_0, of both Lorentzian-shape noise component linearly depend on current. Results are shown for a 1,4-Benzenediamine molecule bridging the nanogap of MCBJ at fixed gap size between two nanoelectrodes.

We propose a phenomenological model that correlates the charge transport via a single molecule with reconfiguration of its coupling to the metal electrodes. It is well known that $1/f^2$ noise may appear in mesoscopic structures, for example in field-effect transistors with submicron gate area.[173] This kind of the noise is generated due to random processes of electron trapping/detrapping by a single defect. This mechanism is not likely to be applied to the case of a single molecule bridging the nanocontacts.[163] We suggest that the $1/f^2$ noise components recorded in the low-bias regime with low values of the characteristic frequencies f_0 can be understood as a result of a dynamic reconfiguration of molecular coupling to the metal electrodes.[174–177]

We start with discussion of the surprising fact of small frequencies of the observed $1/f^2$ noises. All existing times characterizing the motion of the electrons and nuclei in a molecule and metal contacts under equilibrium, as well as relaxation times in contacts, are smaller by many orders of magnitude than the characteristic noise times ($\sim 1/f_0$) recorded. We assume that large values of the characteristic noise times are related to non-equilibrium processes in the molecules induced by low currents. These processes can be considered as follows. When current flows through a molecule, the electron subsystem of the latter becomes polarized. The processes induce *small* structural/configuration changes. The charge transfer and structural/configuration changes are coupled. Small currents determine the smallness of the forces inducing the changes and, thus, large characteristic times of these changes. Let $X(t)$ is the configuration coordinate, generally dependent on time t. The junction resistance is taken to be a function of X: $R = R[X(t)]$. Then, fluctuations of X lead to changes in the resistance: $\Delta R(t) = (\mathrm{d}R/\mathrm{d}X)\, \Delta X(t)$. Assuming the current J is constant, then fluctuations of the voltage V is $\Delta V(t) = J\, \Delta R(t)$. In the frequency domain, the spectral density of voltage fluctuations is $S_V(f) = (\Delta V)_f^{\,2} = J^2\, (\Delta R)_f^{\,2}$.

To write an equation for $X(t)$, the phenomenological approach developed by L.D. Landau et al. can be taken.[178] This approach is based on the existence of a system with two sets of strongly distinct characteristic times: due to short relaxation times the system

reaches so-called "incomplete equilibrium", then it slowly ("quasistationary") relaxes during a longer period of time. The Lorentz fluctuator can be introduced for this situation. According to the above analysis, the system under consideration possesses very distinct characteristic times and we can apply the approach of L.D. Landau et al.[178] and introduce the following equation for the configuration coordinate, $X(t)$,

$$\frac{\mathrm{d}X}{\mathrm{d}t} - \lambda X = \xi(t). \tag{V.2}$$

Here, λ (>0) describes the slow relaxation of X, $\xi(t)$ is a "random force", the correlator which is proportional to λ, $<\xi(0)\,\xi(t)> = 2\,\lambda <X^2> \delta\,(t)$ with $<X^2>$ being total thermal fluctuation of the quantity X. From these equations we readily obtain the spectral density of voltage fluctuations in the Lorentz form:

$$S_V(f) = 2J^2\left(\frac{dR}{dX}\right)^2 \frac{< X^2 >}{\pi f_0} \frac{1}{1+\left(\frac{f}{f_0}\right)^2} = \frac{B}{1+\left(\frac{f}{f_0}\right)^2}. \tag{V.3}$$

where $f_0 = \lambda / (2\pi)$. Since non-equilibrium processes (i.e. currents) are responsible for the long times and λ describes the rate of relaxation, we can assume that λ is proportional to J. The proposed model predicts that $f_0\, S_V(f) \sim J^2$. Experimental results (Figure V.17(b)) are in good agreement with these theoretical predictions.

To conclude, we measured and compared the electronic noise of molecule-free and single-molecule-containing mechanically controlled break junctions. Both junctions revealed typical $1/f$ noise characteristics. An additional $1/f^2$ noise component was clearly observed only in junctions when a single molecule bridged the nanoelectrodes. The recorded $1/f^2$ electric noise components in the case of a single bridging molecule are interpreted as a manifestation of a dynamic reconfiguration of molecular coupling to the metal electrodes during current flow. The reconfiguration changes occur without complete bond breaking and involve near-configuration states with very similar electric properties. Using the fact of the existence of strongly distinct characteristic times in the system, we developed a phenomenological model that relates the charge transfer via a single molecule with its reconfiguration and describes the $1/f^2$ noise behavior of a single molecule. The $1/f^2$ noise component found can be used to study quantitative properties of individual electrically addressed molecules. The results should be taken into account for the development of molecular electronics.

2. Nanowires noise properties compared with SWCNT based structures

We showed the results obtained for different type of CNT devices, such as for individual SWCNT-FETs, multiple SWCNTs-FETs and CNT bundles. As carbon nanotubes has quasi-1D transport in comparison with other materials we used nanowires (NW), fabricated on the basis of AlGaN/GaN nanowires and Au wires with constriction tuned by

mechanically controlled break junction. The 2D electron gas (2DEG) forms at the interface of AlGaN/GaN heterostructure induced by piezoelectric fields and spontaneous polarizations. By decreasing the width of the structure we can achieve 1D transport with increased electron mobility comparable with that in CNTs. Therefore, this represents of one of the ways creation the structure that will be comparable with the nanotubes.

On the other hand, using usual materials, such as gold, silicon, etc. by decreasing their dimensions, it is possible to create the few-atomic width and height NWs-based devices. But any defects of such a structure will increase the electron scattering, i.e. decrease the mobility. This demands using the semiconductor materials without any doping. In this case the value of free charges will be very low and therefore the total noise can be quite large.

One of the interesting approaches is the obtaining 1D transport in mechanically controlled break junction (MCBJ). It is metallic nanowire that breaks under the bending process. After its break the nanoelectrodes are formed that can be used for the connecting of different molecules. Using such a technique we can obtain molecular devices or devices based on few metal atoms.

For comparison of the noise characteristics of different devices we can use the dimensionless Hooge parameter as a value related with level of flicker noise, as well as obtained activation energies of traps, and temperature behavior characteristic for definite types of transport at different temperature, applied voltage, etc.

For individual SWCNT-FETs we obtained the Hooge constant of α_H=3.8x10^{-2}. Such value of the parameter is explained by the strong influence of the Schottky barriers to the transport and noise at gate voltages from -1V to 0V. The value estimated for multiple SWCNT-FETs is comparable (3.8x10^{-3}) with usually obtained value for different materials of 2x10^{-3}. AlGaN/GaN nanowires showed dependence of the Hooge constant on width of the wires. The lowest value was obtained to be ~10^{-4} for the 160nm effective width. Here, the 2DEG starting to be quantized with width forming quasi-1D channel, and therefore decreasing the scattering effects which may lead to increased mobility and low value of noise. Devices with Au break junction also showed that the Hooge constant is dependent on width. In the width, when one or several gold atoms are connected, the constant α_H is equal to ~2x10^{-4}. For such type of devices the flicker noise is related with modulating of the tunneling current with reorganization of the gold atoms on the surfaces between contacts. Therefore, the small value of Hooge constant can be explained by the existence of different channels of the tunneling processes.

Concerning the GR-noises of different materials, in CNT-based devices and AlGaN/GaN–based nanowires additionally to GR-centers with energies of several hundreds meV we found the shallow impurities. In the case of CNT-FETs we obtained the exact values of energies of the impurities. For the case of heterojunction the noise spectroscopy allows to scan the energy diagram of the quantum well.

The Lorentzian-shaped noise component is observed in the noise spectra of MCBJ under study. In the time domain it shows the radio-telegraph signal (RTS) noise component, which indicated two metastable levels in the system. Such a behavior is observed when the last chains of gold atoms break or when the molecules were connected

to the electrodes. Therefore, we suppose that RTS-noise of MCBJ is directly related to the molecule characteristic properties.

VI. SUMMARY AND OUTLOOK

1. Summary

In this thesis, we show that noise spectroscopy can be used to study transport properties in advanced devices, especially at nanoscale.

The individual carbon nanotube (CNT) field-effect transistors (FETs) with top, side and back gate topographies are investigated before and after gamma radiation treatment. It is demonstrated that the transport characteristics are improved after gamma-irradiation treatment with small dose of $1x10^6$ rad. The analysis of flicker noise component allows to reveal the FET operation regimes, where the noise properties are related with the fluctuations in channel conductivity and fluctuations in the Schottky barrier regions, respectively. The FETs demonstrate stable properties that are promising for biosensors applications. The decreasing of the channel noise was registered after the gamma treatment. This fact was explained by increasing the number of carriers in the channel due to rearrangements of native defects in the structure. The analysis of Lorentzian-shaped noise components allows us to find the energy of traps near the interfaces CNT/SiO_2 and CNT/Al_2O_3. The obtained data are listed in Table IV.2. Their traps concentration was found to be higher than the concentration of carriers in the CNT channel. The number of carriers in the working point with maximum transconductance of FETs was found to be no more than 320. The detailed analysis of the flicker noise component allows to obtain information about the influence of the gate voltage not only on the channel region, but also on the contacts ones. The analysis of flicker noise related with fluctuations in Schottky barrier regions showed stronger influence of side and back gates compared to top gate. Such a behaviour is explained by increased influence of potential field on the contact regions taking into account the side or back gates geometry of the FETs. The flicker noise component related with channel shows characteristic temperature dependence related with traps-assisted scattering mechanism in whole measured temperature range. The estimatimated mobility values at 200K were found to be $4100cm^2V^{-1}s^{-1}$ that demonstrated advanced quality of CNT-FET devices.

Our analysis of multiple SWCNT-FETs shows that the difference in output characteristics of the FETs before and after small doses of gamma radiation treatment is due to a reduced contribution of parasitic channel to the total current parallel to the nanotube resistance. The transconductance of the CNT-FETs and level of noise did not change strongly after γ-irradiation at doses of 1×10^6 and 2×10^6 rad. The results show that active γ-radiation treatment can improve the transport and noise properties of CNT-FETs at some small optimal dose. The radiation treatment was found to decrease the influence of parasitic conduction channels on dc characteristics of the device. The Hooge parameters obtained are comparable with typical values reported for conventional semiconductors.

The results obtained on bundles CNTs allow us to analyze the mechanisms of conductivity in the system with carbon nanotube bundles and find their correlation with noise characteristics. Three different mechanisms of conductivity are considered depending on temperature. Experimental data show that the transition temperature from hopping conductivity to Luttinger liquid conductivity is about 20K. It should be emphasized that also in this case the noise characteristics display a transition from the value of the logarithmic slope of the current dependence of noise equal to 1 to a value equal to 1.95. The transition region corresponds to the range of temperatures T = (8 - 25) K, which includes the transition temperature from hopping conductivity to Luttinger liquid conductivity.

At higher temperatures, the logarithmic slope increases to a value of about 1.95, while above T = 200 K, the slope is equal to 2. In contrast to relatively weak resistance dependence on temperature, more pronounced changes in the behavior of the transport at T> 200 K are registered in the temperature dependence of the normalized current noise. The latter demonstrates a slow increase in the noise level as the temperature increases from T = 20 K to T = 215 K. At higher temperatures, the noise increases sharply. There is a roughly threefold increase in the range T = 215 K to 300 K. The temperature of the sharp change in behavior of the temperature dependence of the noise corresponds to the upper temperature of the existence of Luttinger liquid in bundles of carbon nanotubes.

The nanowires based on AlGaN/GaN heterostructure with 10% of Al were investigated and compared with CNT-based devices. The nanowires with different widths were studied, starting from 1110nm with 2D electron gas down to 185nm with 1D conductivity. The measured current dependence on width showed the depletion layer of 200nm that is the reason of the decreased effective length of the 2DEG in comparison with processed width. The energy potential and profile charge distribution were calculated. The quantum well at the interface of AlGaN/GaN heterostructure contained several energy levels. The lowest of them was almost completely filled by electrons at room temperature. Current-voltage characteristics of the samples contain three regions: linear, saturation and power dependence. The regions on the I-V characteristic correlate with the behavior of the measured noise spectra. Using Hall bar structure we measured the concentration of the electrons in the 2DEG and their mobility ($1200 cm^2 s^{-1}$ at room temperature). The measured concentration was perfectly correlated with calculated values. Using the ultraviolet and

high-voltage treatments we observed the effect of electrons trapping to deep energy traps. The noise investigation at room temperature showed that the sample with 360nm width has the lowest noise. This was explained by the formation of the low noise 1D-conductivite channel, when the depletion layers have no strong influence to the noise properties. The Hooge constant was found to be $\alpha_H \simeq 10^{-4}$. The temperature investigation of the GR-noise components allows to reveal the traps with different activation energies. These energies correlate with energy levels in quantum well. The proposed mechanism of the GR-processes is related to trapping/detrapping processes with participation of the trap states near the interface of AlGaN/GaN heterostructure. The further analysis of the GR-noise component with 200meV energy for W_{eff} =725nm nanowires revealed in addition to GR-centers the shallow impurities with concentration higher than the centers. This concentration was found to be decreased after gamma-irradiation treatment with dose of $1x10^6$ rad, which explained by the relaxation processes at the interface of AlGaN/GaN herostructure after the treatment.

We measured and compared the electronic noise of molecule-free and single-molecule-containing mechanically controllable break junctions. Both junctions revealed typical $1/f$ noise characteristics. An additional $1/f^2$ noise component was clearly observed only in MSM junctions when a single molecule bridged the nanoelectrodes. The recorded $1/f^2$ electric noise components relative to a single bridging molecule are interpreted as a manifestation of a dynamic reconfiguration of molecular coupling to the metal electrodes during current flow. The reconfiguration changes occur without complete bond breaking and involve near-configuration states with very similar electric properties. Using the fact of the existence of strongly distinct characteristic times in the system, we developed a phenomenological model that relates the charge transfer via a single molecule with its reconfiguration. The model describes very well the $1/f^2$ noise behavior of a single molecule. The $1/f^2$ noise component found can be used to study quantitative properties of individual electrically addressed molecules.

The high values of the obtained mobility in the case of CNT-FETs and AlGaN/GaN nanowires are characteristic of high-speed transport, and demonstrate promising perspectives for high-speed sensors applications.

2. Future work

As was discussed above, the fabrication technology of carbon nanotube (CNT) based devices was developed, however, their properties still can be improved in term of stabilities and performance.

The variations of the diameter of nanotubes can give information concerning the best surface to volume ratio for sensing application. Here the growing process is important, where the size of obtained nanotubes directly depends on catalytic particles and on the atmosphere. Therefore, it is important to optimize the growth process of nanotubes.

In this thesis we used two dielectric materials for CNT field-effect transistors (FETs), such as SiO_2 and Al_2O_3. The noise properties of the devices were found to be dependent on them. Therefore, it is important to analyze the FETs with other materials and even to use the suspended nanotubes.

We showed the influence of Schottky contacts to the transport properties of CNT-FETs. The dependences on gate voltage were shown for different gate topographies. Here it is important to investigate the dependence of the influence to the barrier regions on the gate size and on the dielectric thickness using one of the presented topographies. This will help to optimize the topographies and to obtain the conditions when Schottky barriers have the lowest role in transport and noise properties of the FETs.

During this work we started to test the CNT-FETs as a sensor of alcoholic liquids. We obtained the sensitive level of 0.2mM/L, which is not the best for today. We didn't present the data here, but it should to be improved by using different topographies and functionalization of nanotubes. In the future, the measurements with different concentration of the biomolecules need to be performed to develop high-sensitive chemical and biological sensors.

Bibliography

1. Moore, G.E. Cramming More Components Onto Integrated Circuits. *Proceedings of the IEEE* **86**, 82-85 (1998).
2. Leaked Intel Roadmap Reveals 10nm Process In 2018. *www.expreview.com* (2011).at <http://en.expreview.com/2011/07/26/leaked-intel-roadmap-reveals-10nm-process-in-2018/18466.html>
3. Carbon nanotube. *www.wikipedia.org* at <http://en.wikipedia.org/wiki/Carbon_nanotube>
4. Wang, X. *et al.* Fabrication of ultralong and electrically uniform single-walled carbon nanotubes on clean substrates. *Nano letters* **9**, 3137-41 (2009).
5. Радушкувич, Л.В. & Лукьянович, В.М. О структуре углерода, образующегося при термическом разложении окиси углерода на железном контакте. *Журнал Физической Химии* **26**, 88-95 (1952).
6. Iijima, S. Helical microtubules of graphitic carbon. *Nature* **354**, 56-58 (1991).
7. Krätschmer, W., Lamb, L.D., Fostiropoulos, K. & Huffman, D.R. Solid C60: a new form of carbon. *Nature* **347**, 354-358 (1990).
8. Mintmire, J.W., Dunlap, B.I. & White, C.T. Are fullerene tubules metallic? *Physical Review Letters* **68**, 631-634 (1992).
9. Komarov, F.F. & Mironov, A.M. Carbon Nanotubes : Present and Future. *Physics and Chemistry of Solid State* **5**, 411-429 (2004).
10. Reich, S., Thomsen, C. & Maultzsch, J. *Carbon nanotubes: basic concepts and physical properties*. 215 (Wiley-VCH Verlag GmbH & Co. KGaA: 2004).
11. Qin, L.C. *et al.* The smallest carbon nanotube. *Nature* **408**, 50 (2000).
12. Guan, L., Suenaga, K. & Iijima, S. Smallest carbon nanotube assigned with atomic resolution accuracy. *Nano Letters* **8**, 459-62 (2008).
13. Hamada, N., Sawada, S. & Oshiyama, A. New one-dimensional conductors: Graphitic microtubules. *Physical Review Letters* **68**, 1579-1581 (1992).
14. Saito, R., Fujita, M., Dresselhaus, G. & Dresselhaus, M. Electronic structure of graphene tubules based on C60. *Physical Review B* **46**, 1804-1811 (1992).
15. Reich, S., Maultzsch, J., Thomsen, C. & Ordejón, P. Tight-binding description of graphene. *Physical Review B* **66**, 035412 (2002).
16. Kataura, H. *et al.* Optical properties of single-wall carbon nanotubes. *Synthetic Metals* **103**, 2555-2558 (1999).
17. Dresselhaus, M.S., Dresselhaus, G. & Eklund, P.C. *Science of fullerenes and carbon nanotubes*. **965**, 965 (Academic Press: 1996).
18. Odom, T.W., Huang, J.L., Kim, P. & Lieber, C.M. Atomic structure and electronic properties of single-walled carbon nanotubes. *Nature* **391**, 62–64 (1998).
19. Wildoer, J.W.G., Venema, L.C., Rinzler, A.G., Smalley, R.E. & Dekker, C. Electronic structure of atomically resolved carbon nanotubes. *Nature* **391**, 59–62 (1998).
20. Kleiner, A. & Eggert, S. Curvature, hybridization, and STM images of carbon nanotubes. *Physical Review B* **64**, 113402 (2001).
21. Park, C.-J., Kim, Y.-H. & Chang, K. Band-gap modification by radial deformation in carbon nanotubes. *Physical Review B* **60**, 10656-10659 (1999).
22. Mazzoni, M.S.C. & Chacham, H. Bandgap closure of a flattened semiconductor carbon nanotube: A first-principles study. *Applied Physics Letters* **76**, 1561-1563 (2000).
23. Lammert, P.E., Zhang, P. & Crespi, V.H. Gapping by squashing: Metal-insulator and insulator-metal transitions in collapsed carbon nanotubes. *Physical Review Letters* **84**, 2453–2456 (2000).
24. Ren, Y., Chen, K.-Q., Wan, Q., Zou, B.S. & Zhang, Y. Transitions between semiconductor and metal induced by mixed deformation in carbon nanotube devices. *Applied Physics Letters* **94**, 183506 (2009).
25. Barboza, A. *et al.* Deformation Induced Semiconductor-Metal Transition in Single Wall Carbon Nanotubes Probed by Electric Force Microscopy. *Physical Review Letters* **100**, 256804 (2008).

26. Ebbesen, T.W. & Ajayan, P.M. Large-scale synthesis of carbon nanotubes. *Nature* **358**, 220-222 (1992).
27. Gamaly, E. & Ebbesen, T. Mechanism of carbon nanotube formation in the arc discharge. *Physical Review B* **52**, 2083-2089 (1995).
28. Journet, C. *et al.* Large-scale production of single-walled carbon nanotubes by the electric-arc technique. *Nature* **388**, 756-758 (1997).
29. Guo, T., Nikolaev, P., Thess, A., Colbert, D.T. & Smalley, R.E. Catalytic growth of single-walled manotubes by laser vaporization. *Chemical Physics Letters* **243**, 49–54 (1995).
30. Thess, A. *et al.* Crystalline Ropes of Metallic Carbon Nanotubes. *Science* **273**, 483-487 (1996).
31. Maser, W.K. *et al.* Production of high-density single-walled nanotube material by a simple laser-ablation method. *Chemical Physics Letters* **292**, 587–593 (1998).
32. Yudasaka, M. *et al.* Causes of different catalytic activities of metals in formation of single-wall carbon nanotubes. *Applied Physics A: Materials Science & Processing* **74**, 377-385 (2002).
33. José-Yacamán, M., Miki-Yoshida, M., Rendón, L. & Santiesteban, J.G. Catalytic growth of carbon microtubules with fullerene structure. *Applied Physics Letters* **62**, 657 (1993).
34. Wei, B. *et al.* Structural Characterizations of Long Single-Walled Carbon Nanotube Strands. *Nano Letters* **2**, 1105-1107 (2002).
35. Zhu, H.W. *et al.* Direct synthesis of long single-walled carbon nanotube strands. *Science (New York, N.Y.)* **296**, 884-886 (2002).
36. Hata, K. *et al.* Water-assisted highly efficient synthesis of impurity-free single-walled carbon nanotubes. *Science (New York, N.Y.)* **306**, 1362-1364 (2004).
37. Gruner, G. Carbon nanotube transistors for biosensing applications. *Analytical and Bioanalytical Chemistry* **384**, 322-335 (2006).
38. Tans, S.J., Verschueren, A.R.M. & Dekker, C. Room-temperature transistor based on a single carbon nanotube. *Nature* **393**, 49-52 (1998).
39. Buonocore, F. *et al.* Ab initio calculations of electron affinity and ionization potential of carbon nanotubes. *Nanotechnology* **19**, 025711 (2008).
40. Javey, A., Wang, Q., Kim, W. & Dai, H. Advancements in complementary carbon nanotube field-effect transistors. *IEEE International Electron Devices Meeting 2003* **00**, 31.2.1-31.2.4 (2003).
41. Chen, Z., Appenzeller, J., Knoch, J., Lin, Y. & Avouris, P. The role of metal-nanotube contact in the performance of carbon nanotube field-effect transistors. *Nano Letters* **5**, 1497-1502 (2005).
42. Bachtold, A., Hadley, P., Nakanishi, T. & Dekker, C. Logic circuits with carbon nanotube transistors. *Science (New York, N.Y.)* **294**, 1317-1320 (2001).
43. Franklin, A.D., Lin, A. & Wong, H.-S.P. Current Scaling in Aligned Carbon Nanotube Array Transistors With Local Bottom Gating. *IEEE Electron Device Letters* **31**, 644-646 (2010).
44. Franklin, A.D., Tulevski, G., Hannon, J.B. & Chen, Z. Can carbon nanotube transistors be scaled without performance degradation? *2009 IEEE International Electron Devices Meeting (IEDM)* 1-4 (2009).doi:10.1109/IEDM.2009.5424296
45. Wind, S.J., Appenzeller, J., Martel, R., Derycke, V. & Avouris, P. Vertical scaling of carbon nanotube field-effect transistors using top gate electrodes. *Applied Physics Letters* **80**, 3817-3819 (2002).
46. Javey, A. *et al.* Self-Aligned Ballistic Molecular Transistors and Electrically Parallel Nanotube Arrays. *Nano Letters* **4**, 1319-1322 (2004).
47. Chen, Z., Farmer, D., Xu, S., Gordon, R. & Avouris, P. Externally Assembled Gate-All-Around Carbon Nanotube Field-Effect Transistor. *IEEE Electron Device Letters* **29**, 183-185 (2008).
48. Farmer, D.B. & Gordon, R.G. Atomic layer deposition on suspended single-walled carbon nanotubes via gas-phase noncovalent functionalization. *Nano Letters* **6**, 699-703 (2006).
49. Robinson, L.A.W. *et al.* Fabrication of self-aligned side gates to carbon nanotubes. *Nanotechnology* **14**, 290-293 (2003).
50. Lu, F. *et al.* Advances in Bioapplications of Carbon Nanotubes. *Advanced Materials* **21**, 139-152 (2009).
51. Besteman, K., Lee, J.-O., Wiertz, F.G.M., Heering, H.A. & Dekker, C. Enzyme-Coated Carbon Nanotubes as Single-Molecule Biosensors. *Nano Letters* **3**, 727-730 (2003).

52. Byon, H.R. & Choi, H.C. Network single-walled carbon nanotube-field effect transistors (SWNT-FETs) with increased Schottky contact area for highly sensitive biosensor applications. *Journal of the American Chemical Society* **128**, 2188-2189 (2006).
53. Chen, R.J. *et al.* An investigation of the mechanisms of electronic sensing of protein adsorption on carbon nanotube devices. *Journal of the American Chemical Society* **126**, 1563-1568 (2004).
54. Li, C. *et al.* Complementary detection of prostate-specific antigen using In2O3 nanowires and carbon nanotubes. *Journal of the American Chemical Society* **127**, 12484-12485 (2005).
55. Maehashi, K. *et al.* Label-free protein biosensor based on aptamer-modified carbon nanotube field-effect transistors. *Analytical Chemistry* **79**, 782-787 (2007).
56. Yamamoto, Y., Maehashi, K., Ohno, Y. & Matsumoto, K. Electrical Detection of Negatively Charged Proteins Using n-Type Carbon Nanotube Field-Effect Transistor Biosensors. *Japanese Journal of Applied Physics* **49**, 02BD10 (2010).
57. Star, A. *et al.* Label-free detection of DNA hybridization using carbon nanotube network field-effect transistors. *Proceedings of the National Academy of Sciences of the United States of America* **103**, 921-926 (2006).
58. Gui, E.L. *et al.* DNA sensing by field-effect transistors based on networks of carbon nanotubes. *Journal of the American Chemical Society* **129**, 14427-14432 (2007).
59. Siqueira, J.R. *et al.* Carbon nanotubes in nanostructured films: Potential application as amperometric and potentiometric field-effect (bio-)chemical sensors. *physica status solidi (a)* **206**, 462-467 (2009).
60. Claussen, J.C., Franklin, A.D., Ul Haque, A., Porterfield, D.M. & Fisher, T.S. Electrochemical biosensor of nanocube-augmented carbon nanotube networks. *ACS Nano* **3**, 37-44 (2009).
61. Dong, X. *et al.* Electrical Detection of Femtomolar DNA via Gold-Nanoparticle Enhancement in Carbon-Nanotube-Network Field-Effect Transistors. *Advanced Materials* **20**, 2389-2393 (2008).
62. Salimi, A., Noorbakhsh, A. & Ghadermarzi, M. Amperometric detection of nitrite, iodate and periodate at glassy carbon electrode modified with catalase and multi-wall carbon nanotubes. *Sensors and Actuators B: Chemical* **123**, 530-537 (2007).
63. Ishikawa, F.N. *et al.* Importance of controlling nanotube density for highly sensitive and reliable biosensors functional in physiological conditions. *ACS Nano* **4**, 6914-6922 (2010).
64. Heller, I. *et al.* Identifying the mechanism of biosensing with carbon nanotube transistors. *Nano Letters* **8**, 591-595 (2008).
65. Kauffman, D.R. & Star, A. Electronically monitoring biological interactions with carbon nanotube field-effect transistors. *Chemical Society Reviews* **37**, 1197-1206 (2008).
66. Tobias, D.A. 1/f noise and Luttinger liquid phenomena in carbon nanotubes. *PhD thesis* 110 (2007).
67. Collins, P.G., Fuhrer, M.S. & Zettl, A. 1/f noise in carbon nanotubes. *Applied Physics Letters* **76**, 894-896 (2000).
68. Hooge, F.N. 1/f noise is no surface effect. *Physics Letters A* **29**, 139-140 (1969).
69. Ishigami, M. *et al.* Hooge's constant for carbon nanotube field effect transistors. *Applied Physics Letters* **88**, 203116 (2006).
70. Tobias, D. *et al.* Origins of 1/f noise in individual semiconducting carbon nanotube field-effect transistors. *Physical Review B* **77**, 033407 (2008).
71. Lin, Y.-M., Appenzeller, J., Knoch, J., Chen, Z. & Avouris, P. Low-frequency current fluctuations in individual semiconducting single-wall carbon nanotubes. *Nano Letters* **6**, 930-936 (2006).
72. Kim, K. *et al.* Influence of electrical contacts on the 1/f noise in individual multi-walled carbon nanotubes. *Nanotechnology* **21**, 335702 (2010).
73. Behnam, A., Biswas, A., Bosman, G. & Ural, A. Temperature-dependent transport and 1/f noise mechanisms in single-walled carbon nanotube films. *Physical Review B* **81**, 125407 (2010).
74. Snow, E.S., Novak, J.P., Lay, M.D. & Perkins, F.K. 1/f noise in single-walled carbon nanotube devices. *Applied Physics Letters* **85**, 4172-4174 (2004).
75. Wang, N.-P., Heinze, S. & Tersoff, J. Random-telegraph-signal noise and device variability in ballistic nanotube transistors. *Nano Letters* **7**, 910-913 (2007).

76. Liu, F. *et al.* Giant random telegraph signals in the carbon nanotubes as a single defect probe. *Applied Physics Letters* **86**, 163102 (2005).
77. Appenzeller, J., Lin, Y.-M., Knoch, J., Chen, Z. & Avouris, P. 1/f Noise in Carbon Nanotube Devices—On the Impact of Contacts and Device Geometry. *IEEE Transactions On Nanotechnology* **6**, 368-373 (2007).
78. Lee, H., Lee, M., Namgung, S. & Hong, S. Wide Contact Structures for Low-Noise Nanochannel Devices Based on a Carbon Nanotube Network. *ACS Nano* **4**, 7612-8 (2010).
79. Nanowire. *www.wikipedia.org* at <http://en.wikipedia.org/wiki/Nanowire>
80. Dresselhaus, M.S. *et al.* Nanowires and nanotubes. *Materials Science and Engineering: C* **23**, 129-140 (2003).
81. Schottky, W. Über spontane Stromschwankungen in verschiedenen Elektrizitätsleitern. *Annalen der Physik* **362**, 541-567 (1918).
82. Johnson, J.B. Thermal agitation of electricity in conductors. *Physical Review* **32**, 97-109 (1928).
83. Nyquist, H. Thermal agitation of electric charge in conductors. *Physical Review* **32**, 110–113 (1928).
84. Buckingham, M.J. *Noise in electronic devices and systems.* 372 (Ellis Horwood Ltd.: 1983).
85. Wiener, N. Generalized harmonic analysis. *Acta Mathematica* **55**, 117-258 (1930).
86. Khintchine, A. Korrelationstheorie der stationaeren stochastischen Prozesse. *Mathematische Annalen* **109**, 604-615 (1934).
87. Buckingham, M.J. & Faulkner, E.A. The theory of inherent noise in p-n junction diodes and bipolar transistors. *Radio and Electronic Engineer* **44**, 125-140 (1974).
88. Lukyanchikova, N.B. *Noise research in semiconductor physics*. 416 (CRC Press: 1996).
89. Van der Ziel, A. *Noise. Sources, characterization, measurement*. 184 (Prentice-Hall: 1970).
90. Hoffmann, H.J. & Sohn, W. Analysis of localized levels in semiconducting CdS from generation–recombination noise spectra. *physica status solidi (a)* **44**, 237–246 (1977).
91. Van Vliet, K.M. & Fassett, J.R. *Fluctuation phenomena in Solids*. 389 (Academic Press: 1965).
92. Van der Ziel, A. Carrier density fluctuation noise in field-effect transistors. *Proceedings of the IEEE* **51**, 1670-1671 (1963).
93. Van Vliet, K.M. & Hiatt, C.F. Theory of generation-recombination noise in the channel of junction field-effect transistors. *IEEE Transactions on Electron Devices* **22**, 616-617 (1975).
94. Pay, R.G. Excess Noise in Semiconductors. *M.Sc. Thesis* (1956).
95. Lee, H., Yoon, Y., Cho, S. & Shin, H. Accurate Extraction of the Trap Depth from RTS Noise Data by Including Poly Depletion Effect and Surface Potential Variation in MOSFETs. *IEICE Transactions on Electronics* **E90-C**, 968-972 (2007).
96. Voss, R.F. & Clarke, J. "1/f noise" in music: Music from 1/f noise. *The Journal of the Acoustical Society of America* **63**, 258-263 (1978).
97. Johnson, J.B. The Schottky Effect in Low Frequency Circuits. *Physical Review* **26**, 71-85 (1925).
98. Musha, T. 1/f fluctuations in biological systems. *Proceedings of the 6th International Conference on Noise in Physical Systems* 143-146 (1981).
99. Musha, T., Takeuchi, H. & Inoue, T. 1/f Fluctuations in the Spontaneous Spike Discharge Intervals of a Giant Snail Neuron. *IEEE Transactions on Biomedical Engineering* **BME-30**, 194-197 (1983).
100. Musha, T. & Yamamoto, M. 1/f fluctuations in biological systems. *Proceedings of the 19th Annual International Conference of the IEEE Engineering in Medicine and Biology Society. "Magnificent Milestones and Emerging Opportunities in Medical Engineering" (Cat. No.97CH36136)* **6**, 2692-2697 (1997).
101. Schönfeld, H. Beitrag zum 1/f-Gesetz beim Rauschen von Halbleitern. *Zeitschrift Naturforschung Teil A* **10**, 291-300 (1955).
102. Van der Ziel, A. Flicker noise in electronic devices. *Advances in Electronics and Electron Physics* **49**, 225-297 (1979).
103. McWhorter, A.L. 1/f noise and related surface effects in germanium. *Semiconductor Surface Physics* 207–228 (1957).
104. Kleinpenning, T.G.M. 1/f noise in thermo EMF of intrinsic and extrinsic semiconductors. *Physica* **77**, 78-98 (1974).

105. Hooge, F.N. Discussion of recent experiments on 1/f noise. *Physica* **60**, 130-144 (1972).
106. Hooge, F.N. & Vandamme, L.K.J. Lattice scattering causes 1/f noise. *Physics Letters A* **66A**, 315-316 (1978).
107. De Los Rios, P. & Zhang, Y.-C. Universal 1/f Noise from Dissipative Self-Organized Criticality Models. *Physical Review Letters* **82**, 472-475 (1999).
108. Davidsen, J. & Schuster, H. 1/f^α noise from self-organized critical models with uniform driving. *Physical Review E* **62**, 6111-6115 (2000).
109. Handel, P.H. 1/f Noise-An "Infrared" Phenomenon. *Physical Review Letters* **34**, 1492-1495 (1975).
110. Handel, P.H. Quantum theory of 1/f noise. *Physics Letters A* **53**, 438-440 (1975).
111. Raman Spectroscopy. *www.wikipedia.org* at <http://en.wikipedia.org/wiki/Raman_spectroscopy>
112. Hodkiewicz, J. *Introduction to Raman Spectroscopy as a Characterization Tool for Carbon Nanotubes, Graphene, and other Carbon Nanostructures*. 28 (2009).
113. O'Connell, M.J. *Carbon nanotubes: properties and applications*. *Book* **129**, 313 (CRC press: 2006).
114. Guhel, Y., Boudart, B., Vellas, N. & Gaquiere, C. Power improvement of AlGaAs/InGaAs PHEMTs by using low gamma radiation dose. *Microelectronic Engineering* **87**, 2443-2447 (2010).
115. Gromov, D.V., Elesin, V.V., Polevich, S.A., Adamov, Y.F. & Mokerov, V.G. Ionizing-Radiation Response of the GaAs/(Al, Ga)As PHEMT: A Comparison of Gamma- and X-ray Results. *Russian Microelectronics* **33**, 111-115 (2004).
116. Luo, B., Johnson, J.W., Schoenfeld, D., Pearton, S.J. & Ren, F. Study of radiation induced resistance mechanisms in GaAs MESFET and TLM structures. *Solid-State Electronics* **45**, 1149-1152 (2001).
117. Sze, S.M. *Physics of semiconductor devices*. 868 (Wiley: New York, 1981).
118. Uy, K.J.., Reyes-Abu, P.A. & Chung, W.Y. A high precision temperature insensitive current and voltage reference generator. *World Academy of Science, Engineering and Technology* **50**, 966–969 (2009).
119. Skákalová, V., Hulman, M., Fedorko, P., Lukáč, P. & Roth, S. Effect Of Gamma-Irradiation on Single-Wall Carbon Nanotube Paper. *MOLECULAR NANOSTRUCTURES: XVII International Winterschool Euroconference on Electronic Properties of Novel Materials. AIP Conference Proceedings* **685**, 143-147 (2003).
120. Jovanović, S.P. *et al.* A novel method for the functionalization of gamma-irradiated single wall carbon nanotubes with DNA. *Nanotechnology* **20**, 445602 (2009).
121. Dzhafarov, T.D. Radiation Stimulated Diffusion in Semiconductors. *physica status solidi (b)* **155**, 11-51 (1989).
122. Javey, A., Guo, J., Wang, Q., Lundstrom, M. & Dai, H. Ballistic carbon nanotube field-effect transistors. *Nature* **424**, 654-7 (2003).
123. Shalimova, K.V. *Semiconductor physics (in Russian)*. 416 ("Energy:" Moskow, 1976).
124. Ural, A., Li, Y. & Dai, H. Electric-field-aligned growth of single-walled carbon nanotubes on surfaces. *Applied Physics Letters* **81**, 3464-3466 (2002).
125. Behnam, A., Bosman, G. & Ural, A. Percolation scaling of 1/f noise in single-walled carbon nanotube films. *Physical Review B* **78**, 085431 (2008).
126. Ma, T.P. & Dressendorfer, P.V. *Ionizing radiation effects in MOS devices and circuits*. 608 (Wiley: New York, 1989).
127. Yoshikawa, M. *et al.* Effects of gamma-ray irradiation on cubic silicon carbide metal-oxide-semiconductor structure. *Journal of Applied Physics* **70**, 1309-1313 (1991).
128. Sah, C.T. Origin of Interface States and Oxide Charges Generated by Ionizing Radiation. *IEEE Transactions on Nuclear Science* **23**, 1563-1568 (1976).
129. Schwank, J.R. *et al.* Radiation Effects in MOS Oxides. *IEEE Transactions on Nuclear Science* **55**, 1833-1853 (2008).
130. Bendiab, N., Almairac, R., Sauvajol, J.-. L., Rols, S. & Elkaim, E. Orientation of single-walled carbon nanotubes by uniaxial pressure. *Journal of Applied Physics* **93**, 1769-1773 (2003).
131. Danilchenko, B.A. *et al.* High temperature Luttinger liquid conductivity in carbon nanotube bundles. *Applied Physics Letters* **97**, 072106 (2010).

132. Shklovskii, B.I. Theory of 1/f noise for hopping conduction. *Solid State Communications* **33**, 273-276 (1980).
133. Kozub, V.I. Low-frequency noise due to site energy fluctuations in hopping conductivity. *Solid State Communications* **97**, 843-846 (1996).
134. Burin, A.L., Shklovskii, B.I., Kozub, V.I., Galperin, Y.M. & Vinokur, V. Many electron theory of 1/ f -noise in hopping conductivity. *physica status solidi (c)* **5**, 800-808 (2008).
135. Biermann, S., Georges, A., Lichtenstein, A. & Giamarchi, T. Deconfinement Transition and Luttinger to Fermi Liquid Crossover in Quasi-One-Dimensional Systems. *Physical Review Letters* **87**, 276405 (2001).
136. Maarouf, A.A., Kane, C.L. & Mele, E.J. Electronic structure of carbon nanotube ropes. *Physical Review B* **61**, 11156-11165 (2000).
137. Clevers, R.H.M. Volume and temperature dependence of the 1/f noise parameter α in Si. *Physica B: Condensed Matter* **154**, 214-224 (1989).
138. Kleinpenning, T.G.M. 1/ f noise in p-n junction diodes. *Journal of Vacuum Science & Technology A: Vacuum, Surfaces, and Films* **3**, 176-182 (1985).
139. Kilmer, J., van der Ziel, A. & Bosman, G. Presence of mobility-fluctuation 1/f noise identified in silicon P+NP transistors. *Solid-State Electronics* **26**, 71-74 (1983).
140. Lukyanchikova, N.B. New “universal” relation concerning 1/ƒ noise. *Physics Letters A* **180**, 285-288 (1993).
141. Kang, B.S. *et al.* Electrical detection of deoxyribonucleic acid hybridization with AlGaN⁄GaN high electron mobility transistors. *Applied Physics Letters* **89**, 122102 (2006).
142. Wang, H.-T. *et al.* Comparison of gate and drain current detection of hydrogen at room temperature with AlGaN⁄GaN high electron mobility transistors. *Applied Physics Letters* **87**, 172105 (2005).
143. Doi, K., Higashimaki, N., Kawakami, Y., Nakamura, K. & Tachibana, A. First-principle study on electronic properties of gallium nitride and aluminium nitride nanowires. *physica status solidi (b)* **241**, 2806-2810 (2004).
144. Simpkins, B.S., McCoy, K.M., Whitman, L.J. & Pehrsson, P.E. Fabrication and characterization of DNA-functionalized GaN nanowires. *Nanotechnology* **18**, 355301 (2007).
145. Carter, D., Gale, J., Delley, B. & Stampfl, C. Geometry and diameter dependence of the electronic and physical properties of GaN nanowires from first principles. *Physical Review B* **77**, 115349 (2008).
146. Vitusevich, S.A. *et al.* Dynamic redistribution of the electric field of the channel in AlGaN⁄GaN high electron mobility transistor with nanometer-scale gate length. *Applied Physics Letters* **87**, 192110 (2005).
147. Vitusevich, S.A. *et al.* AlGaN/GaN High Electron Mobility Transistor Structures: Self-Heating Effect and Performance Degradation. *IEEE Transactions on Device and Materials Reliability* **8**, 543-548 (2008).
148. Lehnen, P., Schäpers, T., Kaluza, N., Thillosen, N. & Hardtdegen, H. Enhanced spin-orbit scattering length in narrow AlxGa1−xN⁄GaN wires. *Physical Review B* **76**, 205307 (2007).
149. Green, J.E. *et al.* A 160-kilobit molecular electronic memory patterned at 1011 bits per square centimetre. *Nature* **445**, 414–417 (2007).
150. Galperin, M., Ratner, M.A., Nitzan, A. & Troisi, A. Nuclear coupling and polarization in molecular transport junctions: beyond tunneling to function. *Science (New York, N.Y.)* **319**, 1056-60 (2008).
151. Kushmerick, J.G., Naciri, J., Yang, J.C. & Shashidhar, R. Conductance Scaling of Molecular Wires in Parallel. *Nano Letters* **3**, 897-900 (2003).
152. Chen, X. *et al.* Chemical fabrication of heterometallic nanogaps for molecular transport junctions. *Nano Letters* **9**, 3974-9 (2009).
153. Liu, Y., Offenhäusser, A. & Mayer, D. An electrochemically transduced XOR logic gate at the molecular level. *Angewandte Chemie (International ed. in English)* **49**, 2595-8 (2010).
154. Lörtscher, E., Weber, H. & Riel, H. Statistical Approach to Investigating Transport through Single Molecules. *Physical Review Letters* **98**, 12-15 (2007).
155. Wu, S. *et al.* Molecular junctions based on aromatic coupling. *Nature Nanotechnology* **3**, 569-74 (2008).

156. Jung, T.A., Schlittler, R.R. & Gimzewski, J.K. Conformational identification of individual adsorbed molecules with the STM. *Nature* **386**, 696-698 (1997).
157. Grüter, L., González, M.T., Huber, R., Calame, M. & Schönenberger, C. Electrical conductance of atomic contacts in liquid environments. *Small (Weinheim an der Bergstrasse, Germany)* **1**, 1067-70 (2005).
158. Huang, Z. *et al.* Local ionic and electron heating in single-molecule junctions. *Nature nanotechnology* **2**, 698-703 (2007).
159. Moreland, J. & Ekin, J.W. Electron tunneling experiments using Nb-Sn "'break'" junctions. *Journal of Applied Physics* **58**, 3888-3895 (1985).
160. Zhou, C., Muller, C.J., Deshpande, M.R., Sleight, J.W. & Reed, M.A. Microfabrication of a mechanically controllable break junction in silicon. *Applied Physics Letters* **67**, 1160-1162 (1995).
161. Reed, M.A., Zhou, C., Muller, C.J., Burgin, T.P. & Tour, J.M. Conductance of a Molecular Junction. *Science* **278**, 252-254 (1997).
162. Wu, Z. *et al.* Scaling of 1/f noise in tunable break junctions. *Physical Review B* **78**, 235421 (2008).
163. Kim, Y., Song, H., Kim, D., Lee, T. & Jeong, H. Noise characteristics of charge tunneling via localized states in metal--molecule--metal junctions. *ACS Nano* **4**, 4426-30 (2010).
164. Diez-Perez, I. *et al.* Controlling single-molecule conductance through lateral coupling of π orbitals. *Nature Nanotechnology* **6**, 226-231 (2011).
165. Ochs, R., Secker, D., Elbing, M., Mayor, M. & Weber, H.B. Fast temporal fluctuations in single-molecule junctions. *Faraday Discussions* **131**, 281-289 (2006).
166. Kornyshev, A.A. & Kuznetsov, A.M. Simple theory of current fluctuations and noise in bridge-mediated nano-junctions. *Journal of Physics: Condensed Matter* **20**, 374103 (2008).
167. Solomon, G.C. *et al.* Molecular origins of conduction channels observed in shot-noise measurements. *Nano letters* **6**, 2431-7 (2006).
168. Bezrukov, S.M. & Winterhalter, M. Examining noise sources at the single-molecule level: 1/f noise of an open maltoporin channel. *Physical review letters* **85**, 202-205 (2000).
169. Djukic, D. & van Ruitenbeek, J.M. Shot noise measurements on a single molecule. *Nano letters* **6**, 789-93 (2006).
170. Secker, D. & Weber, H.B. Charge transport across single-molecule junctions: charge reconfiguration and structural dynamics. *physica status solidi (b)* **244**, 4176-4180 (2007).
171. Cuevas, J.C. & Scheer, E. *Molecular electronics: an introduction to theory and experiment*. *Book* **1**, 724 (World Scientific Pub Co Inc: 2010).
172. Dell'Angela, M. *et al.* Relating Energy Level Alignment and Amine-Linked Single Molecule Junction Conductance. *Nano Letters* **10**, 2470-2474 (2010).
173. Bosman, G. & Zijlstra, R.J.J. Generation-recombination noise in p-type silicon. *Solid-State Electronics* **25**, 273-280 (1982).
174. Kiguchi, M. *et al.* Conductance of Single 1,4-Benzenediamine Molecule Bridging between Au and Pt Electrodes. *Journal of Physical Chemistry C* **112**, 13349-13352 (2008).
175. Mishchenko, A. *et al.* Influence of conformation on conductance of biphenyl-dithiol single-molecule contacts. *Nano Letters* **10**, 156-63 (2010).
176. Chang, S. *et al.* Tunnel conductance of Watson-Crick nucleoside-base pairs from telegraph noise. *Nanotechnology* **20**, 185102 (2009).
177. Kihira, Y., Shimada, T., Matsuo, Y., Nakamura, E. & Hasegawa, T. Random telegraphic conductance fluctuation at Au-pentacene-Au nanojunctions. *Nano Letters* **9**, 1442-1446 (2009).
178. Landau, L.D. & Lifshitz, E.M. *Statistical Physics, Part 1*. *Book* **34**, 578 (Pergamon, Elmsford, N. Y.: 1980).

Personal publication list

1. B.A. Danilchenko, N.A. Tripachko, S. Lev, M.V. Petrychuk, V. A. Sydoruk, B. Sundqvist, and S.A. Vitusevich. *1/f noise and mechanisms of the conductivity in carbon nanotube bundles*. Carbon, **49**(15), 5201-5206 (2011).
2. F.V. Gasparyan, A. Poghossian, S.A. Vitusevich, M.V. Petrychuk, V.A. Sydoruk, A.V. Surmalyan, J.R. Siqueira, O.N. Oliveira Jr., A. Offenhäusser, and M.J. Schöning. *Low-frequency noise in field-effect devices functionalized with dendrimer/carbon- nanotube multilayers*. IEEE Sensors Journal, **11**(1), 142-149 (2011).
3. V.A. Sydoruk, M.V. Petrychuk, A. Ural, G. Bosman, A. Offenhäusser, and S.A. Vitusevich. *Noise characterization of transport properties in single wall carbon nanotube field-effect transistors.* Proceedings of the IEEE 21st International Conference on Noise and Fluctuations, ICNF 2011, 238-241 (2011).
4. S.A. Vitusevich, V.A. Sydoruk, M.V. Petrychuk, B.A. Danilchenko, N. Klein, A. Offenhäusser, A. Ural, and G. Bosman. *Transport properties of single-walled carbon nanotube transistors after gamma radiation treatment.* Journal of Applied Physics. **107**(6), 063701 (2010).
5. V.A. Sydoruk, M.V. Petrychuk, B.A. Danilchenko, A. Offenhäusser, and S.A. Vitusevich. *Transport of single-walled carbon nanotube transistors after gamma radiation treatment for high-speed applications.* 2010 International Kharkov Symposium on Physics and Engineering of Microwaves, Millimeter and Submillimeter Waves, MSMW'2010 (2010).
6. S.A. Vitusevich, M.V. Petrychuk, V.A. Sydoruk, T. Schäpers, H. Hardtdegen, A.E. Belyaev, A. Offenhausser, and N. Klein. *Low frequency noise in 2DEG channel of AlGaN/GaN heterostructures scaled to nanosize width.* AIP Conference Proceedings, **1129**, 487-490 (2009).
7. S.A. Vitusevich, V.A. Sydoruk, A.M. Kurakin, N. Klein, M.V. Petrychuk, A.V. Naumov, and A.E. Belyaev. *AlGaN/GaN heterostructures for hot electron and quantum effects.* Journal of Physics: Conference Series, **152**, 012008 (2009).
8. F.V. Gasparyan, A. Poghossian, S.A. Vitusevich, M.V. Petrychuk, V.A. Sydoruk, A.V. Surmalyan, J.R. Siqueira, O.N. Oliveira Jr., A. Offenhäusser, and M.J. Schöning. *Low frequency noise in electrolyte-gate field-effect devices functionalized with Dendrimer/carbon-nanotube multilayers*. Paper presented at the AIP Conference Proceedings, **1129**, 133-136 (2009).
9. V.P. Kladko, A.F. Kolomys, M.V. Slobodian, V.V. Strelchuk, V.G. Raicheva, A.E. Belyaev, S.S. Bukalov, H. Hardtdegen, V.A. Sydoruk, N. Klein, and S.A. Vitusevich. *Internal strains and crystal structure of the layers in AlGaN/GaN heterostructures grown on a sapphire substrate.* Journal of Applied Physics, **105**(6), 063515 (2009).
10. V.A. Sydoruk, S.V. Danylyuk, M.V. Petrychuk, N. Klein, A. Offenhäusser, S.A. Vitusevich. *Noise and transport properties of single-walled carbon nanotube transistors under small dose of γ-irradiation*. Nanoelectronic days 2008, Aachen, Germany (2008).
11. V.A. Sydoruk, M.V. Petrychuk, A. Offenhäusser, S. Vitusevich. *Noise of field-effect transistors based on single carbon nanotube*. Nanoelectronic days 2010, Aachen, Germany (2010).

12. V.A. Sydoruk. *Noise investigation of nanostructures*. Student workshop in Freiburg, Germany (2009).

Appendixes

1. GetNoiseSpectrum v8 program written using HTBasic

The program consists of 7 files:

- GetNoiseSpectrum v8 with relay.bas – *the main part (kernel),*
- LibraryGNS v6.scr – *the interface of the program,*
- LibraryGNS v6 addition.scr – *the addition to the interface of the program,*
- h0.dat – *the calibration curve of manufactured amplifier,*
- h0n.dat – *the calibration curve of homemade preamplifier,*
- k2.dat – *the frequency characteristic of the gain of manufactured amplifier,*
- k2n.dat – *the frequency characteristic of the gain of homemade preamplifier.*

The initialization screenshot of the program:

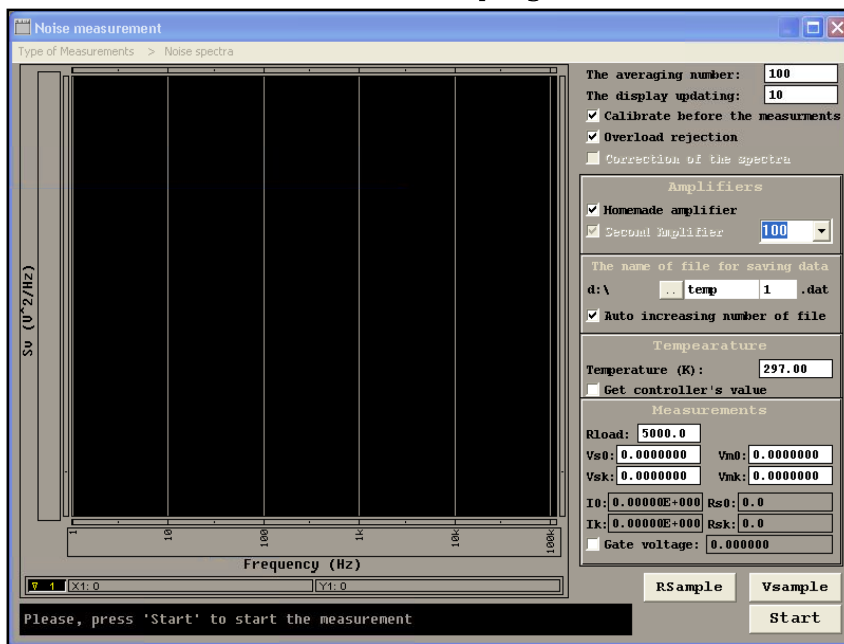

The text of GetNoiseSpectrum v8 with relay.bas file of the program:

```
Home$="D:\v.sydoruk\HP-programs\Get Noise Spectrum\"

DIM Freq1(1600)
DIM Freq2(1600)
DIM Dat1(1600)
DIM Dat2(1600)
DIM H0(1:3175)
DIM H0n(1:3175)
DIM K2(1:3175)
DIM K2n(1:3175)
DIM Data(1:3175),Datalast(1:3175),Datasvtemp(1:3175),Resistance(1:3175)
DIM Xdata(1:30000)
DIM Ydata(1:30000)
DIM Frequency(1:3175),Frequencylast(1:3175)
DIM Acoef(9)
DATA 10,20,50,100,200,500,1000,2000,5000,10000
READ Acoef(*)
REAL Datasize,P,I,Bytes,Calibration,Nmaximum,Vmaximum,Temperature0,Temperaturee,Na
INTEGER
Naver,Bcal,Nupdate,Bover,Nfile,Hmampl,Nminus,Tcont,Waitseconds,Val,Vsample,Zeronoise,Close,Blocks,Typeofme
asur,Ii,Vgcont
LONG Freqstopvalue,Pfreqstopvalue
```

```
REAL
Voltage,Voltageaver1,Voltageaver2,Rnvalue,Voltageaver01,Voltageaver02,Rsample,Rfreqstopvalue,Gatevoltage
DIM Y(1:900,1:1024)
DIM Time(32766)
DIM Measurdat(32766)

Typeofmeasur=1
Waitseconds=5
Vsample=1
Zeronoise=0
Pfreqstopvalue=1600
Freqstopvalue=1600
Blocks=600
Continuemeasur=1

LOAD BIN "BPLUS"
COM @Sys
COM @Filepath

!GOTO 75

CLEAR SCREEN
ASSIGN @Sys TO WIDGET "SYSTEM"
CONTROL @Sys;SET ("*LOAD":Home$&"LibraryGNS v6.scr")
CONTROL @Sys;SET ("*NAME":"Noisepanel","VISIBLE":1)
CONTROL @Sys;SET ("*LOAD":Home$&"LibraryGNS v6 addition.scr")
CONTROL @Sys;SET ("*NAME":"Multimetrpanel","VISIBLE":0)
!STATUS @Sys;RETURN ("*WIDGETS":Num_widgets)
!ALLOCATE Names$(1:Num_widgets)[80]
!STATUS @Sys;RETURN ("*WIDGET NAMES":Names$(*))
!PRINT Names$(*)
ASSIGN @Analyzer TO 706
ASSIGN @Analyzer_bin TO 706;FORMAT OFF
ASSIGN @Volt TO 723
!ASSIGN @Voltgate TO 722

!==== Temperature controller ====
!ASSIGN @Temp TO 713                    ! LakeShore controller
!ASSIGN @Temp TO 715                     ! Conductus controller
ASSIGN @Temp TO 8                       ! LakeShore small controller

CLEAR 7                                  ! Clear GPIB
OUTPUT @Volt;"*RST"                      ! Reset Volt
OUTPUT @Volt;"*CLS"                      ! Clear Volt status registers
OUTPUT @Volt;"*OPC?"                     ! Assure synchronization
ENTER @Volt;Val
OUTPUT @Volt;"VOLT:DC:NPLC 10"           ! Set the integration time to 10 PLCs
OUTPUT @Volt;"TRIG:COUN 10"              ! Dmm will accept 10 triggers
OUTPUT @Volt;"SYST:BEEP:STAT OFF"        ! Turns off the beeper
OUTPUT @Volt;"INP:IMP:AUTO ON"           ! Switch <10GOhm input resistance mode
OUTPUT @Volt;"CALC:FUNC AVER;STAT OFF"
OUTPUT @Volt;"SENS:VOLT:DC:RANG:AUTO ON"
LOCAL @Volt



!CONTROL @Sys;SET ("*QUEUE EVENTS":1)
ON EVENT @Sys,"SYSTEM CLOSE" GOTO Finish
ON EVENT @Sys,"CHANGED" GOTO Checkbutton
ON EVENT @Sys,"ACTIVATED" GOTO Checkbutton
!ON EVENT @Sys,"DONE" GOTO Checkbutton
ASSIGN @Filepath TO WIDGET "FILE"
CONTROL @Filepath;SET ("VISIBLE":0,"DIRECTORY":"d:\","CLOSEABLE":1,"TITLE":"Those the folder")
CONTROL @Filepath;SET ("SELECTION":"d:\*.dat","BACKGROUND":24)
ON EVENT @Filepath,"SYSTEM CLOSE" GOTO Readdirectory
GOTO First_loging

!-------------- Waiting loop ----------------------
GOTO Circle
 Circle2:!
LOOP
OUTPUT @Volt;"VOLT:DC:NPLC 1"               ! Set the integration time to 10 PLCs
OUTPUT @Volt;"TRIG:COUN 1"                  ! Dmm will accept 10 triggers
OUTPUT @Volt;"INP:IMP:AUTO ON"               ! Switch <10GOhm input resistance mode
OUTPUT @Volt;"SENS:VOLT:DC:RANG:AUTO ON"

OUTPUT @Analyzer;"OUTPUT:STAT ON"
```

```
       GOSUB Get_voltage
       Voltageaver01=Voltage
       CONTROL @Sys;SET ("*NAME":"Multimetrpanel/Vsvalue","VALUE":Voltageaver01)

       OUTPUT @Analyzer;"OUTPUT:STAT OFF"
       CONTROL @Sys;SET ("*NAME":"Noisepanel/Vsample")
       CONTROL @Sys;SET ("LABEL":"Vsample")
       Vsample=1
       GOSUB Get_voltage
       Voltageaver02=Voltage
       CONTROL @Sys;SET ("*NAME":"Multimetrpanel/Vmvalue","VALUE":Voltageaver02)
       CONTROL @Sys;SET ("*NAME":"Noisepanel/Measurementspanel/Rloadvalue")
       STATUS @Sys;RETURN ("VALUE":Rnvalue)
       IF Voltageaver02<>Voltageaver01 THEN
       CONTROL @Sys;SET ("*NAME":"Multimetrpanel/Ivalue","VALUE":(Voltageaver02-Voltageaver01)/Rnvalue)
       CONTROL   @Sys;SET   ("*NAME":"Multimetrpanel/Rsvalue","VALUE":Voltageaver01*Rnvalue/(Voltageaver02-
Voltageaver01))
       END IF

       WAIT FOR EVENT;TIMEOUT 2
       END LOOP
       GOTO Checkbutton
        Circle:!
       CONTROL @Sys;SET ("*NAME":"Noisepanel/Start")
       CONTROL @Sys;SET ("VISIBLE":1)
       CONTROL @Sys;SET ("*NAME":"Noisepanel/Abort")
       CONTROL @Sys;SET ("VISIBLE":0)
       CONTROL @Sys;SET ("*NAME":"Noisepanel/Vsample")
       CONTROL @Sys;SET ("VISIBLE":1)
       LOOP
       WAIT FOR EVENT;TIMEOUT 2
       END LOOP

       !-------------- Event handler ---------------------
        Checkbutton:!
       STATUS @Sys;RETURN ("*QUEUED EVENT":Ev$(*))
       OUTPUT @Volt;"VOLT:DC:NPLC 10"                ! Set the integration time to 10 PLCs
       OUTPUT @Volt;"TRIG:COUN 10"                   ! Dmm will accept 10 triggers
       OUTPUT @Volt;"INP:IMP:AUTO ON"                ! Switch <10GOhm input resistance mode
       OUTPUT @Volt;"SENS:VOLT:DC:RANG:AUTO ON"
       SELECT Ev$(0)
       CASE "Noisepanel/Start"
       IF Typeofmeasur=1 THEN GOTO Start
       IF Typeofmeasur=2 THEN GOTO Start2
       CASE "Noisepanel/Abort"
       CONTROL @Sys;SET ("*NAME":"Noisepanel/Status")
       CONTROL  @Sys;SET  ("VALUE":"The  measuremets  were  aborted.  Press  'Start'  to  take  the  sample
voltage.")
       IF Typeofmeasur=1 THEN OUTPUT @Analyzer;"Abort"
       IF Typeofmeasur=2 THEN OUTPUT @Analyzer;"TCAP:ABORT"
       GOTO Circle
       CASE "Noisepanel/Filepathpanel/Filedirbutton"
       CONTROL @Filepath;SET ("VISIBLE":1)
       GOTO Circle
       CASE "Noisepanel/Vsample"
       CONTROL @Sys;SET ("*NAME":"Noisepanel/Vsample")
       IF Vsample=1 THEN
       CONTROL @Sys;SET ("LABEL":"Vmain")
       Vsample=0
       OUTPUT @Analyzer;"OUTPUT:STAT ON"
       ELSE
       CONTROL @Sys;SET ("LABEL":"Vsample")
       Vsample=1
       OUTPUT @Analyzer;"OUTPUT:STAT OFF"
       END IF
       LOCAL @Volt
       GOTO Circle
       CASE "Noisepanel/Openpanelersample"
       CONTROL @Sys;SET ("*NAME":"Noisepanel/Status")
       CONTROL @Sys;SET ("VALUE":"Close addition window to start the measurement.")
       CONTROL @Sys;SET ("*NAME":"Noisepanel/Start","VISIBLE":0)
       CONTROL @Sys;SET ("*NAME":"Noisepanel/Vsample","VISIBLE":0)
       CONTROL @Sys;SET ("*NAME":"Multimetrpanel","VISIBLE":1)
       GOTO Circle2
       CASE "Noisepanel/Typeofmeasurements/Noisespectra"
       Typeofmeasur=1
        First_loging:   !
```

```
      FOR N=1 TO 3175
      Datalast(N)=4*1.38E-23*300*5000
      Frequencylast(N)=N
      NEXT N

      CONTROL @Sys;SET ("*NAME":"Noisepanel/Status")
      CONTROL @Sys;SET ("VALUE":"Configuration of the analyzer...")
      OUTPUT @Analyzer;":TCAP:DEL"
      OUTPUT @Analyzer;"INST:SELECT FFT"
      OUTPUT @Analyzer;":INP2 OFF"
      OUTPUT @Analyzer;"CALC1:ACTIVE A"
      OUTPUT @Analyzer;"FORM:DATA REAL, 64"
      OUTPUT @Analyzer;"CALC1:FEED 'XFR:POW 1'"
      OUTPUT @Analyzer;"CALC1:UNIT:VOLT 'V2/HZ'"
      OUTPUT @Analyzer;"CAL:AUTO OFF"
      OUTPUT @Analyzer;"FREQ:RES 1600"
      OUTPUT @Analyzer;"SOUR:VOLTAGE:OFFS 6.6"
      CONTROL @Sys;SET ("*NAME":"Noisepanel/Activetom","LABEL":">   Noise spectra")
      CONTROL @Sys;SET ("*NAME":"Noisepanel/Activetom","SENSITIVE":0)
          !---------- Plot configuration --------------
      CONTROL @Sys;SET ("*NAME":"Noisepanel/Noisespectrum","CURRENT TRACE":1)
      CONTROL @Sys;SET ("*NAME":"Noisepanel/Noisespectrum","CURRENT AXIS":0)
      CONTROL @Sys;SET ("*NAME":"Noisepanel/Noisespectrum","AXIS LABEL":"Frequency (Hz)")
      CONTROL @Sys;SET ("*NAME":"Noisepanel/Noisespectrum","LOGARITHMIC":1)
      CONTROL @Sys;SET ("*NAME":"Noisepanel/Noisespectrum","LOG TICKS":1)
      CONTROL @Sys;SET ("*NAME":"Noisepanel/Noisespectrum","NUMBER FORMAT":0)
      CONTROL @Sys;SET ("*NAME":"Noisepanel/Noisespectrum","AUTOSCALE":0)
      CONTROL @Sys;SET ("*NAME":"Noisepanel/Noisespectrum","ORIGIN":1)
      CONTROL @Sys;SET ("*NAME":"Noisepanel/Noisespectrum","RANGE":5.05)
      CONTROL @Sys;SET ("*NAME":"Noisepanel/Noisespectrum","CURRENT AXIS":1)
      CONTROL @Sys;SET ("*NAME":"Noisepanel/Noisespectrum","AXIS LABEL":"Sv (V^2/Hz)")
      CONTROL @Sys;SET ("*NAME":"Noisepanel/Noisespectrum","LOGARITHMIC":1)
      CONTROL @Sys;SET ("*NAME":"Noisepanel/Noisespectrum","LOG TICKS":1)
      CONTROL @Sys;SET ("*NAME":"Noisepanel/Noisespectrum","NUMBER FORMAT":3)
          !---------- Hiding all not needed components ----------
      CONTROL @Sys;SET ("*NAME":"Noisepanel/Timemeasurpanel","VISIBLE":0)
          !---------- Showing all  needed components ------------
      CONTROL @Sys;SET ("*NAME":"Noisepanel/Averagingnumber","VISIBLE":1)
      CONTROL @Sys;SET ("*NAME":"Noisepanel/Averagingtext","VISIBLE":1)
      CONTROL @Sys;SET ("*NAME":"Noisepanel/Updatetext","VISIBLE":1)
      CONTROL @Sys;SET ("*NAME":"Noisepanel/Updatenumber","VISIBLE":1)
      CONTROL @Sys;SET ("*NAME":"Noisepanel/Calibration","VISIBLE":1)
      CONTROL @Sys;SET ("*NAME":"Noisepanel/Overload","VISIBLE":1)
      CONTROL @Sys;SET ("*NAME":"Noisepanel/Correction","VISIBLE":1)
      CONTROL @Sys;SET ("*NAME":"Noisepanel/Amplifierspanel","X":537)     !540
      CONTROL @Sys;SET ("*NAME":"Noisepanel/Amplifierspanel","Y":105)     !150
      CONTROL @Sys;SET ("*NAME":"Noisepanel/Filepathpanel","X":537)     !540
      CONTROL @Sys;SET ("*NAME":"Noisepanel/Filepathpanel","Y":180)     !225
      CONTROL @Sys;SET ("*NAME":"Noisepanel/Temperaturepanel","X":537)     !540
      CONTROL @Sys;SET ("*NAME":"Noisepanel/Temperaturepanel","Y":255)     !300
      CONTROL @Sys;SET ("*NAME":"Noisepanel/Noisespectrum","WIDTH":520)
      CONTROL @Sys;SET ("*NAME":"Noisepanel/Noisespectrum","HEIGHT":505)
      CONTROL @Sys;SET ("*NAME":"Noisepanel/Start")
      CONTROL @Sys;SET ("VISIBLE":1)
      CONTROL @Sys;SET ("*NAME":"Noisepanel/Status")
      CONTROL @Sys;SET ("VALUE":"Please, press 'Start' to start the measurement")
      GOTO Circle
      CASE "Noisepanel/Typeofmeasurements/Timedependences"
      Typeofmeasur=2
      OUTPUT @Analyzer;"SOUR:VOLTAGE:OFFS 6.6"
      OUTPUT @Analyzer;"inp2 off"
      CONTROL @Sys;SET ("*NAME":"Noisepanel/Activetom","LABEL":">   Time dependences")
      CONTROL @Sys;SET ("*NAME":"Noisepanel/Activetom","SENSITIVE":0)
          !---------- Plot configuration --------------
      CONTROL @Sys;SET ("*NAME":"Noisepanel/Noisespectrum")
      DIM Zero(1)
      DATA Null
      RESTORE
      CONTROL @Sys;SET ("*NAME":"Noisepanel/Noisespectrum")
      CONTROL @Sys;SET ("CURRENT TRACE":1,"CURRENT AXIS":0,"AXIS LABEL":"Time (s)","LOGARITHMIC":0)
      CONTROL @Sys;SET ("LOG TICKS":1,"NUMBER FORMAT":2,"AUTOSCALE":1,"CURRENT AXIS":1)
      CONTROL  @Sys;SET  ("AUTOSCALE":1,"AXIS  LABEL":"Vsample  (V)","LOGARITHMIC":0,"LOG  TICKS":1,"NUMBER
FORMAT":2)
      CONTROL @Sys;SET ("CURRENT TRACE":1,"X DATA":Zero(*),"Y DATA":Zero(*))
      CONTROL @Sys;SET ("CURRENT TRACE":2,"X DATA":Zero(*),"Y DATA":Zero(*))
      CONTROL @Sys;SET ("CURRENT TRACE":3,"X DATA":Zero(*),"Y DATA":Zero(*))
```

```
       CONTROL @Sys;SET ("CURRENT TRACE":4,"X DATA":Zero(*),"Y DATA":Zero(*))
       CONTROL @Sys;SET ("CURRENT TRACE":5,"X DATA":Zero(*),"Y DATA":Zero(*))
           !---------- Hiding all not needed components ----------
       CONTROL @Sys;SET ("*NAME":"Noisepanel/Averagingnumber","VISIBLE":0)
       CONTROL @Sys;SET ("*NAME":"Noisepanel/Averagingtext","VISIBLE":0)
       CONTROL @Sys;SET ("*NAME":"Noisepanel/Updatetext","VISIBLE":0)
       CONTROL @Sys;SET ("*NAME":"Noisepanel/Updatenumber","VISIBLE":0)
       CONTROL @Sys;SET ("*NAME":"Noisepanel/Calibration","VISIBLE":0)
       CONTROL @Sys;SET ("*NAME":"Noisepanel/Overload","VISIBLE":0)
       CONTROL @Sys;SET ("*NAME":"Noisepanel/Correction","VISIBLE":0)
           !---------- Showing all needed components ------------
       CONTROL @Sys;SET ("*NAME":"Noisepanel/Amplifierspanel","X":7)
       CONTROL @Sys;SET ("*NAME":"Noisepanel/Amplifierspanel","Y":320)
       CONTROL @Sys;SET ("*NAME":"Noisepanel/Filepathpanel","X":272)
       CONTROL @Sys;SET ("*NAME":"Noisepanel/Filepathpanel","Y":320)
       CONTROL @Sys;SET ("*NAME":"Noisepanel/Temperaturepanel","X":272)
       CONTROL @Sys;SET ("*NAME":"Noisepanel/Temperaturepanel","Y":400)
       CONTROL @Sys;SET ("*NAME":"Noisepanel/Noisespectrum","WIDTH":777)
       CONTROL @Sys;SET ("*NAME":"Noisepanel/Noisespectrum","HEIGHT":310)
       CONTROL @Sys;SET ("*NAME":"Noisepanel/Timemeasurpanel","VISIBLE":1)
       CONTROL @Sys;SET ("*NAME":"Noisepanel/Start")
       CONTROL @Sys;SET ("VISIBLE":1)
       CONTROL @Sys;SET ("*NAME":"Noisepanel/Status")
       CONTROL @Sys;SET ("VALUE":"Please, press 'Start' to start the measurement")
       GOTO Circle
       CASE "Noisepanel/Timemeasurpanel/Freqstopvalue"
       CONTROL @Sys;SET ("*NAME":"Noisepanel/Timemeasurpanel/Freqstopvalue")
       STATUS @Sys;RETURN ("VALUE":Rfreqstopvalue)
       Freqstopvalue=INT(Rfreqstopvalue)
       IF Pfreqstopvalue>Freqstopvalue THEN
       FOR I=1 TO 9
       IF 100*2^I>Freqstopvalue THEN
       Freqstopvalue=100*2^(I-1)
       Pfreqstopvalue=100*2^(I-1)
       CONTROL @Sys;SET ("*NAME":"Noisepanel/Timemeasurpanel/Freqstopvalue","VALUE":Freqstopvalue)
       CONTROL                                                                                     @Sys;SET
("*NAME":"Noisepanel/Timemeasurpanel/Timevalue","NVALUE":Blocks*400.0/Freqstopvalue)
       CONTROL                                                                                     @Sys;SET
("*NAME":"Noisepanel/Timemeasurpanel/Timestepvalue","NVALUE":400.0/(Freqstopvalue*1024))
       GOTO Circle
       END IF
       NEXT I
       END IF
       IF Pfreqstopvalue<Freqstopvalue THEN
       FOR I=8 TO 0 STEP -1
       IF 100*2^I<Freqstopvalue THEN
       Freqstopvalue=100*2^(I+1)
       Pfreqstopvalue=100*2^(I+1)
       CONTROL @Sys;SET ("*NAME":"Noisepanel/Timemeasurpanel/Freqstopvalue","VALUE":Freqstopvalue)
       CONTROL                                                                                     @Sys;SET
("*NAME":"Noisepanel/Timemeasurpanel/Timevalue","NVALUE":Blocks*400.0/Freqstopvalue)
       CONTROL                                                                                     @Sys;SET
("*NAME":"Noisepanel/Timemeasurpanel/Timestepvalue","NVALUE":400.0/(Freqstopvalue*1024))
       GOTO Circle
       END IF
       NEXT I
       END IF
       GOTO Circle
       CASE "Noisepanel/Timemeasurpanel/Numberofblockvalue"
       CONTROL @Sys;SET ("*NAME":"Noisepanel/Timemeasurpanel/Numberofblockvalue")
       STATUS @Sys;RETURN ("VALUE":Blocks)
       CONTROL                                                                                     @Sys;SET
("*NAME":"Noisepanel/Timemeasurpanel/Timevalue","NVALUE":Blocks*400.0/Freqstopvalue)
       CONTROL                                                                                     @Sys;SET
("*NAME":"Noisepanel/Timemeasurpanel/Timestepvalue","NVALUE":400.0/(Freqstopvalue*1024))
       GOTO Circle

       END SELECT

       !------------ Directory reading -------------------
        Readdirectory:!
       STATUS @Filepath;RETURN ("DIRECTORY":Dir$)
       CONTROL @Filepath;SET ("VISIBLE":0)
       CONTROL @Sys;SET ("*NAME":"Noisepanel/Filepathpanel/Filedir")
       IF Dir$[LEN(Dir$)]<>"\" THEN Dir$=Dir$&"\"
       CONTROL @Sys;SET ("VALUE":Dir$)
       GOTO Circle
```

```
!---------- Starting measurements -----------------

 Start:!

CONTROL @Sys;SET ("*NAME":"Noisepanel/Start")
CONTROL @Sys;SET ("VISIBLE":0)
CONTROL @Sys;SET ("*NAME":"Noisepanel/Vsample")
CONTROL @Sys;SET ("VISIBLE":0)
CONTROL @Sys;SET ("*NAME":"Noisepanel/Abort")
CONTROL @Sys;SET ("VISIBLE":1)

GOSUB Check_file

    !CONTROL @Sys;SET ("*NAME":"Noisepanel/Status")
    !CONTROL @Sys;SET ("VALUE":F$&Part$)

   !Enter the number of time records used to average the measurement data
CONTROL @Sys;SET ("*NAME":"Noisepanel/Averagingnumber")
STATUS @Sys;RETURN ("VALUE":Naver)
IF Naver<0 THEN Naver=1
IF Naver>9999999 THEN Naver=9999999
CONTROL @Sys;SET ("VALUE":Naver)

   !Enter the number of how often the display is updated when fast average mode is on
CONTROL @Sys;SET ("*NAME":"Noisepanel/Updatenumber")
STATUS @Sys;RETURN ("VALUE":Nupdate)
IF Nupdate<0 THEN Nupdate=1
IF Nupdate>9999999 THEN Nupdate=9999999
CONTROL @Sys;SET ("VALUE":Nupdate)

   !Checking either turned overload rejection on or off
CONTROL @Sys;SET ("*NAME":"Noisepanel/Overload")
STATUS @Sys;RETURN ("VALUE":Bover)

   !Checking the calibration toggle
CONTROL @Sys;SET ("*NAME":"Noisepanel/Calibration")
STATUS @Sys;RETURN ("VALUE":Bcal)


GOSUB Get_temp_1


OUTPUT @Analyzer;"*CLS"
CONTROL @Sys;SET ("*NAME":"Noisepanel/Status")
CONTROL @Sys;SET ("PEN":24)
IF Bcal=1 THEN
CONTROL @Sys;SET ("*NAME":"Noisepanel/Status")
CONTROL @Sys;SET ("VALUE":"Calibration in progress")
OUTPUT @Analyzer;"*CAL?;*WAI"
ENTER @Analyzer;Calibration
IF Calibration=0 THEN CONTROL @Sys;SET ("VALUE":"Calibration is Ok")
IF Calibration=1 THEN
CONTROL  @Sys;SET  ("VALUE":"Calibration  failed!!!  Please,  check  the  analyzer  to  continue
measurements","PEN":2)
GOTO Circle
END IF
END IF
OUTPUT @Analyzer;":AVER ON"
OUTPUT @Analyzer;"SENS:AVERAGE:IRES:RATE ";Nupdate
OUTPUT @Analyzer;"SENS:AVERAGE:COUNT ";Naver
OUTPUT @Analyzer;"SENS:REJ:STAT ";Bover
OUTPUT @Analyzer;"CALC1:DATA:HEAD:POIN?"
ENTER @Analyzer;P
CONTROL @Sys;SET ("*NAME":"Noisepanel/Status")
CONTROL @Sys;SET ("VALUE":"Number of points: "&VAL$(P-1))

CONTROL @Sys;SET ("*NAME":"Noisepanel/Noisespectrum")
CONTROL @Sys;SET ("CURRENT TRACE":5,"X DATA":Frequencylast(*))
CONTROL @Sys;SET ("CURRENT TRACE":5,"Y DATA":Datalast(*))


GOSUB Get_voltage_1

!--------- Starting the measurement -------------------
REDIM Freq1(P-1)
REDIM Dat1(P-1)
```

```
REDIM Freq2(P-1)
REDIM Dat2(P-1)

FOR N=0 TO P-1
Freq1(N)=N
Freq2(N)=N*64
NEXT N
Freq1(0)=.0000001
Freq2(0)=.0000001

CONTROL @Sys;SET ("*NAME":"Noisepanel/Status")
CONTROL @Sys;SET ("VALUE":"Getting the first range of spectrum")
OUTPUT @Analyzer;"SENS:FREQ:STAR 0.0"
OUTPUT @Analyzer;"SENS:FREQ:STOP 1.6 KHZ"
OUTPUT @Analyzer;"ABORT;:INIT;*WAI"
OUTPUT @Analyzer;"CALC1:DATA?"
ENTER @Analyzer USING "%,A,D";Term$,Digits
ENTER @Analyzer USING "%,"&VAL$(Digits)&"D";Num_of_bytes
Num_points=Num_of_bytes DIV 8
ENTER @Analyzer_bin;Dat1(*)
ENTER @Analyzer;Term$
CONTROL @Sys;SET ("VALUE":"Ok")
FOR N=0 TO P-1
IF Dat1(N)<=0 THEN Dat1(N)=1.E-20
NEXT N

CONTROL @Sys;SET ("*NAME":"Noisepanel/Noisespectrum")
CONTROL @Sys;SET ("CURRENT TRACE":1,"X DATA":Freq1(*))
CONTROL @Sys;SET ("CURRENT TRACE":1,"Y DATA":Dat1(*))

CONTROL @Sys;SET ("*NAME":"Noisepanel/Status")
CONTROL @Sys;SET ("VALUE":"Getting the second range of spectrum")
OUTPUT @Analyzer;"SENS:FREQ:STOP 102.4 KHZ"
OUTPUT @Analyzer;":INIT;*WAI"
OUTPUT @Analyzer;"CALC1:DATA?;*WAI"
ENTER @Analyzer USING "%,A,D";Term$,Digits
ENTER @Analyzer USING "%,"&VAL$(Digits)&"D";Num_of_bytes
Num_points=Num_of_bytes DIV 8
ENTER @Analyzer_bin;Dat2(*)
ENTER @Analyzer;Term$
CONTROL @Sys;SET ("VALUE":"Ok")
FOR N=0 TO P-1
IF Dat2(N)<=0 THEN Dat2(N)=1.E-20
NEXT N

CONTROL @Sys;SET ("*NAME":"Noisepanel/Noisespectrum")
CONTROL @Sys;SET ("CURRENT TRACE":2,"X DATA":Freq2(*))
CONTROL @Sys;SET ("CURRENT TRACE":2,"Y DATA":Dat2(*))
    !ASSIGN @Sys TO *

    !==================== Saving =======================
CONTROL @Sys;SET ("*NAME":"Noisepanel/Status")
CONTROL @Sys;SET ("VALUE":"Saving...")
    !--------- Taking the calibration curves -----------
ASSIGN @File TO Home$&"h0.dat";FORMAT ON
RESET @File
ENTER @File;H0(*)
ASSIGN @File TO *
ASSIGN @File TO Home$&"h0n.dat";FORMAT ON
RESET @File
ENTER @File;H0n(*)
ASSIGN @File TO *
ASSIGN @File TO Home$&"k2.dat";FORMAT ON
RESET @File
ENTER @File;K2(*)
ASSIGN @File TO *
ASSIGN @File TO Home$&"k2n.dat";FORMAT ON
RESET @File
ENTER @File;K2n(*)
ASSIGN @File TO *
    !--------- Taking the amplified coeficient ---------
CONTROL @Sys;SET ("*NAME":"Noisepanel/Amplifierspanel/Nsecondamplifier")
STATUS @Sys;RETURN ("SELECTION":N)
CONTROL @Sys;SET ("*NAME":"Noisepanel/Amplifierspanel/Hmamplifier")
STATUS @Sys;RETURN ("VALUE":Hmampl)

PRINT Acoef(N)
```

```
FOR I=1 TO 1600
Data(I)=(Dat1(I)/Acoef(N)/Acoef(N)-H0(I))/K2(I)
IF Hmampl=1 THEN
Data(I)=(Data(I)-H0n(I))/K2n(I)
Data(I)=Data(I)/(178*178)
END IF
Frequency(I)=I
NEXT I
FOR I=26 TO 1600
Data(I+1575)=(Dat2(I)/Acoef(N)/Acoef(N)-H0(I+1575))/K2(I+1575)
IF Hmampl=1 THEN
Data(I+1575)=(Data(I+1575)-H0n(I+1575))/K2n(I+1575)
Data(I+1575)=Data(I+1575)/(178*178)
END IF
Frequency(I+1575)=I*64
NEXT I
Nminus=0
FOR N=1 TO 3175
IF Data(N)<=0 THEN
Nminus=Nminus+1
END IF
NEXT N

IF Nminus>=3175 THEN
CONTROL @Sys;SET ("*NAME":"Noisepanel/Status")
CONTROL @Sys;SET ("VALUE":"The amplifier was grounded or the gain is not set correctly","PEN":2)
GOTO Circle
END IF

IF  Nminus<3175  THEN  REDIM  Frequencylast(1:3175-Nminus),Datalast(1:3175-Nminus),Datasvtemp(1:3175-
Nminus),Resistance(1:3175-Nminus)
Nminus=0
FOR N=1 TO 3175
IF Data(N)>0 THEN
Datalast(N-Nminus)=Data(N)
Frequencylast(N-Nminus)=Frequency(N)
ELSE
Nminus=Nminus+1
END IF
NEXT N


CONTROL @Sys;SET ("*NAME":"Noisepanel/Noisespectrum")
CONTROL @Sys;SET ("CURRENT TRACE":3,"X DATA":Frequencylast(*))
CONTROL @Sys;SET ("CURRENT TRACE":3,"Y DATA":Datalast(*))

GOSUB Get_voltage_2
GOSUB Get_temp_2

!-------------- Show thermal noise -------------
Rsample=Voltageaver1/(Voltageaver2-Voltageaver1)*Rnvalue
FOR N=1 TO 3175-Nminus
Resistance(N)=(Rnvalue+Voltageaver2*1000/(Voltageaver2*1000*2*PI*Frequencylast(N)*9.4E-
3+6.3))*Rsample/(Rnvalue+Voltageaver2*1000/(Voltageaver2*1000*2*PI*Frequencylast(N)*9.4E-3+6.3)+Rsample)
    !PRINT Voltageaver2*1000/(Voltageaver2*1000*2*PI*Frequencylast(N)*9.4E-3+6.3),Rsample
Datasvtemp(N)=4*1.38E-23*Temperaturee*Resistance(N)/(1+(2*PI*Resistance(N)*Frequencylast(N)*3.2E-
10*2*PI*Resistance(N)*Frequencylast(N)*3.2E-10))
NEXT N
CONTROL @Sys;SET ("*NAME":"Noisepanel/Noisespectrum")
IF Rsample>0 THEN
CONTROL @Sys;SET ("CURRENT TRACE":4,"X DATA":Frequencylast(*))
CONTROL @Sys;SET ("CURRENT TRACE":4,"Y DATA":Datasvtemp(*))
END IF


!-------------- Saving ------------------
CONTROL @Sys;SET ("*NAME":"Noisepanel/Status")
CONTROL @Sys;SET ("VALUE":"Saving")

CREATE Directory$&F$&"a"&Part$,20
ASSIGN @File TO Directory$&F$&"a"&Part$;FORMAT ON
FOR N=0 TO P-1
OUTPUT @File;Dat1(N);CHR$(13);
NEXT N

CREATE Directory$&F$&"b"&Part$,20
ASSIGN @File TO Directory$&F$&"b"&Part$;FORMAT ON
```

```
FOR N=0 TO P-1
OUTPUT @File;Dat2(N);CHR$(13);
NEXT N

CREATE Directory$&F$&Part$,20
ASSIGN @File TO Directory$&F$&""&Part$;FORMAT ON
FOR N=1 TO 3175-Nminus
IF (Datalast(N)-Datasvtemp(N))*(1+(2*PI*Resistance(N)*Frequencylast(N)*3.2E-10*2*PI*Resistance(N)*Frequencylast(N)*3.2E-10))<0 THEN
OUTPUT @File;Frequencylast(N);CHR$(9);Datalast(N);CHR$(9);"-";CHR$(13);
ELSE
OUTPUT @File;Frequencylast(N);CHR$(9);Datalast(N);CHR$(9);(Datalast(N)-Datasvtemp(N))*(1+(2*PI*Resistance(N)*Frequencylast(N)*3.2E-10*2*PI*Resistance(N)*Frequencylast(N)*3.2E-10));CHR$(13);
END IF
NEXT N

ASSIGN @File TO *
CONTROL @Sys;SET ("*NAME":"Noisepanel/Filepathpanel/Fileautoincrease")
STATUS @Sys;RETURN ("VALUE":N)
IF N=1 THEN
CONTROL @Sys;SET ("*NAME":"Noisepanel/Filepathpanel/Filenumber")
CONTROL @Sys;SET ("VALUE":Nfile+1)
END IF
ASSIGN @File TO Directory$&"MeasurData.dat";FORMAT ON,RETURN S
ASSIGN @File TO *
IF S=0 THEN
ASSIGN @File TO Directory$&"MeasurData.dat";FORMAT ON,APPEND
ELSE
CREATE Directory$&"MeasurData.dat",20
ASSIGN @File TO Directory$&"MeasurData.dat";FORMAT ON
OUTPUT @File;"U\-(sample)";CHR$(9);"Current";CHR$(9);"R\-(Eq)";CHR$(9);"Filename";CHR$(9);"R\-(load)";CHR$(9);"U\-(Whole)";CHR$(9);"U\-(0sample)";CHR$(9);"U\-(0Whole)";CHR$(9);
OUTPUT @File;"R\-(0sample)";CHR$(9);"R\-(Esample)";CHR$(9);"Temperature\-(0)";CHR$(9);"Temperature\-(E)";CHR$(9);"k\-(ampl)";CHR$(9);"N\-(aver)";CHR$(9);"V\-(Gate)";CHR$(13);
OUTPUT
@File;"V";CHR$(9);"A";CHR$(9);"\g(W)";CHR$(9);"";CHR$(9);"\g(W)";CHR$(9);"V";CHR$(9);"V";CHR$(9);"V";CHR$(9);
OUTPUT
@File;"\g(W)";CHR$(9);"\g(W)";CHR$(9);"K";CHR$(9);"K";CHR$(9);"";CHR$(9);"";CHR$(9);"V";CHR$(13);
END IF
CONTROL @Sys;SET ("*NAME":"Noisepanel/Amplifierspanel/Nsecondamplifier")
STATUS @Sys;RETURN ("SELECTION":N)
OUTPUT @File;Voltageaver1;CHR$(9);(Voltageaver2-Voltageaver1)/Rnvalue;CHR$(9);Rsample*Rnvalue/(Rsample+Rnvalue);CHR$(9);F$&Part$;CHR$(9);Rnvalue;CHR$(9);Voltageaver2;CHR$(9);Voltageaver01;CHR$(9);Voltageaver02;CHR$(9);
OUTPUT @File;Voltageaver01*Rnvalue/(Voltageaver02-Voltageaver01);CHR$(9);Rsample;CHR$(9);Temperature0;CHR$(9);Temperaturee;CHR$(9);Acoef(N);CHR$(9);Naver;CHR$(9);Gatevoltage;CHR$(13)
ASSIGN @File TO *
CONTROL @Sys;SET ("*NAME":"Noisepanel/Status")
CONTROL @Sys;SET ("VALUE":"The data were saved.")
BEEP
GOTO Circle

!--------------- Time capture module ---------------------------------
 Start2:!

CONTROL @Sys;SET ("*NAME":"Noisepanel/Start")
CONTROL @Sys;SET ("VISIBLE":0)
CONTROL @Sys;SET ("*NAME":"Noisepanel/Vsample")
CONTROL @Sys;SET ("VISIBLE":0)
CONTROL @Sys;SET ("*NAME":"Noisepanel/Abort")
CONTROL @Sys;SET ("VISIBLE":1)

GOSUB Check_file
GOSUB Get_temp_1
GOSUB Get_voltage_1
!GOSUB Get_gvolt


CONTROL @Sys;SET ("*NAME":"Noisepanel/Status")
CONTROL @Sys;SET ("VALUE":"Configuration of the analyzer...")
!OUTPUT @Analyzer;"SENS:FEED TCAPTURE"
OUTPUT @Analyzer;"FREQ:STAR 0"
OUTPUT @Analyzer;"FREQ:STOP "&VAL$(Freqstopvalue)&" HZ"
OUTPUT @Analyzer;"CALC1:UNIT:VOLT 'V'"
```

```
Timestep=400/(Freqstopvalue-0)/1024

OUTPUT @Analyzer;"MEM:DEL:ALL"
OUTPUT @Analyzer;"TCAP:LENG "&VAL$(Blocks)&" BLK"
CONTROL @Sys;SET ("*NAME":"Noisepanel/Status")
CONTROL @Sys;SET ("PEN":24)
CONTROL @Sys;SET ("VALUE":"Getting data...")
OUTPUT @Analyzer;"TCAP:MALL"
OUTPUT @Analyzer;"TCAP;*WAI"
OUTPUT @Analyzer;"FORM REAL,64"
OUTPUT @Analyzer;"SENSE:DATA? TCAP1;*WAI"
ENTER @Analyzer USING "%,A,D";Term$,Ii
ENTER @Analyzer USING "%,"&VAL$(Ii)&"D";Bytes
P=Bytes/8
Records=P/1024
!PRINT Records
REDIM Y(1:Blocks,1:1024)
Step=INT(P/30000)+1
!REDIM Ydata(1:30000)
!REDIM Xdata(1:30000)
CONTROL @Sys;SET ("*NAME":"Noisepanel/Noisespectrum","POINT CAPACITY":30000)
IF Step=1 THEN
REDIM Ydata(1:INT(P))
REDIM Xdata(1:INT(P))
END IF
ENTER @Analyzer_bin;Y(*)
ENTER @Analyzer;Term$
CREATE Directory$&F$&Part$,20
ASSIGN @File TO Directory$&F$&Part$;FORMAT ON

!--------- Geting the amplified coeficient ---------
CONTROL @Sys;SET ("*NAME":"Noisepanel/Amplifiers/Nsecondamplifier")
STATUS @Sys;RETURN ("SELECTION":N)
CONTROL @Sys;SET ("*NAME":"Noisepanel/Amplifiers/Hmamplifier")
STATUS @Sys;RETURN ("VALUE":Hmampl)
Namplifiers=Acoef(N)
IF Hmampl=1 THEN
Namplifiers=-Namplifiers*178
END IF

K=1
N=1
FOR K=1 TO Records
FOR N=1 TO 1024
X=1024*(K-1)+N-1
T=X*Timestep
OUTPUT @File;T;CHR$(9);Y(K,N)/Namplifiers;CHR$(13)
IF ((K-1)*1024+N) MOD Step=0 THEN
Xdata(((K-1)*1024+N)/Step)=T
Ydata(((K-1)*1024+N)/Step)=Y(K,N)/Namplifiers
END IF
NEXT N
NEXT K
CONTROL @Sys;SET ("*NAME":"Noisepanel/Noisespectrum")
CONTROL @Sys;SET ("CURRENT TRACE":1,"X DATA":Xdata(*))
CONTROL @Sys;SET ("CURRENT TRACE":1,"Y DATA":Ydata(*))

CONTROL @Sys;SET ("*NAME":"Noisepanel/Filepathpanel/Fileautoincrease")
STATUS @Sys;RETURN ("VALUE":N)
IF N=1 THEN
CONTROL @Sys;SET ("*NAME":"Noisepanel/Filepathpanel/Filenumber")
CONTROL @Sys;SET ("VALUE":Nfile+1)
END IF

GOSUB Get_temp_2
GOSUB Get_voltage_2


Rsample=Voltageaver1/(Voltageaver2-Voltageaver1)*Rnvalue

ASSIGN @File TO Directory$&"MeasurDataCapture.dat";FORMAT ON,RETURN S
ASSIGN @File TO *
IF S=0 THEN
ASSIGN @File TO Directory$&"MeasurDataCapture.dat";FORMAT ON,APPEND
ELSE
CREATE Directory$&"MeasurDataCapture.dat",20
```

```
        ASSIGN @File TO Directory$&"MeasurDataCapture.dat";FORMAT ON
        OUTPUT  @File;"U\-(sample)";CHR$(9);"Current";CHR$(9);"R\-(0sample)";CHR$(9);"Filename";CHR$(9);"R\-(load)";CHR$(9);"U\-(Whole)";CHR$(9);"U\-(0sample)";CHR$(9);"U\-(0Whole)";CHR$(9);
        OUTPUT @File;"R\-(0sample)";CHR$(9);"R\-(Esample)";CHR$(9);"Temperature\-(0)";CHR$(9);"Temperature\-(E)";CHR$(9);"k\-(ampl)";CHR$(9);"V\-(Gate)";CHR$(13);
        OUTPUT @File;"V";CHR$(9);"A";CHR$(9);"\g(W)";CHR$(9);"";CHR$(9);"\g(W)";CHR$(9);"V";CHR$(9);"V";CHR$(9);"V";CHR$(9);
        OUTPUT @File;"\g(W)";CHR$(9);"\g(W)";CHR$(9);"K";CHR$(9);"K";CHR$(9);"";CHR$(9);"V";CHR$(13);
        END IF
        CONTROL @Sys;SET ("*NAME":"Noisepanel/Amplifierspanel/Nsecondamplifier")
        STATUS @Sys;RETURN ("SELECTION":N)
        OUTPUT @File;Voltageaver1;CHR$(9);(Voltageaver2-Voltageaver1)/Rnvalue;CHR$(9);Rsample;CHR$(9);F$&Part$;CHR$(9);Rnvalue;CHR$(9);Voltageaver2;CHR$(9);Voltageaver01;CHR$(9);Voltageaver02;CHR$(9);
        OUTPUT @File;Voltageaver01*Rnvalue/(Voltageaver02-Voltageaver01);CHR$(9);Rsample;CHR$(9);Temperature0;CHR$(9);Temperaturee;CHR$(9);Acoef(N);CHR$(9);Gatevoltage;CHR$(13)
        ASSIGN @File TO *


        CONTROL @Sys;SET ("*NAME":"Noisepanel/Status")
        CONTROL @Sys;SET ("VALUE":"Done")
        BEEP
        GOTO Circle


         Finish:!

        STATUS @Sys;RETURN ("*QUEUED EVENT":Ev$(*))
        IF Ev$(0)="Multimetrpanel" THEN
        CONTROL @Sys;SET ("*NAME":"Multimetrpanel","VISIBLE":0)
        CONTROL @Sys;SET ("*NAME":"Noisepanel/Status")
        CONTROL @Sys;SET ("VALUE":"Please, press 'Start' to start the measurement")
        CONTROL @Sys;SET ("*NAME":"Noisepanel/Start","VISIBLE":1)
        CONTROL @Sys;SET ("*NAME":"Noisepanel/Vsample","VISIBLE":1)
        GOTO Circle
        END IF

        STOP


         Get_voltage: WAIT Waitseconds
        OUTPUT @Volt;"CALC:FUNC AVER;STAT ON"
        OUTPUT @Volt;"INIT"
        OUTPUT @Volt;"CALC:AVER:AVER?"
        ENTER @Volt;Voltage
        OUTPUT @Volt;"CALC:FUNC AVER;STAT OFF"
        OUTPUT @Volt;"SENS:VOLT:DC:RANG:AUTO ON"
        LOCAL @Volt
        RETURN

         Check_file: CONTROL @Sys;SET ("*NAME":"Noisepanel/Status")
        CONTROL @Sys;SET ("VALUE":"Checking path and name of file...")
        CONTROL @Sys;SET ("*NAME":"Noisepanel/Filepathpanel/Filedir")
        STATUS @Sys;RETURN ("VALUE":Part$)
        Directory$=Part$
        CONTROL @Sys;SET ("*NAME":"Noisepanel/Filepathpanel/Filename")
        STATUS @Sys;RETURN ("VALUE":Part$)
        F$=Part$
        CONTROL @Sys;SET ("*NAME":"Noisepanel/Filepathpanel/Filenumber")
        STATUS @Sys;RETURN ("VALUE":Nfile)
        F$=F$&VAL$(Nfile)
        CONTROL @Sys;SET ("*NAME":"Noisepanel/Filepathpanel/Fileextention")
        STATUS @Sys;RETURN ("VALUE":Part$)

        ASSIGN @File TO Directory$&F$&Part$;FORMAT ON,RETURN S
        IF S=0 THEN
        CONTROL @Sys;SET ("*NAME":"Noisepanel/Status")
        CONTROL @Sys;SET ("VALUE":"The file "&F$&Part$&" exist. Change the file name and press 'Start' to continue","PEN":2)
        GOTO Circle
        END IF
        RETURN
        !----------- Get temperature ---------
         Get_temp_1: CONTROL @Sys;SET ("*NAME":"Noisepanel/Status")
        CONTROL @Sys;SET ("VALUE":"Geting temperature...")
```

```
CONTROL @Sys;SET ("PEN":24)
     !Checking reading value from temperature controller
CONTROL @Sys;SET ("*NAME":"Noisepanel/Temperaturepanel/Tcontroller")
STATUS @Sys;RETURN ("VALUE":Tcont)
Temperature0=300
IF Tcont=1 THEN
      !OUTPUT @Temp;"KRDG?A1"                ! LakeShore controller
      !OUTPUT @Temp;"QSAMP?<1>;OUTPACTI;"
OUTPUT @Temp;"KRDG?"                         ! small LakeShore controller 211
WAIT 1
ENTER @Temp;Temperature0
CONTROL @Sys;SET ("*NAME":"Noisepanel/Temperaturepanel/Temperaturenumber")
CONTROL @Sys;SET ("NVALUE":Temperature0)
END IF
CONTROL @Sys;SET ("*NAME":"Noisepanel/Temperaturepanel/Temperaturenumber")
STATUS @Sys;RETURN ("NVALUE":Temperature0)
RETURN

 Get_temp_2: CONTROL @Sys;SET ("*NAME":"Noisepanel/Temperaturepanel/Tcontroller")
STATUS @Sys;RETURN ("VALUE":Tcont)

IF Tcont=1 THEN
      !OUTPUT @Temp;"KRDG?A1"
      !OUTPUT @Temp;"QSAMP?<1>;OUTPACTI;"
OUTPUT @Temp;"KRDG?A1"
WAIT 1
ENTER @Temp;Temperaturee
CONTROL @Sys;SET ("*NAME":"Noisepanel/Temperaturepanel/Temperaturenumber")
CONTROL @Sys;SET ("NVALUE":Temperaturee)
END IF
CONTROL @Sys;SET ("*NAME":"Noisepanel/Temperaturepanel/Temperaturenumber")
STATUS @Sys;RETURN ("NVALUE":Temperaturee)
RETURN

!----------- Get gate voltage ---------
 Get_gvolt: CONTROL @Sys;SET ("*NAME":"Noisepanel/Status")
CONTROL @Sys;SET ("VALUE":"Geting gate voltage...")
CONTROL @Sys;SET ("PEN":24)
     !Checking reading value from temperature controller
CONTROL @Sys;SET ("*NAME":"Noisepanel/Measurementspanel/Vgate")
STATUS @Sys;RETURN ("VALUE":Vgcont)
Gatevoltage=0
IF Vgcont=1 THEN
OUTPUT 722;"SYST:BEEP:STAT OFF"              ! Turns off the beeper
OUTPUT 722;"MEAS:VOLTAGE:DC?"
ENTER 722;Gatevoltage
LOCAL 722
CONTROL @Sys;SET ("*NAME":"Noisepanel/Measurementspanel/Vgatenumber")
CONTROL @Sys;SET ("NVALUE":Gatevoltage)
END IF
CONTROL @Sys;SET ("*NAME":"Noisepanel/Measurementspanel/Vgatenumber")
STATUS @Sys;RETURN ("NVALUE":Gatevoltage)
RETURN

!-------------- Get voltage ------------
 Get_voltage_1: OUTPUT @Analyzer;"OUTPUT:STAT ON"
CONTROL @Sys;SET ("*NAME":"Noisepanel/Vsample")
CONTROL @Sys;SET ("LABEL":"Vmain")
Vsample=0
    !------------ Get the voltage on the sample --------
CONTROL @Sys;SET ("*NAME":"Noisepanel/Status")
CONTROL @Sys;SET ("VALUE":"Getting the voltage applied to the sample")
CONTROL @Sys;SET ("PEN":24)
GOSUB Get_voltage
Voltageaver01=Voltage
CONTROL @Sys;SET ("*NAME":"Noisepanel/Measurementspanel/Vs0value")
CONTROL @Sys;SET ("VALUE":Voltageaver01)
GOSUB Get_gvolt


    !------------ Get the whole voltage ---------
OUTPUT @Analyzer;"OUTPUT:STAT OFF"
CONTROL @Sys;SET ("*NAME":"Noisepanel/Vsample")
CONTROL @Sys;SET ("LABEL":"Vsample")
Vsample=1
CONTROL @Sys;SET ("*NAME":"Noisepanel/Status")
CONTROL @Sys;SET ("VALUE":"Getting the whole voltage")
```

```
GOSUB Get_voltage
Voltageaver02=Voltage
CONTROL @Sys;SET ("*NAME":"Noisepanel/Measurementspanel/Vm0value")
CONTROL @Sys;SET ("VALUE":Voltageaver02)
CONTROL @Sys;SET ("*NAME":"Noisepanel/Measurementspanel/Rloadvalue")
STATUS @Sys;RETURN ("VALUE":Rnvalue)
CONTROL @Sys;SET ("*NAME":"Noisepanel/Measurementspanel/I0value")
CONTROL @Sys;SET ("VALUE":(Voltageaver02-Voltageaver01)/Rnvalue)
CONTROL @Sys;SET ("*NAME":"Noisepanel/Measurementspanel/Rs0value")
CONTROL @Sys;SET ("VALUE":Voltageaver01*Rnvalue/(Voltageaver02-Voltageaver01))
LOCAL @Volt
RETURN

 Get_voltage_2:!------------ Get the voltage on the sample --------
OUTPUT @Analyzer;"OUTPUT:STAT ON"
CONTROL @Sys;SET ("*NAME":"Noisepanel/Vsample")
CONTROL @Sys;SET ("LABEL":"Vmain")
Vsample=0
CONTROL @Sys;SET ("*NAME":"Noisepanel/Status")
CONTROL @Sys;SET ("VALUE":"Getting the voltage applied to the sample")
GOSUB Get_voltage
Voltageaver1=Voltage
CONTROL @Sys;SET ("*NAME":"Noisepanel/Measurementspanel/Vskvalue")
CONTROL @Sys;SET ("VALUE":Voltageaver1)

    !------------ Get the whole voltage --------
OUTPUT @Analyzer;"OUTPUT:STAT OFF"
CONTROL @Sys;SET ("*NAME":"Noisepanel/Vsample")
CONTROL @Sys;SET ("LABEL":"Vsample")
Vsample=1
CONTROL @Sys;SET ("*NAME":"Noisepanel/Status")
CONTROL @Sys;SET ("VALUE":"Getting the whole voltage")
GOSUB Get_voltage
Voltageaver2=Voltage
CONTROL @Sys;SET ("*NAME":"Noisepanel/Measurementspanel/Vmkvalue")
CONTROL @Sys;SET ("VALUE":Voltageaver2)
CONTROL @Sys;SET ("*NAME":"Noisepanel/Measurementspanel/Rloadvalue")
STATUS @Sys;RETURN ("VALUE":Rnvalue)
CONTROL @Sys;SET ("*NAME":"Noisepanel/Measurementspanel/Ikvalue")
CONTROL @Sys;SET ("VALUE":(Voltageaver2-Voltageaver1)/Rnvalue)
CONTROL @Sys;SET ("*NAME":"Noisepanel/Measurementspanel/Rskvalue")
CONTROL @Sys;SET ("VALUE":Voltageaver1*Rnvalue/(Voltageaver2-Voltageaver1))
LOCAL @Volt

RETURN
```

2. Getting Flicker & GR v9.1 Optimized program written using Wolfram Mathematica

The interface of the program:

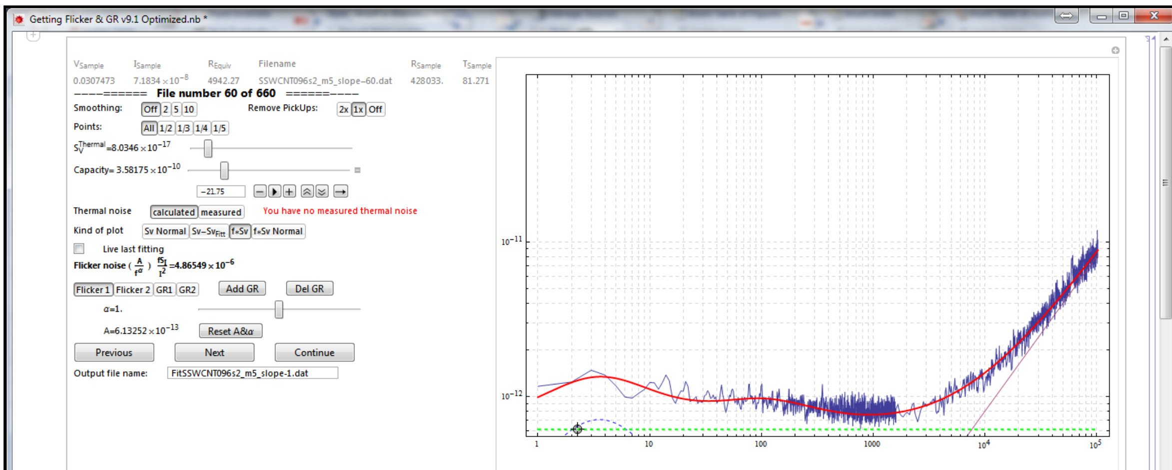

The program code:

```
Manipulate[
 If[AdMessage != "Could not find data files" &&
   AdMessage !=
    "Could not find " <> NameDirectory <> "MeasurData.dat file",
  CFlicker[[NumberFile]] = Exp[Capacity];
  If[ttlast != tt,
   If[tt > 2,
    ttlast = tt;
    pt = Log[{ParGR[[tt, 2]], ParGR[[tt, 1]]*ParGR[[tt, 2]]*0.5}];
    pt1 = Log[{ParGR[[tt, 2]], ParGR[[tt, 1]]*0.5}],
    ttlast = tt;
    \[Alpha] = ParGR[[tt, 2]];
    pt = {0, Log[ParGR[[tt, 1]]]};
    pt1 = pt;
    ],
   If[tt > 2,
     If[NofGraphic <= 1,
      ParGR[[tt, 2]] = Exp[pt1[[1]]];
      ParGR[[tt, 1]] = 2 Exp[pt1[[2]]];
      pt[[1]] = pt1[[1]]; pt[[2]] = pt1[[2]] + pt1[[1]];
      ];
     If[NofGraphic == 2,
      ParGR[[tt, 2]] = Exp[pt[[1]]];
      ParGR[[tt, 1]] = 2 Exp[pt[[2]] - pt[[1]]];
      pt1[[1]] = pt[[1]]; pt1[[2]] = pt[[2]] - pt[[1]];
      ],
     If[NofGraphic <= 1,
      ParGR[[tt, 1]] = Exp[pt1[[2]] + pt1[[1]]*\[Alpha]];
      ParGR[[tt, 2]] = \[Alpha];
      pt[[1]] = pt1[[1]]; pt[[2]] = pt1[[2]] + pt1[[1]];
      ];
     If[NofGraphic == 2,
      ParGR[[tt, 1]] = Exp[pt[[2]] + pt[[1]]*\[Alpha] - pt[[1]]];
      ParGR[[tt, 2]] = \[Alpha];
      pt1[[1]] = pt[[1]]; pt1[[2]] = pt[[2]] - pt[[1]];
      ]
     ];
   ];
  AfGR[[NumberFile]] = ParGR;
  If[ShowThermal == 1, SvE = 0, SvE = SvTher];
  If[NofGraphic <= 1,
   PlotGR =
    Join[Table[(
      ParGR[[GR, 1]]*ParGR[[GR, 2]]^2)/(ParGR[[GR, 2]]^2 + fg^2), {GR,
        3, NGRNoises + 2}], {ParGR[[1, 1]]*fg^-ParGR[[1, 2]],
```

```
    ParGR[[2, 1]]*fg^-ParGR[[2, 2]],
    Plus @@ Append[
       Table[(ParGR[[GR, 1]]*
         ParGR[[GR, 2]]^2)/(ParGR[[GR, 2]]^2 + fg^2), {GR, 3,
         NGRNoises + 2}],
       ParGR[[1, 1]]*fg^-ParGR[[1, 2]] +
        ParGR[[2, 1]]*fg^-ParGR[[2, 2]]] + SvE}],
 PlotGR =
  Join[Table[(
    ParGR[[GR, 1]]*ParGR[[GR, 2]]^2*
     fg)/(ParGR[[GR, 2]]^2 + fg^2), {GR, 3,
     NGRNoises + 2}], {ParGR[[1, 1]]*fg^(1 - ParGR[[1, 2]]),
    ParGR[[2, 1]]*fg^(1 - ParGR[[2, 2]]),
    Plus @@ Append[
       Table[(ParGR[[GR, 1]]*ParGR[[GR, 2]]^2*
         fg)/(ParGR[[GR, 2]]^2 + fg^2), {GR, 3, NGRNoises + 2}],
       ParGR[[1, 1]]*fg^(1 - ParGR[[1, 2]]) +
        ParGR[[2, 1]]*fg^(1 - ParGR[[2, 2]])] + SvE*fg}]];
If[NofGraphic == 2,
 If[pt[[2]] <= LogMinfSv,
  If[pt[[2]] <= LogMinfSv - 2.3,
   PlotfSvRangeY = {LogMinfSv - 4, LogMaxfSv},
   PlotfSvRangeY = {LogMinfSv - 2.35, LogMaxfSv}],
  PlotfSvRangeY = {LogMinfSv, LogMaxfSv}];
 If[pt[[1]] <= 0,
  PlotfSvRangeX = {-2.3026, 11.5366},
  If[pt[[1]] >= 11.5366,
   PlotfSvRangeX = {0, 13.84},
   PlotfSvRangeX = {0, 11.5366}]
  ];
 PlotfSvRange = {PlotfSvRangeX, PlotfSvRangeY}
 ];
PStyle = If[tt > 2,
  Join[ReplacePart[
    Table[Directive[Blue, Dashed], {GR, 3, NGRNoises + 2}],
    tt - 2 -> Directive[Blue, Thick, Dashed]], {Directive[Green,
     Dashed], Directive[Green, Dashed], Directive[Red, Thick]}],
  If[tt == 1,
   Join[Table[
     Directive[Blue, Dashed], {GR, 3, NGRNoises + 2}], {Directive[
      Green, Thick, Dashed], Directive[Green, Dashed],
     Directive[Red, Thick]}],
   Join[Table[
     Directive[Blue, Dashed], {GR, 3, NGRNoises + 2}], {Directive[
      Green, Dashed], Directive[Green, Thick, Dashed],
     Directive[Red, Thick]}]]];
Switch[NofGraphic,
 0,
 LocatorPane[Dynamic[pt1],
  Show[{ListLogLogPlot[{Transpose[{Frequency,
        Sv*CorrectCapacity}], {Transpose[{Frequency,
         Table[MeanSvT, {i,
           Length[Frequency]}]}]}, {Transpose[{Frequency,
         Table[Sv0, {i, Length[Frequency]}]}]}}, Joined -> True,
     GridLines -> Automatic,
     GridLinesStyle -> Directive[LightGray, Dashed], Frame -> True,
     PlotRange -> All, ImageSize -> 700],
    LogLogPlot[PlotGR, {fg, 1, 102400}, PlotStyle -> PStyle]},
   PlotRange -> All, Frame -> True, ImageSize -> Scaled[1],
   ImageMargins -> None]],
 1,
 Svtemp :=
  Sv*CorrectCapacity - ParGR[[1, 1]]*MFrequency^ParGR[[1, 2]] -
   ParGR[[2, 1]]*MFrequency^ParGR[[2, 2]] -
   Plus @@ Table[ParGR[[GR, 1]]/(
     1 + (Frequency/ParGR[[GR, 2]])^2), {GR, 3, NGRNoises + 2}];
 LocatorPane[Dynamic[pt1],
  Show[{ListLogLogPlot[{Transpose[{Frequency,
        Svtemp}], {Transpose[{Frequency,
         Table[MeanSvT, {i,
           Length[Frequency]}]}]}, {Transpose[{Frequency,
         Table[Sv0, {i, Length[Frequency]}]}]}}, Joined -> True,
     GridLines -> Automatic,
     GridLinesStyle -> Directive[LightGray, Dashed],
     PlotRange -> All, PlotRangePadding -> None],
    LogLogPlot[PlotGR, {fg, 1, 102400}, PlotStyle -> PStyle,
     PlotRangePadding -> None]}, Frame -> True,
```

```
     ImageSize -> Scaled[1], ImageMargins -> None],
    FrameMargins -> None],
   2,
   LocatorPane[Dynamic[pt],
    Show[{ListLogLogPlot[{Transpose[{Frequency,
          Sv*CorrectCapacity*Frequency}],
        Transpose[{Frequency, Frequency*MeanSvT}]},
       Joined -> True, GridLines -> Automatic,
       GridLinesStyle -> Directive[LightGray, Dashed], Frame -> True,
       ImageSize -> 700, PlotRange -> All],
      LogLogPlot[PlotGR, {fg, 1, 102400}, PlotStyle -> PStyle]},
     PlotRange -> PlotfSvRange, Frame -> True, ImageSize -> Scaled[1],
      ImageMargins -> None]
    ],
   3,
   Show[{ListLogLogPlot[{Transpose[{Frequency,
         Sv*CorrectCapacity*Frequency}]},
      Joined -> True, GridLines -> Automatic,
      GridLinesStyle -> Directive[LightGray, Dashed], Frame -> True,
      ImageSize -> 700, PlotRange -> All],
     LogLogPlot[PlotGR, {fg, 1, 102400}, PlotStyle -> PStyle]},
    Frame -> True, ImageSize -> Scaled[1], ImageMargins -> None]
   ]
  ],(* ----------------------------- 1st Block \
----------------------------- *)
 Dynamic[If[
   AdMessage != "Could not find data files" &&
    AdMessage !=
     "Could not find " <> NameDirectory <>
      "MeasurData.dat file", {{"\!\(\*SubscriptBox[\(V\), \(Sample\)]\
\)", "\!\(\*SubscriptBox[\(I\), \(Sample\)]\)",
      "\!\(\*SubscriptBox[\(R\), \(Equiv\)]\)", "Filename",
      "\!\(\*SubscriptBox[\(R\), \(Sample\)]\)",
      "\!\(\*SubscriptBox[\(T\), \(Sample\)]\)"}, {MeasurData[[
       NumberFile + 1, 1]], MeasurData[[NumberFile + 1, 2]],
      MeasurData[[NumberFile + 1, 3]],
      MeasurData[[NumberFile + 1, 4]],
      MeasurData[[NumberFile + 1, 10]],
      MeasurData[[NumberFile + 1, 12]]}} // TableForm, ""],
  BaseStyle ->
   Gray],(* ----------------------------- 2nd Block \
----------------------------- *)
 Dynamic[Style[
   "---=====   File number " <> ToString[NumberFile] <> " of " <>
    ToString[Length[MeasurData] - 1] <> "   =====----", Bold,
   14]],(* ----------------------------- 3th Block \
----------------------------- *)
 Dynamic[{{Dynamic["Smoothing:"],
     SetterBar[
      Dynamic[NumberIter], {0 -> "Off", 2 -> "2", 5 -> "5",
       10 -> "10"}], Dynamic["Remove PickUps:"],
     SetterBar[
      Dynamic[PickUpsCoef], {2 -> "2x", 1 -> "1x",
       0 -> "Off"}]}, {Dynamic["Points:"],
     SetterBar[
      Dynamic[c], {1 -> "All", 2 -> "1/2", 3 -> "1/3", 4 -> "1/4",
       5 -> "1/5"}],
     Dynamic[If[
       NumberIter0 != NumberIter || PickUpsCoef0 != PickUpsCoef ||
        ca != c, Style[RefreshMes, Red], Style["", Red]],
      ContinuousAction -> False],
     Dynamic[If[
       NumberIter0 != NumberIter || PickUpsCoef0 != PickUpsCoef ||
        ca != c, ca = c; NumberIter0 = NumberIter;
       PickUpsCoef0 = PickUpsCoef; FGetData; "", ""]]}} // TableForm],
 (* ----------------------------- 4th Block \
----------------------------- *)
 Dynamic[If[ShowThermal == 0, MeanSvT = SvE;
   SvThermal[[NumberFile]] =
    MeanSvT; {{Dynamic[
       StringJoin[
        "\!\(\*SubsuperscriptBox[\(S\), \(V\), \(Thermal\)]\)=",
        ToString[MeanSvT, TraditionalForm]]],
      Slider[Dynamic[SvE], {Abs[SvEt*0.1], Abs[SvEt*10],
        Abs[SvEt*0.01]}]}} // TableForm,
   StringJoin[
    "Mean \!\(\*SubsuperscriptBox[\(S\), \(V\), \(Thermal\)]\)=",
```

```
    ToString[MeanSvT, TraditionalForm]]; MeanSvT = SvTher;
   SvThermal[[NumberFile]] = MeanSvT]],
 (* ----------------------------- 5th Block \
----------------------------- *)
 {{Capacity, Log[CFlicker[[NumberFile]]],
   Dynamic[CorrectCapacity = (1 + (Exp[
          Capacity])^2 Req^2 (2 \[Pi] Frequency)^2);
    "Capacity= " <>
     ToString[N[Exp[Capacity]], TraditionalForm]]}, -25, -10,
  0.05},(* ----------------------------- 6th Block \
----------------------------- *)
 Dynamic[{{"Thermal noise",
     SetterBar[
      Dynamic[ShowThermal], {0 -> "calculated", 1 -> "measured"}],
     Dynamic[If[ValueQ[SvThermal],
       If[Abs[MeasurData[[NumberFile + 1, 1]]] < 0.001,
        "This is measured thermal noise", ""],
       "You have no measured thermal noise"], BaseStyle -> Red]}} //
   TableForm],
 (* ----------------------------- 7th Block \
----------------------------- *)
 Dynamic[{{"Kind of plot",
     SetterBar[
      Dynamic[NofGraphic], {0 -> "Sv Normal",
       1 -> "Sv-\!\(\*SubscriptBox[\(Sv\), \(Fitt\)]\)", 2 -> "f*Sv",
       3 -> "f*Sv Normal"}]}} //
   TableForm],(* ----------------------------- 8th Block \
----------------------------- *)
 Dynamic[{{Checkbox[Dynamic[LiveLastFitting]], "Live last fitting"}} //
    TableForm],
 (* ----------------------------- 9th Block \
----------------------------- *)
 Dynamic[If[tt > 2,
   Style[{{"Generation-Recombination noise " <> ToString[tt - 2] <>
        " (", DisplayForm[
        FractionBox["A" <> ToString[tt - 2],
         "1+(f/f" <> ToString[tt - 2] <>
          "\!\(\*SuperscriptBox[\()\), \(2\)]\)"]], ") "}} //
     TableForm, Bold],
   Style["Flicker noise ( \!\(\*FractionBox[\(A\), SuperscriptBox[\(f\
\), \(\[Alpha]\)]]\) ) " <>
     " \!\(\*FractionBox[SubscriptBox[\(fS\), \(I\)], SuperscriptBox[\
\(I\), \(2\)]]\)=" <>
     ToString[ParGR[[tt, 1]]*I2Req2, TraditionalForm], Bold]]],
 (* ----------------------------- 10th Block \
----------------------------- *)
 Dynamic[
  If[NGRNoises !=
    0, {{SetterBar[Dynamic[tt],
       Prepend[Prepend[
         Table[j -> "GR" <> ToString[j - 2], {j, 3, NGRNoises + 2}],
         2 -> "Flicker 2"], 1 -> "Flicker 1"]],
      If[NGRNoises != MaxGR,
       Button["Add GR",
        If[NGRNoises < MaxGR, NGRNoises++; tt = NGRNoises + 2;
         ParGR[[tt]] = Exp[{-40, -4}]], ImageSize -> {60, 20}], ""],
      Button["Del GR",
       If[NGRNoises > 0, ParGR[[NGRNoises + 2]] = {0, 0}; NGRNoises--;
         If[NGRNoises == 0, tt = 2, tt = 3]], ImageSize -> {60, 20}]
      }} //
    TableForm, {{SetterBar[
       Dynamic[tt], {1 -> "Flicker 1", 2 -> "Flicker 2"}],
      Button["Add GR",
       If[NGRNoises < MaxGR + 2, NGRNoises++; tt = NGRNoises + 2;
        ParGR[[tt]] = Exp[{-40, -4}]], ImageSize -> {60, 20}], ""
      }} // TableForm]],
 Dynamic[If[tt > 2,
   "\tf" <> ToString[tt - 2] <> "= " <>
    ToString[N[ParGR[[tt, 2]]], TraditionalForm] <> "\n\tA" <>
    ToString[tt - 2] <> "= " <>
    ToString[N[ParGR[[tt, 1]]], TraditionalForm] <> "\n\t\[Tau]" <>
    ToString[tt - 2] <> "= " <>
    ToString[N[1/(2 \[Pi] ParGR[[tt, 2]]), 2],
     TraditionalForm], {{Dynamic[
       StringJoin["\t\[Alpha]=",
        ToString[\[Alpha], TraditionalForm]]],
      Slider[Dynamic[\[Alpha]], {0.5, 1.5, 0.01}]}, {StringJoin[
```

```
      "\tA=", ToString[N[Exp[pt[[2]]]], TraditionalForm]],
     If[pt[[2]] != -40,
      Button["Reset A&\[Alpha]", pt = {0, -40};
       pt1 = pt; \[Alpha] = 1, ImageSize -> {80, 20}], ""]}} //
   TableForm]],
Dynamic[{{Button["Previous", pNumberFile--;
     Export[name,
      Prepend[Prepend[
        Transpose[
         Join[{Transpose[Delete[MeasurData, 1]][[4]],
           N[Transpose[Transpose[AfGR][[1]]][[1]] /.
             Exp[-40] -> "--"],
           N[Transpose[Transpose[AfGR][[1]]][[2]]],
           N[Transpose[Transpose[AfGR][[2]]][[1]] /.
             Exp[-40] -> "--"],
           N[Transpose[Transpose[AfGR][[2]]][[2]]], N[CFlicker],
           N[SvThermal], N[Transpose[Delete[MeasurData, 1]][[1]]],
           Mean[N[Transpose[Delete[MeasurData, 1]][[
               1 ;; 7 ;; 6]]]/{N[
               Transpose[Delete[MeasurData, 1]][[10]]],
              N[Transpose[Delete[MeasurData, 1]][[9]]]}],
           Abs[Mean[
              N[Transpose[Delete[MeasurData, 1]][[1 ;; 7 ;; 6]]]/{N[
                 Transpose[Delete[MeasurData, 1]][[10]]],
                N[Transpose[Delete[MeasurData, 1]][[9]]]}] - (N[

                Transpose[Delete[MeasurData, 1]][[1 ;; 7 ;; 6]]]/{N[
                  Transpose[Delete[MeasurData, 1]][[10]]],
                 N[Transpose[Delete[MeasurData, 1]][[9]]]})[[1]]],
           Round[Abs[
               Mean[N[Transpose[Delete[MeasurData, 1]][[
                   1 ;; 7 ;; 6]]]/{N[
                   Transpose[Delete[MeasurData, 1]][[10]]],
                   N[Transpose[Delete[MeasurData, 1]][[9]]]}] - (N[
                   Transpose[Delete[MeasurData, 1]][[
                   1 ;; 7 ;; 6]]]/{N[
                   Transpose[Delete[MeasurData, 1]][[10]]],
                   N[Transpose[Delete[MeasurData, 1]][[9]]]})[[1]]]/
              Mean[N[Transpose[Delete[MeasurData, 1]][[
                  1 ;; 7 ;; 6]]]/{N[
                  Transpose[Delete[MeasurData, 1]][[10]]],
                 N[Transpose[Delete[MeasurData, 1]][[9]]]}]*100,
            0.01], Mean[
            N[Transpose[Delete[MeasurData, 1]][[9 ;; 10]]]],
           Abs[Mean[N[Transpose[Delete[MeasurData, 1]][[9 ;; 10]]]] -
              N[Transpose[Delete[MeasurData, 1]][[9]]]],
           N[(N[Transpose[Transpose[AfGR][[1]]][[1]] /.
                Exp[-40] -> 0])/((Transpose[Delete[MeasurData, 1]][[
                 3]])^2 /. {0 -> -1})] /. x_ /; x <= 0 -> "--",

           N[(N[Transpose[Transpose[AfGR][[1]]][[1]] /.
                 Exp[-40] ->
                  0])/((Transpose[Delete[MeasurData, 1]][[
                   3]])^2*(Transpose[Delete[MeasurData, 1]][[
                   2]])^2 /. {0 -> -1})] /. x_ /; x <= 0 -> "--",
           N[Mean[{(N[
                   Transpose[Transpose[AfGR][[1]]][[1]] /.
                   Exp[-40] -> 0]*(Transpose[Delete[MeasurData, 1]][[
                   5]] + Transpose[Delete[MeasurData, 1]][[
                   10]])^2)/((Transpose[Delete[MeasurData, 1]][[
                   5]])^2*(Transpose[Delete[MeasurData, 1]][[
                   1]])^2 /. {0 -> -1}), (N[
                   Transpose[Transpose[AfGR][[1]]][[1]] /.
                   Exp[-40] -> 0]*(Transpose[Delete[MeasurData, 1]][[
                   5]] + Transpose[Delete[MeasurData, 1]][[
                   9]])^2)/((Transpose[Delete[MeasurData, 1]][[
                   5]])^2*(Transpose[Delete[MeasurData, 1]][[
                   7]])^2 /. {0 -> -1})}]] /. x_ /; x <= 0 -> "--",
           N[Abs[Mean[{(N[
                   Transpose[Transpose[AfGR][[1]]][[1]] /.
                   Exp[-40] -> 0]*(Transpose[Delete[MeasurData, 1]][[
                   5]] + Transpose[Delete[MeasurData, 1]][[
                   10]])^2)/((Transpose[Delete[MeasurData, 1]][[
                   5]])^2*(Transpose[Delete[MeasurData, 1]][[
                   1]])^2 /. {0 -> -1}), (N[
                   Transpose[Transpose[AfGR][[1]]][[1]] /.
                   Exp[-40] -> 0]*(Transpose[Delete[MeasurData, 1]][[
```

```
                    5]] + Transpose[Delete[MeasurData, 1]][[
                    9]])^2)/((Transpose[Delete[MeasurData, 1]][[
                    5]])^2*(Transpose[Delete[MeasurData, 1]][[
                    7]])^2 /. {0 -> -1})}] - (N[
                    Transpose[Transpose[AfGR][[1]]][[1]] /.
                    Exp[-40] -> 0]*(Transpose[Delete[MeasurData, 1]][[
                    5]] + Transpose[Delete[MeasurData, 1]][[
                    9]])^2)/((Transpose[Delete[MeasurData, 1]][[
                    5]])^2*(Transpose[Delete[MeasurData, 1]][[
                    7]])^2 /. {0 -> -1})]] /. x_ /; x <= 0 -> "--",
            N[(N[Transpose[Transpose[AfGR][[2]]][[1]] /.
                 Exp[-40] -> 0])/((Transpose[Delete[MeasurData, 1]][[
                  3]])^2 /. {0 -> -1})] /. x_ /; x <= 0 -> "--",
            N[(N[Transpose[Transpose[AfGR][[2]]][[1]] /.
                  Exp[-40] ->
                   0])/((Transpose[Delete[MeasurData, 1]][[
                    3]])^2*(Transpose[Delete[MeasurData, 1]][[
                    2]])^2 /. {0 -> -1})] /. x_ /; x <= 0 -> "--",
            Mean[N[Transpose[Delete[MeasurData, 1]][[11 ;; 12]]]],

            Abs[Mean[
               N[Transpose[Delete[MeasurData, 1]][[11 ;; 12]]]] -
              N[Transpose[Delete[MeasurData, 1]][[11]]]]},
           N[Transpose[
             Table[Flatten[
                Transpose[
                 Append[Transpose[AfGR[[k]][[3 ;; -1]]],
                  Transpose[Delete[MeasurData, 1]][[12]][[k]]^2/(
                  2*\[Pi]*(Transpose[AfGR[[k]]][[2]][[
                    3 ;; -1]] /. {0 -> -1}))]]], {k,
                Length[MeasurData] - 1}] /. x_ /; x <= 0 -> "--"]]]],
         Flatten[{{"", "V\+(2)*Hz\+(-1)", "", "V\+(2)*Hz\+(-1)", "",
            "F", "V\+(2)*Hz\+(-1)", "V", "A", "A", "%", "\\g(W)",
            "\\g(W)", "A\+(2)", "", "", "", "A\+(2)", "", "K", "K"},
           Table[{"V\+(2)*Hz\+(-1)", "Hz", "sK\+(2)"}, {k, MaxGR}]}]],
         Flatten[{{"Filename", "S\=(V,Flicker)", "\\g(a)\-(1)",
           "S\=(V,Flicker2)", "\\g(a)\-(2)", "Capacity",
           "S\=(V,Thermal)", "V\-(Sample)", "I", "\\g(D)I",
           "\\g(D)I/I", "R\-(Sample)", "\\g(D)R", "f*S\=(I,Flicker)",
           "f*S\=(I,Flicker)/I\+(2)", "<f*S\=(I,Flicker)/I\+(2)>",
           "\\g(D)(f*S\=(I,Flicker)/I\+(2))", "f*S\=(I,Flicker2)",
           "f*S\=(I,Flicker2)/I\+(2)", "Temperature", "\\g(D)T"},
          Table[{"S\=(V0,GR" <> ToString[k] <> ")",
            "f\-(0" <> ToString[k] <> ")", "\\g(t)*T\+(2)"}, {k,
            MaxGR}]}]], "TSV"];
      Export["n_" <> MeasurData[[NumberFile + 1, 4]],
       Prepend[Prepend[
         Transpose[{Frequency,
           Sv*(1 + (Exp[Capacity])^2 Req^2 (2 \[Pi] Frequency)^2), (
           Sv*(1 + (Exp[
                 Capacity])^2 Req^2 (2 \[Pi] \
Frequency)^2))/(MeasurData[[NumberFile + 1,
             3]])^2, (Frequency*((Sv*(1 + (Exp[
                    Capacity])^2 Req^2 (2 \[Pi] Frequency)^2) -
                   MeanSvT) /.
                 x_ /; x < MeanSvT/5 -> 0))/(MeasurData[[
               NumberFile + 1, 3]])^2 /.
            x_ /; x <= 0 ->
             "--", (Frequency*((Sv*(1 + (Exp[
                    Capacity])^2 Req^2 (2 \[Pi] Frequency)^2) -
                   MeanSvT) /.
                 x_ /; x < MeanSvT/5 -> 0))/(MeasurData[[
                NumberFile + 1, 3]]*
               MeasurData[[NumberFile + 1, 2]])^2 /.
            x_ /; x <= 0 -> "--"}], {"Hz", "V\+(2)*Hz\+(-1)",
          "A\+(2)*Hz\+(-1)", "A\+(2)", ""}], {"Frequency", "S\-(V)",
         "S\-(I)", "fS\-(I)", "fS\-(I)/I\+(2)"}], "TSV"];
      Export["p_" <> MeasurData[[NumberFile + 1, 4]] <> ".jpg",
       Show[{ListLogLogPlot[{Transpose[{Frequency,
             Sv*(1 + (Exp[Capacity])^2 Req^2 (2 \[Pi] Frequency)^2)*
              Frequency}], Transpose[{Frequency, Frequency*MeanSvT}]},
           Joined -> True, GridLines -> Automatic,
           GridLinesStyle -> Directive[LightGray, Dashed],
           Frame -> True, ImageSize -> 700, PlotRange -> All],
          LogLogPlot[PlotGR, {fg, 1, 102400}, PlotStyle -> PStyle]},
         PlotRange -> PlotfSvRange]];
      If[pNumberFile > 0, AdMessage = ""; FGetData, AdMessage = "End";
```

```
   pNumberFile++; FGetData], ImageSize -> 100],
Button["Next", pNumberFile++;
 Export[name,
  Prepend[Prepend[
    Transpose[
     Join[{Transpose[Delete[MeasurData, 1]][[4]],
       N[Transpose[Transpose[AfGR][[1]]][[1]] /.
         Exp[-40] -> "--"],
       N[Transpose[Transpose[AfGR][[1]]][[2]]],
       N[Transpose[Transpose[AfGR][[2]]][[1]] /.
         Exp[-40] -> "--"],
       N[Transpose[Transpose[AfGR][[2]]][[2]]], N[CFlicker],
       N[SvThermal], N[Transpose[Delete[MeasurData, 1]][[1]]],
       Mean[N[Transpose[Delete[MeasurData, 1]][[
           1 ;; 7 ;; 6]]]/{N[
           Transpose[Delete[MeasurData, 1]][[10]]],
          N[Transpose[Delete[MeasurData, 1]][[9]]]}],
       Abs[Mean[
          N[Transpose[Delete[MeasurData, 1]][[1 ;; 7 ;; 6]]]/{N[
             Transpose[Delete[MeasurData, 1]][[10]]],
            N[Transpose[Delete[MeasurData, 1]][[9]]]}] - (N[
             Transpose[Delete[MeasurData, 1]][[1 ;; 7 ;; 6]]]/{N[
              Transpose[Delete[MeasurData, 1]][[10]]],
             N[Transpose[Delete[MeasurData, 1]][[9]]]})[[1]]],
       Round[Abs[
           Mean[N[Transpose[Delete[MeasurData, 1]][[
               1 ;; 7 ;; 6]]]/{N[
               Transpose[Delete[MeasurData, 1]][[10]]],
               N[Transpose[Delete[MeasurData, 1]][[9]]]}] - (N[
               Transpose[Delete[MeasurData, 1]][[
               1 ;; 7 ;; 6]]]/{N[
               Transpose[Delete[MeasurData, 1]][[10]]],
               N[Transpose[Delete[MeasurData, 1]][[9]]]})[[1]]]/
          Mean[N[Transpose[Delete[MeasurData, 1]][[
              1 ;; 7 ;; 6]]]/{N[
              Transpose[Delete[MeasurData, 1]][[10]]],
             N[Transpose[Delete[MeasurData, 1]][[9]]]}]*100,
        0.01],
       Mean[N[Transpose[Delete[MeasurData, 1]][[9 ;; 10]]]],
       Abs[Mean[N[Transpose[Delete[MeasurData, 1]][[9 ;; 10]]]] -
          N[Transpose[Delete[MeasurData, 1]][[9]]]],
       N[(N[Transpose[Transpose[AfGR][[1]]][[1]] /.
            Exp[-40] -> 0])/((Transpose[Delete[MeasurData, 1]][[
             3]])^2 /. {0 -> -1})] /. x_ /; x <= 0 -> "--",
       N[(N[Transpose[Transpose[AfGR][[1]]][[1]] /.
             Exp[-40] ->
              0])/((Transpose[Delete[MeasurData, 1]][[
               3]])^2*(Transpose[Delete[MeasurData, 1]][[
               2]])^2 /. {0 -> -1})] /. x_ /; x <= 0 -> "--",
       N[Mean[{(N[
               Transpose[Transpose[AfGR][[1]]][[1]] /.
               Exp[-40] -> 0]*(Transpose[Delete[MeasurData, 1]][[
               5]] + Transpose[Delete[MeasurData, 1]][[
               10]])^2)/((Transpose[Delete[MeasurData, 1]][[
               5]])^2*(Transpose[Delete[MeasurData, 1]][[
               1]])^2 /. {0 -> -1}), (N[
               Transpose[Transpose[AfGR][[1]]][[1]] /.
               Exp[-40] -> 0]*(Transpose[Delete[MeasurData, 1]][[
               5]] + Transpose[Delete[MeasurData, 1]][[
               9]])^2)/((Transpose[Delete[MeasurData, 1]][[
               5]])^2*(Transpose[Delete[MeasurData, 1]][[
               7]])^2 /. {0 -> -1})}]] /. x_ /; x <= 0 -> "--",
       N[Abs[Mean[{(N[
               Transpose[Transpose[AfGR][[1]]][[1]] /.
               Exp[-40] -> 0]*(Transpose[Delete[MeasurData, 1]][[
               5]] + Transpose[Delete[MeasurData, 1]][[
               10]])^2)/((Transpose[Delete[MeasurData, 1]][[
               5]])^2*(Transpose[Delete[MeasurData, 1]][[
               1]])^2 /. {0 -> -1}), (N[
               Transpose[Transpose[AfGR][[1]]][[1]] /.
               Exp[-40] -> 0]*(Transpose[Delete[MeasurData, 1]][[
               5]] + Transpose[Delete[MeasurData, 1]][[
               9]])^2)/((Transpose[Delete[MeasurData, 1]][[
               5]])^2*(Transpose[Delete[MeasurData, 1]][[
               7]])^2 /. {0 -> -1})}] - (N[
               Transpose[Transpose[AfGR][[1]]][[1]] /.
               Exp[-40] -> 0]*(Transpose[Delete[MeasurData, 1]][[
```

```
                  5]] + Transpose[Delete[MeasurData, 1]][[
                  9]])^2)/((Transpose[Delete[MeasurData, 1]][[
                  5]])^2*(Transpose[Delete[MeasurData, 1]][[
                  7]])^2 /. {0 -> -1})]] /. x_ /; x <= 0 -> "--",
          N[(N[Transpose[Transpose[AfGR][[2]]][[1]] /.

               Exp[-40] -> 0])/((Transpose[Delete[MeasurData, 1]][[
                3]])^2 /. {0 -> -1})] /. x_ /; x <= 0 -> "--",
          N[(N[Transpose[Transpose[AfGR][[2]]][[1]] /.
                Exp[-40] ->
                 0])/((Transpose[Delete[MeasurData, 1]][[
                  3]])^2*(Transpose[Delete[MeasurData, 1]][[
                  2]])^2 /. {0 -> -1})] /. x_ /; x <= 0 -> "--",
          Mean[N[Transpose[Delete[MeasurData, 1]][[11 ;; 12]]]],
          Abs[Mean[
             N[Transpose[Delete[MeasurData, 1]][[11 ;; 12]]]] -
            N[Transpose[Delete[MeasurData, 1]][[11]]]]},
         N[Transpose[
           Table[Flatten[
              Transpose[
               Append[Transpose[AfGR[[k]][[3 ;; -1]]],
                Transpose[Delete[MeasurData, 1]][[12]][[k]]^2/(
                2*\[Pi]*(Transpose[AfGR[[k]]][[2]][[
                  3 ;; -1]] /. {0 -> -1}))]]], {k,
              Length[MeasurData] - 1}] /. x_ /; x <= 0 -> "--"]]]],
       Flatten[{{"", "V\+(2)*Hz\+(-1)", "", "V\+(2)*Hz\+(-1)", "",
          "F", "V\+(2)*Hz\+(-1)", "V", "A", "A", "%", "\\g(W)",
          "\\g(W)", "A\+(2)", "", "", "", "A\+(2)", "", "K", "K"},
         Table[{"V\+(2)*Hz\+(-1)", "Hz", "sK\+(2)"}, {k, MaxGR}]}]],
       Flatten[{{"Filename", "S\=(V,Flicker)", "\\g(a)\-(1)",
         "S\=(V,Flicker2)", "\\g(a)\-(2)", "Capacity",
         "S\=(V,Thermal)", "V\-(Sample)", "I", "\\g(D)I",
         "\\g(D)I/I", "R\-(Sample)", "\\g(D)R", "f*S\=(I,Flicker)",
         "f*S\=(I,Flicker)/I\+(2)", "<f*S\=(I,Flicker)/I\+(2)>",
         "\\g(D)(f*S\=(I,Flicker)/I\+(2))", "f*S\=(I,Flicker2)",
         "f*S\=(I,Flicker2)/I\+(2)", "Temperature", "\\g(D)T"},
        Table[{"S\=(V0,GR" <> ToString[k] <> ")",
          "f\-(0" <> ToString[k] <> ")", "\\g(t)*T\+(2)"}, {k,
          MaxGR}]}]], "TSV"];
    Export["n_" <> MeasurData[[NumberFile + 1, 4]],
     Prepend[Prepend[
       Transpose[{Frequency,
         Sv*(1 + (Exp[Capacity])^2 Req^2 (2 \[Pi] Frequency)^2), (
         Sv*(1 + (Exp[
               Capacity])^2 Req^2 (2 \[Pi] \
Frequency)^2))/(MeasurData[[NumberFile + 1,
           3]])^2, (Frequency*((Sv*(1 + (Exp[
                  Capacity])^2 Req^2 (2 \[Pi] Frequency)^2) -
                 MeanSvT) /.
               x_ /; x < MeanSvT/5 -> 0))/(MeasurData[[
             NumberFile + 1, 3]])^2 /.
          x_ /; x <= 0 ->
           "--", (Frequency*((Sv*(1 + (Exp[
                  Capacity])^2 Req^2 (2 \[Pi] Frequency)^2) -
                 MeanSvT) /.
               x_ /; x < MeanSvT/5 -> 0))/(MeasurData[[
              NumberFile + 1, 3]]*
             MeasurData[[NumberFile + 1, 2]])^2 /.
          x_ /; x <= 0 -> "--"}], {"Hz", "V\+(2)*Hz\+(-1)",
        "A\+(2)*Hz\+(-1)", "A\+(2)", ""}], {"Frequency", "S\-(V)",
       "S\-(I)", "fS\-(I)", "fS\-(I)/I\+(2)"}], "TSV"];
    Export["p_" <> MeasurData[[NumberFile + 1, 4]] <> ".jpg",
     Show[{ListLogLogPlot[{Transpose[{Frequency,
           Sv*(1 + (Exp[Capacity])^2 Req^2 (2 \[Pi] Frequency)^2)*
            Frequency}], Transpose[{Frequency, Frequency*MeanSvT}]},
        Joined -> True, GridLines -> Automatic,
        GridLinesStyle -> Directive[LightGray, Dashed],
        Frame -> True, ImageSize -> 700, PlotRange -> All],
       LogLogPlot[PlotGR, {fg, 1, 102400}, PlotStyle -> PStyle]},
      PlotRange -> PlotfSvRange]];
    If[pNumberFile < Length[MeasurData], AdMessage = ""; FGetData,
     AdMessage = "End"; pNumberFile--; FGetData], ImageSize -> 100],
   (*Button["New Data",ClearAll[StartingProgram];AdMessage="";
   FGetData,ImageSize->100],*)
   Button["Continue", If[FileType[name] == File,
     PreviousDataImport =
      Delete[Transpose[
```

```
          Delete[Import[name,
            "TSV"], {{1}, {2}}]], {{1}, {6}, {7}, {8}, {9}, {10}, \
{11}, {12}, {13}, {14}, {15}, {16}, {17}, {18}, {19}, {20}, {21}, \
{24}, {27}, {30}, {33}, {36}}] /. "--" -> 0;
       PreviousData =
        Transpose[
         Table[Partition[Transpose[PreviousDataImport][[i]], 2], {i,
           Length[Transpose[PreviousDataImport]]}]];
       PreviousData[[1]] = PreviousData[[1]] /. {0 -> Exp[-40]};
       PreviousData[[2]] = PreviousData[[2]] /. {0 -> Exp[-40]};
       PreviousData = Transpose[PreviousData];
       If[
        Length[AfGR] == Length[PreviousData] &&
         Length[AfGR[[1]]] == Length[PreviousData[[1]]],
        AfGR = PreviousData;
        CFlicker =
         Transpose[Delete[Import[name, "TSV"], {{1}, {2}}]][[6]];
        AdMessage = "";
        pNumberFile =
         Position[PreviousData,
           Select[PreviousData, #[[1, 1]] > Exp[-40] &][[-1]]][[1,
          1]]; Capacity = Log[CFlicker[[pNumberFile]]];,
        AdMessage =
         "Cannot import the file " <> name <> " with fitted data"
        ],
       AdMessage =
        "Cannot find the file " <> name <> " with fitted data"
       ]; FGetData, ImageSize -> 100]}} // TableForm],
 Dynamic[{{"Output file name:", InputField[Dynamic[name], String]}} //
    TableForm],
 Dynamic[Style["\n" <> AdMessage, Bold, 14], BaseStyle -> Red],
 Initialization :> (If[ValueQ[StartingProgram] == False,
     Func[x_, i_] :=
      Interpolation[{{{Ftemp[[i - 1]]}, Svtemp[[i - 1]], (
          Svtemp[[i]] - Svtemp[[i - 1]])/(
          Ftemp[[i]] - Ftemp[[i - 1]])}, {{Ftemp[[i + 1]]},
          Svtemp[[i + 1]], (Svtemp[[1 + i]] - Svtemp[[i]])/(
          Ftemp[[1 + i]] - Ftemp[[i]])}}][x];
     FGetData := (
       (* Find existed file *)
       If[pNumberFile > NumberFile,
        NumberFile = pNumberFile;
        While[
         FileType[MeasurData[[NumberFile + 1, 4]]] == None &&
          NumberFile < Length[MeasurData], NumberFile++;
         If[NumberFile >= Length[MeasurData], NumberFile--;
          AdMessage = "No next data";

          While[FileType[MeasurData[[NumberFile + 1, 4]]] == None &&
            NumberFile > 0, NumberFile--; pNumberFile = NumberFile]];
         pNumberFile = NumberFile];
        If[LiveLastFitting, AfGR[[NumberFile]] = ParGR,
         ParGR = AfGR[[NumberFile]]],
        NumberFile = pNumberFile;
        While[
         FileType[MeasurData[[NumberFile + 1, 4]]] == None &&
          NumberFile > -1, NumberFile--;
         If[NumberFile <= 0, NumberFile = 1;
          AdMessage = "No previous data";

          While[FileType[MeasurData[[NumberFile + 1, 4]]] == None &&
            NumberFile < Length[MeasurData], NumberFile++;
           pNumberFile = NumberFile]];
         pNumberFile = NumberFile];
        ParGR = AfGR[[NumberFile]]
        ];
       Data1 = Import[MeasurData[[NumberFile + 1, 4]]];
       {Frequency, Sv} = {Transpose[Data1][[1]],
         Transpose[Data1][[2]]};
       If[CFlicker[[NumberFile]] > Exp[-25],
        Capacity = Log[CFlicker[[NumberFile]]]];
       tt = 1; ttlast = 0;
       NGRNoises = MaxGR - Length[Position[ParGR, {0, 0}]];
       RsE = MeasurData[[NumberFile + 1, 10]];
       TsE = MeasurData[[NumberFile + 1, 12]];
       Rs0 = MeasurData[[NumberFile + 1, 9]];
       Ts0 = MeasurData[[NumberFile + 1, 11]];
```

```
        RL = MeasurData[[NumberFile + 1, 5]];
        Req = MeasurData[[NumberFile + 1, 3]];
        I2Req2 = 1/(
         MeasurData[[NumberFile + 1, 2]]^2 MeasurData[[NumberFile + 1,
            3]]^2);
        TL = 297;
        SvE = 4*1.38*^-23*((TL*RsE + TsE*RL)*RsE*RL)/(RsE + RL)^2;
        SvEt = SvE;
        SvTher = SvE;
        Sv0 = 4*1.38*^-23*((TL*Rs0 + Ts0*RL)*Rs0*RL)/(Rs0 + RL)^2;
        LogMinfSv =
         Log[Min[Sv*

            Frequency*(1 + (Exp[
                 Capacity])^2 Req^2 (2 \[Pi] Frequency)^2)]];
        LogMaxfSv =
         Log[Max[Sv*
            Frequency*(1 + (Exp[
                 Capacity])^2 Req^2 (2 \[Pi] Frequency)^2)]];
        (*For[i=0,i<Length[AmpCorr],i++;Sv[[i]]=Sv[[i]]-SvE*AmpCorr[[
        i]]+SvE];*)
        Ftemp = Frequency;
        If[ValueQ[SvThermalMeasur] == False,
         If[Abs[MeasurData[[NumberFile + 1, 1]]] < 0.0009,
          SvThermalMeasur = Sv; FreqThermal = Frequency],
         If[Abs[MeasurData[[NumberFile + 1, 1]]] < 0.0009,
           SvThermalMeasur = Sv; FreqThermal = Frequency;
           MeanSvT =
            N[Exp[Mean[
               Log[Take[
                 Sv*(1 + (Exp[
                     Capacity])^2 Req^2 (2 \[Pi] Frequency)^2), {510, \
-1}]]]]]; SvEt = MeanSvT,

           If[ShowThermal == 1,
            SvThermalMeasur =
             Interpolation[Transpose[{FreqThermal, SvThermalMeasur}],
               InterpolationOrder -> 1][Ftemp]; FreqThermal = Ftemp;
            Sv = Sv - SvThermalMeasur; SvE = 0; Sv0 = 0;
            tSvThermalMeasur = SvThermalMeasur;

            For[i = 30, i < Length[Sv], i++;
             If[10*Sv[[i]] < tSvThermalMeasur[[i]], Sv = Delete[Sv, i];
               Ftemp = Delete[Ftemp, i];
              tSvThermalMeasur = Delete[tSvThermalMeasur, i]; i--]];
            ]
           ];
         ];
        (*For[i=30,i<Length[Sv]-1,i++;If[(Sv[[i]]-Sv[[i-1]])/Sv[[i-1]]>
        NumberErrorPickUps,Sv=Delete[Sv,i];Ftemp=Delete[Ftemp,i];
        i--]];*)
        For[i = 0, i < Length[Sv], i++;
         If[Sv[[i]] < 0, Sv = Delete[Sv, i]; Ftemp = Delete[Ftemp, i];
          i--]];
        If[Ftemp[[-1]] != Frequency[[-1]],
         Ftemp = Append[Ftemp, Frequency[[-1]]];
         Sv = Append[Sv, Sv[[-1]]]];
        If[Ftemp[[1]] != Frequency[[1]],
         Ftemp = Prepend[Ftemp, Frequency[[1]]];
         Sv = Prepend[Sv, Sv[[1]]]];
        DataList = Transpose[{Ftemp, Sv}];
        Sv =
         Interpolation[DataList, InterpolationOrder -> 1][Frequency];
        Svtemp2 = {{}};
        Ftemp = Log[Frequency];
        (* Deleting pick ups *)
        StartPoint = 3;
        If[PickUpsCoef != 0,(*NumberErrorPickUps=100;*)
         While[Length[Svtemp2] < NumberErrorPickUps,
          StartPoint++;
          Svtemp2 = Log[Sv];
          Ftemp = Log[Frequency];
          For[i = StartPoint, i < Length[Svtemp2] - 1, i++;
           If[(Svtemp2[[i + 1]] <
               Log[Exp[Svtemp2[[i]]] - (2*Exp[Svtemp2[[i]]])/(
                  PickUpsCoef Sqrt[
                   MeasurData[[NumberFile + 1, 14]]])] +
```

```
          2 (Ftemp[[i]] - Ftemp[[i + 1]])) || (Svtemp2[[i + 1]] >
          Log[Exp[Svtemp2[[i]]] + (2*Exp[Svtemp2[[i]]])/(
           PickUpsCoef Sqrt[MeasurData[[NumberFile + 1, 14]]])]),
       Svtemp2 = Delete[Svtemp2, i + 1];
      Ftemp = Delete[Ftemp, i + 1]; i--]
     ];
    For[i = StartPoint, i > 1, i--;


     If[(Svtemp2[[i - 1]] >
         Log[Exp[Svtemp2[[i]]] + (2*Exp[Svtemp2[[i]]])/(
            PickUpsCoef Sqrt[
             MeasurData[[NumberFile + 1, 14]]])] +
          2 (Ftemp[[i]] - Ftemp[[i - 1]])) || (Svtemp2[[i - 1]] <
          Log[Exp[Svtemp2[[i]]] - (2*Exp[Svtemp2[[i]]])/(
           PickUpsCoef Sqrt[MeasurData[[NumberFile + 1, 14]]])]),
       Svtemp2 = Delete[Svtemp2, i - 1];
      Ftemp = Delete[Ftemp, i - 1]; i++]
     ];
    If[StartPoint >= Length[Svtemp2] - NumberErrorPickUps,
     Svtemp2 = Log[Sv]; Ftemp = Log[Frequency]];
    ], Svtemp2 = Log[Sv];
   Ftemp = Log[Frequency];];
  If[Ftemp[[-1]] != Log[Frequency[[-1]]],
   Ftemp = Append[Ftemp, Log[Frequency[[-1]]]];
   Svtemp2 = Append[Svtemp2, Svtemp2[[-1]]]];
  If[Ftemp[[1]] != Log[Frequency[[1]]],
   Ftemp = Prepend[Ftemp, Log[Frequency[[1]]]];
   Svtemp2 = Prepend[Svtemp2, Svtemp2[[1]]]];
  DataList = Transpose[{Ftemp, Svtemp2}];

  Sv =
   Exp[Interpolation[DataList, InterpolationOrder -> 1][
     Log[Frequency]]];
  Svtemp = Log[Sv];
  SvT = Svtemp;
  Ftemp = Log[Frequency];
  For[k = 0, k < NumberIter, k++;
   For[j = k + 1, j < Length[Svtemp] - 1, j++;
    SvT[[j]] = Func[Ftemp[[j]], j]]; Svtemp = SvT];
  Sv = Exp[Svtemp];
  Frequency =
   Join[Frequency[[1 ;; 9 ;; 1]], Frequency[[10 ;; ;; ca]]];
  Sv = Join[Sv[[1 ;; 9 ;; 1]], Sv[[10 ;; ;; ca]]];
  Sv = Re[Sv];
  MFrequency = 1/Frequency;
  CorrectCapacity = (1 + (Exp[
        Capacity])^2 Req^2 (2 \[Pi] Frequency)^2);
  );
(* Initialization *)
NameDirectory = "E:\\Temp\\Flicker";
SetDirectory[NameDirectory];
PickUpsCoef0 = 1; PickUpsCoef = 1;
ShowThermal = 0;
LiveLastFitting = False;
MaxGR = 5;
NumberFile = 0; pNumberFile = 1;
tt = 1; ttlast = 0;
ParGR = {{Exp[-40], 1}, {Exp[-40], 1}, {0, 0}, {0, 0}, {0,
   0}, {0, 0}, {0, 0}};
NGRNoises = 0;
NofGraphic = 0;
pt = {-40, 1}; pt1 = {-40, 1};
ca := 5;
NumberIter0 = 0; NumberIter = 0;
NumberErrorPickUps0 = 100; NumberErrorPickUps = 100;
\[Alpha] = 1;
RefreshMes = "Refreshing...";
AdMessage = "";
StartingProgram = 1;
(* Reading measurements data *)
If[FileType["MeasurData.dat"] == File,
 MeasurData = Import["MeasurData.dat", "TSV"];
 MaxLength = Length[MeasurData[[1]]];
 For[i = 1, i < Length[MeasurData], i++;
  If[Length[MeasurData[[i]]] > MaxLength,
   MaxLength = Length[MeasurData[[i]]]];
```

```
        ];
       For[i = 0, i < Length[MeasurData], i++;
        If[Length[MeasurData[[i]]] < MaxLength,
         MeasurData[[i]] =
          Join[MeasurData[[i]],
           Table[0, {j, MaxLength - Length[MeasurData[[i]]]}]]];
        ];
       MeasurData = Delete[MeasurData, 2];
       If[Length[MeasurData[[1]]] <= 13,
        MeasurData =
         Transpose[
          Append[Transpose[MeasurData],
           Table[100, {i, Length[MeasurData]}]]]];
       (*-===============-*)
       name = "Fit" <> MeasurData[[2, 4]];
       If[Length[
          Position[

           Table[FileType[MeasurData[[i + 1, 4]]], {i,
             Length[MeasurData] - 1}], None]] != Length[MeasurData] - 1,
        CFlicker = Table[Exp[-25], {i, Length[MeasurData] - 1}];
        SvThermal = Table[0, {i, Length[MeasurData] - 1}];
        AfGR =
         Table[{{Exp[-40], 1}, {Exp[-40], 1}, {0, 0}, {0, 0}, {0,
            0}, {0, 0}, {0, 0}}, {i, 1, Length[MeasurData] - 1}];
        If[FileType[name] == File,
         AdMessage =
          "File " <> name <>
           " was found. It will be rewrited, or press \"Continue\" to \
continue fitting",
         AdMessage =
          "Cannot find the file " <> name <> " with fitted data"
         ];
        FGetData,
        AdMessage = "Cannot find data files"
        ], ,
       AdMessage =
        "Could not find " <> NameDirectory <> "MeasurData.dat file"];
      ];
    ), Paneled -> True, SynchronousUpdating -> False,
 ContinuousAction -> False, SynchronousInitialization -> False,
 FrameMargins -> 0, ImageMargins -> 0, Alignment -> Top]
```

3. Diameters and radial breathing mode (RBM) frequency of typical SWCNTs

The diameter of metallic SWCNTs are shown in red color, semiconductor – in blue.

n	m	Diameter nm	RBM cm^{-1}	n	m	Diameter nm	RBM cm^{-1}	n	m	Diameter nm	RBM cm^{-1}
0	5	0.39168	633.169	7	7	0.949774	261.115	8	11	1.29432	191.606
3	3	0.407046	609.268	2	11	0.949774	261.115	1	16	1.29432	191.606
2	4	0.414515	598.289	6	8	0.952999	260.231	7	12	1.30377	190.217
1	5	0.436157	568.603	5	9	0.96261	257.633	3	15	1.30847	189.534
0	6	0.470016	527.641	4	10	0.978417	253.471	6	13	1.31782	188.19
4	3	0.4765	520.462	1	12	0.981548	252.662	0	17	1.33171	186.226
2	5	0.489209	506.941	3	11	1.00013	247.968	5	14	1.33631	185.585
1	6	0.513684	482.787	8	7	1.01837	243.527	2	16	1.33861	185.267
4	4	0.542728	456.951	0	13	1.01837	243.527	10	10	1.35682	182.78
3	5	0.548352	452.264	6	9	1.02438	242.098	9	11	1.35908	182.476
0	7	0.548352	452.264	2	12	1.02737	241.394	4	15	1.35908	182.476
2	6	0.564889	439.024	5	10	1.03629	239.316	8	12	1.36584	181.574
1	7	0.591424	419.327	4	11	1.0539	235.316	1	17	1.37256	180.684
5	4	0.611824	405.345	1	13	1.05971	234.026	7	13	1.37702	180.099
3	6	0.621773	398.859	3	12	1.07694	230.281	3	16	1.38591	178.944
0	8	0.626689	395.731	8	8	1.08546	228.475	6	14	1.39253	178.093
2	7	0.641208	386.77	7	9	1.08828	227.883	0	18	1.41005	175.88
1	8	0.669304	370.534	6	10	1.0967	226.132	5	15	1.41222	175.61
5	5	0.67841	365.561	0	14	1.0967	226.132	2	17	1.41656	175.072
4	6	0.682918	363.148	2	13	1.10507	224.421	11	10	1.4252	174.011
3	7	0.696266	356.186	5	11	1.11061	223.302	9	12	1.4295	173.487
0	9	0.705025	351.761	4	12	1.12978	219.512	4	16	1.43592	172.711
2	8	0.717962	345.422	1	14	1.1379	217.946	8	13	1.43806	172.455
6	5	0.747278	331.871	9	8	1.15396	214.912	7	14	1.4508	170.94
1	9	0.747278	331.871	3	13	1.15396	214.912	1	18	1.4508	170.94
4	7	0.755446	328.283	7	10	1.15927	213.928	3	17	1.46344	169.464
3	8	0.771521	321.443	6	11	1.16981	212.001	6	15	1.46763	168.98
0	10	0.783361	316.585	0	15	1.17504	211.056	5	16	1.48839	166.624
2	9	0.795024	311.94	2	14	1.18285	209.663	0	19	1.48839	166.624
6	6	0.814092	304.634	5	12	1.18544	209.205	11	11	1.4925	166.164
5	7	0.817853	303.233	4	13	1.20597	205.644	10	12	1.49456	165.935
1	10	0.825322	300.489	1	15	1.2161	203.93	2	18	1.49456	165.935
4	8	0.829031	299.144	9	9	1.22114	203.089	9	13	1.5007	165.256
3	9	0.847334	292.683	8	10	1.22365	202.673	8	14	1.51089	164.142
0	11	0.861697	287.804	7	11	1.23115	201.438	4	17	1.51292	163.921
2	10	0.872313	284.301	3	14	1.23115	201.438	7	15	1.52504	162.619
7	6	0.882803	280.924	6	12	1.24355	199.43	1	19	1.52906	162.191
5	8	0.889727	278.737	0	16	1.25338	197.865	3	18	1.54105	160.929
4	9	0.903416	274.514	5	13	1.2607	196.716	6	16	1.54304	160.722
1	11	0.903416	274.514	2	15	1.2607	196.716	12	11	1.56083	158.889
3	10	0.923569	268.524	4	14	1.28242	193.385	10	13	1.56476	158.491
0	12	0.940033	263.821	10	9	1.28957	192.312	5	17	1.56476	158.491